

Multifunctional Self-Bearing Linear-Rotary Actuators with Wireless Power Transfer

Spasoje Mirić, Rosario V. Giuffrida, Prasad Jayathurathnage, Johann W. Kolar



Swiss Federal Institute of Technology (ETH) Zurich
Power Electronic Systems Laboratory
www.pes.ee.ethz.ch

December 5, 2022, Fiji



Outline

Part 1

- ▶ *Introduction*
- ▶ *LiRA Examples / Applications*
- ▶ *Linear Actuator with Integrated MBs*
- ▶ *Position Sensors*
- ▶ *Dynamic Modeling, Controller Design*
- ▶ *Generalized Complex Space Vector*
- ▶ *Double Stator LiRA*

- ▶ *Outlook*

Part 2

- ▶ *Introduction*
- ▶ *Application: Blood Pumps*
- ▶ *Sensors for SB-LiRAs*
- ▶ *Design Example: the ShuttlePump*

- ▶ *Outlook*

Part 3

- ▶ *Introduction*
- ▶ *WPT to Linear Actuators*
- ▶ *Orthogonal and Parallel Field Concept*
- ▶ *Supplying Multiple Receivers*
Voltage & Current Impressed WPT

- ▶ *Outlook*

Outline

Part 1

- ▶ *Introduction*
- ▶ *LiRA Examples / Applications*
- ▶ *Linear Actuator with Integrated MBs*
- ▶ *Position Sensors*
- ▶ *Dynamic Modeling, Controller Design*
- ▶ *Generalized Complex Space Vector*
- ▶ *Double Stator LiRA*

- ▶ *Outlook*

Part 2

- ▶ *Introduction*
- ▶ *Application: Blood Pumps*
- ▶ *Sensors for SB-LiRAs*
- ▶ *Design Example: the ShuttlePump*

- ▶ *Outlook*

Part 3

- ▶ *Introduction*
- ▶ *WPT to Linear Actuators*
- ▶ *Orthogonal and Parallel Field Concept*
- ▶ *Supplying Multiple Receivers*
Voltage & Current Impressed WPT

- ▶ *Outlook*

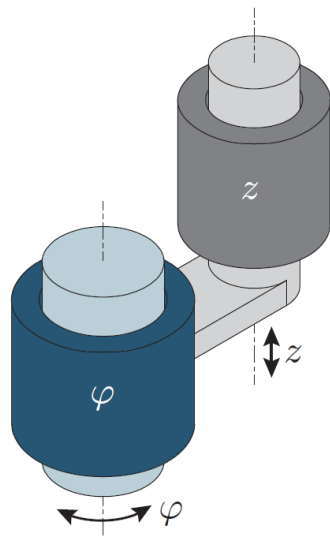


Introduction

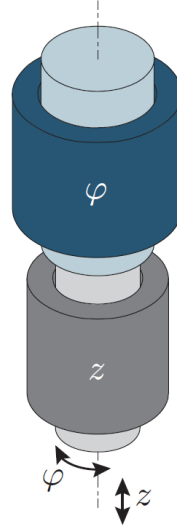
———— *Linear Rotary Actuators (LiRAs)* ————
Applications
LiRA Examples

Linear-Rotary Actuator (LiRA)

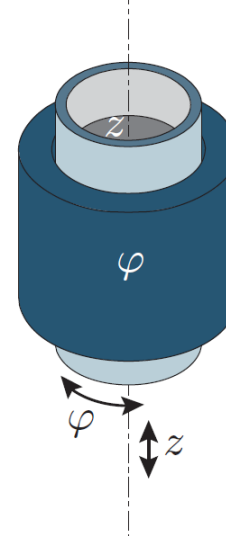
- LiRA is conceived by coupling Linear and Rotary actuators (machines)
- Types of coupling: Mechanical, Magnetic, Double Stator



■ Parallel Mechanical Coupling



■ Series Mechanical Coupling



■ Double Stator

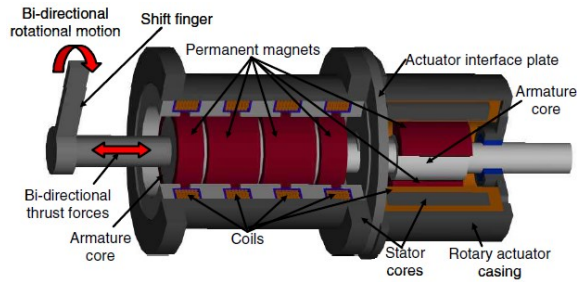


■ Magnetic Coupling

- Intended use determines the type of the LiRA, i.e., the type of coupling
- Parallel mechanical coupling → simple to realize, but low dynamics & moving cables

LiRA Application Examples

A wide spectrum of application areas: servo, tools, industrial automation, robot end-effector, blood pumps



Source: IEEE

■ Servo



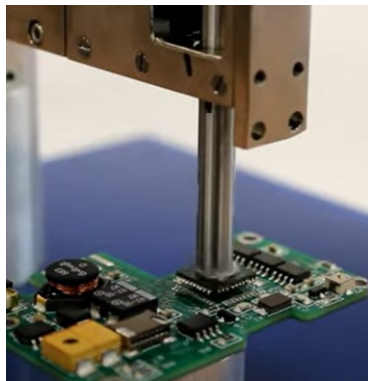
Source: RIDGID

■ Lathe



Source: FOOD manufacture

■ Industry Assembly Lines



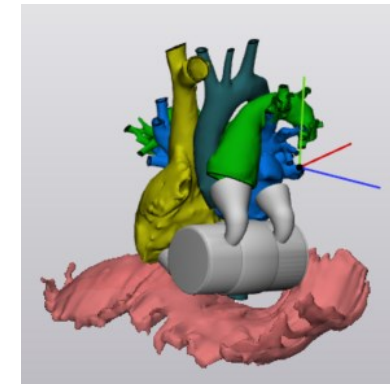
Source: SMAC Moving Coil Actuators

■ Pick & Place Robot in Electronics/Semiconductor Industry



Source: camfil

■ Handling/Dosing in Pharmaceutical/Chemical Industry

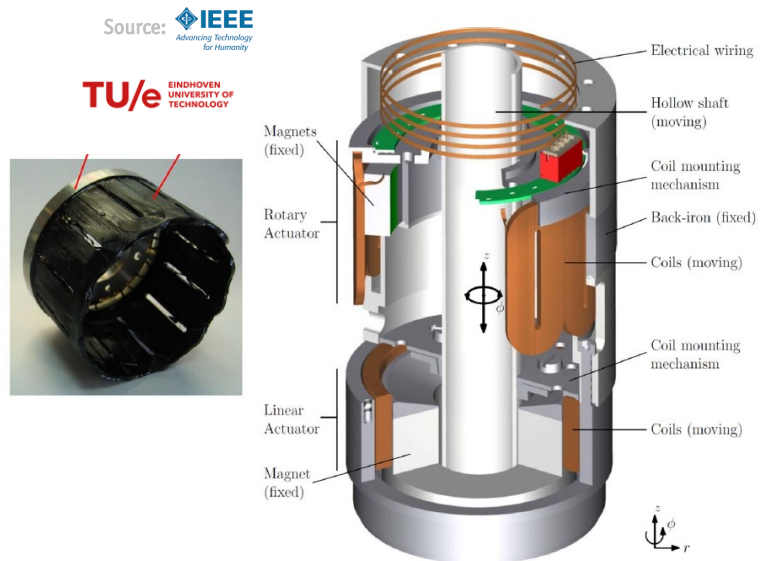


Source: MEDIZINISCHE UNIVERSITÄT WIEN

■ ShuttlePump

LiRA Example 1

- Series mechanical coupling → three-phase slotless PM rotary actuator (top) & linear actuator (bottom)
- Pick&Place LiRA enables rotational and translational motion for small component placement



■ LiRA or $z\phi$ -Actuator

Parameter	Value
z_{stroke}	± 5 mm
ϕ_{stroke}	$\pm 180^\circ$ degrees
z_{err}	5 μ m
ϕ_{err}	3 mrad
α_z	150 $m\ s^{-2}$
α_ϕ	7700 $rad\ s^{-2}$
v_{max}	3 $m\ s^{-1}$
ω_{max}	135 $rad\ s^{-1}$
d_z	0.22
d_ϕ	0.39
$L_{z\phi}$	105 mm
$r_{o,max}$	30 mm
$r_{i,min}$	18 mm

■ Specifications

➔ High accelerations required

➔ Rather a low max. speed

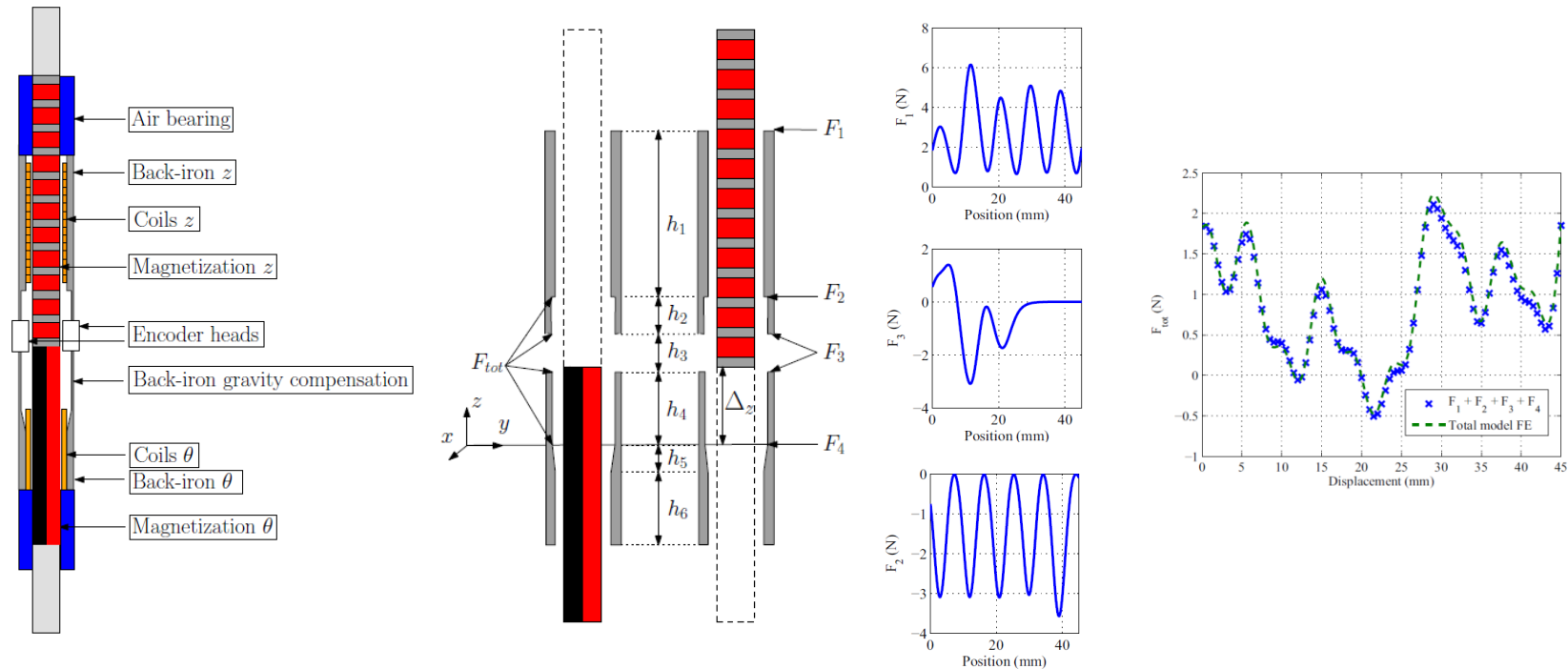
- Component placement throughput → high dynamics/accelerations
- Actuator operation → low speeds due to limited stroke (acceleration/deceleration)

[ref] Overboom, T. T., et al. "Design and Optimization of a Rotary Actuator for a Two-Degree-of-Freedom $z\phi$ -Module." IEEE Transactions on Industry Applications 46.6 (2010): 2401-2409.

LiRA Example 2

- Series mechanical coupling → three-phase rotary actuator & three-phase linear actuator
- Pick&Place LiRA enables rotational and translational motion for small component placement

Source:  Advancing Technology for Humanity
 Eindhoven University of Technology



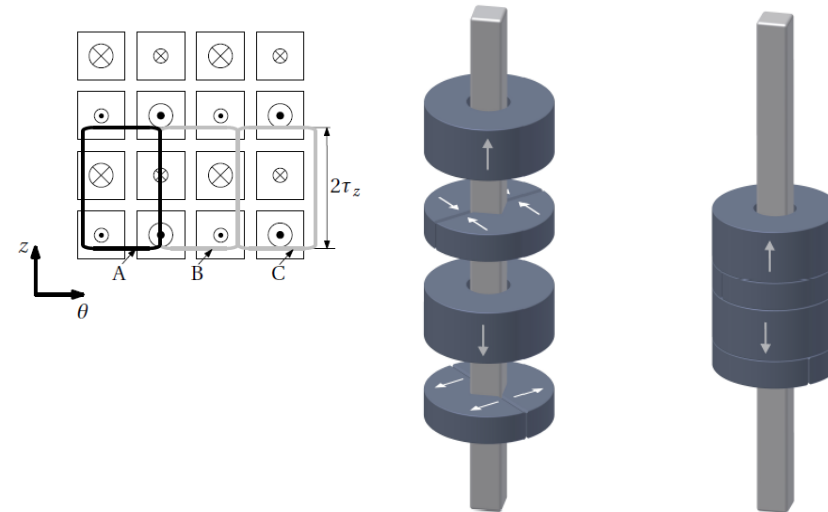
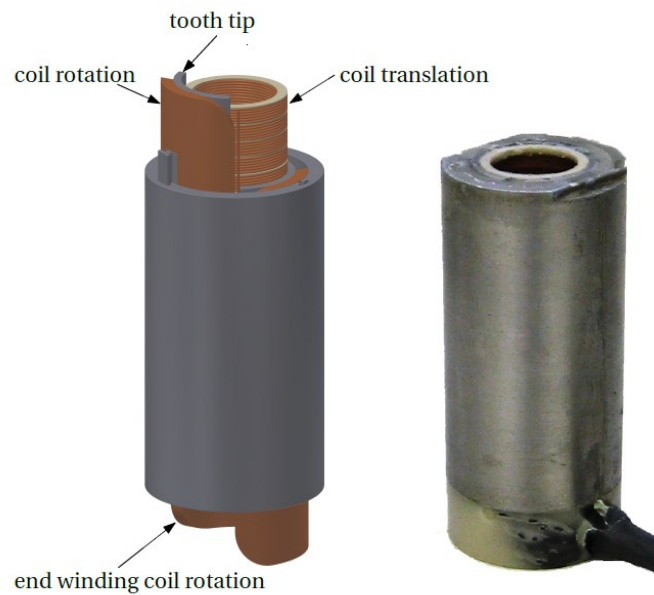
- Cogging force due to end effects → minimization by optimizing stator core geometry / placement
- Passive gravity compensation → force profile optimized in 3D-FEM by varying geometry

[ref] Meessen, K. J., J. J. H. Paulides, and E. A. Lomonova. "Analysis and design considerations of a 2-DoF rotary-linear actuator." 2011 IEEE International Electric Machines & Drives Conference (IEMDC). IEEE, 2011.

LiRA Example 3

- Three-phase rotary actuator & slotless linear actuator winding in the air gap
- Pick&Place LiRA enables rotational and translational motion for small component placement

Source:  Advancing Technology for Humanity
 Eindhoven University of Technology

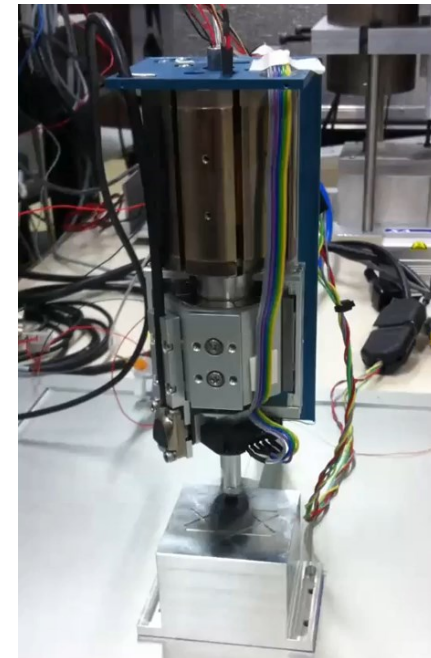
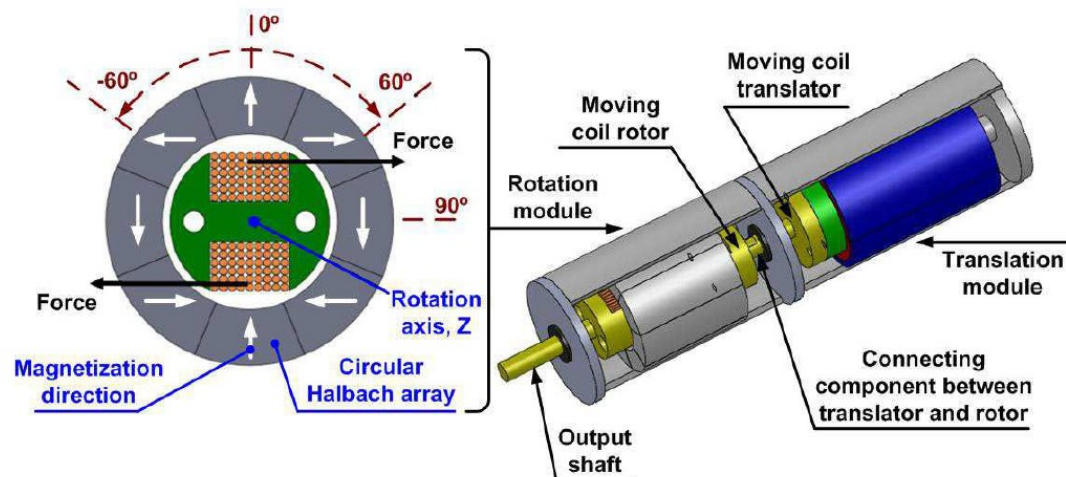


- Single set of mover permanent magnets → special arrangement to interact with rotary and linear windings
- Large air gap → low cogging force; but low machine constant

[ref] Meessen, Koen Joseph. "Electromagnetic fields and interactions in 3D cylindrical structures: Modeling and application." Dept. Electric Eng., Eindhoven Univ. Technol., the Netherlands (2012).

LiRA Example 4

- **Moving coil rotary actuator & moving coil linear actuator**
- **Pick&Place LiRA enables rotational and translational motion for small component placement**

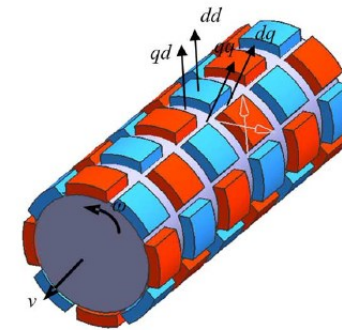
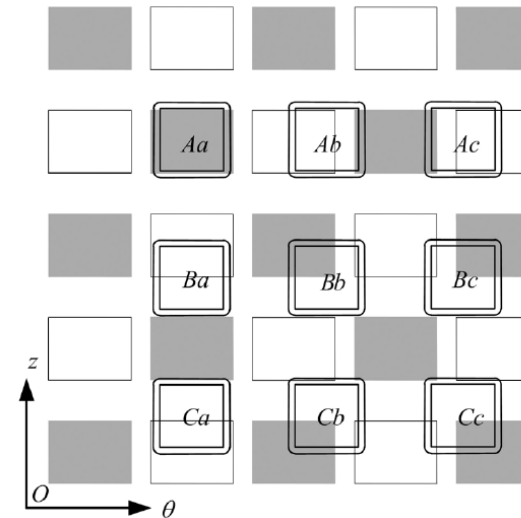
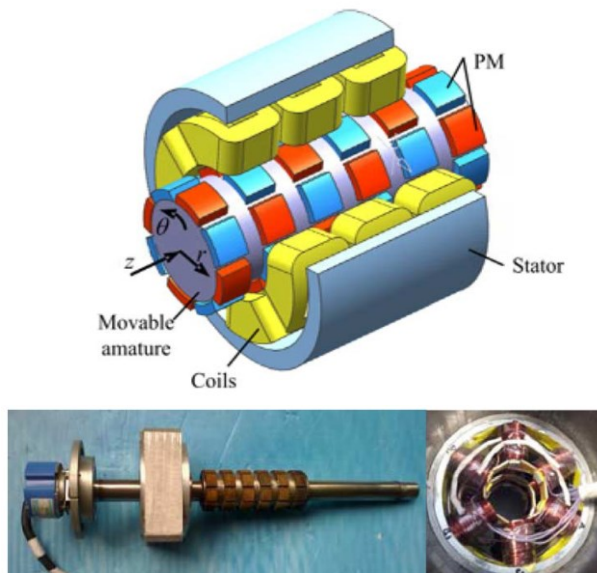


- **Limited rotary stroke due to permanent magnet field arrangement → parts with no radial field**
- **Moving coils → moving cables limit lifetime**

[ref] Teo, Tat Joo, et al. "Principle and modeling of a novel moving coil linear-rotary electromagnetic actuator." IEEE Transactions on Industrial Electronics 63.11 (2016): 6930-6940.

LiRA Example 5

- Concentrated coils in linear and rotary direction → 'checkerboard actuator'
- Checkerboard direct drive LiRA enables rotational and translational motion

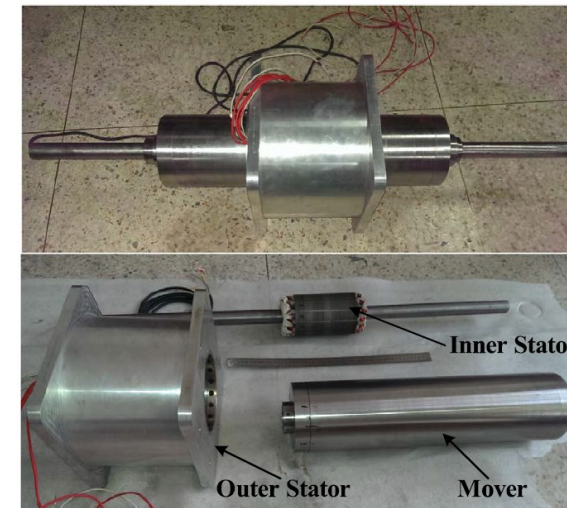
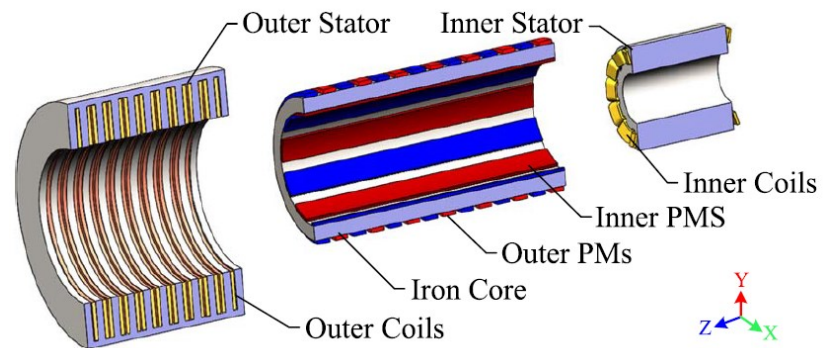


- LiRA with magnetic coupling → highest compactness, increased number of phases, increased control effort
- Ideally no end windings → end winding for the linear direction is an active part of the winding for rotary direction

[ref] Jin, Ping, et al. "3-D analytical linear force and rotary torque analysis of linear and rotary permanent magnet actuator." IEEE transactions on magnetics 49.7 (2013): 3989-3992.

LiRA Example 6

- **Double stator LiRA** → 'magnetically insulated' linear and rotary parts
- **Three-phase linear and rotary machines, controlled independently**

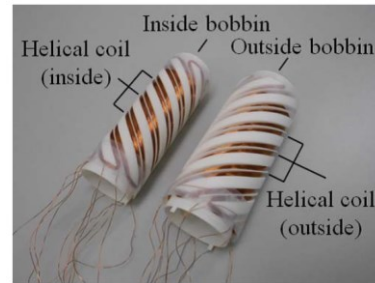
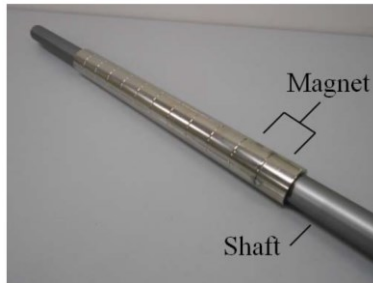
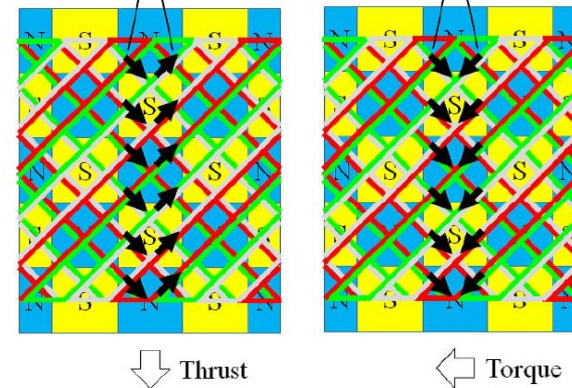
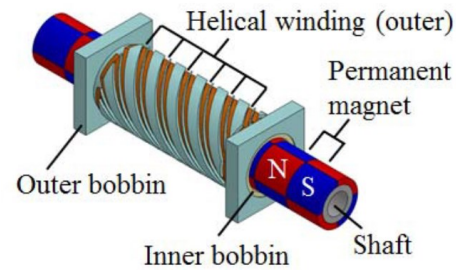


- **Large force (650 N) / torque (10 Nm), dynamics limited due to the large moving mass of the mover**
- **Challenging design** → cooling of the inner stator, mover back iron with two sets of PMs

[ref] Xu, Lei, et al. "Design and analysis of a double-stator linear-rotary permanent-magnet motor." IEEE Transactions on Applied Superconductivity 26.4 (2016): 1-4.

LiRA Example 7

- Helical winding (inner and outer) → independent thrust force and torque generation/control
- Slotless LiRA proposed usage for surgery robots in medicine



- Limited force (5 N)/torque (0.1 Nm) due to slotless winding, helical winding complicated to realize
- Mover PMs the same as for the checkerboard actuator

[ref] Tanaka, Shodai, Tomoyuki Shimono, and Yasutaka Fujimoto. "Optimal design of length factor for cross-coupled 2-DOF motor with Halbach magnet array." 2015 IEEE International Conference on Mechatronics (ICM). IEEE, 2015.



Need for Improvements

—————

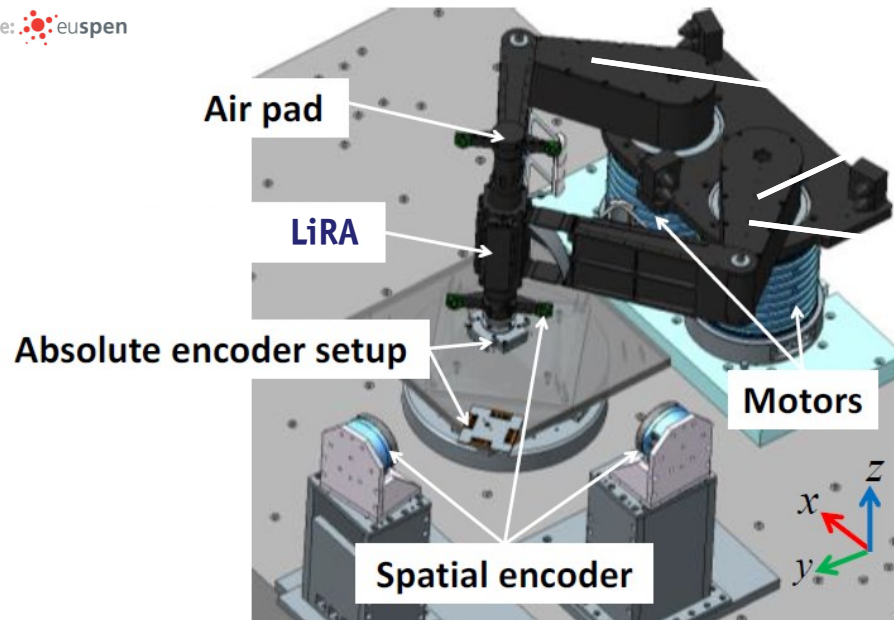
Application Requirements
Conventional Bearings
Bearingless / Self-bearing

—————

High Precision Requirement

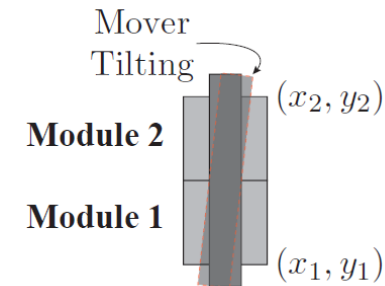
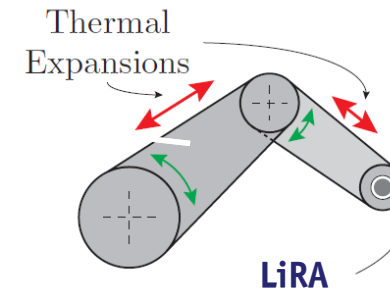
- High dynamics robot → reaches accelerations of 150 m/s^2 and speeds of 5 m/s
- Horizontal workspace of $300 \text{ mm} \times 300 \text{ mm}$; repeatability $< 10 \mu\text{m}$

Source:  euspen



Parallel Kinematics

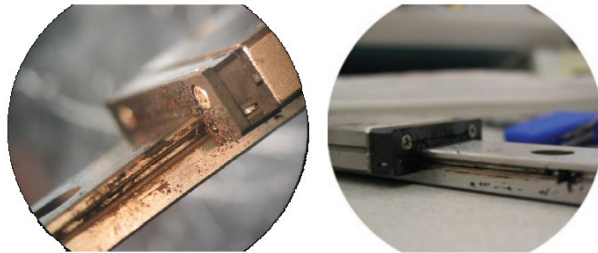
Can be water cooled to limit thermal expansions



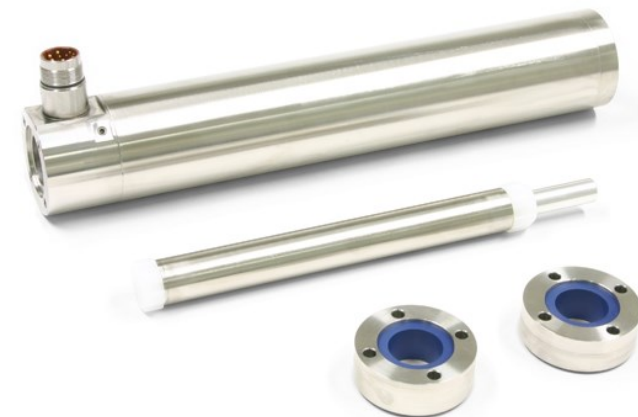
- Thermal expansions in parallel kinematics deteriorate precision → LiRA with radial position control
- Handling smaller components/dies → mover tilting necessary
- Mechanical/air bearings used in conventional LiRAs can not control radial position nor tilting

High Purity Requirement

- Applications requiring high purity → clean rooms, bioprocessing, pharmaceutical
- Mechanical bearings → limited lifetime / limited purity levels / often disassembling for cleaning



■ Mechanical bearings compromise high purity



Source: **LinMot®**

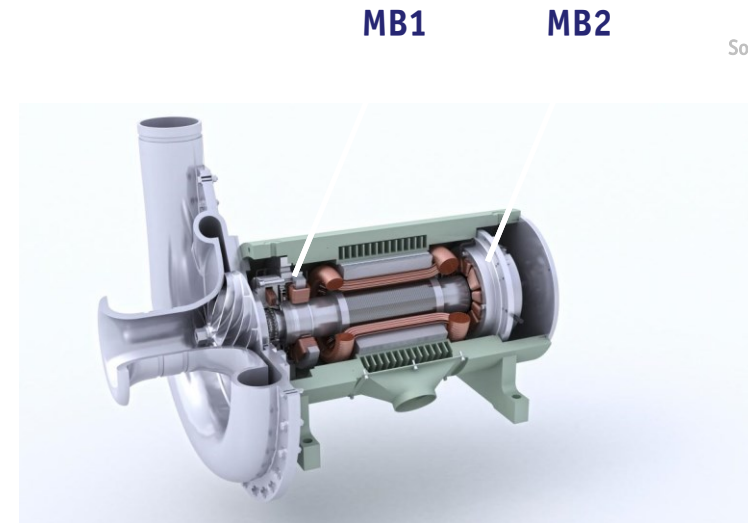
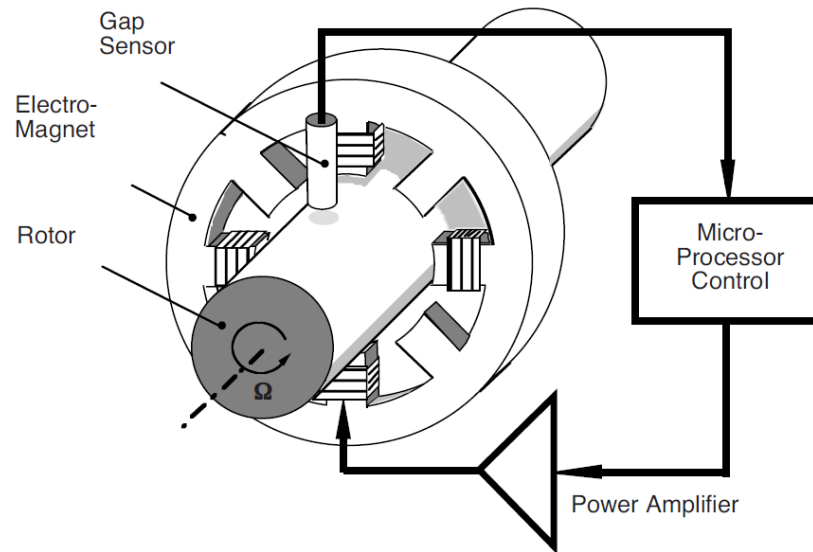
■ Disassembling for regular high-pressure washdowns

- Air bearings → require air supply / prohibited operation in low-pressure environments
- High precision & high purity requirements limit usage of LiRAs with conventional bearings

[ref] Paulides, Johannes JH, Jeroen LG Janssen, and Elena A. Lomonova. "Bearing lifetime of linear PM machines." 2009 IEEE Energy Conversion Congress and Exposition. IEEE, 2009.

Magnetic Bearings (MBs)

- **Magnetic bearings** → generate radial forces to keep the rotor/mover centered
- **Closed loop position controller** → sensor, microcontroller, power converter, MB windings



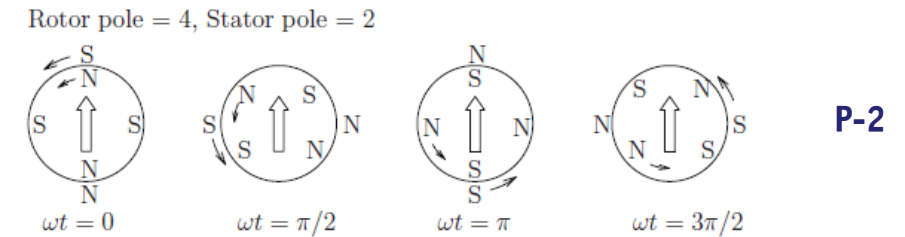
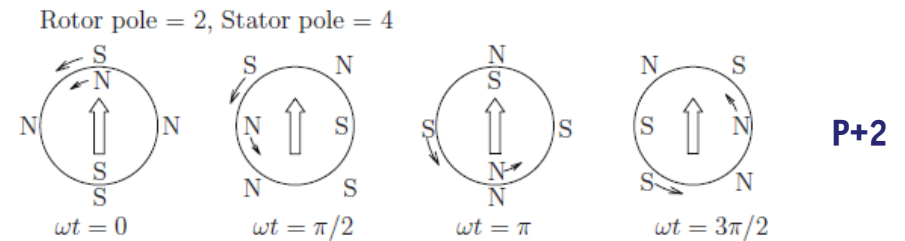
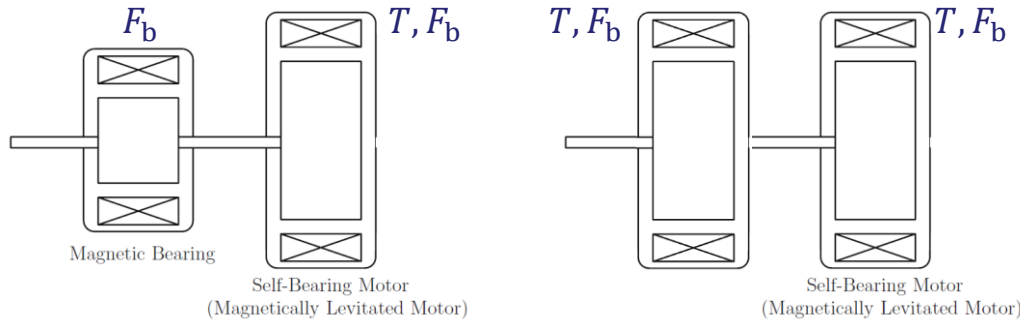
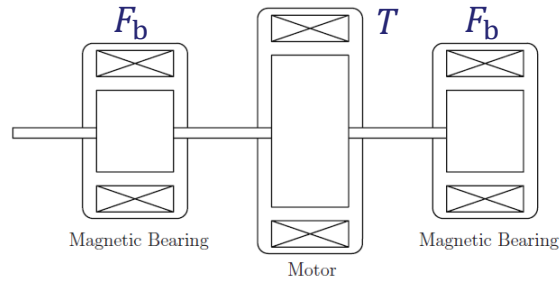
Source: 

- **Characteristics** → free of contact, no contaminating wear, bearing stiffness control, low maintenance
- **Applications** → vacuum and clean room system, high-speed pumps, high-purity pumps, flywheels

[ref] Maslen, Eric H., and Gerhard Schweitzer, eds. Magnetic bearings: theory, design, and application to rotating machinery. Berlin, Heidelberg: Springer-Verlag Berlin Heidelberg, 2009.

Standalone MBs and Self-bearing/Bearingless Machines

- **Self-bearing/Bearingless** → integrate MBs into the existing machine structure
- **Achieve self-bearing function** → superimpose the main field (torque, p poles) with the $p \pm 2$ type

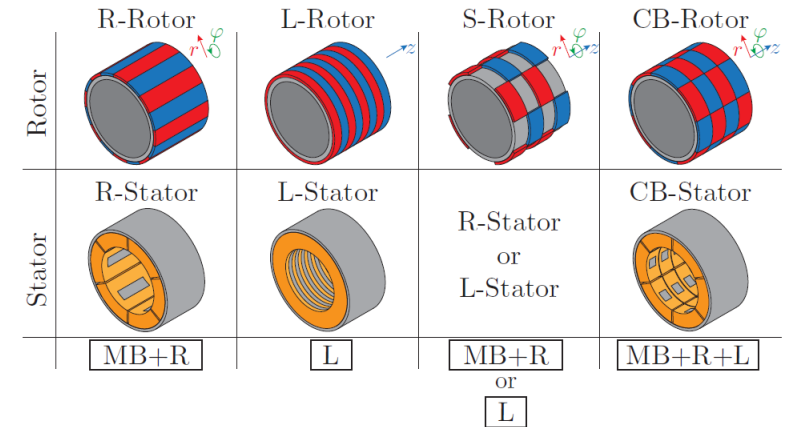
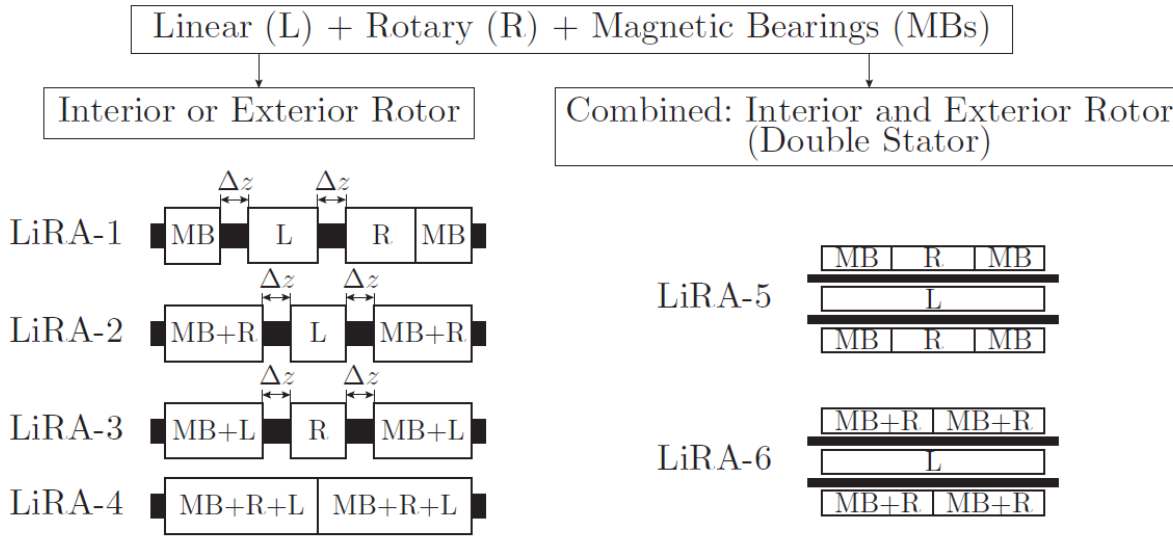


- **Tilting control of the long shaft** → either (F_b) & (T, F_b) or (T, F_b) & (T, F_b)
- $p \pm 2$ type is achieved by winding scheme or current distribution in the existing main windings

[ref] Maslen, Eric H., and Gerhard Schweitzer, eds. Magnetic bearings: theory, design, and application to rotating machinery. Berlin, Heidelberg: Springer-Verlag Berlin Heidelberg, 2009.

LiRA with MBs

- Integrating MBs into a LiRA → various combinations of standalone and self-bearing options are possible
- Tilting control of the mover necessary → MBs always at each axial end of a LiRA

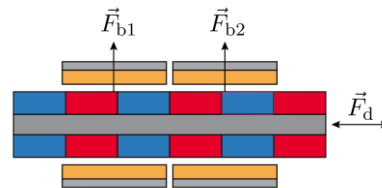


- Distance between the segments $\Delta z = \text{linear stroke}$ → due to different PM arrangements in the mover
- MB + R → conventional; MB + L → interesting for further investigation!

[ref] Mirić, Spasoje, Dominik Bortis, and Johann Walter Kolar. "Design and comparison of permanent magnet self-bearing linear-rotary actuators." 2019 12th International Symposium on Linear Drives for Industry Applications (LDIA). IEEE, 2019.

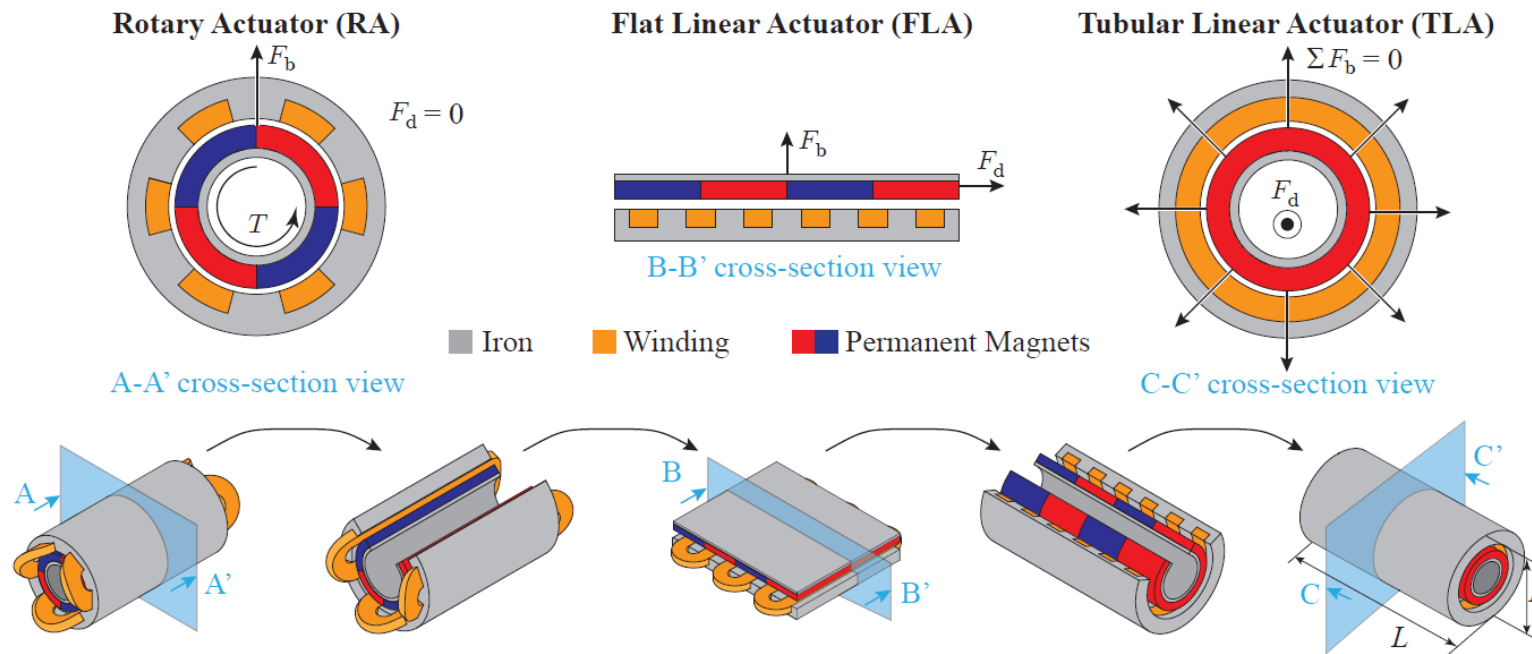
Linear Actuator with Integrated MBs

Topology Derivation
Bearing Force Generation
Inverter Supply Requirements



Tubular Linear Actuator Derivation

- Derivation of TLA → tangential force for generating T in RA, generates drive F_d force in TLA
- TLA has fewer stray field compared to FLA due to the closed structure

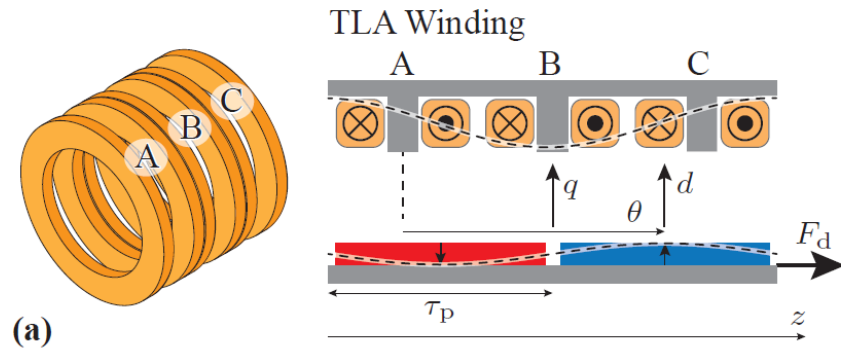


- TLA has circumferential symmetry → it can not generate bearing (radial) force, i.e., no MBs are possible
- FLA can generate bearing force F_b , but there is an attraction force between the mover PMs and the stator iron

[ref] Mirić, Spasoje, Johann W. Kolar, and Dominik Bortis. "Novel tubular linear actuator with integrated magnetic bearing." e & i Elektrotechnik und Informationstechnik 139.2 (2022): 230-242.

Tubular Linear Actuator (TLA)

- **Three-phase ring windings** → maximum usage of copper, no end winding
- ***d* axis aligned with the peak flux density wave of the mover; θ is the electrical angle in a linear direction**

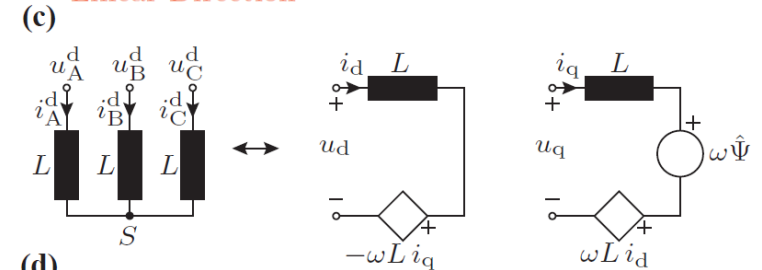


$$\begin{bmatrix} x_A^d & x_B^d & x_C^d \end{bmatrix} = \begin{bmatrix} x_d & x_q \end{bmatrix} \begin{bmatrix} \cos(\theta + \gamma_A) & \cos(\theta + \gamma_B) & \cos(\theta + \gamma_C) \\ -\sin(\theta + \gamma_A) & -\sin(\theta + \gamma_B) & -\sin(\theta + \gamma_C) \end{bmatrix}$$

(b)

$$\begin{bmatrix} x_d & x_q \end{bmatrix} = \begin{bmatrix} x_A^d & x_B^d & x_C^d \end{bmatrix} \times \frac{2}{3} \begin{bmatrix} \cos(\theta + \gamma_A) & -\sin(\theta + \gamma_A) \\ \cos(\theta + \gamma_B) & -\sin(\theta + \gamma_B) \\ \cos(\theta + \gamma_C) & -\sin(\theta + \gamma_C) \end{bmatrix}$$

Linear Direction



(d)

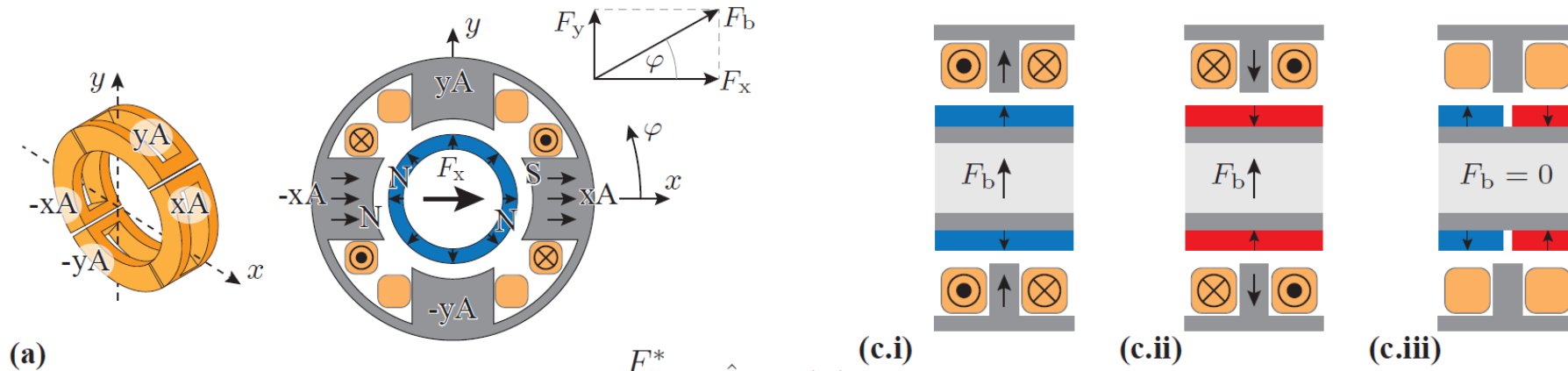
$$\begin{aligned} i_A^d &= \hat{I}_d \cos(\theta + \theta_i^d + \gamma_A) \\ i_B^d &= \hat{I}_d \cos(\theta + \theta_i^d + \gamma_B) \\ i_C^d &= \hat{I}_d \cos(\theta + \theta_i^d + \gamma_C) \end{aligned} \quad i_d^* = 0 \quad i_q^* = \hat{I}_d = \frac{F_d^*}{K_d} \quad K_d = \frac{3\pi}{2\tau_p} \hat{\Psi}$$

- **TLA can generate linear drive force F_d ; bearing force F_b is not possible to achieve with the TLA**
- ***dq* coordinated in a linear direction** → stationary coordinates representation of the three-phase winding

[ref] Mirić, Spasoje, Dominik Bortis, and Johann Walter Kolar. "Design and comparison of permanent magnet self-bearing linear-rotary actuators." 2019 12th International Symposium on Linear Drives for Industry Applications (LDIA). IEEE, 2019.

xy Winding for Bearing Force Generation/Control

- A coil of the TLA split into 4 pieces, x – and y –direction \rightarrow bearing force F_b generation possible
- Bearing force generation capability \rightarrow depends on the linear position of the mover/PM poles



$$F_b = \sqrt{F_x^2 + F_y^2}$$

$$\varphi = \arctan 2(F_x, F_y)$$

$$i_x^* = \frac{F_x^*}{K_b} = \hat{I}_b \cos(\varphi)$$

$$i_y^* = \frac{F_y^*}{K_b} = \hat{I}_b \sin(\varphi)$$

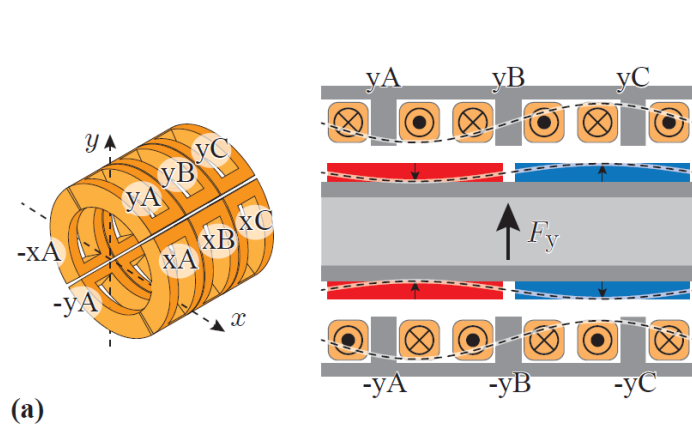
■ d – current component in a linear direction needed

- F_b generation possible if PM is facing the stator teeth \rightarrow as long as there is non-zero flux linkage
- Mover/PM linear position changes in during the operation of the actuator

[ref] Mirić, Spasoje, Dominik Bortis, and Johann Walter Kolar. "Design and comparison of permanent magnet self-bearing linear-rotary actuators." 2019 12th International Symposium on Linear Drives for Industry Applications (LDIA). IEEE, 2019.

xy Winding and Three-Phase ABC Linear Winding

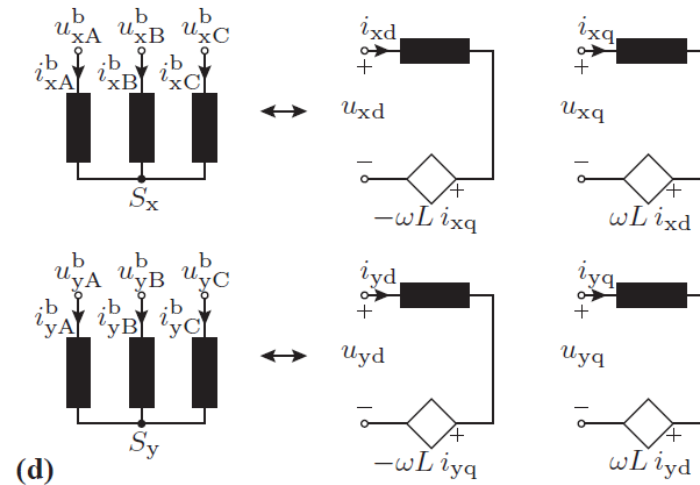
- Bearing force currents \rightarrow 'd - component' in a linear direction, must not generate drive (linear) force
- xy - current components (circumferential) \rightarrow determined by the desired force direction



(a)

$$i_{xd}^* = i_x^* = \frac{F_x^*}{K_b} \quad i_{xq}^* = 0$$

$$i_{yd}^* = i_y^* = \frac{F_y^*}{K_b} \quad i_{yq}^* = 0,$$



(d)

$$i_{x\{A,B,C\}}^* = i_{xd}^* \cdot \cos(\theta + \theta_i^b + \gamma_{\{A,B,C\}})$$

$$i_{y\{A,B,C\}}^* = i_{yd}^* \cdot \cos(\theta + \theta_i^b + \gamma_{\{A,B,C\}})$$

- i_{xd}^* and i_{yd}^* calculated from the force components that should act on the mover (e.g., obtained by position controller)
- θ is the electrical angle determined by the mover's axial position $z \rightarrow \theta = \pi \cdot z / \tau_p$

[ref] Mirić, Spasoje, Dominik Bortis, and Johann Walter Kolar. "Design and comparison of permanent magnet self-bearing linear-rotary actuators." 2019 12th International Symposium on Linear Drives for Industry Applications (LDIA). IEEE, 2019.

xydq Transformation

- 4 stationary components → xy for bearing force (rotary dir.) & dq for drive force (linear dir.)
- Variable x can be vottage v, current i or flux linkage ψ

$$\begin{array}{c} \text{Rotary Direction} \\ \downarrow \end{array} \begin{array}{c} \xrightarrow{\text{Linear Direction}} \\ \left[\begin{array}{cc} x_{xd} & x_{xq} \\ x_{yd} & x_{yq} \end{array} \right] = \begin{array}{c} \xrightarrow{\text{Linear Direction}} \\ \left[\begin{array}{ccc} x_{xA}^b & x_{xB}^b & x_{xC}^b \\ x_{yA}^b & x_{yB}^b & x_{yC}^b \end{array} \right] \times \frac{2}{3} \left[\begin{array}{cc} \cos(\theta + \gamma_A) & -\sin(\theta + \gamma_A) \\ \cos(\theta + \gamma_B) & -\sin(\theta + \gamma_B) \\ \cos(\theta + \gamma_C) & -\sin(\theta + \gamma_C) \end{array} \right] \end{array} \begin{array}{c} \downarrow \text{Linear Direction} \\ \text{xydq Transformation} \end{array} \\ \text{xydq} \qquad \text{xyABC}
 \end{array}$$

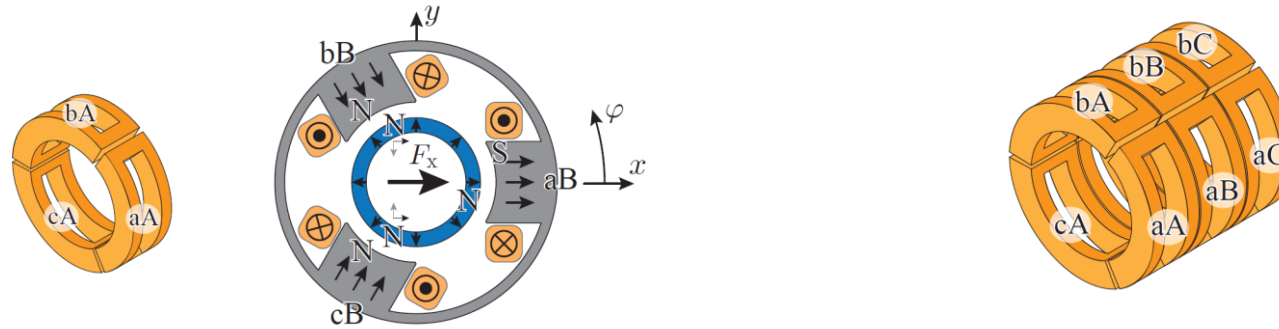
$$\begin{array}{c} \text{Rotary Direction} \\ \downarrow \end{array} \begin{array}{c} \xrightarrow{\text{Linear Direction}} \\ \left[\begin{array}{ccc} x_{xA}^b & x_{xB}^b & x_{xC}^b \\ x_{yA}^b & x_{yB}^b & x_{yC}^b \end{array} \right] = \begin{array}{c} \xrightarrow{\text{Linear Direction}} \\ \left[\begin{array}{cc} x_{xd} & x_{xq} \\ x_{yd} & x_{yq} \end{array} \right] \times \left[\begin{array}{ccc} \cos(\theta + \gamma_A) & \cos(\theta + \gamma_B) & \cos(\theta + \gamma_C) \\ -\sin(\theta + \gamma_A) & -\sin(\theta + \gamma_B) & -\sin(\theta + \gamma_C) \end{array} \right] \end{array} \begin{array}{c} \xrightarrow{\text{Linear Direction}} \\ \text{Inverse xydq Transformation} \end{array} \\ \text{xyABC} \qquad \text{xydq}
 \end{array}$$

- 12 phase windings, but 6 phase quantities → windings on the same axis connected in series
- Linear direction → ABC – three-phase quantities; dq – stationary coordinates quantities

[ref] Mirić, Spasoje, Dominik Bortis, and Johann Walter Kolar. "Design and comparison of permanent magnet self-bearing linear-rotary actuators." 2019 12th International Symposium on Linear Drives for Industry Applications (LDIA). IEEE, 2019.

abc Winding for Bearing and ABC Winding for Linear Motion

- Bearing force control with a three-phase winding *abc* → *xy* current components determine the \hat{I}_b and φ
- φ - electrical angle for rotary direction; θ - electrical angle for linear direction



$$i_{xd}^* = i_x^* = \frac{F_x^*}{K_b}$$

$$i_{yd}^* = i_y^* = \frac{F_y^*}{K_b}$$

$$i_{xq}^* = 0$$

$$i_{yq}^* = 0,$$



$$\hat{I}_b = \sqrt{(i_{xd}^*)^2 + (i_{yd}^*)^2}$$

$$\varphi = \arctan 2(i_{xd}^*, i_{yd}^*)$$



$$i_{a\{A,B,C\}}^b = \hat{I}_b \cos(\varphi + \gamma_a) \cdot \cos(\theta + \theta_i^b + \gamma_{\{A,B,C\}})$$

$$i_{b\{A,B,C\}}^b = \hat{I}_b \cos(\varphi + \gamma_b) \cdot \cos(\theta + \theta_i^b + \gamma_{\{A,B,C\}})$$

$$i_{c\{A,B,C\}}^b = \hat{I}_b \cos(\varphi + \gamma_c) \cdot \cos(\theta + \theta_i^b + \gamma_{\{A,B,C\}})$$

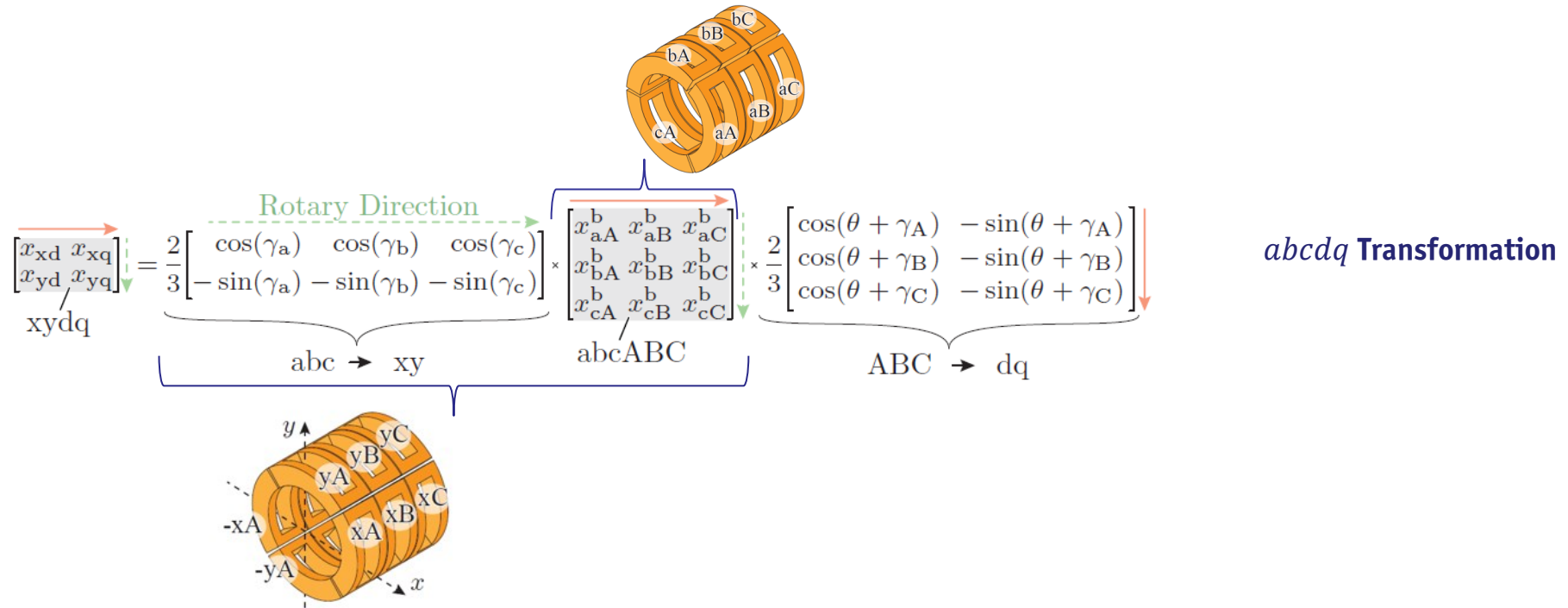
$$\gamma_A = 0, \gamma_B = -2\pi/3, \gamma_C = 2\pi/3$$

- Comparison between *xy* and *abc* winding type → capability for the bearing F_b and the drive F_d force generation
- Rotary direction → *abc* - three-phase quantities; *xy* - stationary coordinates quantities

[ref] Mirić, Spasoje, Dominik Bortis, and Johann Walter Kolar. "Design and comparison of permanent magnet self-bearing linear-rotary actuators." 2019 12th International Symposium on Linear Drives for Industry Applications (LDIA). IEEE, 2019.

abcdq Transformation

- 4 stationary components → *xy* for bearing force (rotary dir.) & *dq* for drive force (linear dir.)
- Variable *x* can be vottage *v*, current *i* or flux linkage ψ



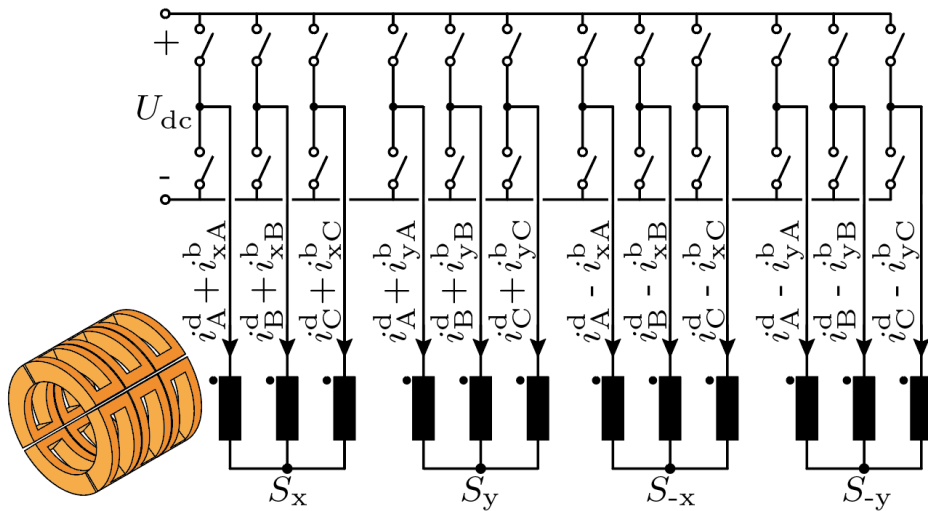
- *abcABC* winding, three-phase rotary and three-phase linear → 9 phase quantities
- Bearing current component & Drive current component → *combined* or *separated* windings

[ref] Mirić, Spasoje, Dominik Bortis, and Johann Walter Kolar. "Design and comparison of permanent magnet self-bearing linear-rotary actuators." 2019 12th International Symposium on Linear Drives for Industry Applications (LDIA). IEEE, 2019.

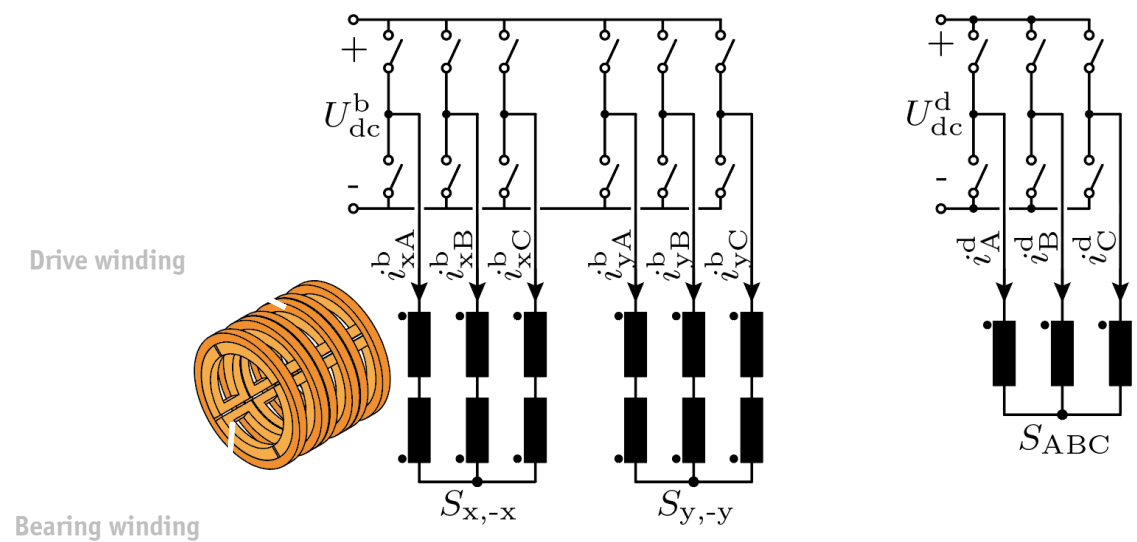
xyABC Winding Inverter Supply

- Bearing force and driving force function → realized with the *combined* or *separated* windings
- Combined winding → each phase winding contains the *bearing* and the *drive* current components

■ Combined winding, 12 half-bridges



■ Separated winding, 9 half-bridges



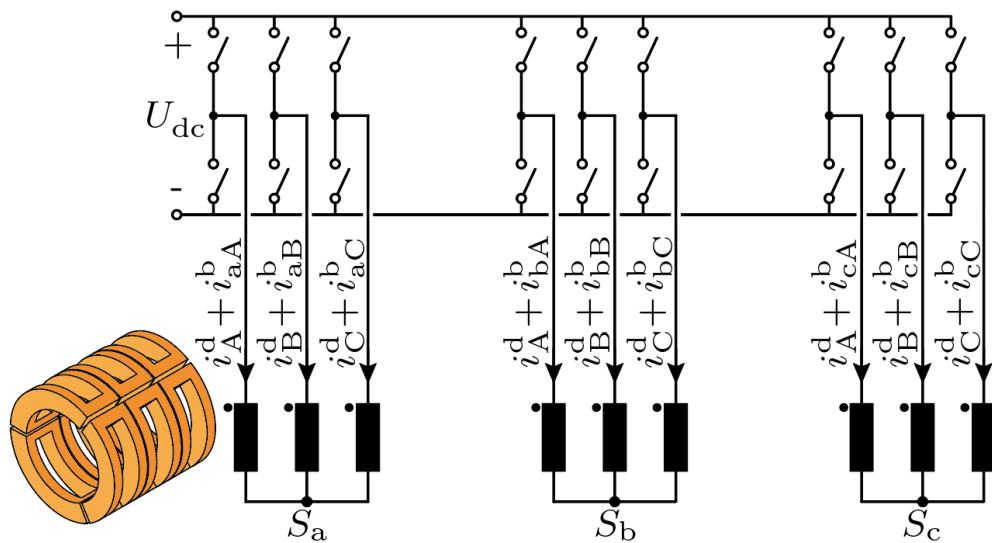
- Combined winding → each winding needs a dedicated half-bridge; star points with the linear three-phase system
- Separated winding → anti-series connection of the bearing windings, no induced back EMF

[ref] Mirić, Spasoje, Dominik Bortis, and Johann Walter Kolar. "Design and comparison of permanent magnet self-bearing linear-rotary actuators." 2019 12th International Symposium on Linear Drives for Industry Applications (LDIA). IEEE, 2019.

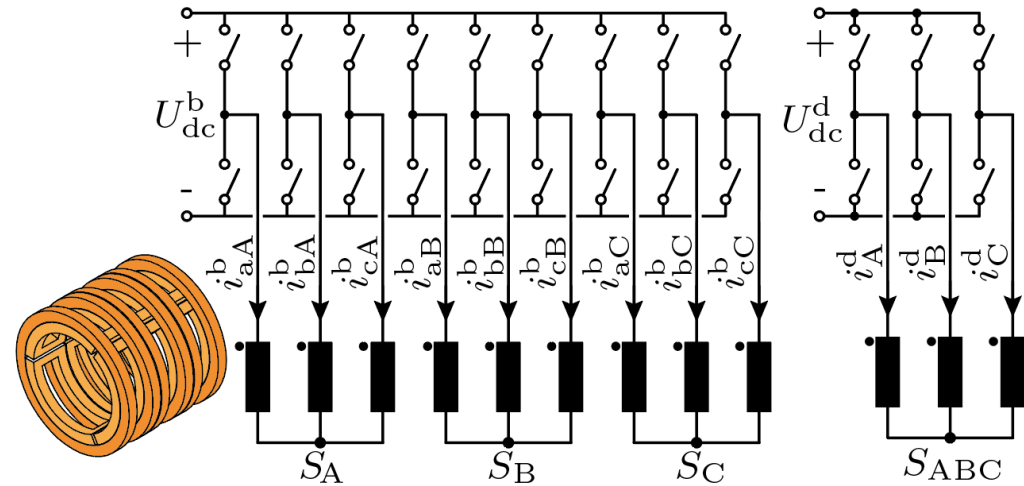
abcABC Winding Inverter Supply

- Bearing force and driving force function → realized with the *combined* or *separated* windings
- Combined winding → each phase winding contains the *bearing* and the *drive* current components

■ Combined winding, 9 half-bridges



■ Separated winding, 12 half-bridges

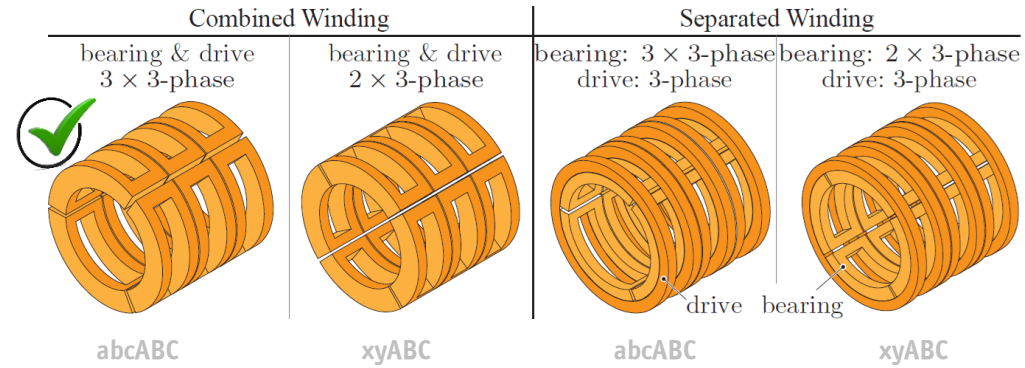
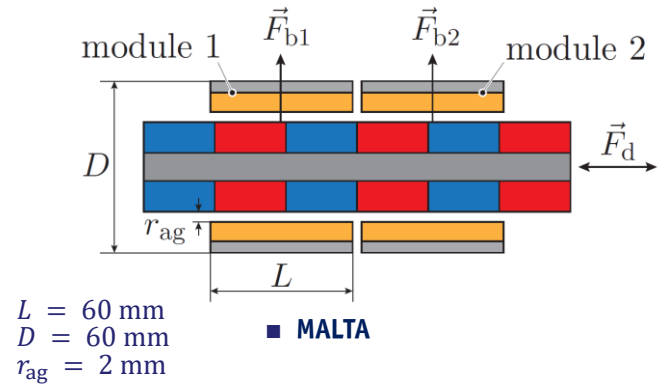


- Combined winding → each winding needs a dedicated half-bridge; star points with the linear three-phase system
- Comparison in terms of the bearing and the drive force generation capability → combined versus separated windings

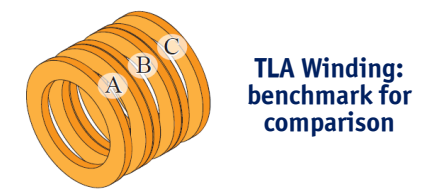
[ref] Mirić, Spasoje, Dominik Bortis, and Johann Walter Kolar. "Design and comparison of permanent magnet self-bearing linear-rotary actuators." 2019 12th International Symposium on Linear Drives for Industry Applications (LDIA). IEEE, 2019.

Comparison of the Winding Types

- **Magnetically Levitated Tubular Actuator (MALTA)**
- **2 modules necessary to control the tilting of the mover**



Winding Realization	Shown	Force/ $F_{d,TLA}$		Number of Half-bridges → for 2 modules
		Drive	Bearing	
Combined				
3 × 3-phase	Fig. 4.10(a)	0.78	1.12	18
2 × 3-phase	Fig. 4.10(b)	0.76	1.1	24
Separated				
3 × 3-phase +3-phase	Fig. 4.10(c)	0.57	0.81	24
2 × 3-phase +3-phase	Fig. 4.10(d)	0.29	0.46	18

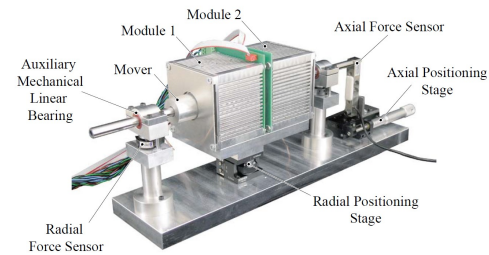


- **Comparison with respect to the driving force of the conventional TLA; 15 W of copper losses; fixed volume**
- **abcABC winding or 3 × 3 phase MALTA → the largest forces; the lowest number of the inverter half-bridges**

[ref] Spasoje Miric, 'Linear-Rotary Bearingless Actuators,' PhD Thesis, ETH Zurich, 2021.

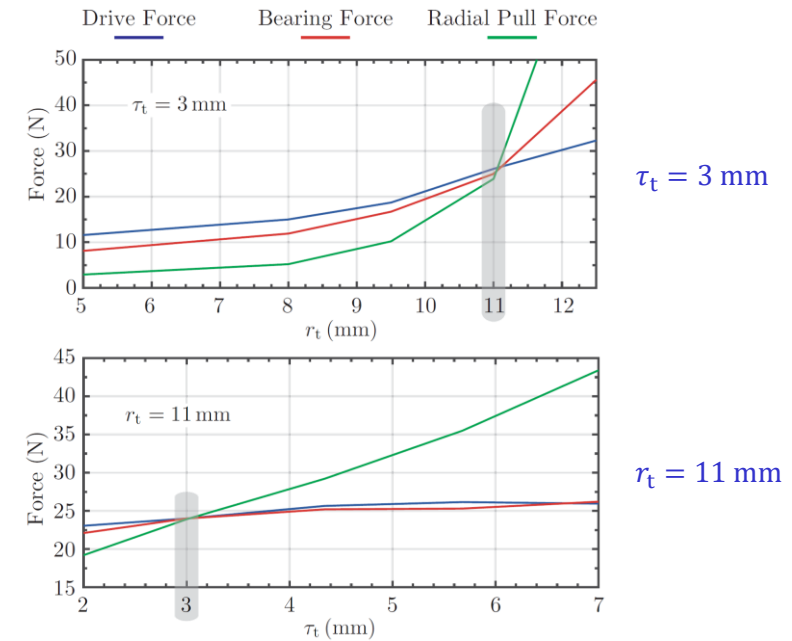
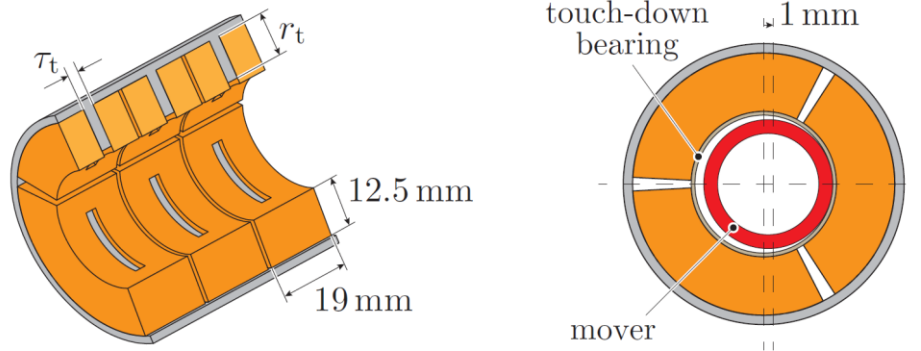
MALTA Prototype Design

Magnetic Design 18-phase Inverter Supply Verification Measurements



Stator Design

- Choice of the tooth width τ_t and the tooth depth r_t → considering drive, bearing, pull forces
- Scenario for the pull force calculation → the mover sitting on the touch-down bearing (start-up of the MBs)

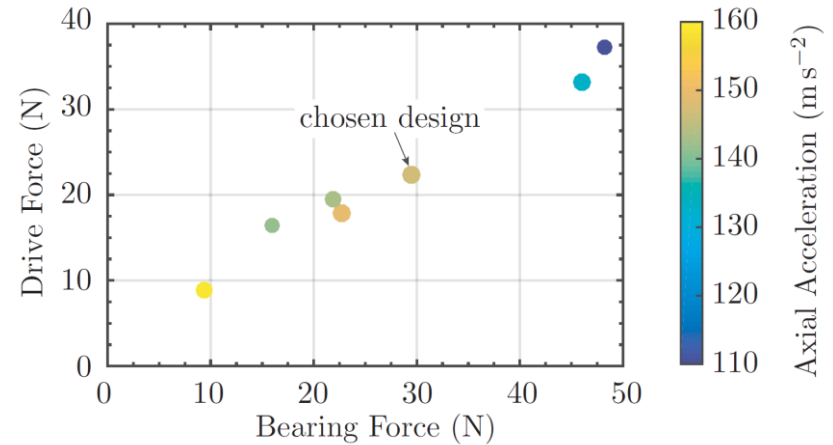
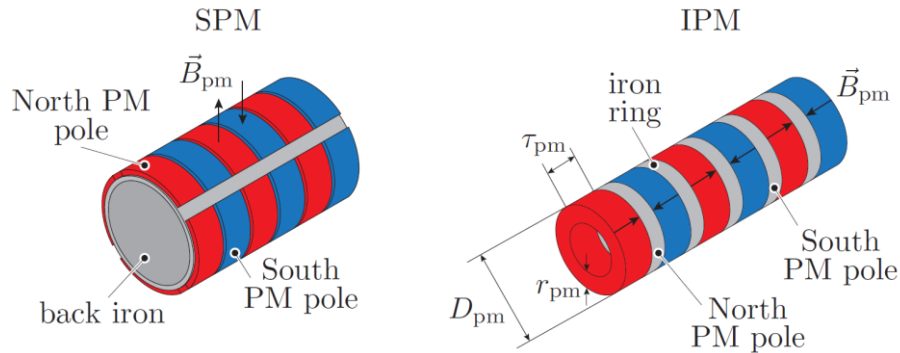


- The drive and the bearing forces → obtained for the maximally possible continuous copper losses
- Geometry parameters τ_t and r_t → chosen such that the pull force is lower than the bearing force

[ref] Mirić, Spasoje, et al. "Design and experimental analysis of a new magnetically levitated tubular linear actuator." IEEE Transactions on Industrial Electronics 66.6 (2018): 4816-4825.

Mover Design

- Two mover types considered → surface-mounted PMs (SPM) and interior PMs (IPM)
- First step → parameter range calculated using scaling laws



■ PM geometry range from the scaling law:

$$\frac{D_{pm} + 2r_{ag}}{D - 2r_{bi}} = [0.5, 0.7] \quad D_{pm} = (D - 2r_{bi}) \cdot [0.5, 0.7] - 2r_{ag}$$

$$= [24 \text{ mm}, 35.2 \text{ mm}]$$

■ Final geometry parameters obtained by 3D-FEM:

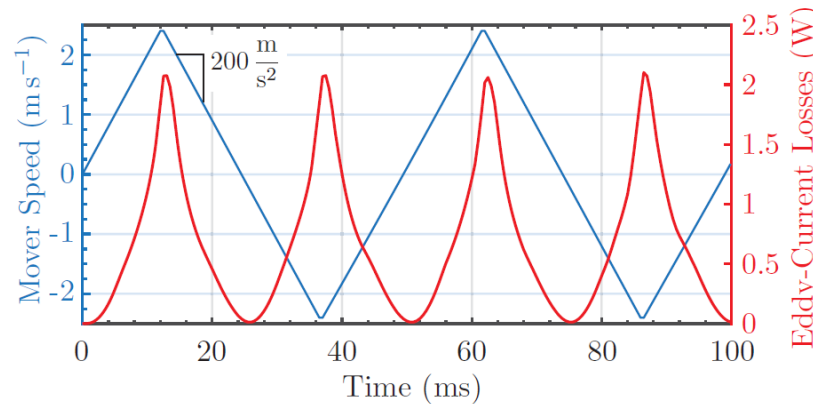
$$\tau_{pp} = 30 \text{ mm} \quad \tau_{pm} = 10 \text{ mm} \quad D_{pm} = 27 \text{ mm} \quad r_{pm} = 3 \text{ mm}$$

- Compromise between performance parameters → drive / bearing forces and axial (linear) acceleration
- The chosen IPM design → axially magnetized PMs and iron rings allow for simplified manufacturing

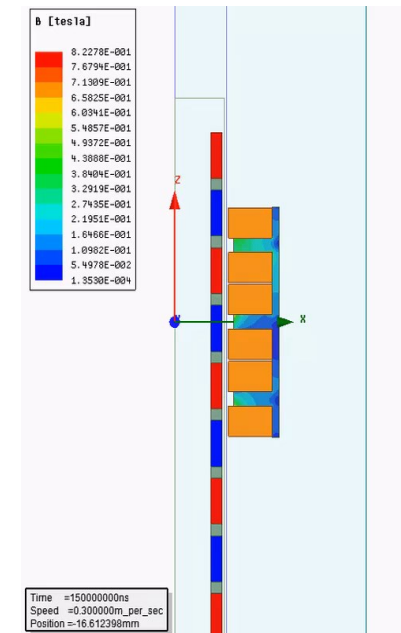
[ref] Spasoje Miric, 'Linear-Rotary Bearingless Actuators,' PhD Thesis, ETH Zurich, 2021.

Eddy Current Losses

- Short stroke linear actuator → average/max. speed of the mover low to induce eddy current losses
- Solid iron used for the core design → final design check for the eddy current losses



Maximum expected operation conditions:
 20g acceleration
 30 mm stroke

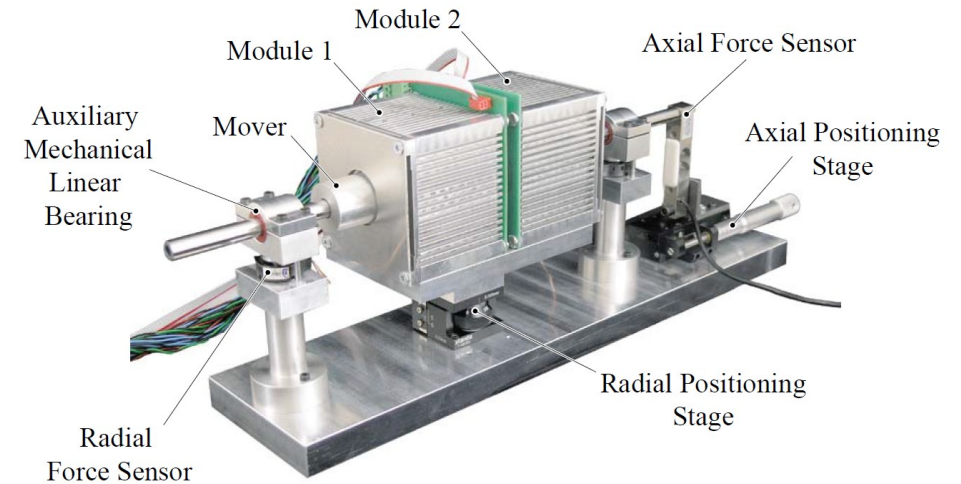
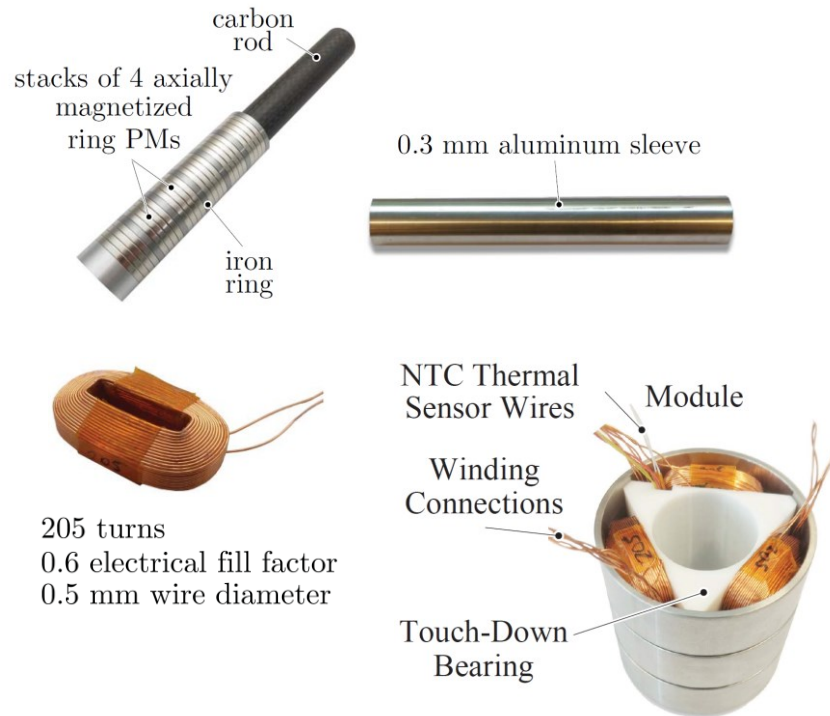


- Average eddy current losses during the operation = 0.7 W → 4.7% of the allowed copper losses
- Long stroke actuators that achieve higher speeds → should use low loss core, e.g., soft magnetic composite (SMC)

[ref] Mirić, Spasoje, Dominik Bortis, and Johann Walter Kolar. "Design and comparison of permanent magnet self-bearing linear-rotary actuators." 2019 12th International Symposium on Linear Drives for Industry Applications (LDIA). IEEE, 2019.
 [ref] Jensen, William R., Thang Q. Pham, and Shanelle N. Foster. "Linear permanent magnet synchronous machine for high acceleration applications." 2017 IEEE International Electric Machines and Drives Conference (IEMDC). IEEE, 2017.

MALTA Hardware Prototype

- **Mover's conductive sleeve** → mechanical protection & eddy current position sensing
- **Test bench with positioning stages and force sensors** → machine constant measurements



Measurements:

▼ **Thermal**
 $R_{th} = 1.51 \text{ K/W}$
 $\tau_{th} \approx 30 \text{ min}$

▼ **Magnetic**
 $\hat{\Psi}_M = 8.5 \text{ mWb}$
 $K_D = 7.6 \text{ N/A}$
 $K_B = 5.9 \text{ N/A}$

MALTA Inverter Supply

Specifications

24 phases (8 × 3 phase)

DC link voltage: 45 V

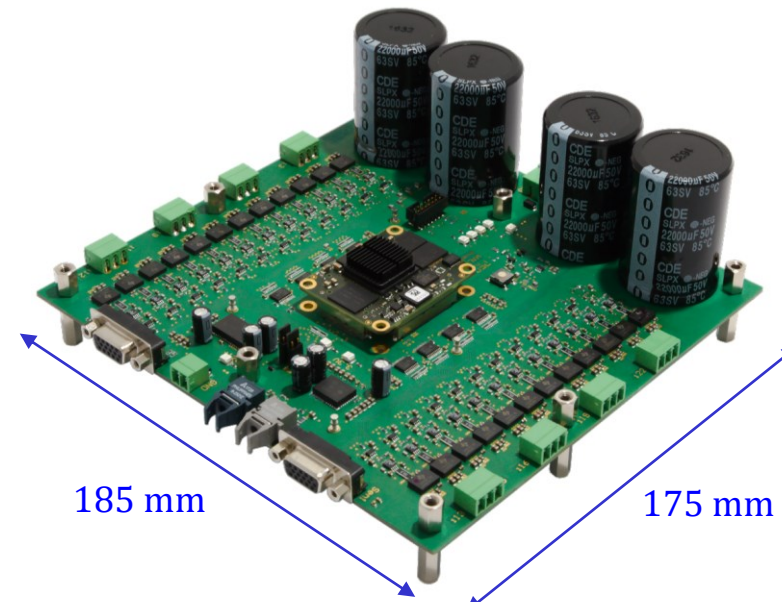
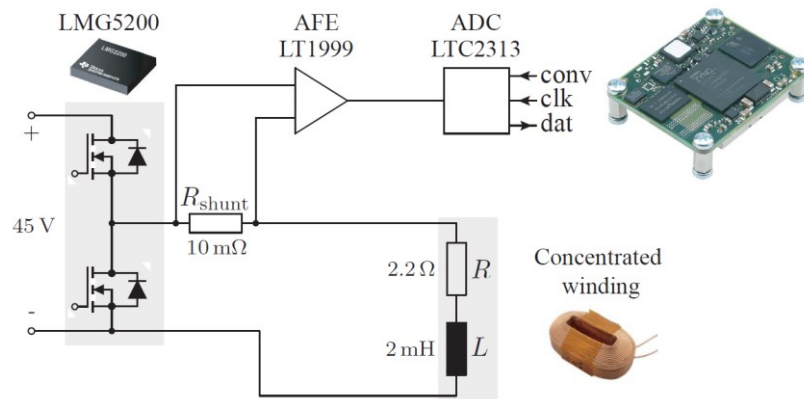
DC link capacitance: 4 × 22 mF (buffer braking energy)

Power Semi.: 80 V, 10 A, 15 mΩ

2 × position sensor interfaces

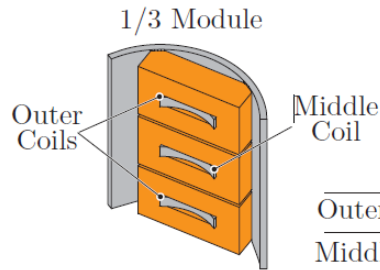
Control Board: ZYNQ, Z-7020 (156 digital IOs)

Current measurement:



MALTA Hardware Prototype Measurements

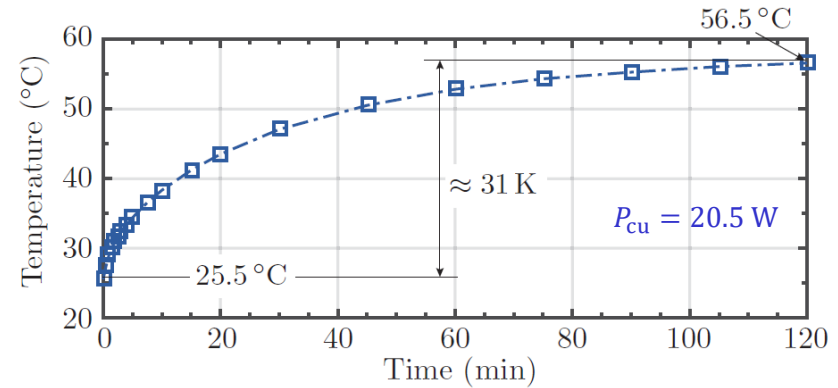
- Measurements: flux linkage, force constants, thermal resistance → prototype characterization/model verification



	Flux Linkage	
	Simulation (mWb)	Measurement (mWb)
Outer Coils:	8.3	8.35
Middle Coil:	9.0	8.85

▼ Magnetic

$\hat{\Psi}_M = 8.5 \text{ mWb}$
 $K_D = 7.6 \text{ N/A}$
 $K_B = 5.9 \text{ N/A}$



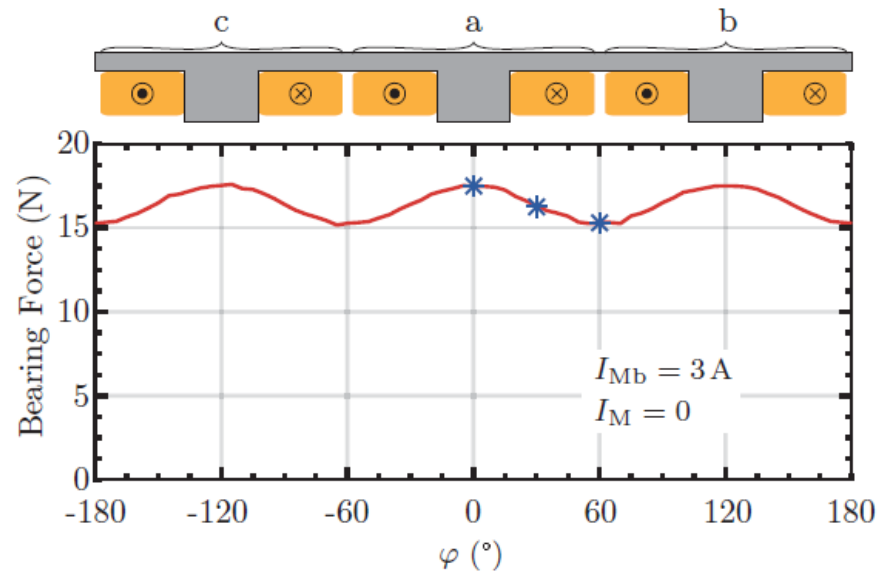
▼ Thermal

$R_{th} = 1.51 \text{ K/W}$
 $\tau_{th} \approx 30 \text{ min}$

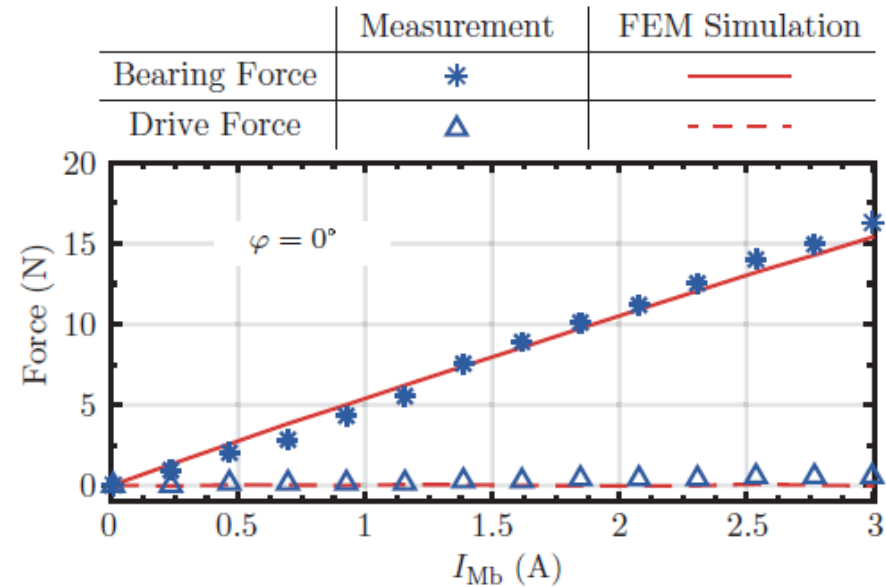
- Flux linkage measurement → measure induced back EMF and integrate to get the flux linkage
- Force constant measurement → apply known current and read the force sensor
- R_{th} measurement (wdg hot spot to ambient) → apply known losses and read the built-in NTC temp. sensors

Bearing Force Constant, Decoupling of Bearing and Drive Forces

- Dependence on the rotary angle \rightarrow measured and simulated with 3D-FEM (saved in a lookup table for control implem.)



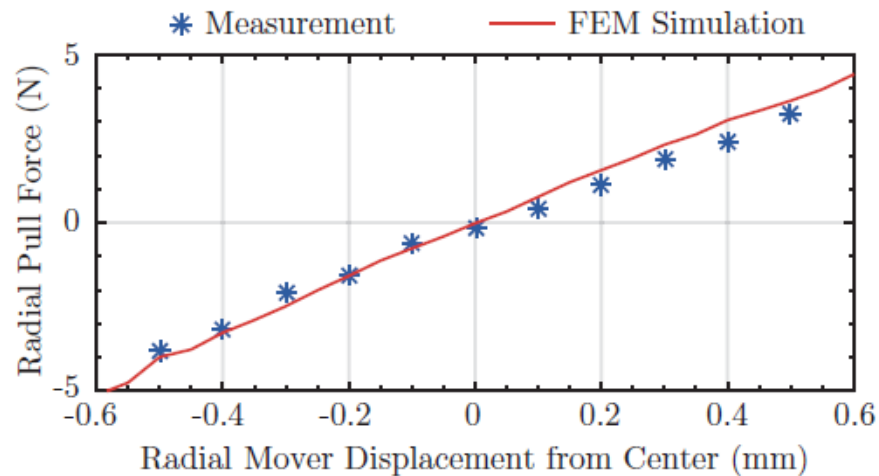
$K_B = 5.9 \text{ N/A}$, measured range [5.6 N/A – 6.26 N/A]



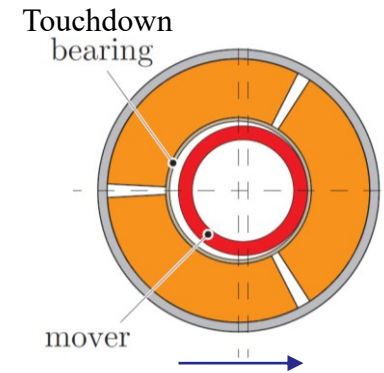
Decoupling of the bearing and the drive force generation!

Attraction/Pull Constant K_A (Pull Force)

- Extremely important parameter for the control system design and implementation
- K_A (also K_{pull}) determines poles of the mechanical dynamic model of the mover



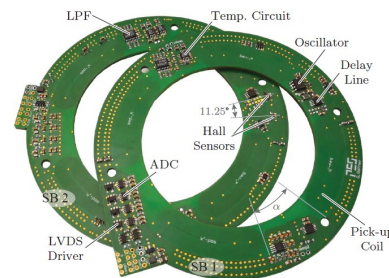
$$K_A = 8.33 \text{ N/mm}$$



- K_A obtained by displacing the mover in radial direction and measuring pull force, with no currents in the winding

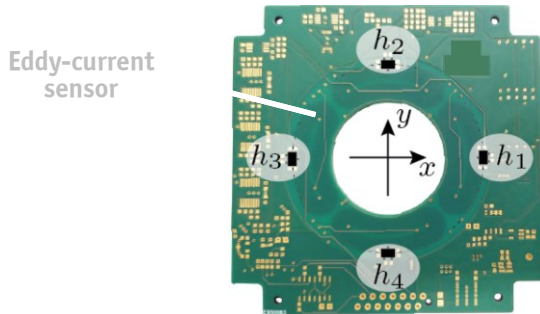
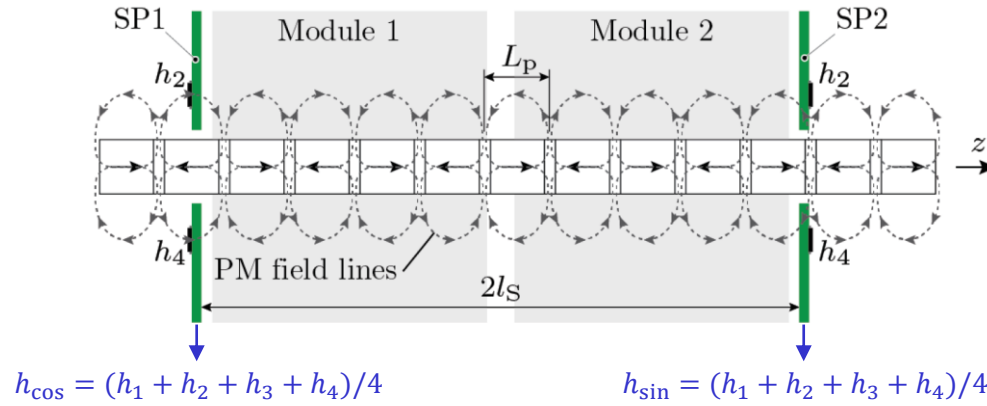
Position Sensor

Operating Principle
Driving Electronics
Geometry Optimization



Position Sensing – Linear & Radial

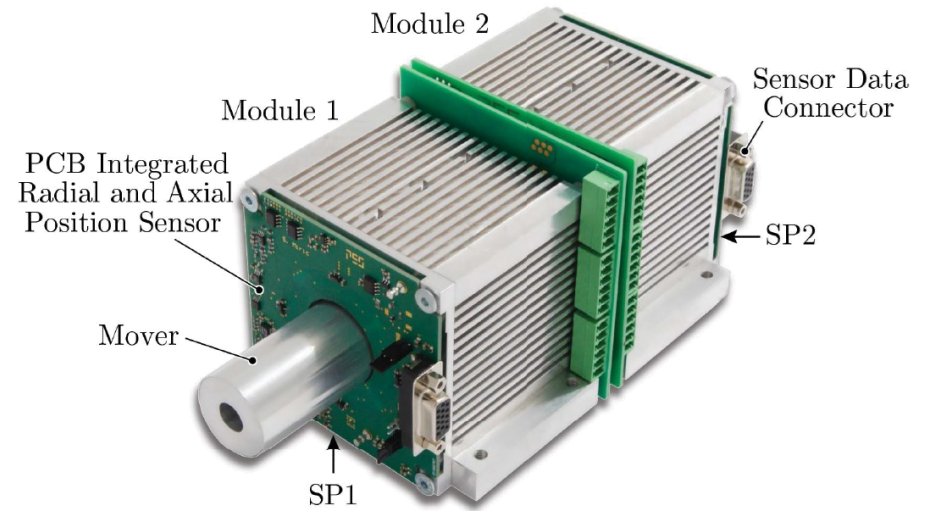
- Sensing locations at the axial ends of the actuator → SP1 and SP2
- Linear position → Hall-effect-based sensors, displaced $\pi/2$ electrical



$$\theta_{el} = \text{atan2}(h_{\sin}, h_{\cos})$$

Axial/Linear Position:

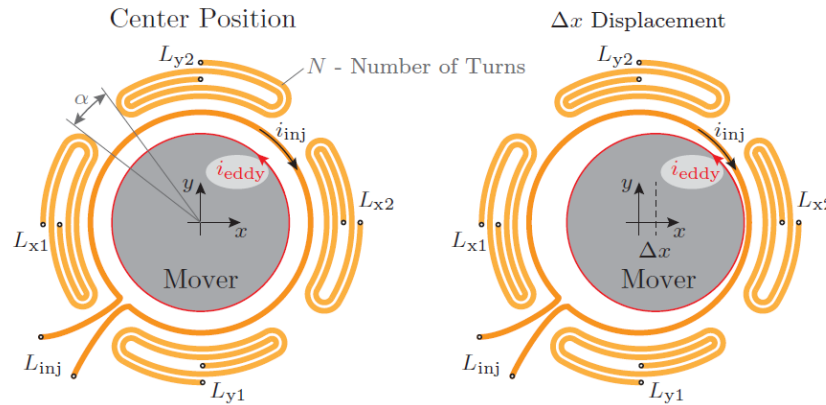
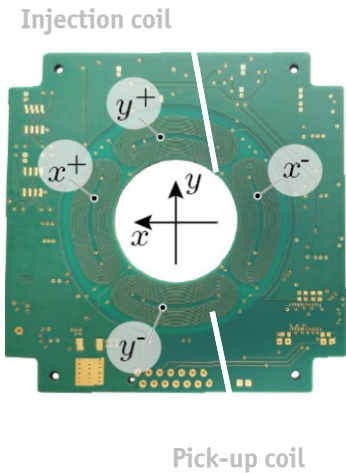
$$z = \frac{L_p}{\pi} (\theta_{el} + k \cdot 2\pi)$$



- Radial position sensor → eddy-current based; conductive mover surface is a sensing target
- Advanced eddy-current sensing techniques → later in the tutorial, blood pump part

Eddy-Current Based Position Sensor

- Injection coil carries high-frequency current → induce voltage in pick-up coils
- Upper limit for the oscillation frequency → resonant frequency of the sensor (layout/size dependent)



Mutual Inductances:

$$\begin{aligned} M_{inj-x1} &= M_0 \\ M_{inj-x2} &= M_0 \\ M_{inj-y1} &= M_0 \\ M_{inj-y2} &= M_0 \end{aligned}$$

Mutual Inductances:

$$\begin{aligned} M_{inj-x1} &> M_0 \\ M_{inj-x2} &< M_0 \\ M_{inj-y1} &= M_0 \\ M_{inj-y2} &= M_0 \end{aligned}$$

$$i_{inj} = \hat{I}_{inj} \sin(\omega_{osc} t)$$

$$\omega_{osc} \approx 3 \text{ MHz}, \hat{I}_{inj} \approx 100 \text{ mA}$$

$$M_{inj-x1} = M_0 + \frac{\partial M_{inj-x1}}{\partial x} \Delta x$$

$$M_{inj-x2} = M_0 + \frac{\partial M_{inj-x2}}{\partial x} \Delta x$$

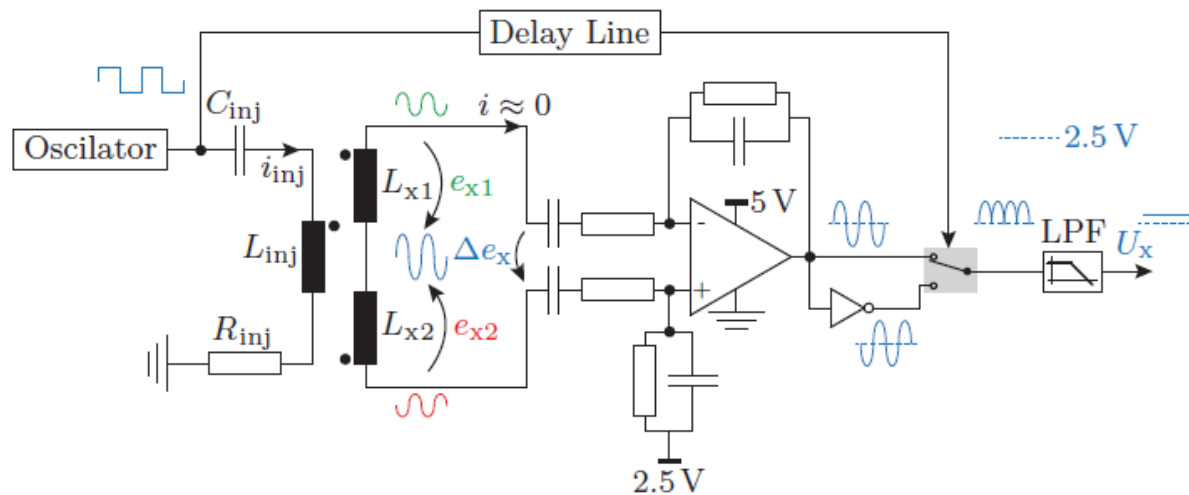
$$M_{inj-y1} = M_0 + \frac{\partial M_{inj-y1}}{\partial y} \Delta y$$

$$M_{inj-y2} = M_0 + \frac{\partial M_{inj-y2}}{\partial y} \Delta y$$

- Anti-series connection of pick-up coils of the same axis → ($L_{x1} \leftrightarrow L_{x2}$) and ($L_{y1} \leftrightarrow L_{y2}$)
- At center position ind. voltage of anti-series connection is zero; it is non-zero if there is mover displacement

Eddy-Current Sensor Electronics

- x – axis example → the induced voltage Δe_x rectified and low-pass filtered results in U_x
- The same electrical circuit is employed for the y – axis



$$U_x \sim 2\omega_{osc} \hat{I}_{inj} \frac{\partial M}{\partial r} \Delta x.$$

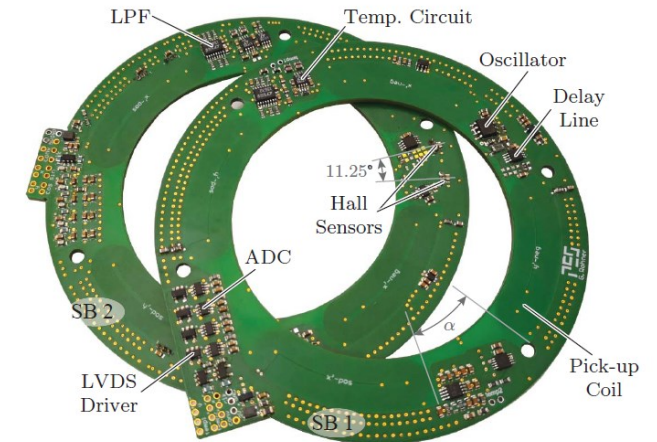
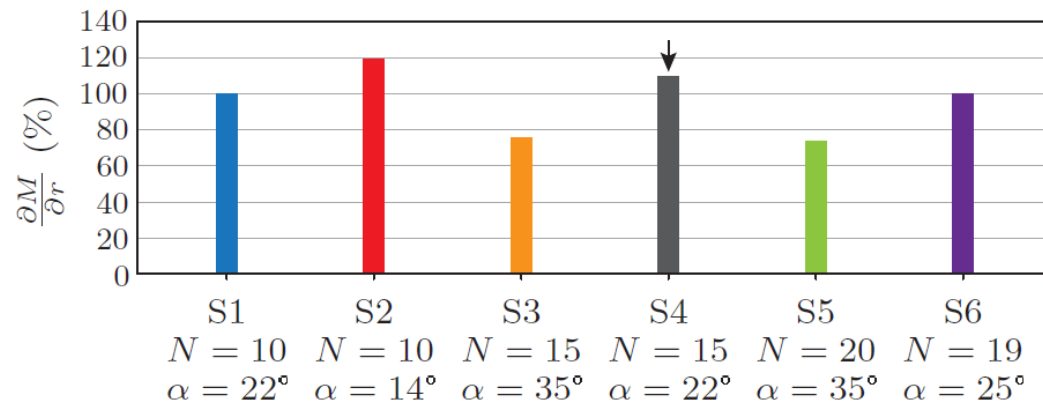
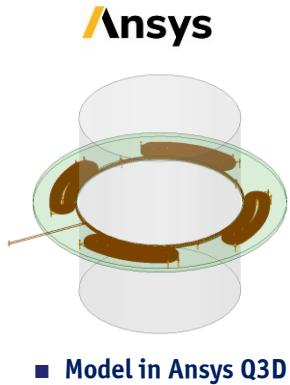
$$\omega_{osc} \approx 3 \text{ MHz}, \hat{I}_{inj} \approx 100 \text{ mA}$$

- Eddy-current position sensor processing electronics

- $\partial M / \partial r$ inductance sensitivity with radial displacement → maximized by the sensor geometry optimization
- Oscillation frequency ω_{osc} limited by the resonance; injection current i_{inj} limited by the oscillator power

Eddy-Current Sensor Geometry Optimization

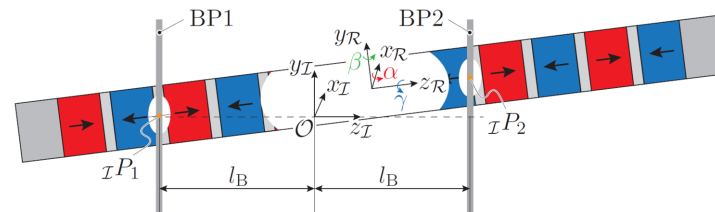
- Optimization parameters → angle between the pick-up coils α and the number of turns N of the pick-up coils
- Maximize sensitivity about the radial displacements of the mover → $\partial M / \partial r$



- Optimum number of turns N → larger N does means larger size of the pick-up coil
- Reasonable angle α → leave space for the signal processing electronics (analog circuits & ADCs)

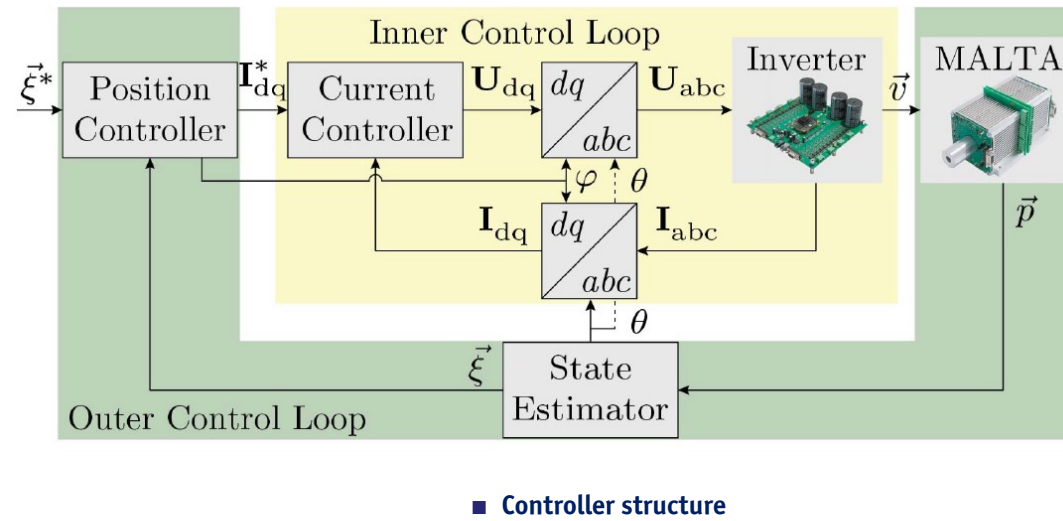
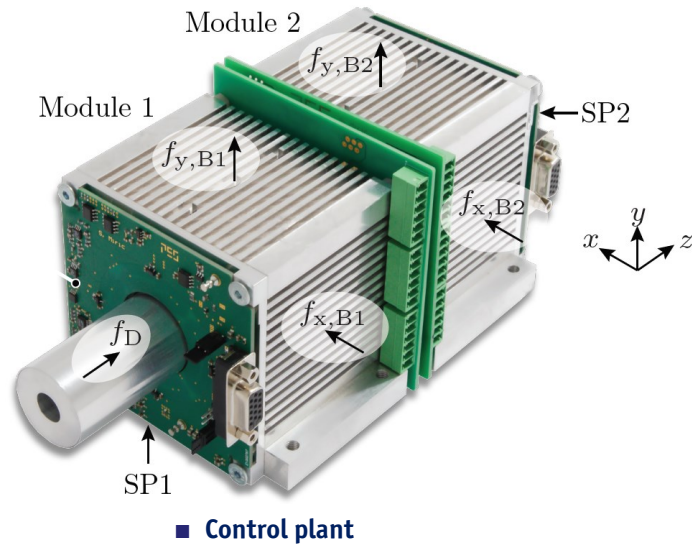
Dynamic Modeling

Dynamic Model Derivation
Model Analysis
Relative Gain Array



Controller Structure

- Linear motion, radial position and tilting of the mover should be controlled
- Interaction (force action) points between the stator and the mover → middle of the stator (module)

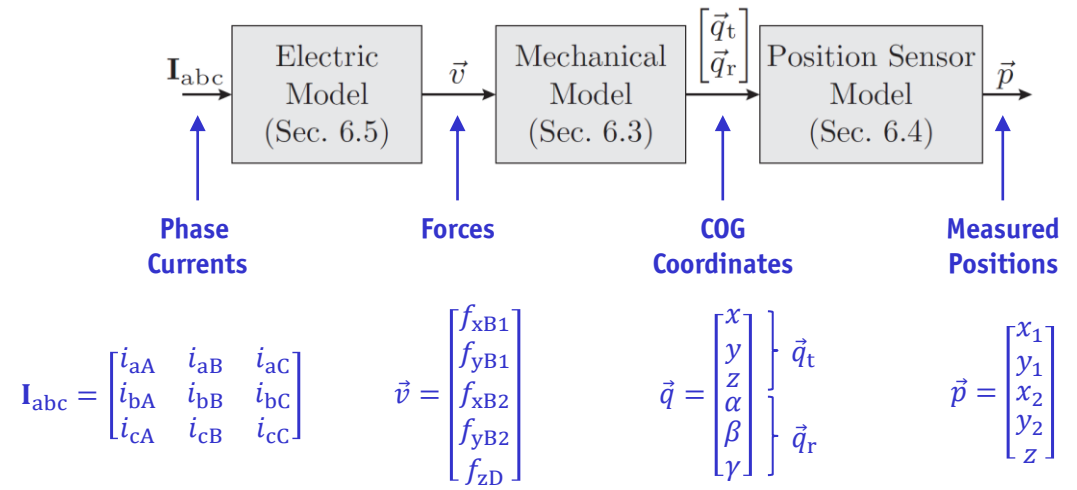
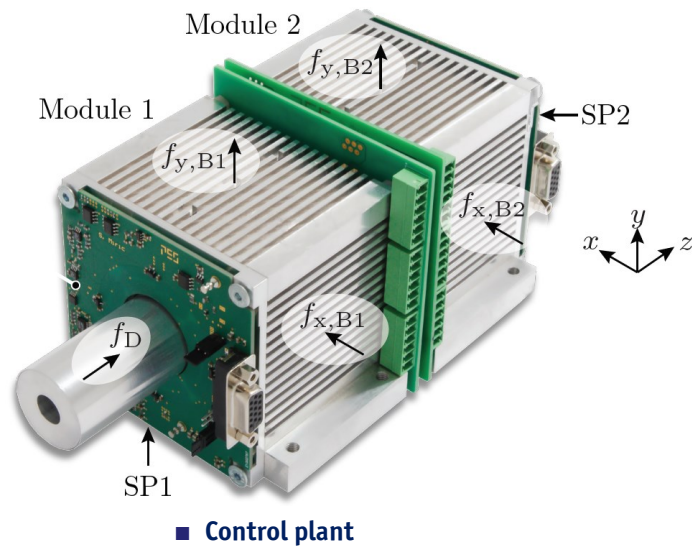


- Cascaded controller structure → outer position controller (slow) and inner current control loop (fast)
- Dynamic modelling of the plant → electrical model, mechanical model, position sensor model

[ref] Mirić, Spasoje, et al. "Dynamic electromechanical model and position controller design of a new high-precision self-bearing linear actuator." IEEE Transactions on Industrial Electronics 68.1 (2020): 744-755.

Dynamic Models for Controller Design

- Dynamic models necessary for the controller design → electric, mechanical, position sensor model
- Electric model → *abcdq* transformation of the phase quantities; *dq* currents control forces on the mover



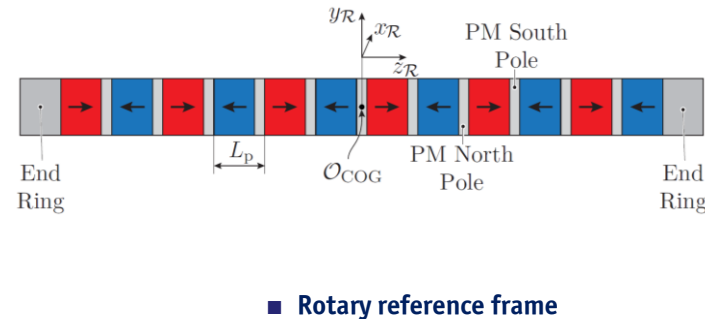
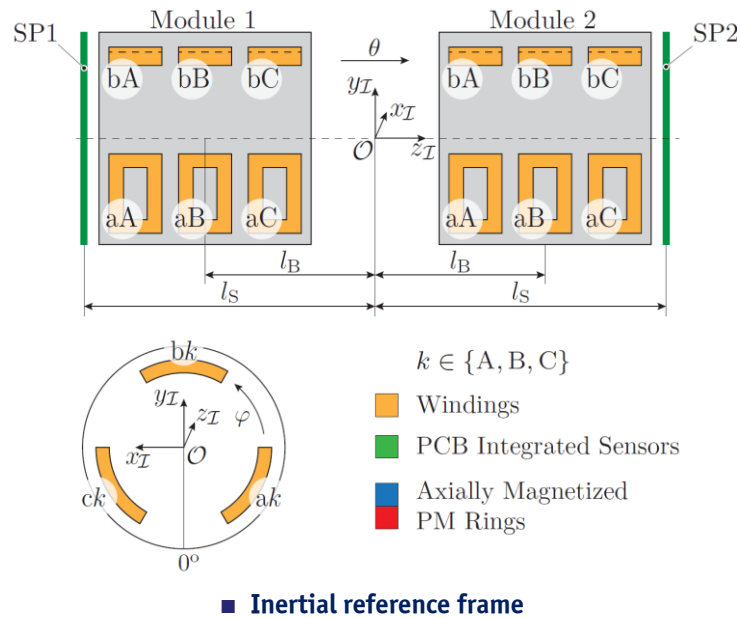
Overview of the dynamic models

- Mechanical model → MIMO model, coupling between the axes of motion; equations of motion must be derived
- Position sensor model → mech. model obtains COG coordinates, position sensor measures displacements

[ref] Mirić, Spasoje, et al. "Dynamic electromechanical model and position controller design of a new high-precision self-bearing linear actuator." IEEE Transactions on Industrial Electronics 68.1 (2020): 744-755.

Inertial \mathcal{I} and Rotary \mathcal{R} Reference Frames

- Inertial reference frame \rightarrow between modules, point \mathcal{O} ; rotary reference frame \rightarrow mover's COG, point \mathcal{O}_{COG}
- Position of the rotary RF with respect to inertial RF determines the mover's position

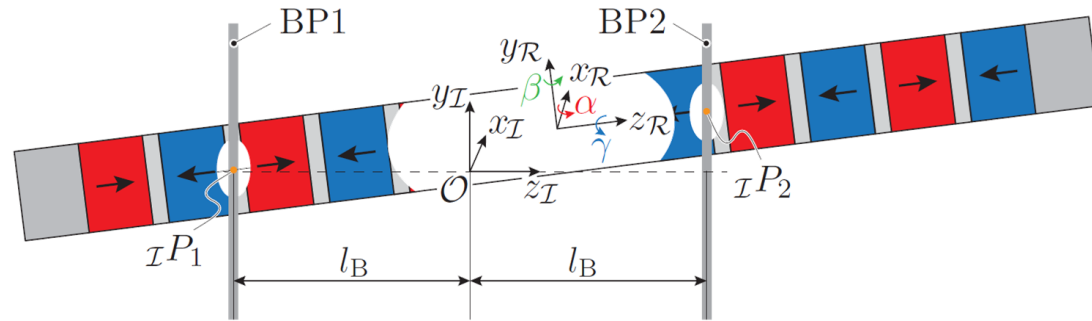


- l_B - the distance between the force action point and \mathcal{O} ; l_S - the distance of the position sensors
- Electrical angles $\rightarrow \theta$ - linear electrical angle; φ - rotary electrical angle (bearing force direction)

[ref] Mirić, Spasoje, et al. "Dynamic electromechanical model and position controller design of a new high-precision self-bearing linear actuator." IEEE Transactions on Industrial Electronics 68.1 (2020): 744-755.

Equations of Motion (EoM)

- **Newton-Euler equations of motion** → equation of motion in IRF (1) and rotation equation in RRF (2)
- **Interaction points ${}_jP_1$ and ${}_jP_2$** → center of the stator (module)



$$\vec{q}_t = \begin{bmatrix} x \\ y \\ z \end{bmatrix} \quad \vec{q}_r = \begin{bmatrix} \alpha \\ \beta \\ \gamma \end{bmatrix}$$

$$m \frac{\partial^2 \vec{q}_t}{\partial t^2} = {}_I \vec{F}_{tot} \quad (1)$$

$${}_{\mathcal{R}} \mathbf{I}_m \cdot \frac{\partial {}_{\mathcal{R}} \vec{\omega}}{\partial t} + {}_{\mathcal{R}} \vec{\omega} \times {}_{\mathcal{R}} \mathbf{I}_m \cdot {}_{\mathcal{R}} \vec{\omega} = {}_{\mathcal{R}} \vec{T}_{tot}, \quad (2)$$

m - mass of the mover
 ${}_{\mathcal{R}} \mathbf{I}_m$ - MoI of the mover
 IRF - inertial reference frame
 RRF - rotary reference frame

$${}_{\mathcal{R}} \mathbf{I}_m = \begin{bmatrix} I_{xx} & 0 & 0 \\ 0 & I_{yy} & 0 \\ 0 & 0 & I_{zz} \end{bmatrix}$$

- **Cardan (Euler) angles α, β, γ** → mover's rotation around respective axes x_j, y_j, z_j
- **In total 6 equations** → 3 for linear motion and 3 for rotation

[ref] Mirić, Spasoje, et al. "Dynamic electromechanical model and position controller design of a new high-precision self-bearing linear actuator." IEEE Transactions on Industrial Electronics 68.1 (2020): 744-755.

Solution of the EoM and Linearization

- **Solution of the EoM is a nonlinear function** → linearized to get the standard form of EoM
- **Standard form of EoM** → characterize the mass and the stiffness distributions within the system

$$\vec{F}_{\text{EoM}} \left(\frac{\partial^2 \vec{q}}{\partial t^2}, \frac{\partial \vec{q}}{\partial t}, \vec{q}, \vec{v} \right) = \left[\begin{array}{c} m \frac{\partial^2 \vec{q}_t}{\partial t^2} - I \vec{F}_{\text{tot}} \\ \mathcal{R} \mathbf{I}_m \cdot \frac{\partial \mathcal{R} \vec{\omega}}{\partial t} + \mathcal{R} \vec{\omega} \times \mathcal{R} \mathbf{I}_m \cdot \mathcal{R} \vec{\omega} - \mathcal{R} \vec{T}_{\text{tot}} \end{array} \right] = \mathbf{0}_{6 \times 1}$$

■ **Nonlinear solution of the EoM**

States: $\vec{q} = \begin{bmatrix} x \\ y \\ z \\ \alpha \\ \beta \\ \gamma \end{bmatrix}$

Inputs: $\vec{v} = \begin{bmatrix} f_{xB1} \\ f_{yB1} \\ f_{xB2} \\ f_{yB2} \\ f_D \end{bmatrix}$

$$\mathbf{M} \frac{\partial^2 \vec{q}}{\partial t^2} + \mathbf{G} \frac{\partial \vec{q}}{\partial t} = \mathbf{S} \vec{q} + \mathbf{V} \vec{v},$$

■ **Linearized solution of the EoM**

$$\mathbf{M}_{6 \times 6} = \mathbf{J} \left(\vec{F}_{\text{EoM}}, \frac{\partial^2 \vec{q}}{\partial t^2} \right) \Big|_{\text{at ss}}$$

$$\mathbf{G}_{6 \times 6} = \mathbf{J} \left(\vec{F}_{\text{EoM}}, \frac{\partial \vec{q}}{\partial t} \right) \Big|_{\text{at ss}}$$

$$\mathbf{S}_{6 \times 6} = -\mathbf{J} \left(\vec{F}_{\text{EoM}}, \vec{q} \right) \Big|_{\text{at ss}}$$

$$\mathbf{V}_{6 \times 5} = -\mathbf{J} \left(\vec{F}_{\text{EoM}}, \vec{v} \right) \Big|_{\text{at ss}}$$

■ **Linearization**

- **EoM matrices** → **M** – mass matrix; **G** – gyroscopic matrix; **S** – stiffness matrix;
- **Second-order differential equations (DE)** → reduction the first order DE, i.e., the state space

[ref] Mirić, Spasoje, et al. "Dynamic electromechanical model and position controller design of a new high-precision self-bearing linear actuator." IEEE Transactions on Industrial Electronics 68.1 (2020): 744-755.

EoM to State-Space Equations

- Transform second order EoM to the first order state-space → double the number of states
- Controller design standardized for state-space equations

\vec{q} → Positions
 $\frac{\partial \vec{q}}{\partial t}$ → Speeds

$$\vec{\xi} = \begin{bmatrix} \vec{q} \\ \frac{\partial \vec{q}}{\partial t} \end{bmatrix}_{[12 \times 1]}$$

$$\mathbf{A} = \mathbf{E}^{-1} \begin{bmatrix} \mathbf{0} & \mathbf{I} \\ \mathbf{S} & \mathbf{0} \end{bmatrix} \quad \mathbf{B} = \mathbf{E}^{-1} \begin{bmatrix} \mathbf{0} \\ \mathbf{V} \end{bmatrix} \quad \mathbf{C} = [\mathbf{P} \quad \mathbf{0}] ,$$

■ Extension of the states

■ Calculation of state space matrices

$$\frac{\partial \vec{\xi}}{\partial t} = \mathbf{A} \vec{\xi} + \mathbf{B} \vec{v},$$

$$\vec{p} = \mathbf{C} \vec{\xi},$$

■ State space equations

$$\mathbf{P}(z) = \begin{bmatrix} 1 & 0 & 0 & 0 & -(l_s + z) & 0 \\ 0 & 1 & 0 & (l_s + z) & 0 & 0 \\ 1 & 0 & 0 & 0 & (l_s - z) & 0 \\ 0 & 1 & 0 & -(l_s - z) & 0 & 0 \\ 0 & 0 & 1 & 0 & 0 & 0 \end{bmatrix}$$

Sensor measurements

$$\vec{p} = \begin{bmatrix} x_1 \\ y_1 \\ x_2 \\ y_2 \\ z \end{bmatrix}$$

COG coordinates (states)

$$\vec{p} = \mathbf{P}(z) \begin{bmatrix} \vec{q}_t \\ \vec{q}_r \end{bmatrix}$$

■ Position sensor model

- Position sensor model → relates sensor measurements with COG coordinates (states) of the mechanical model
- Different quantities in the model (positions, angles, forces) → normalization

[ref] Mirić, Spasoje, et al. "Dynamic electromechanical model and position controller design of a new high-precision self-bearing linear actuator." IEEE Transactions on Industrial Electronics 68.1 (2020): 744-755.

Normalization

- Normalization is important for the implementation & debugging → values get to the similar level, [-1,1]
- Absolute values before normalization → different nature (electrical, mechanical) and value range

$$\vec{\xi}_{pu} = \mathbf{D}_{\xi}^{-1} \vec{\xi} \in \mathbb{R}^{10}, \quad \vec{v}_{pu} = \mathbf{D}_v^{-1} \vec{v} \in \mathbb{R}^5, \quad \vec{p}_{pu} = \mathbf{D}_p^{-1} \vec{p} \in \mathbb{R}^5,$$

■ MIMO normalization

$$\frac{\partial \vec{\xi}_{pu}}{\partial t} = \mathbf{A}_{pu} \vec{\xi}_{pu} + \mathbf{B}_{pu} \vec{v}_{pu},$$

$$\vec{p}_{pu} = \mathbf{C}_{pu} \vec{\xi}_{pu}$$

■ Normalized state-space equations

$$\mathbf{D}_{\xi} = \begin{bmatrix} \mathbf{D}_q & \mathbf{0} \\ \mathbf{0} & \mathbf{D}_{\dot{q}} \end{bmatrix},$$

$$\mathbf{D}_q = \text{diag} (x_{\max} \quad y_{\max} \quad z_{\max} \quad \alpha_{\max} \quad \beta_{\max}),$$

$$\mathbf{D}_{\dot{q}} = \text{diag} (\dot{x}_{\max} \quad \dot{y}_{\max} \quad \dot{z}_{\max} \quad \dot{\alpha}_{\max} \quad \dot{\beta}_{\max}),$$

$$\mathbf{D}_v = \text{diag} (f_{B\max} \quad f_{B\max} \quad f_{B\max} \quad f_{B\max} \quad 2f_{D\max}),$$

$$\mathbf{D}_p = \text{diag} (x_{\max} \quad y_{\max} \quad x_{\max} \quad y_{\max} \quad z_{\max}).$$

■ Normalization matrices diagonal

$$\alpha_{\max} = \text{atan} \left(\frac{x_{\max}}{l_B} \right)$$

Given by the mechanical air gap

Base angle value

Base force value, given by the max winding current

$$\dot{\alpha}_{\max} = \sqrt{\frac{4l_B f_{B\max} \alpha_{\max}}{I_{xx}}}$$

Base rotation value

$$\dot{x}_{\max} = \sqrt{\frac{4f_{B\max} x_{\max}}{m}}$$

Base speed value

■ Choice of normalization values

- Choice of the normalization (base) values → based on physical limits of the actuator
- Normalized state-space equations used for the system analysis and the controller design

[ref] Mirić, Spasoje, et al. "Dynamic electromechanical model and position controller design of a new high-precision self-bearing linear actuator." IEEE Transactions on Industrial Electronics 68.1 (2020): 744-755.

Position Control Bandwidth, SISO or MIMO Controller

- **Eigenvalues of the matrix A** → determine the dynamics of the systems and the minimum required bandwidth
- **Closed-loop position controller bandwidth** → should be at least twice the maximum unstable pole

Symbol	Mode	Eigenvalue
$\lambda_{1,2}$	x	$\pm 218.92 \text{ rad s}^{-1}$
$\lambda_{3,4}$	y	$\pm 218.92 \text{ rad s}^{-1}$
$\lambda_{5,6}$	z	$\pm 0.9893 \text{ rad s}^{-1}$
$\lambda_{7,8}$	α	$\pm 157.53 \text{ rad s}^{-1}$
$\lambda_{9,10}$	β	$\pm 157.53 \text{ rad s}^{-1}$

■ Eigenvalues of the matrix A

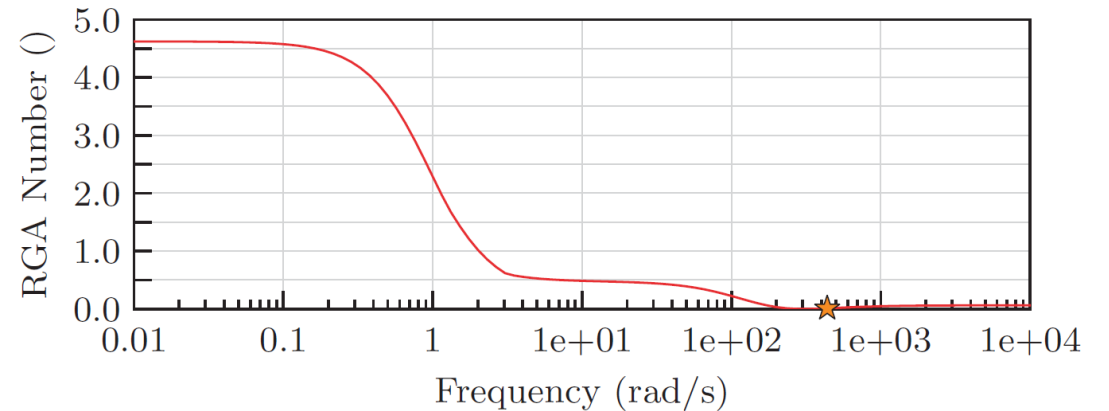
$$\begin{aligned} \omega_c &= 2 \times \max(|\lambda_{\{1,2,3,4,5,6,7,8,9,10\}}|) \\ &= 2 \times 218.92 \text{ rad s}^{-1} \\ &= 436 \text{ rad s}^{-1}. \end{aligned}$$

■ Minimum closed-loop bandwidth of the position controller

- **RGA number** → helps to identify the level of coupling between the input and outputs of the system
- **Low RGA number** → low coupling and SISO control possible

$$G_{ij}(s) = \mathbf{C}_i \cdot (s\mathbf{I} - \mathbf{A})^{-1} \cdot \mathbf{B}_j \quad \rightarrow \quad \Lambda(G(s)) \hat{=} G(s) \times (G(s)^{-1})^T$$

$$\text{RGA-number}(G(s)) = \|\Lambda(G(s)) - I_{Pair}\|_{Sum}$$

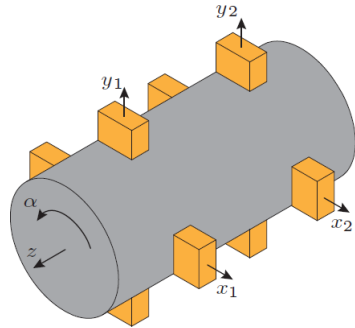


■ RGA number

[ref] Mirić, Spasoje, et al. "Dynamic electromechanical model and position controller design of a new high-precision self-bearing linear actuator." IEEE Transactions on Industrial Electronics 68.1 (2020): 744-755.

Simple Bandwidth Requirement Assessment

- Closed-loop bandwidth requirement → can be imposed by the disturbances
- Disturbance parameters of the LiRA with MBs → m - mass; K_{pull} - attraction/pull constant



$$F_{pull,x} = x K_{pull}, \quad F_{pull,y} = y K_{pull}$$

$$K_{pull} = 8330 \text{ N/m}$$

$$m = 0.360 \text{ kg}$$

$$\omega_{BW} > \omega_D, \quad \omega_D \text{ such that } \|G_D^{pu}(j\omega_D)\| = 1$$

$$G_D^{pu}(s) = \frac{x(s)/\hat{x}}{F_x(s)/\hat{F}_x} = \frac{2 K_{pull}}{m s^2}$$

$$\omega_D = \sqrt{\frac{2K_{pull}}{m}} \quad \longrightarrow \quad \omega_{BW} > \sqrt{\frac{2 K_{pull}}{m}} \approx 220 \text{ rad/s}$$

$$a_x = \frac{2}{m} F_x, \quad a_y = \frac{2}{m} F_y$$

$$G_{OL}(s) = \frac{\{x(s), y(s)\}}{F_{\{x,y\}}(s)} = \frac{2}{m s^2}$$

- Simplified equation of motion

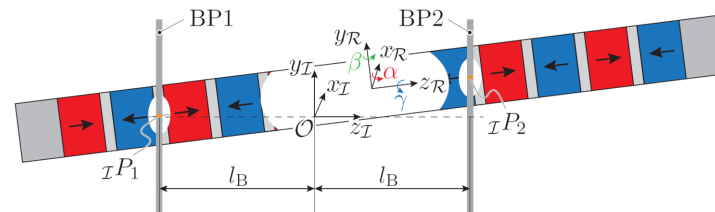
- Bandwidth imposed by disturbance

- Position controller $\omega_{BW} = 2\omega_D \approx 440 \text{ rad/s}$ → current controller bandwidth $> 5 \cdot 440 = 2200 \text{ rad/s}$
- Current controller bandwidth → determines the stiffness capability of the MBs

[ref] Mirić, Spasoje M., et al. "Enhanced complex space vector modeling and control system design of multiphase magnetically levitated rotary-linear machines." IEEE Journal of Emerging and Selected Topics in Power Electronics 8.2 (2019): 1833-1849.

Controller Design

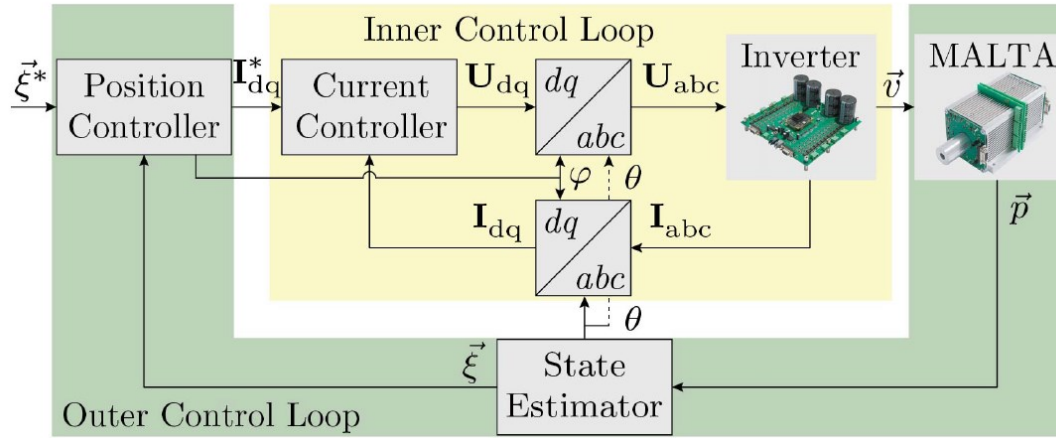
*MIMO and SISO Controllers
Measurement Results
Tilting Control Example*



MIMO Controller

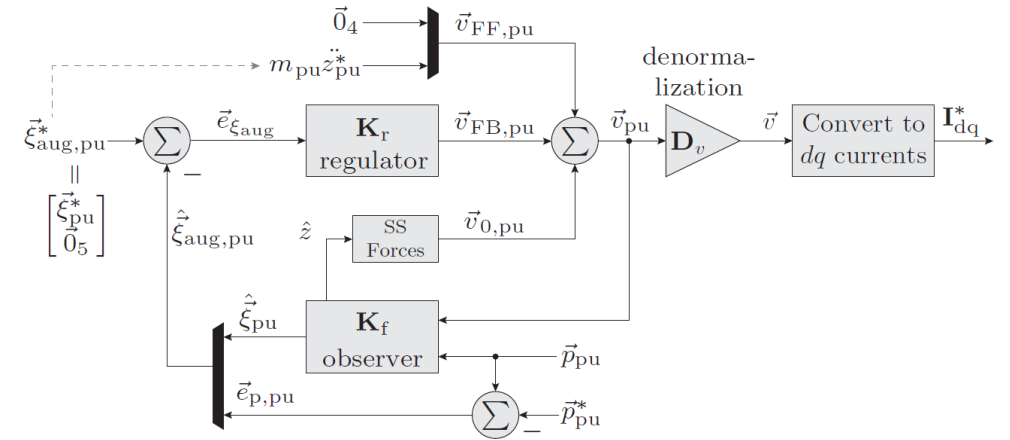
■ Cascaded Control Structure

- Outer Loop: Position Control (BW: 60 Hz)
- Inner Loop: Current Control (BW: 470 Hz)

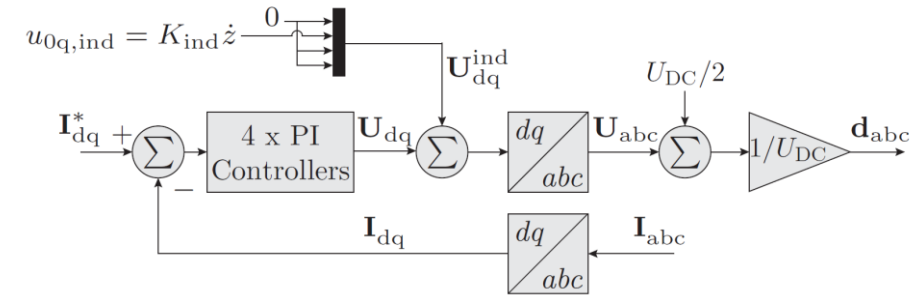


- Position Controller Tuning: LQG
- (MALTA – Magnetically Levitated Tubular Actuator)

■ Position Controller Structure ($\vec{\xi}_{aug,pu} \in \mathbb{R}^{15}$)



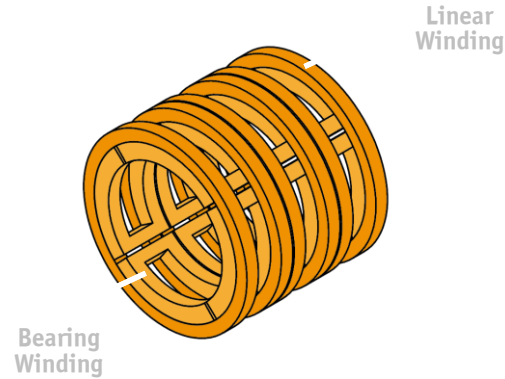
■ Current Controller Structure ($I_{dq} \in \mathbb{R}^{4 \times 4}$)



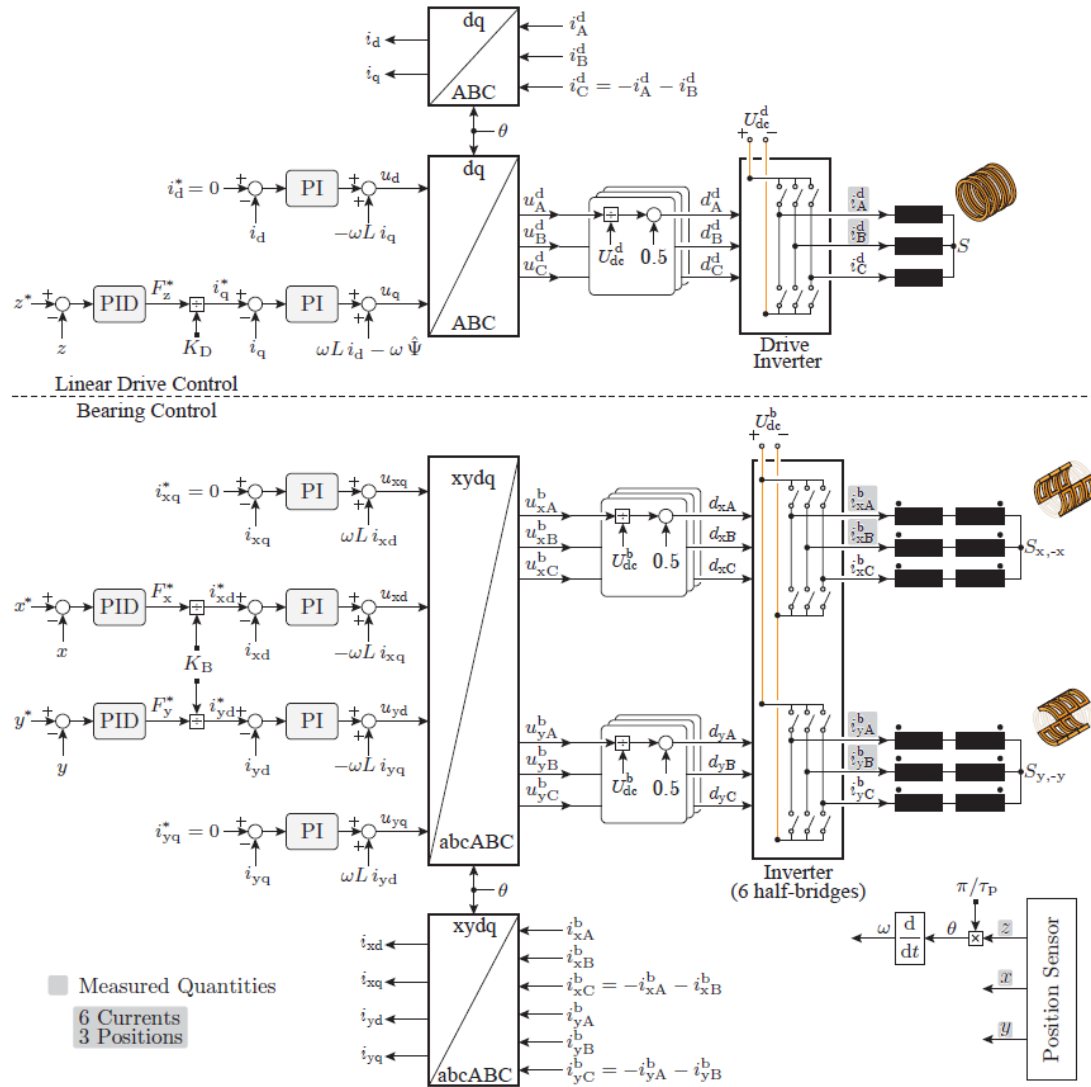
[ref] Mirić, Spasoje, et al. "Dynamic electromechanical model and position controller design of a new high-precision self-bearing linear actuator." IEEE Transactions on Industrial Electronics 68.1 (2020): 744-755.

SISO Controller (1)

- Separated winding example
- xy bearing winding

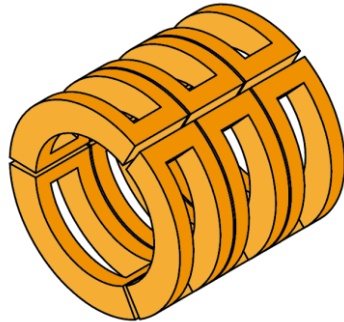


- Linear & bearing controller separated
- Bearing windings in anti-series conn.

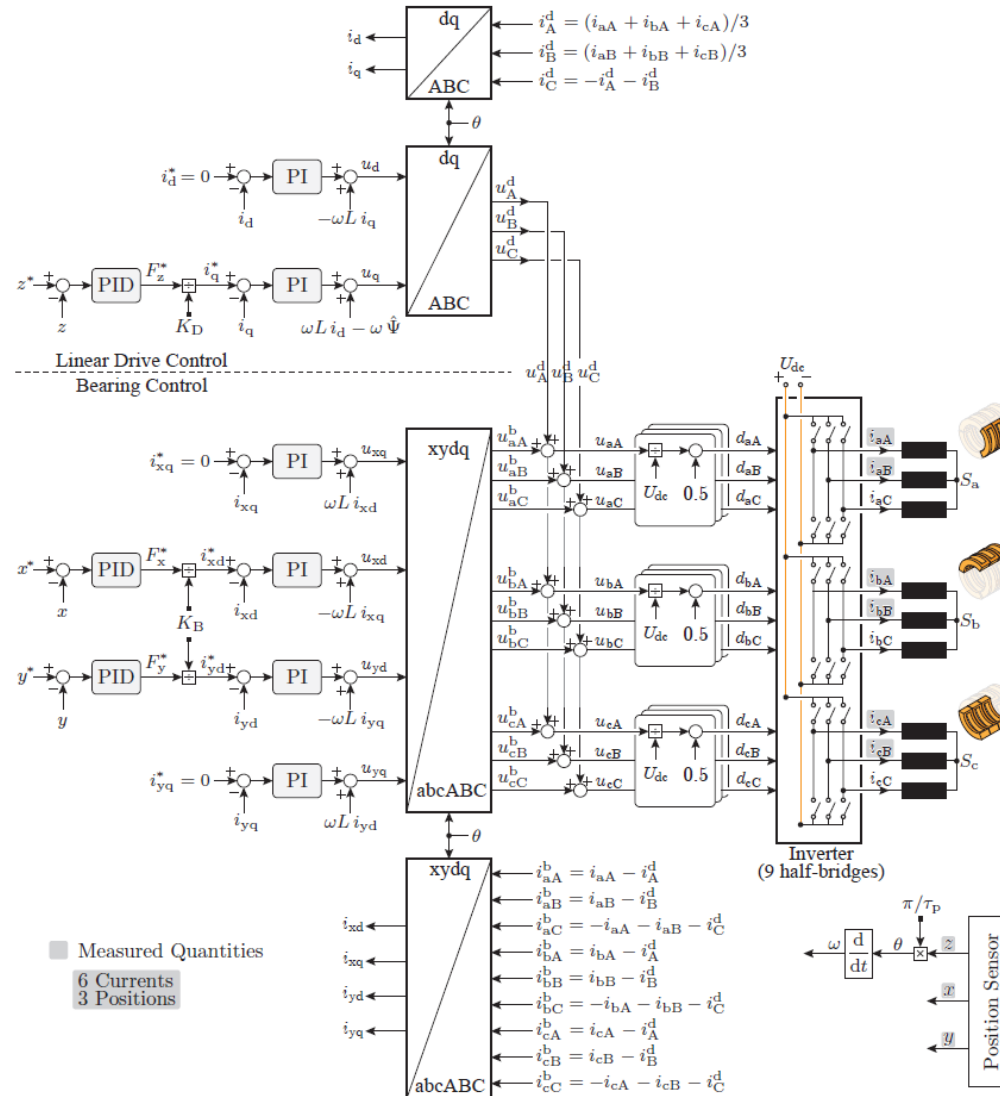


SISO Controller (2)

- Combined winding example
- *abcABC* winding

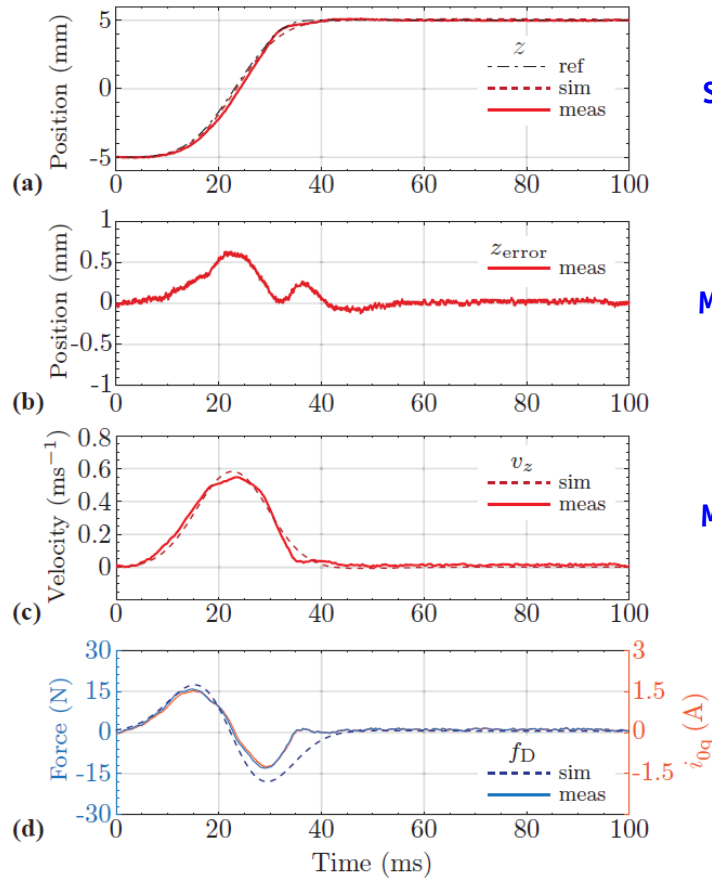


- Superimpose control signals
- 3 three-phase systems in linear dir.



MIMO – Measurement Results

- Axial Reference Tracking
- Axial Position and Force



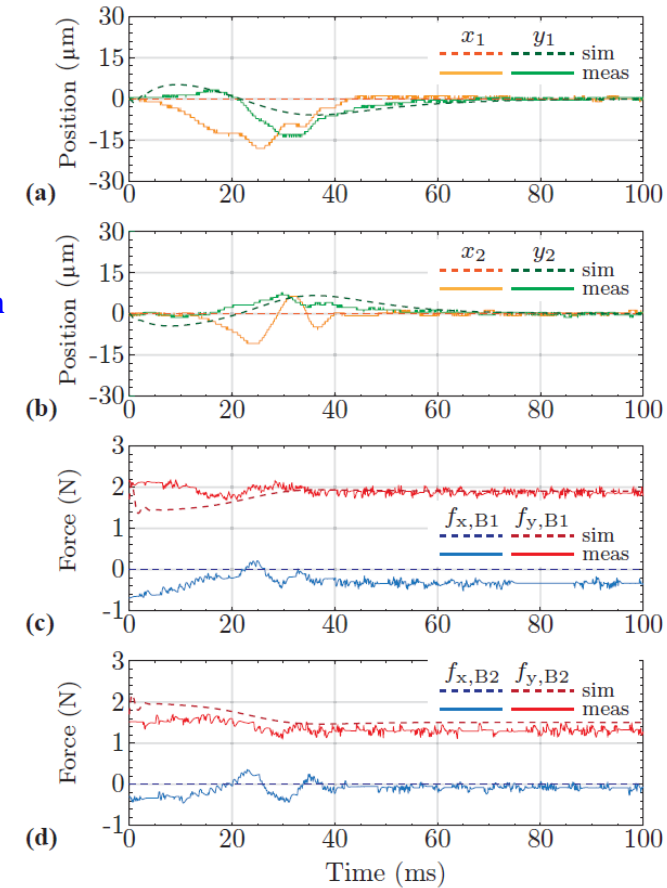
Stroke: 10 mm

Max. Pos. Error: 0.5 mm

Max. Speed: 0.6 m/s

Axial Force: ± 15 N

- Radial Position and Force



Max. Radial Position Oscillation (1.5%): $\pm 15 \mu m$

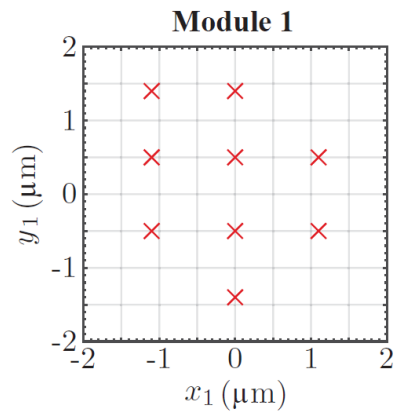
Mechanical Air Gap $\pm 1000 \mu m$

Y-direction Compensates Gravity Force: 3.25 N

MIMO – Measurement Results

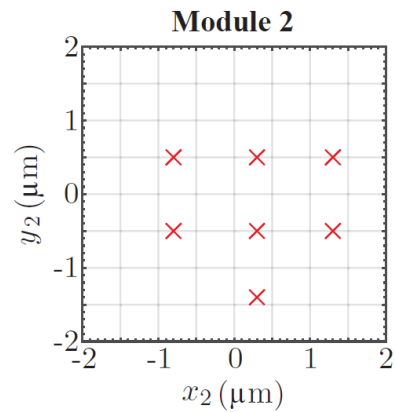
Steady-State Positioning

- Sensor Resolution $\sim 1 \mu\text{m}$
- Number of Measured Samples: 2000



Mean
 $\text{mean}(x_1) = 0.0335 \mu\text{m}$
 $\text{mean}(y_1) = -0.0212 \mu\text{m}$

STD
 $\text{std}(x_1) = 0.3883 \mu\text{m}$
 $\text{std}(y_1) = 0.5579 \mu\text{m}$

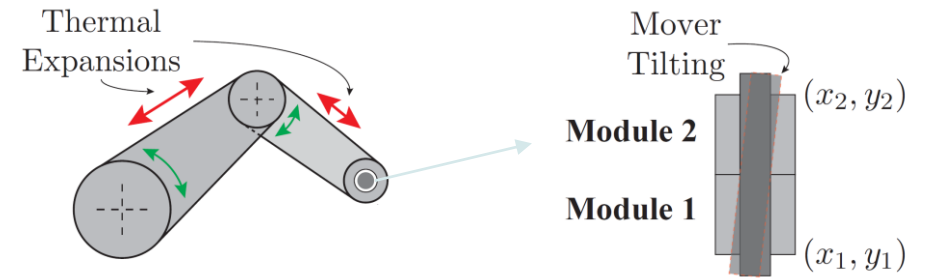


Mean
 $\text{mean}(x_2) = 0.0579 \mu\text{m}$
 $\text{mean}(y_2) = -0.0735 \mu\text{m}$

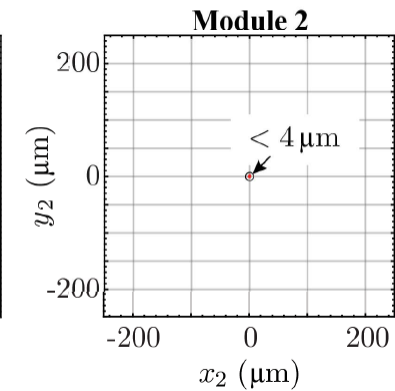
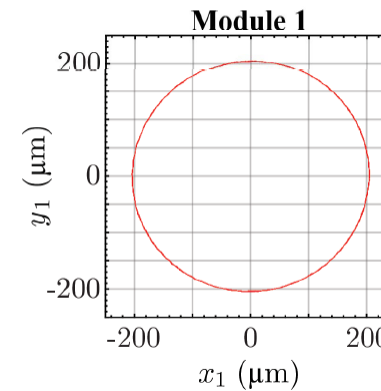
STD
 $\text{std}(x_2) = 0.4827 \mu\text{m}$
 $\text{std}(y_2) = 0.4956 \mu\text{m}$

Mover Tilting Control

- High Precision Applications (e.g. Pick-And-Place)
- Thermal Expansions of Parallel Kinematics

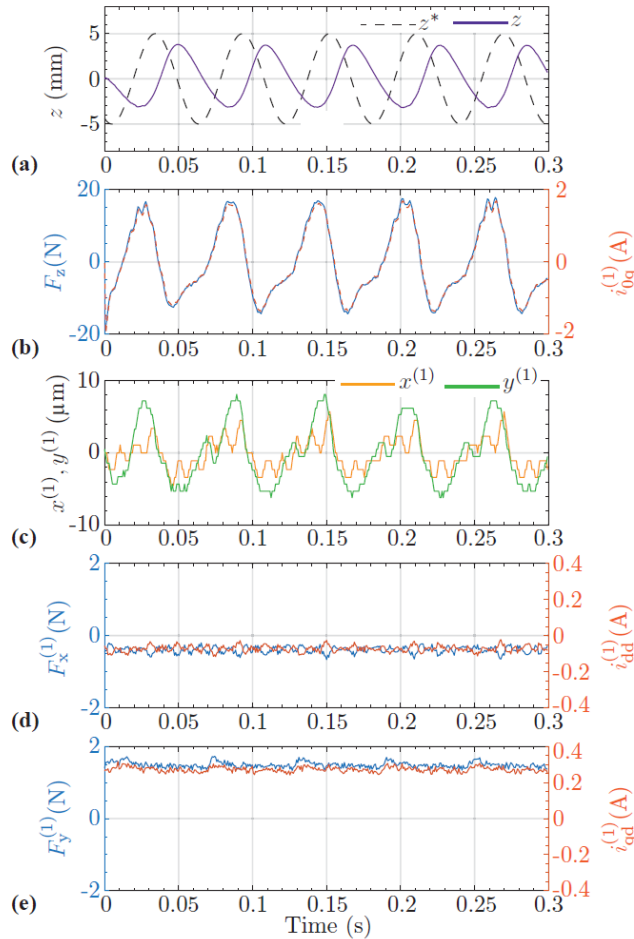


Tilting Experimental Verification:



SISO – Measurement Results

■ Oscillatory Operation



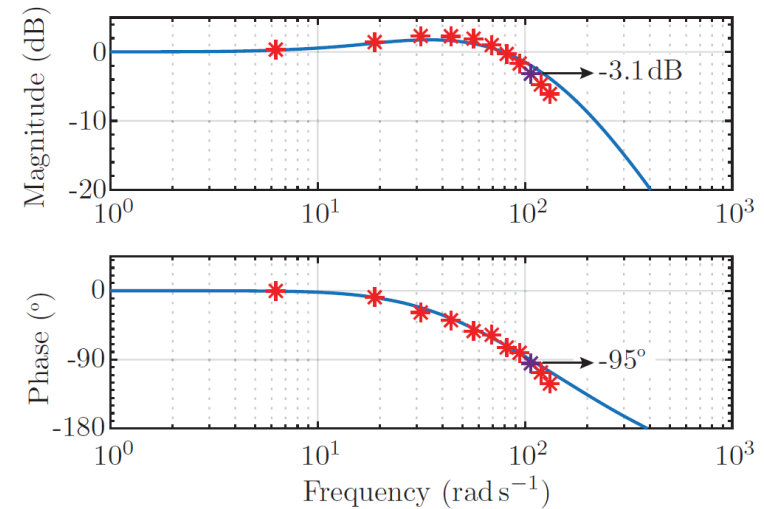
Stroke: 10 mm
Frequency: 17 Hz

Force: $< |\pm 20|$ N

Radial Position:
 $< |\pm 10|$ μ m

■ Axial Sub-plant Bode Plot

- Blue: Analytically Derived Transfer Function
- Red: Experimentally Verified Points: $f_z = \{1,3,5, \dots, 19,21\}$ Hz



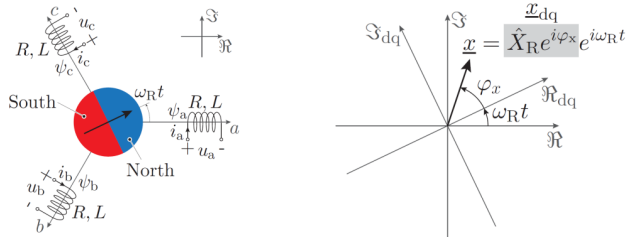
- Demonstration of the Real Life Operation →

Linear Bearingless Actuator

- Video (10 Hz, 1 Hz)

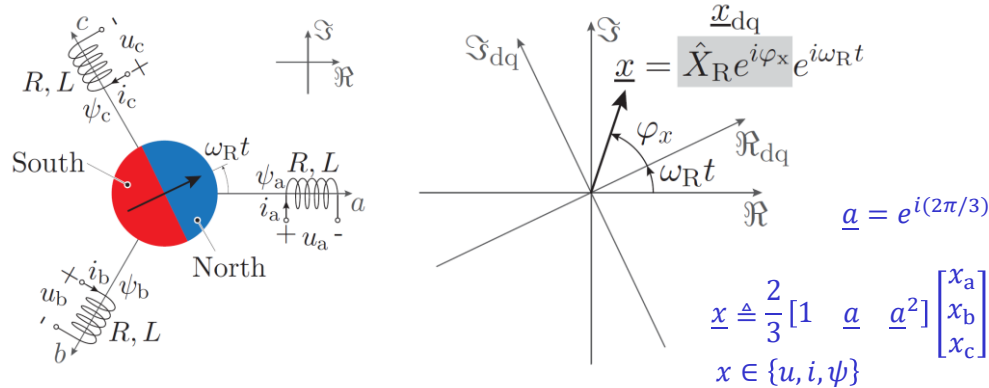


Generalized Complex Space Vector Modelling



Generic Complex Space Vector Modeling (1)

Three-Phase (a, b, c) → Two-Phase (d, q)



Example: Current Space Vector

Three-phase currents

$$\begin{aligned} i_a &= \hat{I}_R \cdot \cos(\omega_R t + \varphi_i) \\ i_b &= \hat{I}_R \cdot \cos(\omega_R t + \varphi_i - 2\pi/3) \\ i_c &= \hat{I}_R \cdot \cos(\omega_R t + \varphi_i + 2\pi/3) \end{aligned}$$

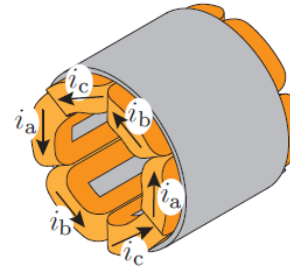
Space vector

$$\underline{i} = \hat{I}_R \cdot e^{i\varphi_i} \cdot e^{i\omega_R t}$$

$$\underline{i}_{dq} = \hat{I}_R \cdot e^{i\varphi_i} = i_d + i \cdot i_q$$

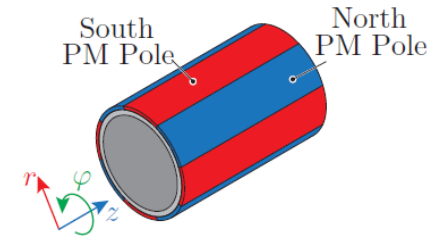
Rotary Machine: Torque

Stator: 6 concentrated coils



$$\underline{\psi}_{dq} = \hat{\Psi}_R$$

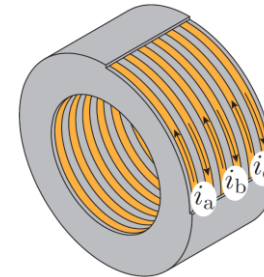
PM Rotor: $N_{pp,R} = 4$



$$T_z = \frac{3}{2} N_{pp,R} \cdot \hat{\Psi}_R \cdot i_q$$

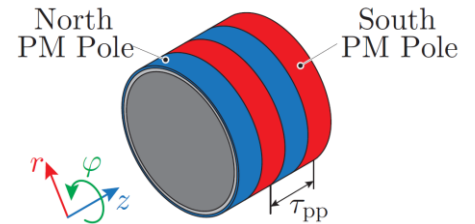
Linear Machine: Thrust Force

Stator: 3 concentrated coils



$$\begin{aligned} \underline{\psi}_{dq} &= \hat{\Psi}_L \\ \omega_L &= \frac{2\pi}{\tau_{pp}} \cdot v_z \end{aligned}$$

PM Rotor: 4 poles

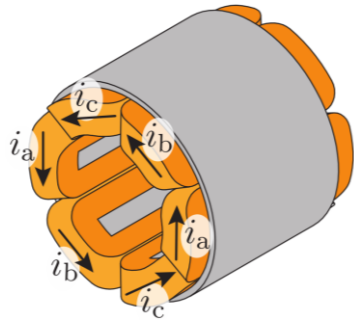


$$F_z = \frac{3\pi}{\tau_{pp}} \cdot \hat{\Psi}_L \cdot i_q$$

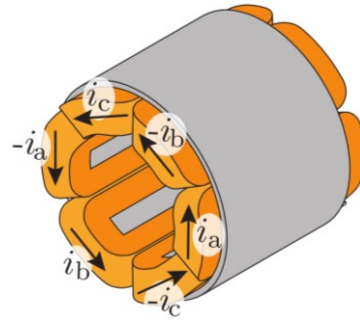
Generic Complex Space Vector Modeling (2)

Rotary Machine: Bearing Force

▼ Torque Generation

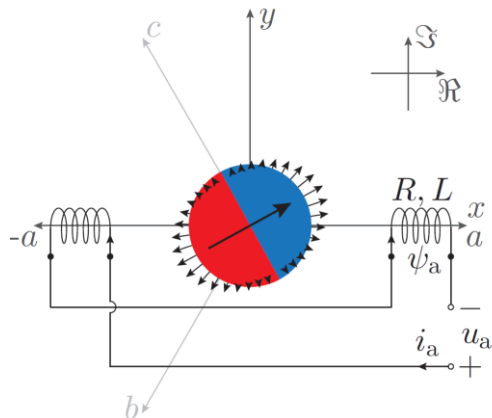


▼ Bearing Force Generation



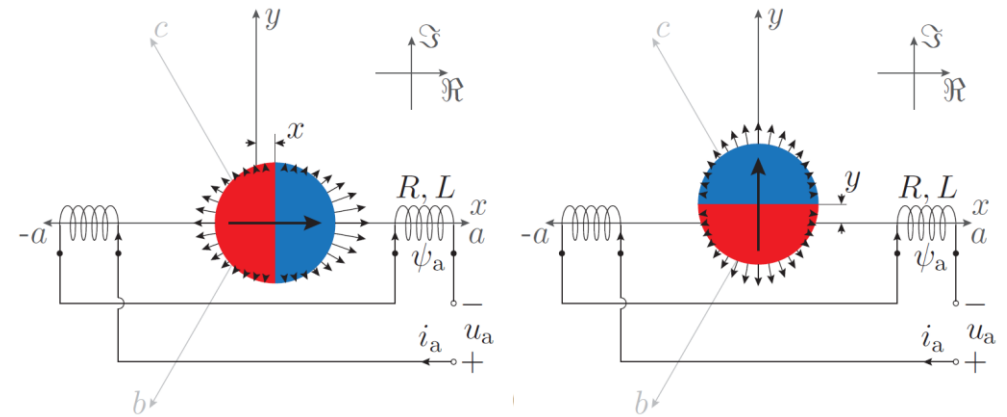
Rotor in Center → No Flux Linkage

- Model: two coils in anti-series connection



Displaced Rotor → $\frac{d\hat{\Psi}_R}{dx} = \frac{d\hat{\Psi}_R}{dy} = \chi_{pm,R}$

- Flux linkage radial sensitivity



Three Phase Flux Linkage

$$\begin{aligned} \psi_a &= \chi_{pm,R} \cdot [x \cdot \cos(\omega_R t + \varphi_\psi) - y \cdot \sin(\omega_R t + \varphi_\psi)] \\ \psi_b &= \chi_{pm,R} \cdot [x \cdot \cos(\omega_R t + \varphi_\psi - 2\pi/3) - y \cdot \sin(\omega_R t + \varphi_\psi - 2\pi/3)] \\ \psi_c &= \chi_{pm,R} \cdot [x \cdot \cos(\omega_R t + \varphi_\psi + 2\pi/3) - y \cdot \sin(\omega_R t + \varphi_\psi + 2\pi/3)] \end{aligned}$$

Space Vector

$$\underline{\psi} = \chi_{pm,R} \cdot (x + i \cdot y) \cdot e^{i \cdot \varphi_\psi} \cdot e^{i \cdot \omega_R t}$$

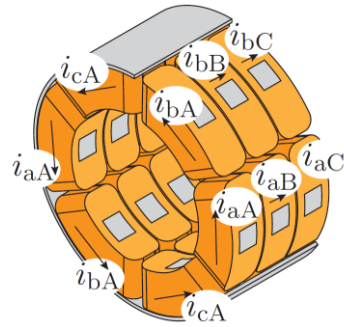
$$\underline{\psi}_{dq} = \chi_{pm,R} \cdot (x + i \cdot y) \cdot e^{i \cdot \varphi_\psi}$$

$$F_x = \frac{3}{2} \cdot \chi_{pm,R} \cdot i_d \quad F_y = \frac{3}{2} \cdot \chi_{pm,R} \cdot i_q$$

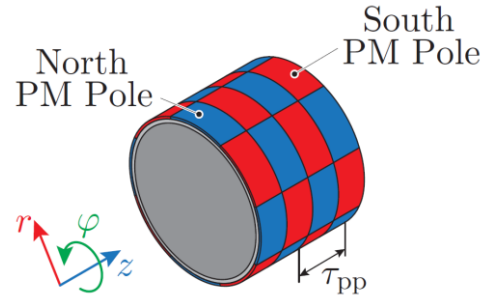
Generic Complex Space Vector Modeling (3)

Linear-Rotary Machine

▼ Stator: 18 concentrated coils



▼ PM Rotor: $N_{pp,R} = 4$



▼ Phase quantity

$$x_{aA} = \hat{X}_{RL} \cdot \cos(\omega_{RT} + \varphi_x) \cdot \cos(\omega_{LT} + \theta_x)$$

$$\hat{X}_{RL} \in \{\hat{U}_{RL}, \hat{I}_{RL}, \hat{\Psi}_{RL}\}$$

▼ Double space vector transformation

$$\underline{\underline{x}} \triangleq \frac{4}{9} [1 \quad \underline{a} \quad \underline{a}^2] \begin{bmatrix} x_{aA} & x_{aB} & x_{aC} \\ x_{bA} & x_{bB} & x_{bC} \\ x_{cA} & x_{cB} & x_{cC} \end{bmatrix} \begin{bmatrix} 1 \\ \underline{b} \\ \underline{b}^2 \end{bmatrix}$$

$$\underline{\underline{x}} \in \{\underline{u}, \underline{i}, \underline{\psi}\}$$

$$\underline{a} = e^{i(2\pi/3)}$$

$$\underline{b} = e^{j(2\pi/3)}$$

▲ Rotary i complex plane

▲ Linear j complex plane

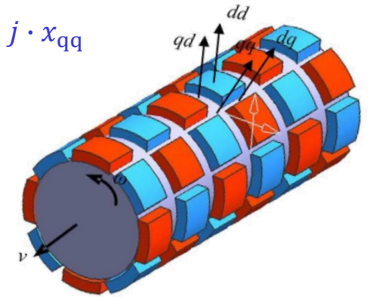
Double Complex Space Vector

$$\underline{\underline{x}} = \underbrace{\hat{X}_{RL} \cdot e^{i \cdot \varphi_x} \cdot e^{j \cdot \theta_x}}_{\text{rotary}} \cdot e^{i \cdot \omega_{RT}} \cdot e^{i \cdot \omega_{LT}}$$

$$\underline{\underline{x}}_{dq} = \hat{X}_{RL} \cdot e^{i \cdot \varphi_x} \cdot e^{j \cdot \theta_x} = x_{dd} + i \cdot x_{qd} + j \cdot x_{dq} + i \cdot j \cdot x_{qq}$$

▼ Flux linkage ($\varphi_\psi = 0$ and $\theta_\psi = 0$)

$$\underline{\underline{\psi}}_{dq} = \psi_{dd} = \hat{\Psi}_{RL}$$



Source: Jin et al., 2012

Torque and Linear Force

$$T_z = \frac{9}{4} N_{pp,R} \cdot \hat{\Psi}_{RL} \cdot i_{qd}$$

$$F_z = \frac{9\pi}{2\tau_{pp}} \cdot \hat{\Psi}_{RL} \cdot i_{dq}$$

Bearing Force

- Rotary phase rescheduling needed

$$F_x = \frac{9}{4} \cdot \chi_{pm,RL} \cdot i_{dd}$$

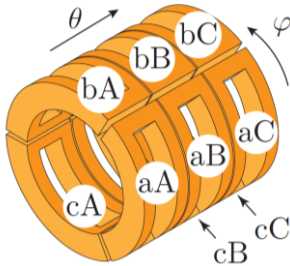
$$F_y = \frac{9}{4} \cdot \chi_{pm,RL} \cdot i_{qd}$$

Generic Complex Space Vector Modeling (4)

Linear Force Generation

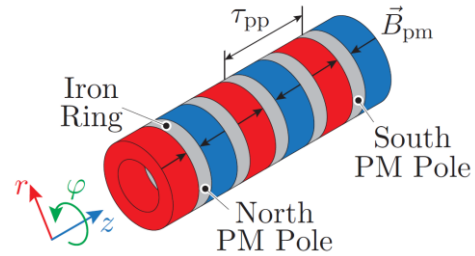
- Simpler than full linear-rotary machine

▼ Stator: 9 concentrated coils



$$\underline{\psi}_{dq} = \hat{\Psi}_M$$

▼ PM Mover



$$F_z = \frac{9\pi}{\tau_{pp}} \cdot \hat{\Psi}_M \cdot i_q$$

Bearing Force Generation

- Linear-rotary machine with $\omega_R = 0$

▼ Flux linkage

$$\underline{\underline{\psi}} = \chi_{pm,M} \cdot (x + i \cdot y) \cdot e^{i \cdot \varphi \psi} \cdot e^{j \cdot \theta \psi} \cdot e^{j \cdot \omega_L}$$

$$\chi_{pm,M} = \frac{d\hat{\Psi}_M}{dx} = \frac{d\hat{\Psi}_M}{dy}$$

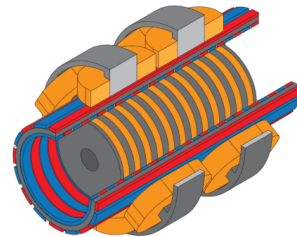
$$\underline{\underline{\psi}}_{dq} = \chi_{pm,M} \cdot (x + i \cdot y) \cdot e^{i \cdot \varphi \psi} \cdot e^{j \cdot \theta \psi}$$

$$F_x = \frac{9}{4} \cdot \chi_{pm,M} \cdot i_{dd}$$

$$F_y = \frac{9}{4} \cdot \chi_{pm,M} \cdot i_{qd}$$

Double Stator LiRA

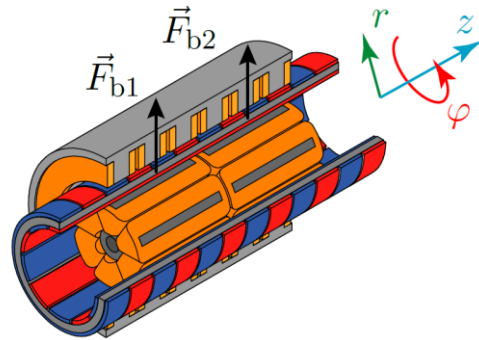
*Stator Arrangement
Cooling of Inner Stator
Geometry Optimization*



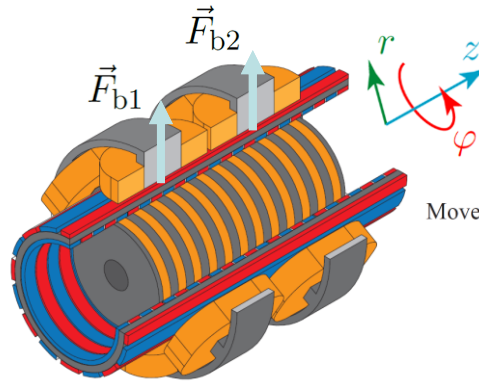
Double Stator (DS) LiRA Realization Options

■ Stator Arrangement

- Outer → Linear, Inner → Rotary

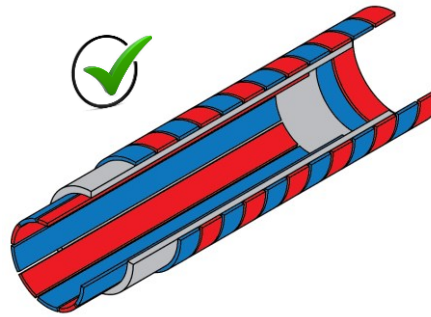


- Outer → Rotary, Inner → Linear

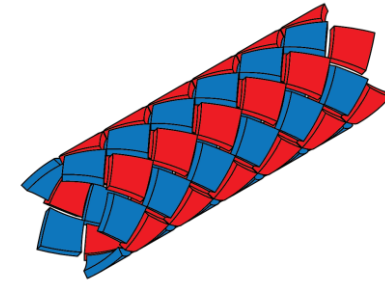


■ Mover Types

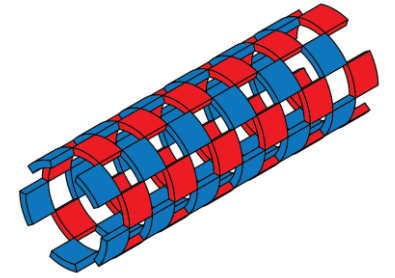
- With and Without Back Iron



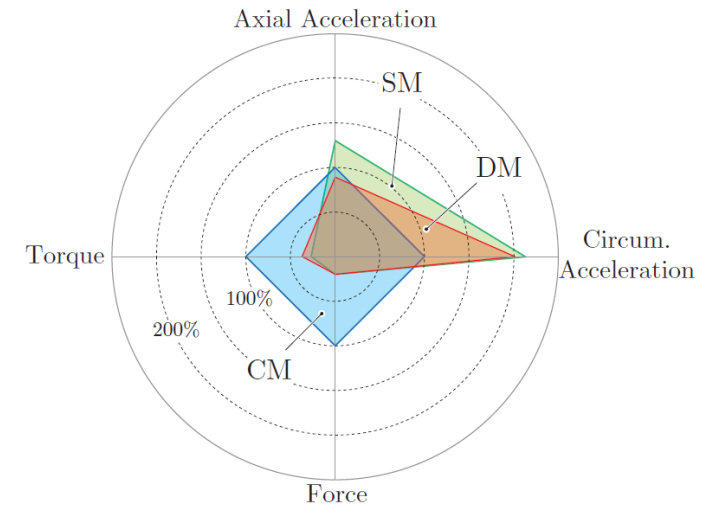
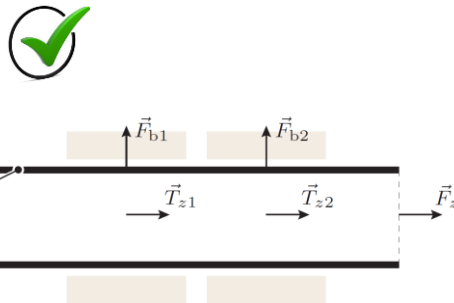
▲ CM



▲ DM

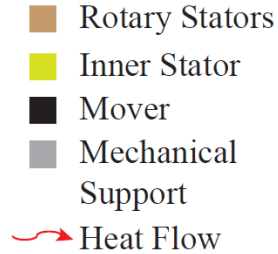
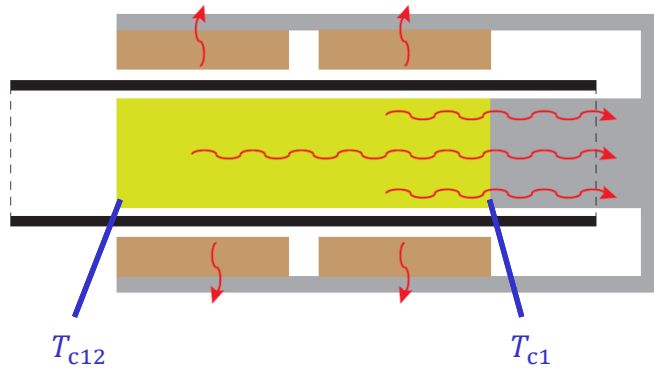


▲ SM



Cooling of the Inner Stator

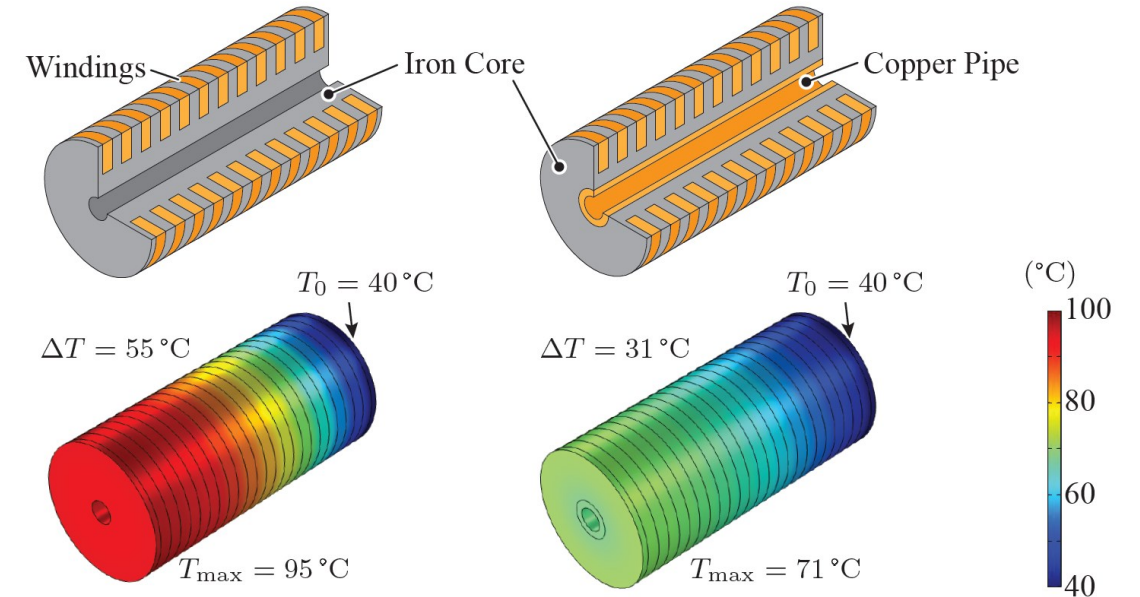
- Heat Flow Conduction Paths
 - Outer Stator: Radial Heat Flow
 - Inner Stator: Axial Heat Flow



- Winding Temperature: $T_{c12} > T_{c1}$
- Unequal Temperature Distribution due to Axial Heat Flow and Thermal Resistance

Reduction of Axial Thermal Conductivity

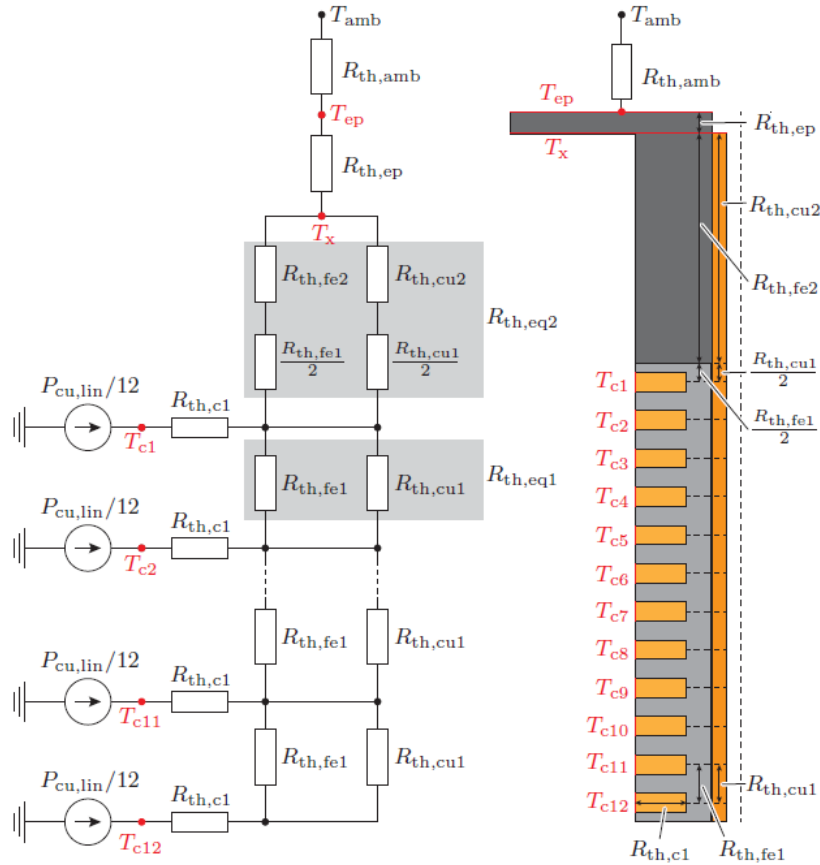
- Iron Core Thermal Conductivity: $\sim 20 \text{ W/(mK)}$
- Copper Pipe Thermal Conductivity: $\sim 400 \text{ W/(mK)}$



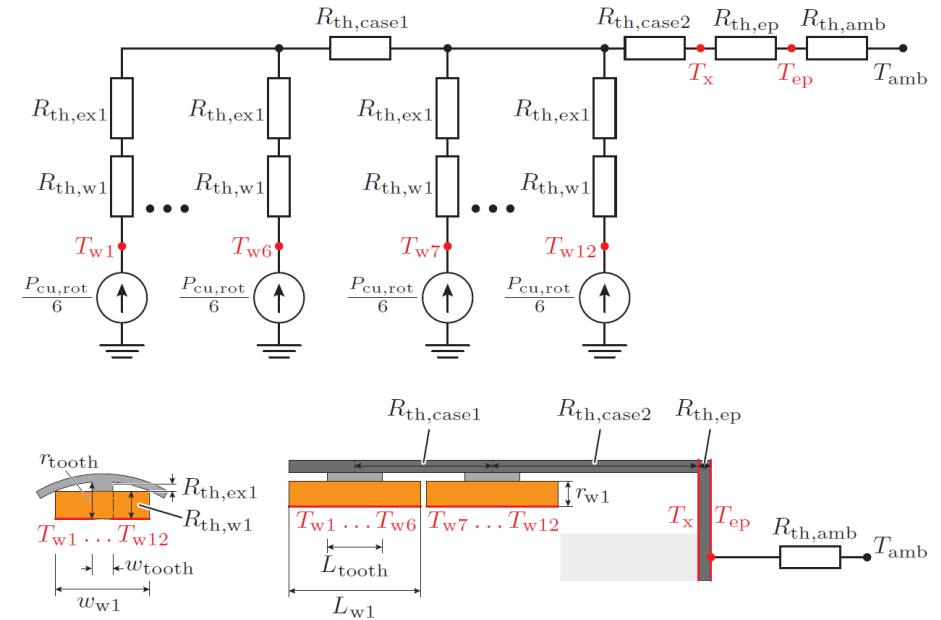
- Optimization Between 'Magnetic' and 'Thermal' Material

Analytic Thermal Model

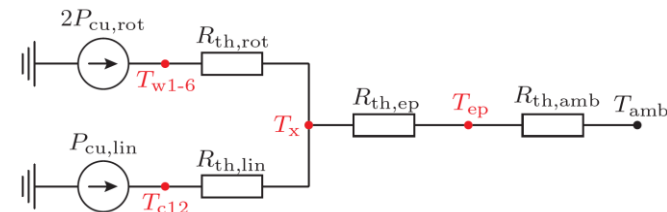
- Inner Linear Stator
 - Hot Spot Temperature: $T_{c12} < 120^\circ\text{C}$



- Outer Rotary Stators
 - Hot Spot Temperature: $T_{w1-6} < 120^\circ\text{C}$

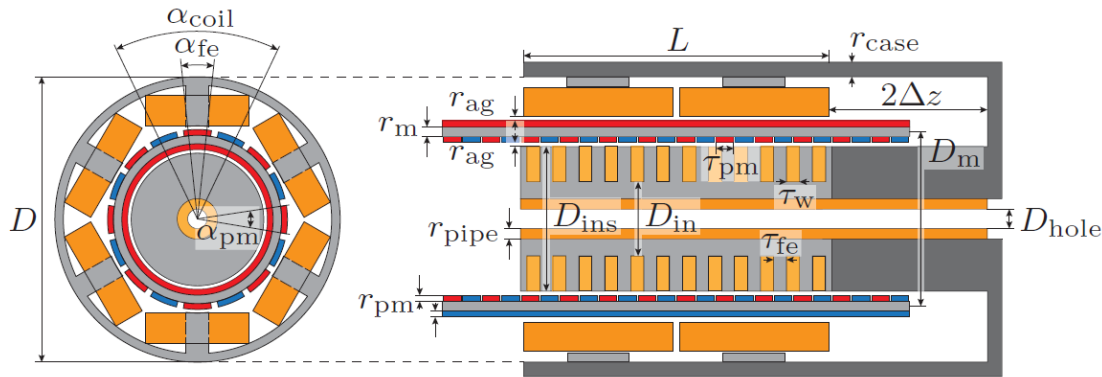


Thermal Model Equivalent Circuit



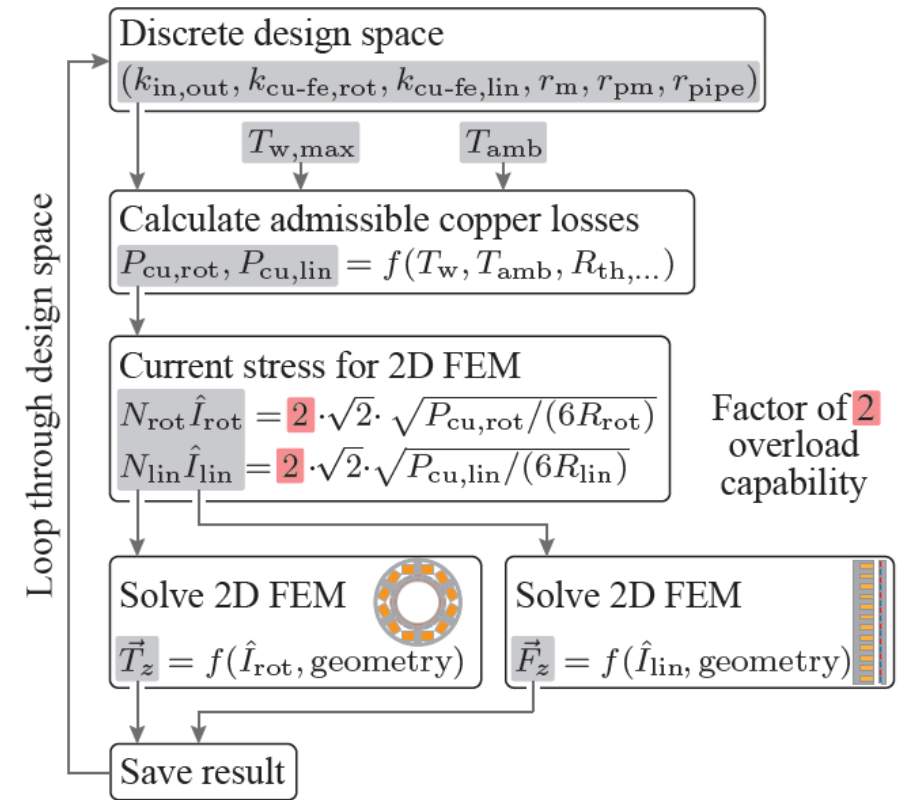
DS LiRA Geometry Optimization

- Parametrize Geometry
 - Outer Dimensions Fixed: $L = 100$ mm, $D = 100$ mm
 - Air Gaps: $r_{ag} = 0.7$ mm
 - Copper Pipe Hole: $D_{hole} = 8$ mm (Sensor Cables)
 - Max. Winding Temp.: 120°C



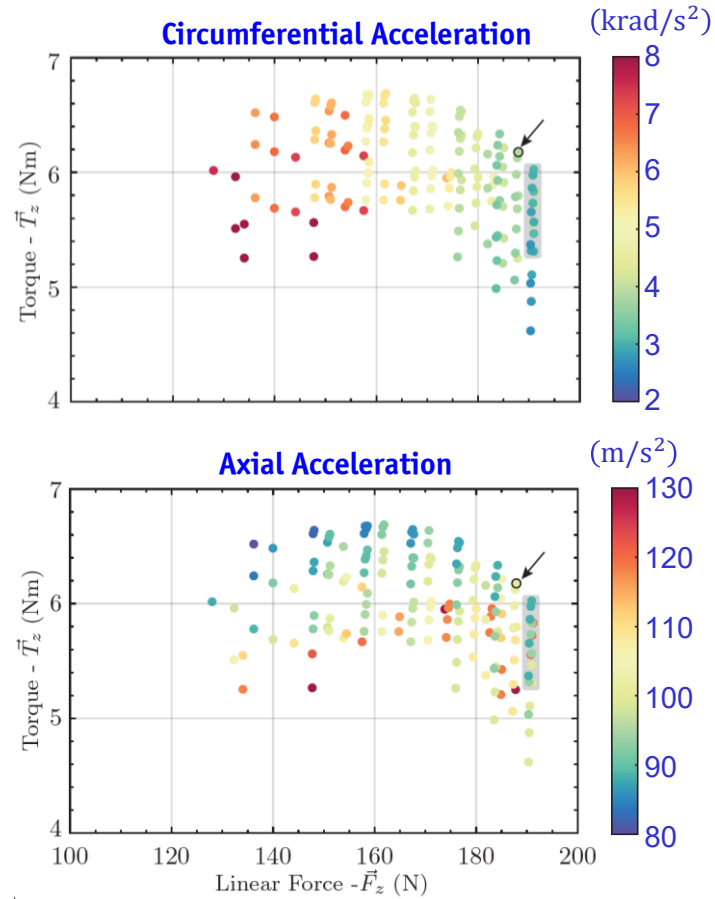
- Models:
 - Magnetic: 2D-FEM
 - Thermal: Analytic Lumped Parameter Circuit Network →

- Automated Optimization Procedure
 - Discrete Design Space



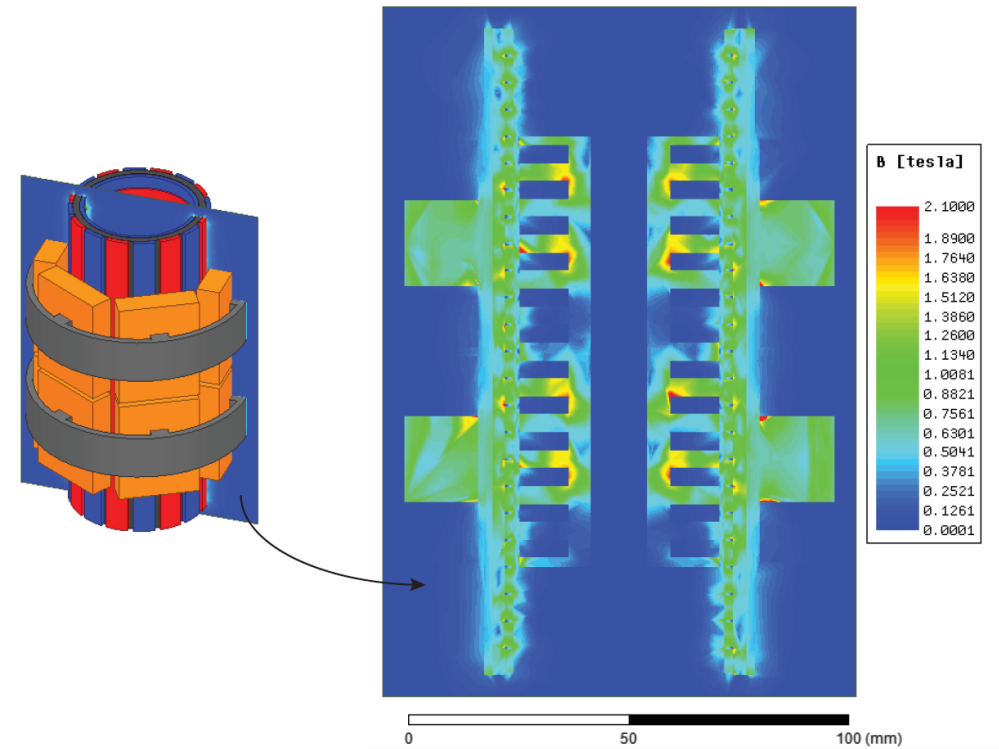
Optimization Results

- Torque vs. Linear Force Pareto Plots
- Compromise Between Torque/Force and Acceleration



Chosen Design:
 5.3 krad/s²
 123.5 m/s²
 6.24 Nm
 181.5 N

- 3D FEM Flux Density Distribution in the Chosen Design
- Flux Density Evaluated for Double the Continues Current
- Outer stator: < 2.1 T, Inner Stator: < 1.4 T, Mover: < 2.1 T

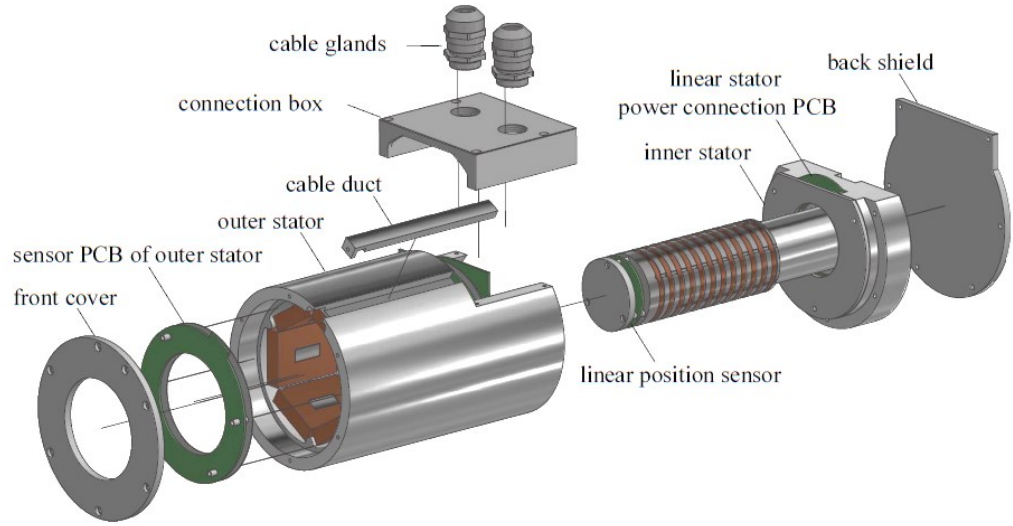


- Hardware Prototype →

DS LiRA Prototype

■ 3D CAD Model

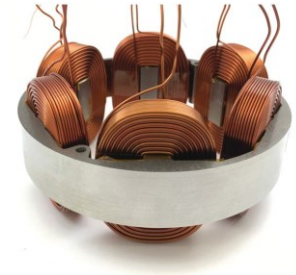
- 'Exploded View' of the Outer Rotary and Inner Linear Stator



- **Inner Stator:** 12 × Coil Windings, 1 × Lin. Pos. Sensor PCB, 1 × Power Connection PCB
- **Outer Stator:** 12 × Concentrated Windings, 2 × Rotary/Radial Pos. Sensor PCBs, 1 × Power Connection PCB

■ Prototype Realization

- Outer Rotary Stator



- Inner Stator



- DS LiRA



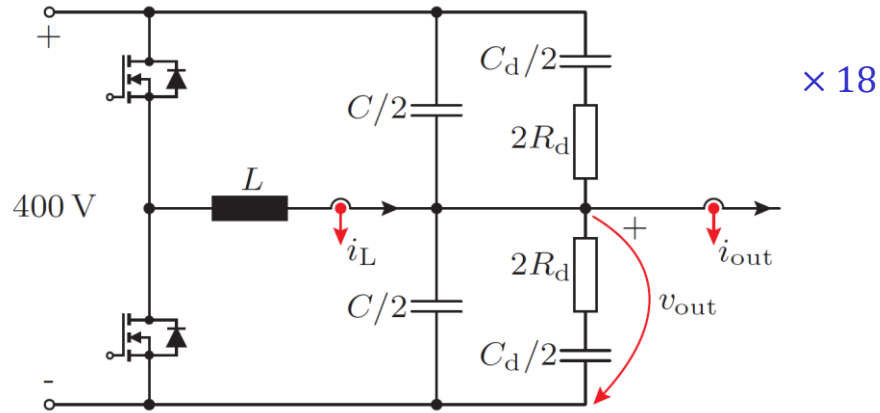
- Mover



18-Phase Inverter Supply

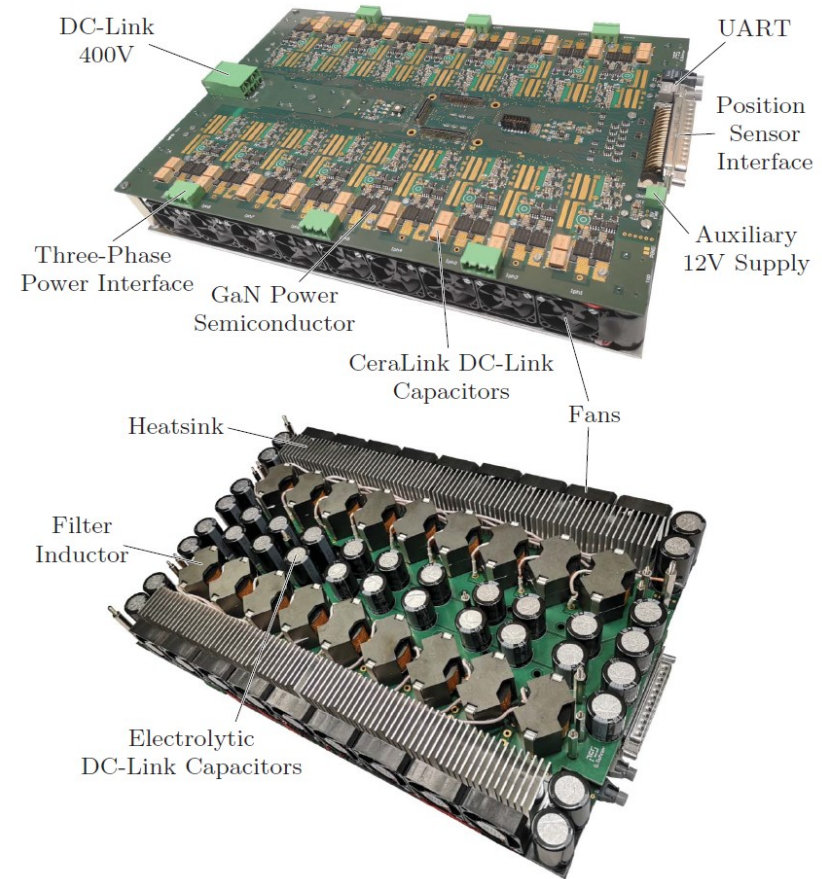
■ Schematic

● LC Output Filter with Parallel RC Damping



- **Power Semiconductors:** 600 V, 70 mΩ, CoolGaN – MOSFET
- **Inductor:** $L = 80\mu\text{H}$, N87, RM12, 23 Turns, 71μm Strand
- **Capacitance:** $C = 4.8\mu\text{F}$ for $THD_{vout} = 1\%$
- **Heatsink Design:** $CSPI = 12 \text{ W}/(\text{Kdm}^3)$

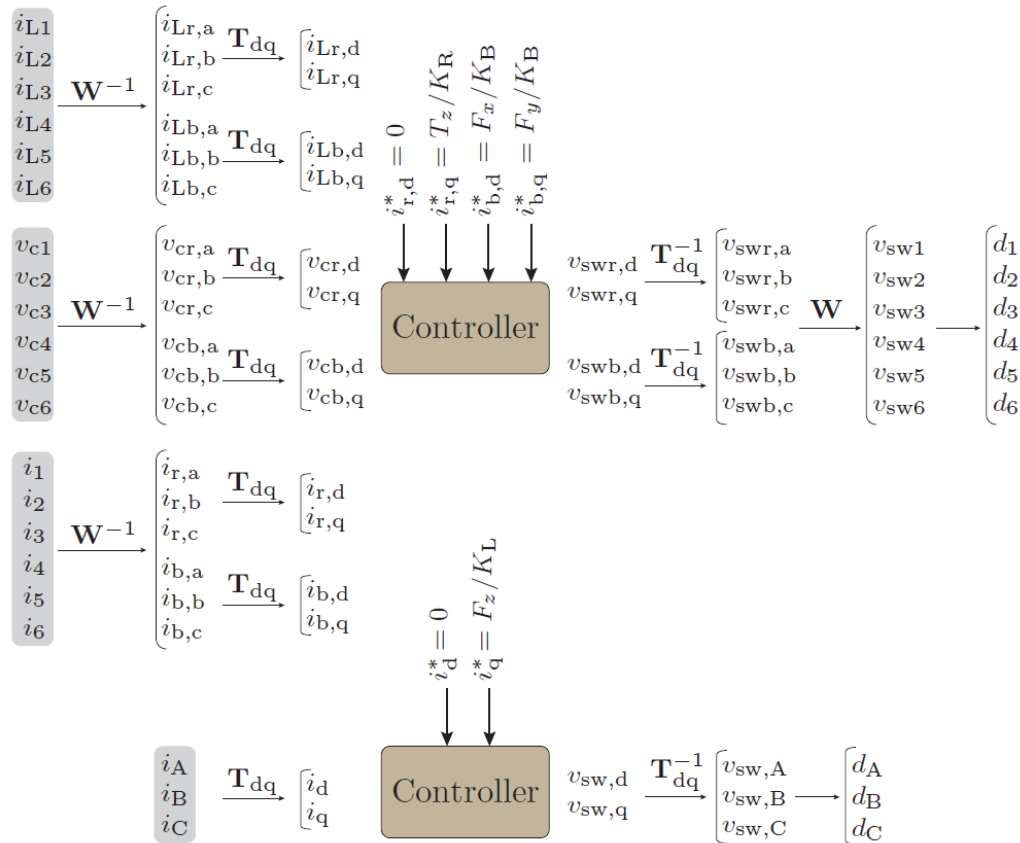
■ Hardware Realization



Current & Position Controller

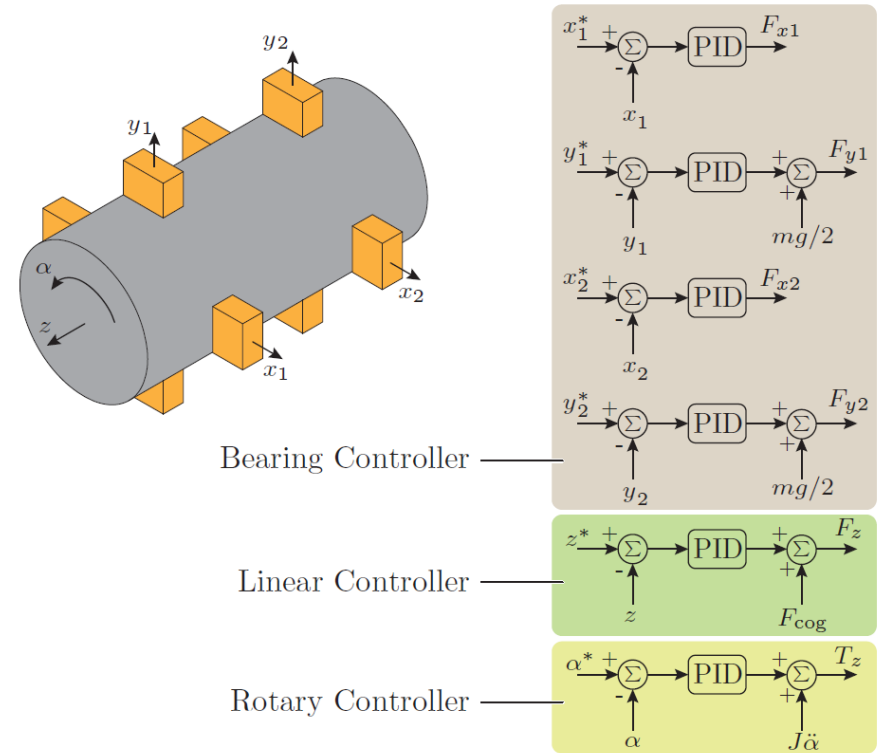
Current Control Structure

- Input: i_{out} References \rightarrow From the Position Controller



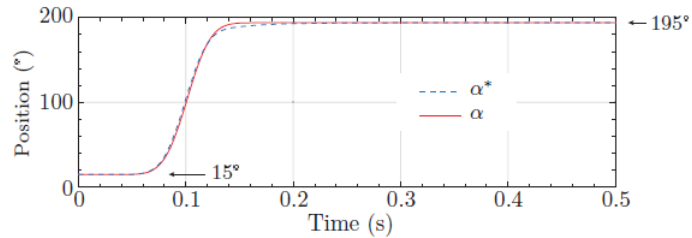
'Decentralized' Position Control

- Dedicated PID Controller for Each Motion Mode

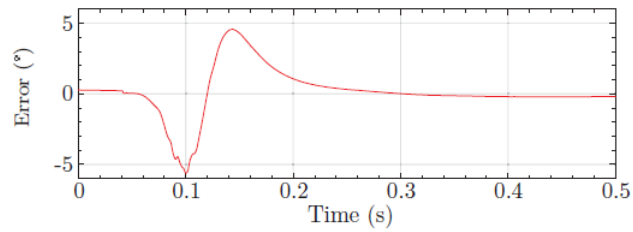


DS LiRA Measurement Results

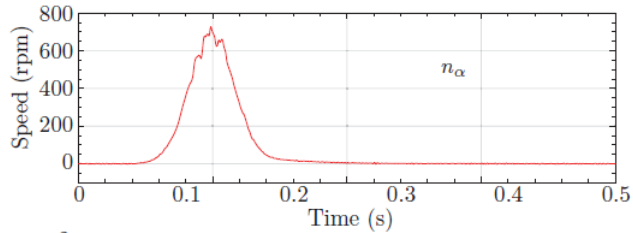
Rotary Step



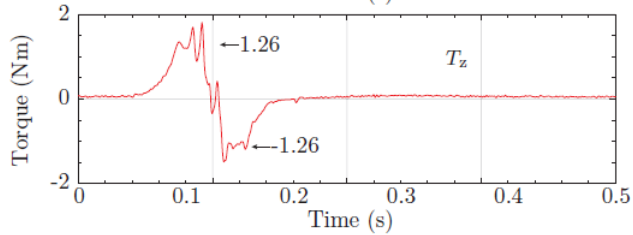
Stroke: 180°



Error: $< |\pm 5|^\circ$

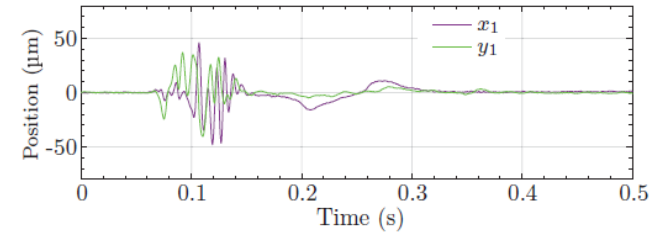


Max. Speed: ~ 700 rpm



Torque Limit: ± 1.26 Nm

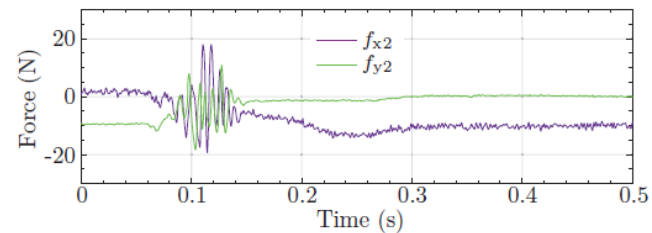
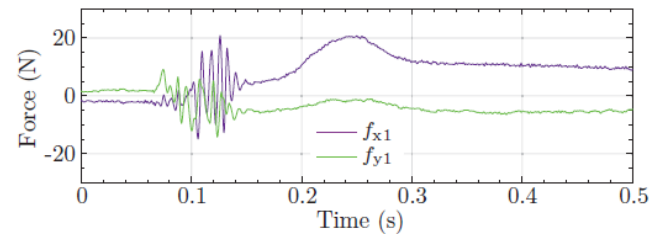
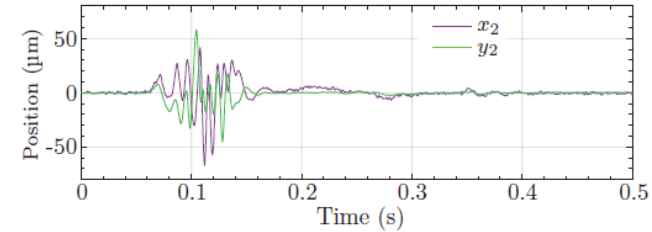
Rotary Step: Radial Positions



References:

- $x_1^* = 0$
- $y_1^* = 0$
- $x_2^* = 0$
- $y_2^* = 0$

Deviations: $\pm 50 \mu\text{m}$



DS LiRA Measurement Results

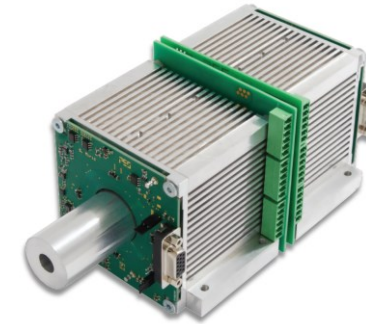
- Video



Part 1 Summary

■ Linear Bearingless Actuator

- Integration of Magnetic Bearings into a Linear Actuator
- Radial Position and Tilting Control in Micro Meter Range
- High-Precision/Purity/Dynamic Linear Motor Applications

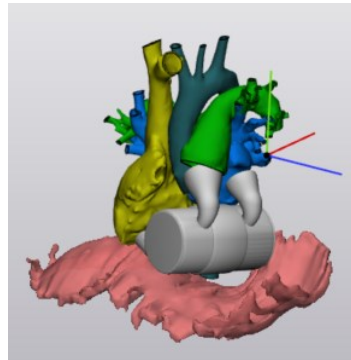


■ Linear-Rotary Bearingless Actuator

- Coupling of Rotation, Linear Motion, Magnetic Bearings
- Automatized Semi-Numerical Optimization Procedure
- High-Precision/Purity Applications



Part 2





Outline

Part 1

- ▶ *Introduction*
- ▶ *LiRA Examples / Applications*
- ▶ *Linear Actuator with Integrated MBs*
- ▶ *Position Sensors*
- ▶ *Dynamic Modeling, Controller Design*
- ▶ *Generalized Complex Space Vector*
- ▶ *Double Stator LiRA*

- ▶ *Outlook*

Part 2

- ▶ *Introduction*
- ▶ *Application: Blood Pumps*
- ▶ *Sensors for SB-LiRAs*
- ▶ *Design Example: the ShuttlePump*

- ▶ *Outlook*

Part 3

- ▶ *Introduction*
- ▶ *WPT to Linear Actuators*
- ▶ *Orthogonal and Parallel Field Concept*
- ▶ *Supplying Multiple Receivers*
Voltage & Current Impressed WPT

- ▶ *Outlook*

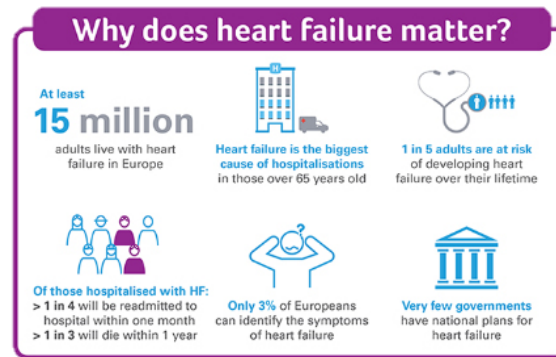
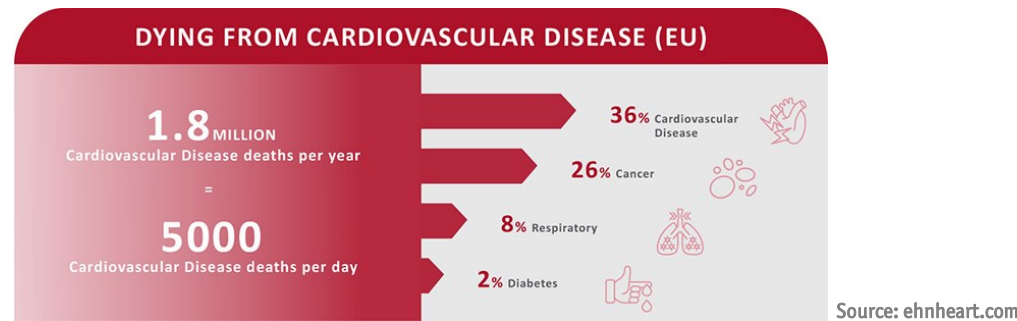


Blood Pumps

Motivation
Types and Applications
Existing Systems

Heart Failure

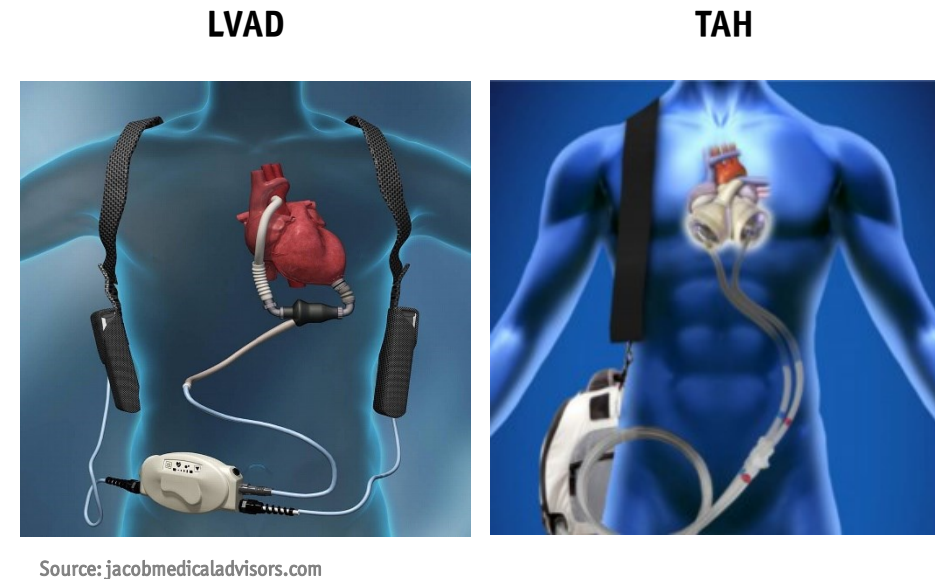
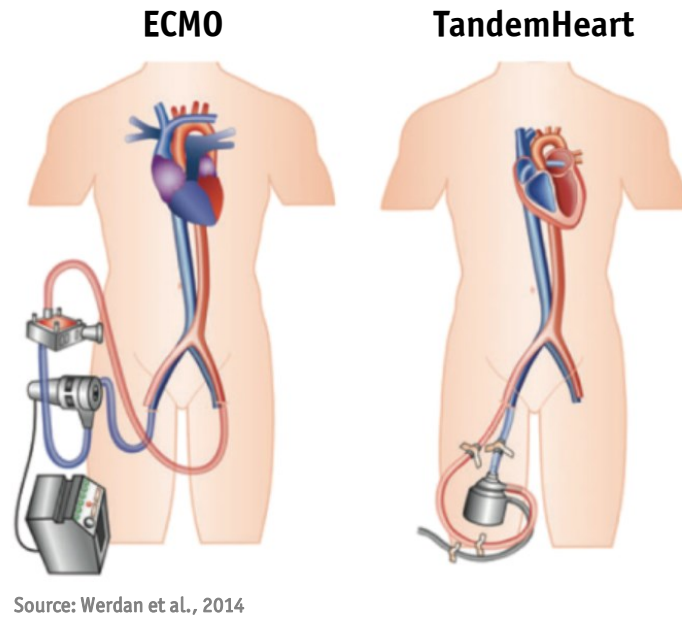
- > 26 million people worldwide, expected to increase with aging of population
- Congenital heart defects: ≈ 1% of newborns → complications



- Heart transplantation: not enough donors → ≈ 20% of patients dies on the waiting list
- Urgent need for short- and long-term solutions → Mechanical Circulatory Supports (MCSs)

Heart Failure – Mechanical Circulatory Support (MCS)

- **Short-term (acute)** → e.g. Extra-Corporeal Membrane Oxygenation (ECMO)
- **Long-term (chronic)** → e.g. Ventricular Assist Devices (VADs) or Total Artificial Hearts (TAH)



- **Either case: keep blood circulating** → **Mechanical Circulatory Support (MCS)**, i.e. a **blood pump**

Blood Pumps – A Taxonomy

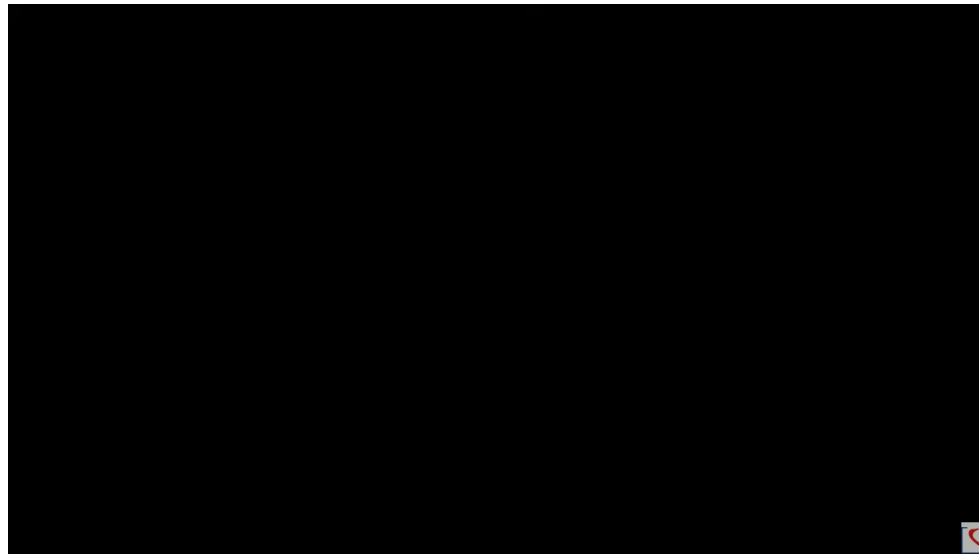


Pulsatile / Continuous Flow | Axial Flow / Centrifugal | Extra-Corporeal / Implantable

■ Common requirements: gentle blood handling (low hemolysis) | small volume

Blood Pumps – Pulsatile vs Continuous Flow

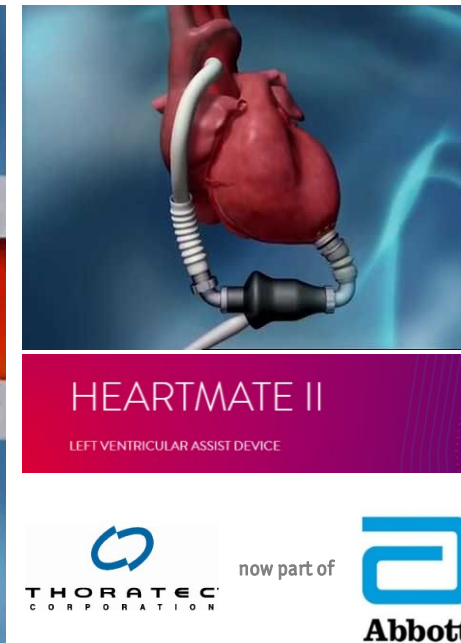
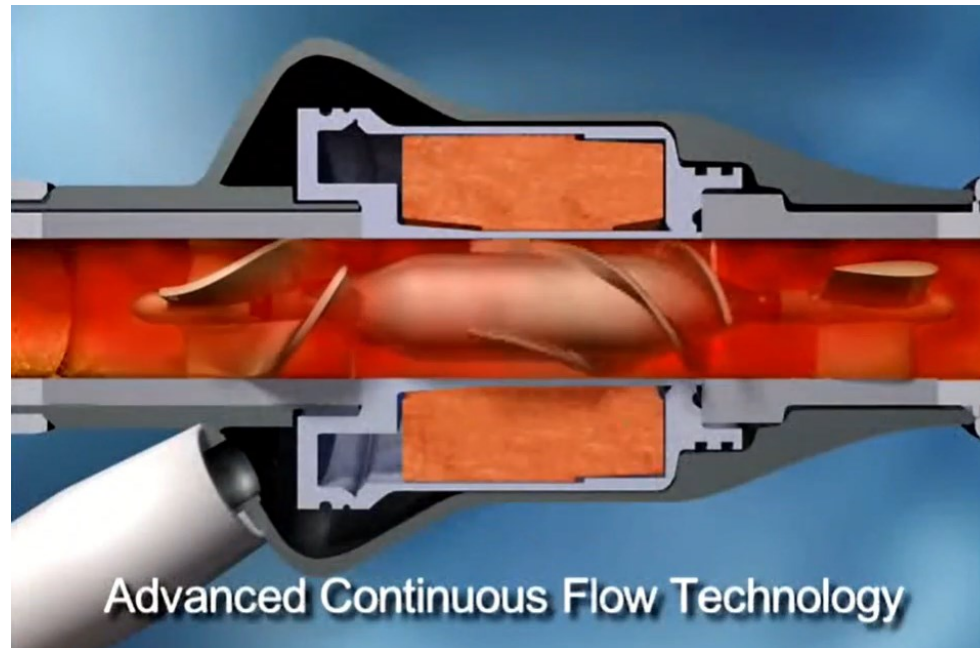
- Pulsatile / “1st gen” / Positive displacement → Physiological, pneumatically or electrically driven
- Example: BerlinHeart EXCOR® | VAD (L/R/Bi), Paracorporeal



- Larger / heavier / valves needed / external driving units

Blood Pumps – Pulsatile vs Continuous Flow

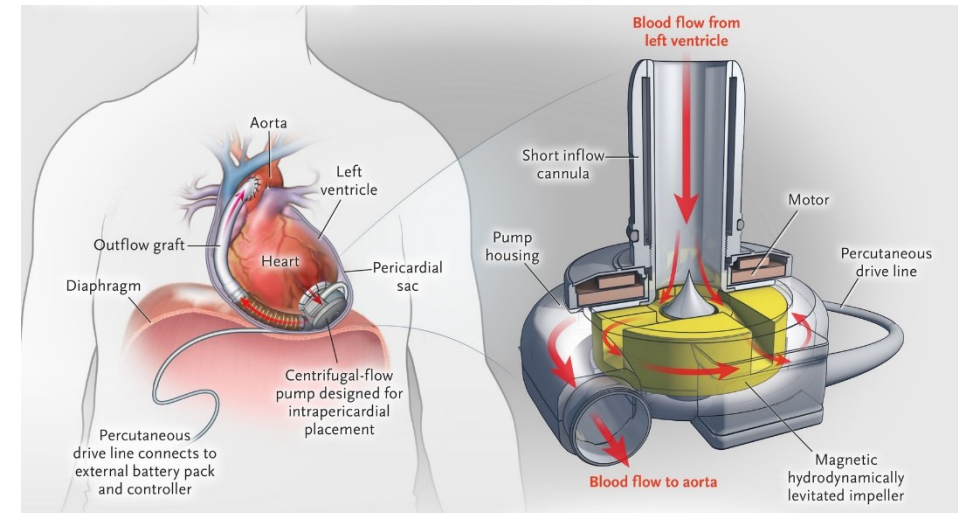
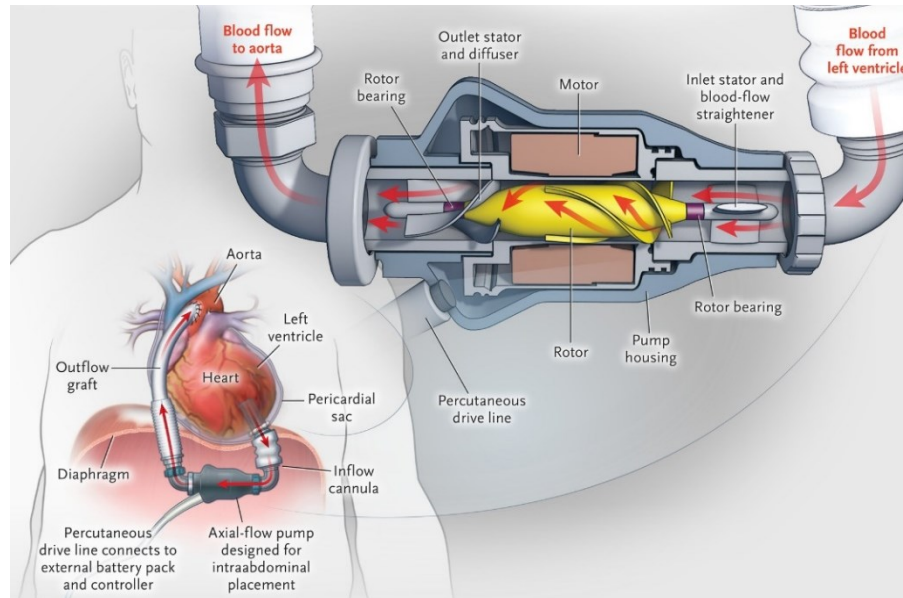
- **Continuous / “2nd gen” / Rotary Blood Pumps (RBPs)** → electrically driven | efficient | compact
- **Example: Abbott HeartMate II | LVAD, Implantable**



- **Can be realized with just one moving part / no need for valves** → reliability, durability

Blood Pumps – Axial Flow vs Centrifugal Flow

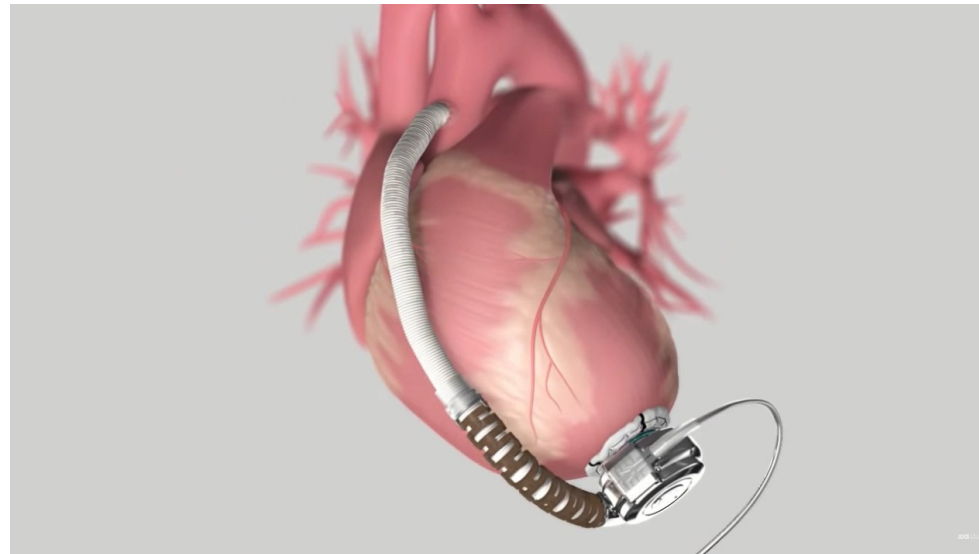
- **Continuous Flow Rotary Blood Pumps: two options**
- **Centrifugal flow** → can integrate non-contact bearing options



Source: Rogers et al, 2017

Blood Pumps – Axial Flow vs Centrifugal Flow

- Centrifugal flow / “2nd gen” / Rotary Blood Pumps (RBPs)
- Example: Medtronic HeartWare HVAD | LVAD, Implantable



HeartWare
Medtronic



- Hybrid passive magnetic + hydrodynamic bearing

Blood Pumps – Magnetically Levitated

- Centrifugal flow / “3rd gen” / Rotary Blood Pumps (RBPs) with Magnetic Bearings
- Example: Abbott HeartMate 3 | LVAD, Implantable

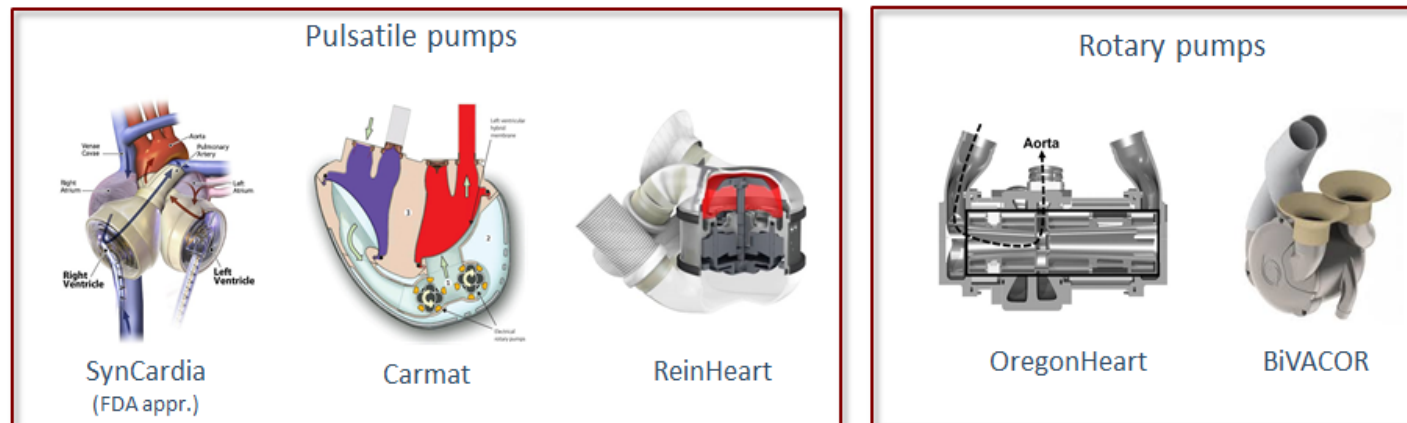


Source: cardiovascular.abbott

- Most advanced LVAD → direction for future systems

Total Artificial Hearts (TAH)

- **Bi-ventricular failure** → more compact wrt 2 x VADs
- Same pump types as for LVADs | Not as mature, research and development needed



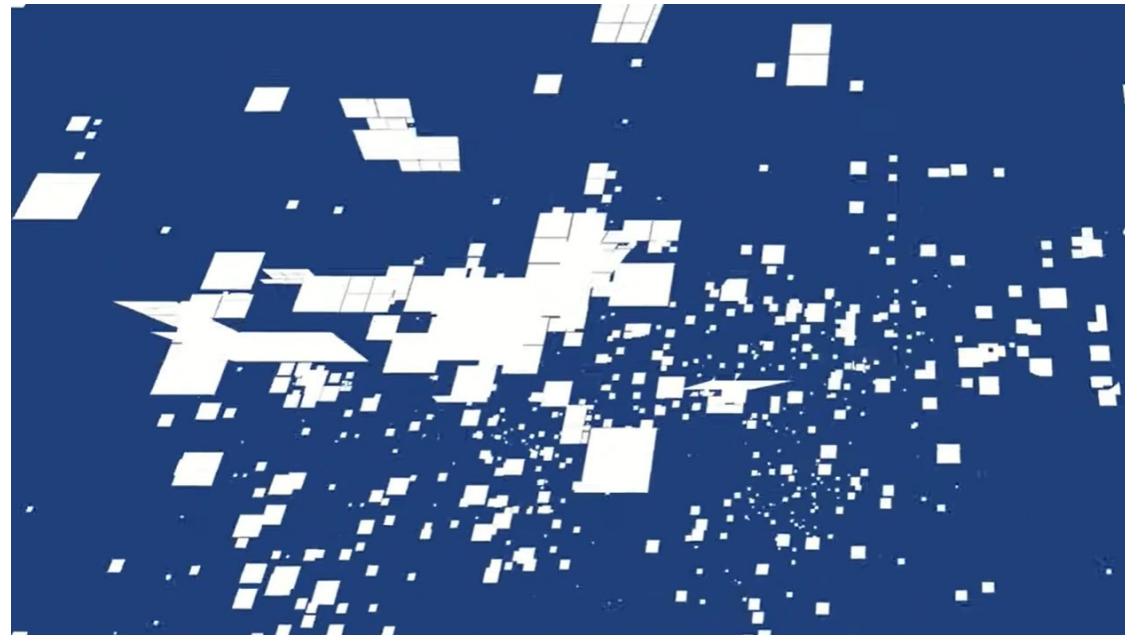
- + Physiological, pulsatile flow
- Valves can promote thrombus formation
- Flexible membranes and valves can be risk prone to device failure
- SynCardia has extracorporeal pneumatic driving unit (not fully implantable)

- + High durability: one moving part, no valves
- High shear stresses because of spinning rotor
- No or limited pulsatile flow

Source:  BIH Innovations
The Technology Transfer Office of BIH and Charité

Total Artificial Hearts (TAH)

- Other research directions: entirely-soft 3D-printed TAH (silicone) | Developed @ ETH Zurich
- Only lasts for ≈ 3000 beats (45 mins) \rightarrow feasibility / more research needed



Extra-Corporeal Blood Pumps

- Short-term treatment: extra-corporeal circulation | bridging strategy | e.g. COVID patients
- Example: Abbott CentriMag ECMO | Rotary / Continuous Flow / Centrifugal



CENTRIMAG
ACUTE CIRCULATORY SUPPORT SYSTEM WITH FULL MAGLEV FLOW TECHNOLOGY

Source: cardiovascular.abbott

Low device-related thrombosis¹ ↓ 2.5%

Low Hemolysis¹ ↓ 5%



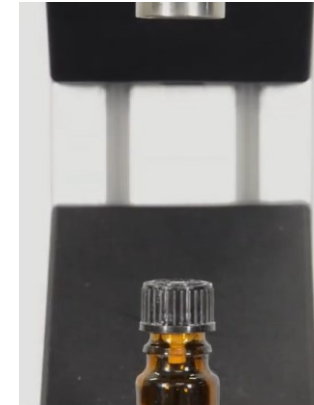
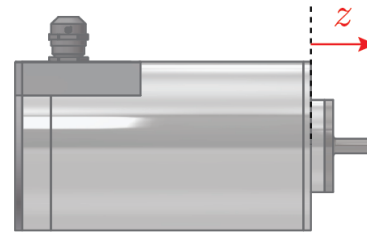
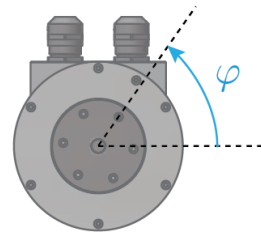


Sensor Systems for SB-LiRAs

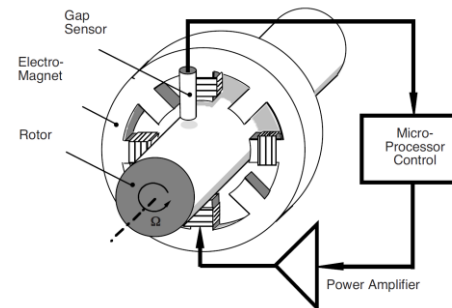
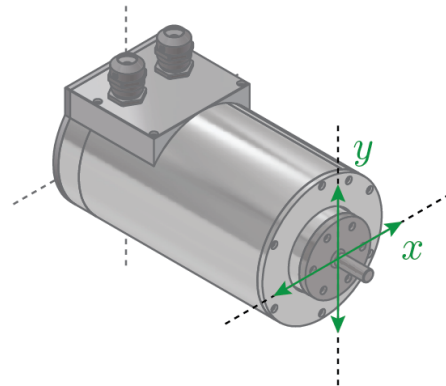
Sensor Types
——— *Non-contact Sensors* ———
Use in SB-LiRAs

Sensors for SB-LiRAs, what to measure?

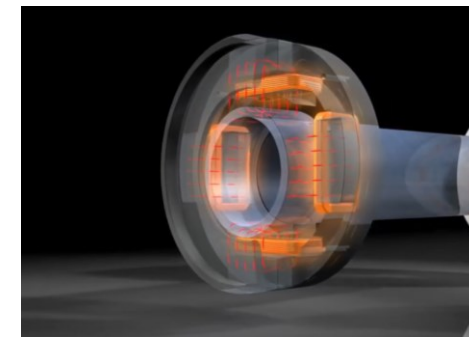
- High precision requirements → Feedback control → Need precise measurements
- Linear, Rotary, Radial position/displacement sensors



Source: linmot.com



Source: Schweitzer, 2009

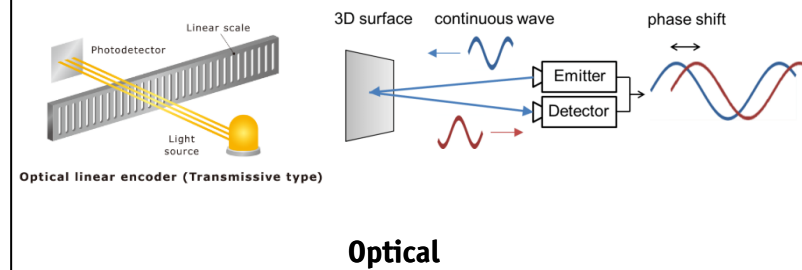
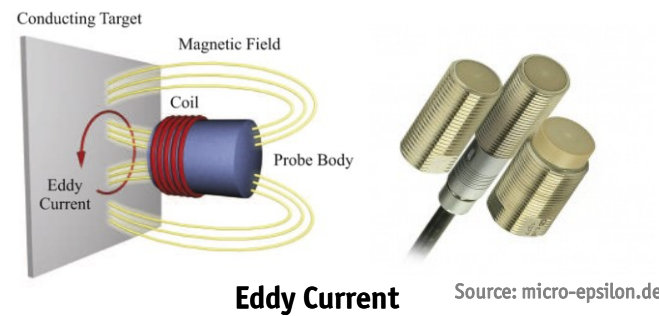
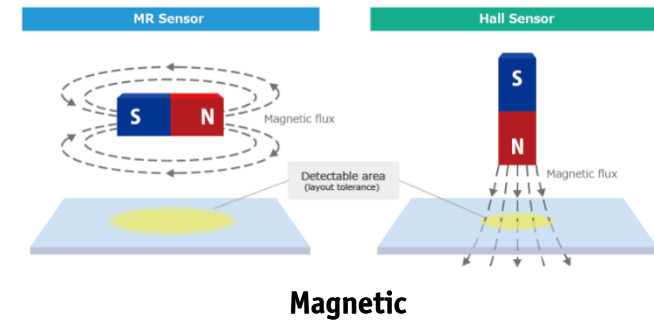
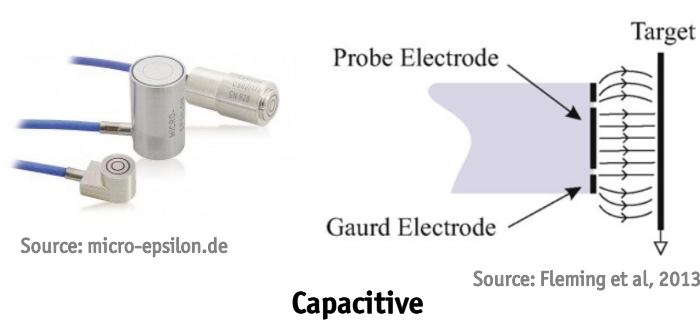


Source: keba.com

- Especially important / demanding to enable MBs!

Position/Displacement Sensors – Non-contact

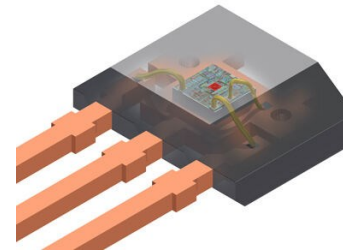
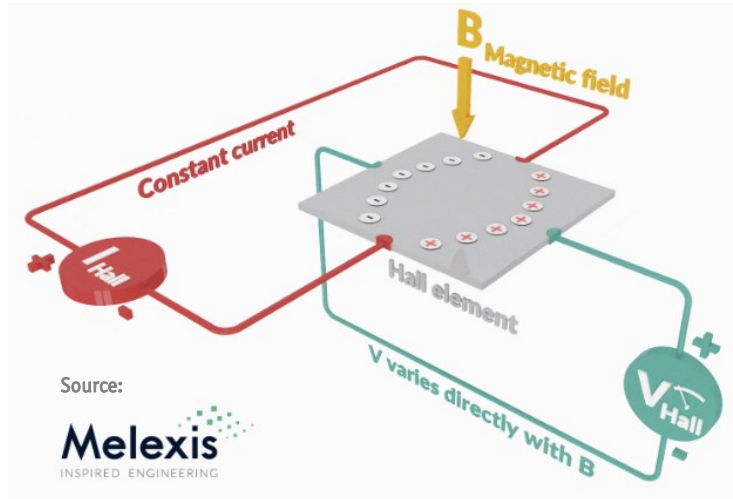
- MBs → Non-contact sensors / large bandwidth (up to 1 kHz) / high precision (sub- μm range)
- Different options / operating principles



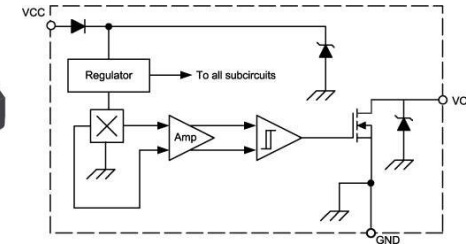
- Capacitive: grounded target | Optical: no objects between sensor and target
→ Mostly suited: Magnetic and Eddy Current

Hall-Effect Sensors

- Magnetic sensors, based on Hall effect | Hall element + conditioning circuit → DC output
- Conveniently packaged as a single IC | Multiple elements (axes) possible in the same package



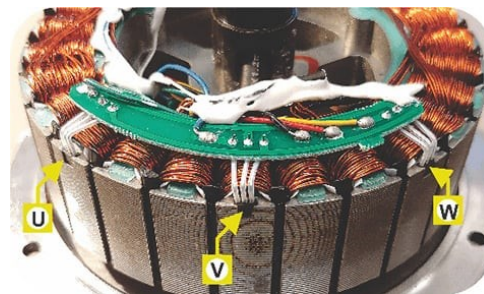
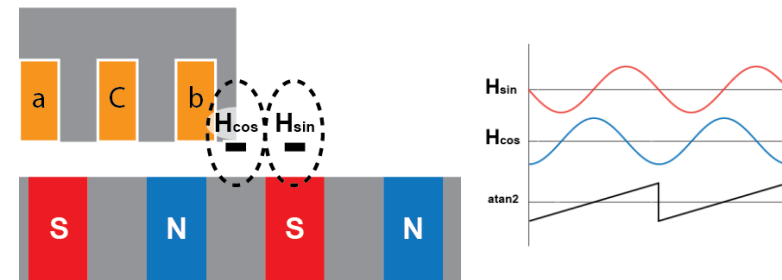
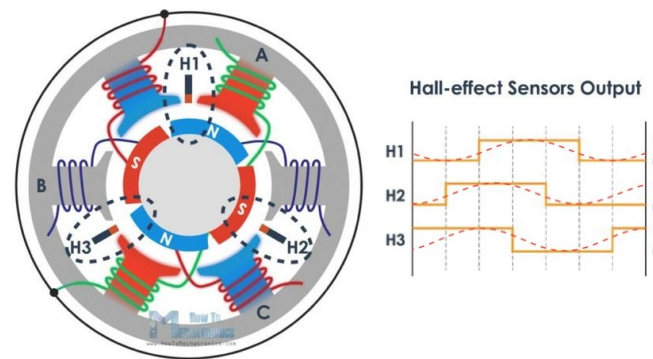
Source: **ALLEGRO** microsystems



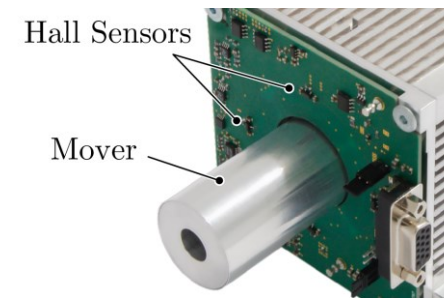
- Bandwidth: typically ≈ 10 kHz range | Resolution: can reach μm → sensor location is crucial!

Hall-Effect Sensors

- Typical use in Rotary Machines: 3 sensors, 120° el displaced, detect (electrical) rotor angle
- Can use analogously for Linear Machines | Alternative: 2 sensors, 90° el displaced ('sin' and 'cos')



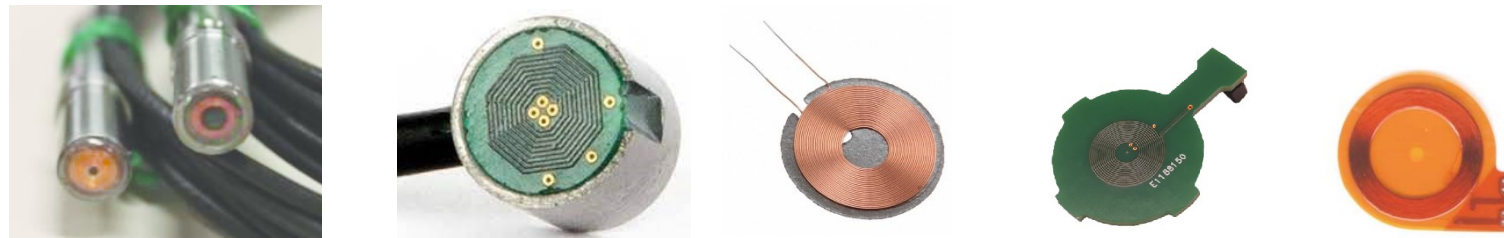
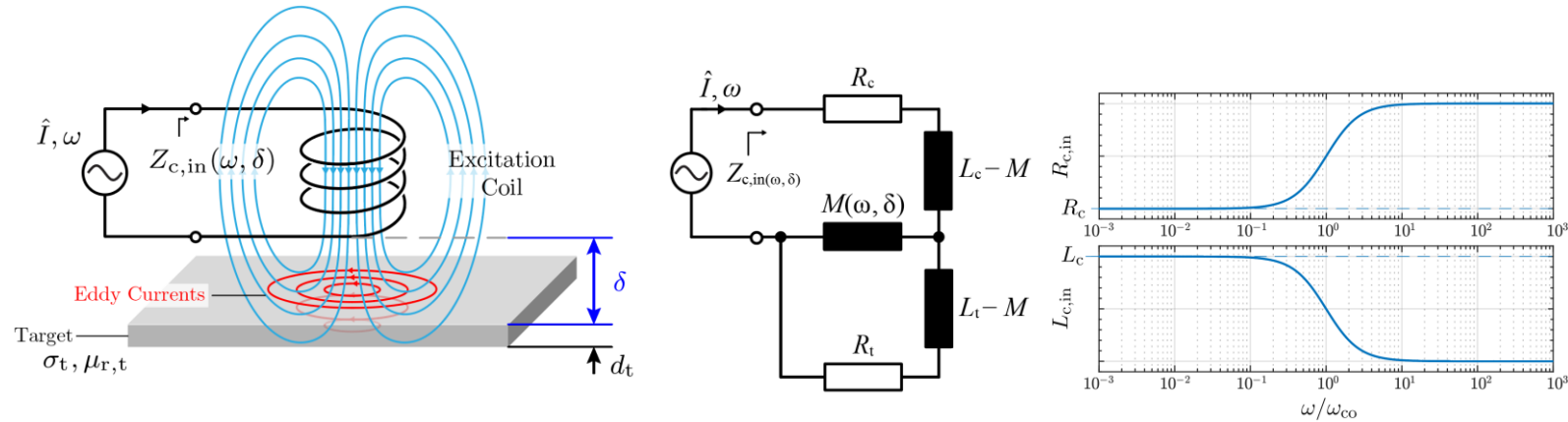
Source: digikey.com



- Main drawbacks: depend on PMs magnetization (irregular, aging, external fields!) / thermal drift

Eddy Current Sensors (ECSs)

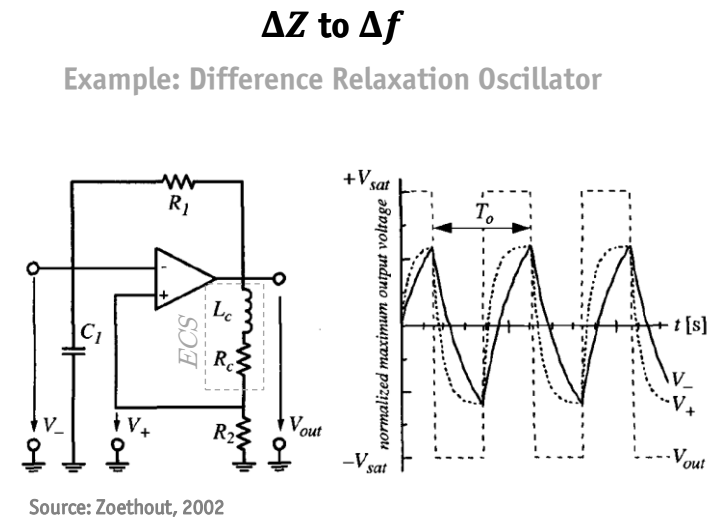
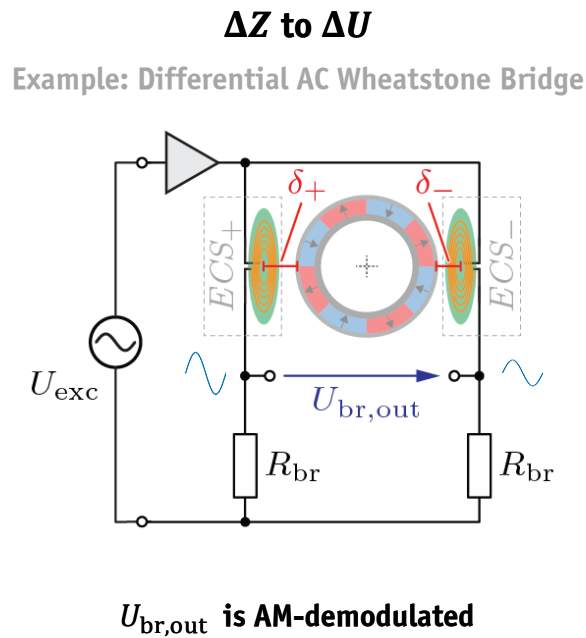
- Coil with high-frequency AC voltage excitation + conductive target → eddy currents induced
- Secondary field influences $Z_{c,in}$ (dep. on coupling factor!) → can measure distance δ (rule of thumb: range \approx radius)



- Coil realization: typically spiral, one layer → low parasitic capacitance, higher SRF, can excite in MHz range
- High level of integration: PCB-embedded coils, also flexible

Eddy Current Sensors (ECSs)

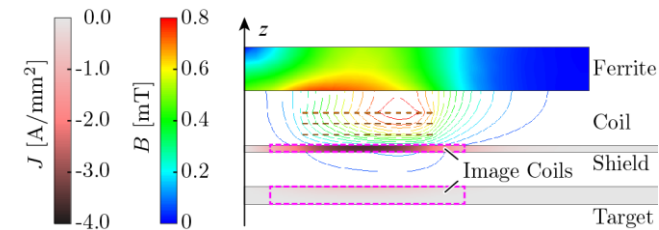
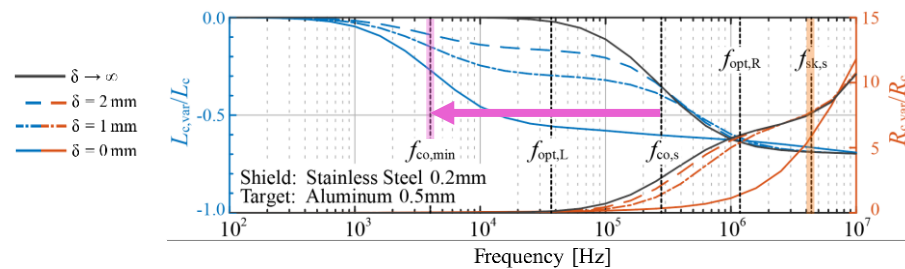
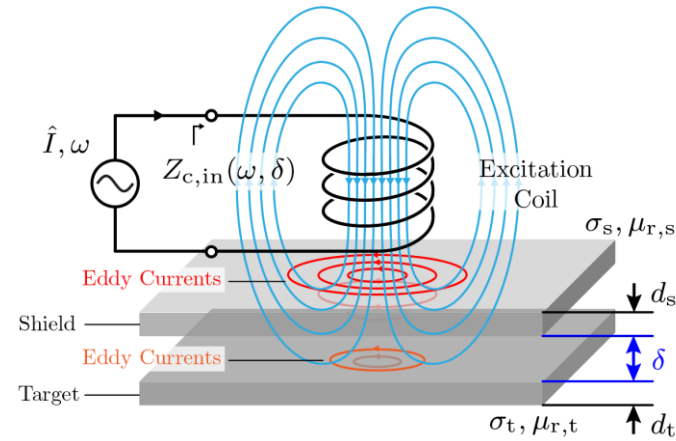
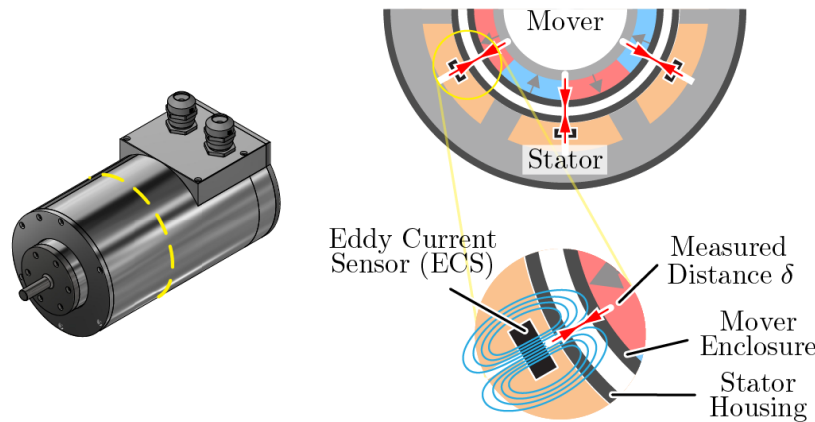
- AC excitation, extract position information from impedance → sensor interface / post-processing circuit
- Extensive literature about ECS interfaces for high performance sensors. Examples:



- Sensor interface determines achievable sensitivity / resolution / bandwidth / (non-)linearity
- Integrated interface solutions are becoming available (e.g. LDC, Texas Instruments)

Eddy Current Sensor "Seeing Through Walls"

- Point of strength of ECSs: can tolerate objects in the air gap → suited for harsh / dirty environments
- Special application: ECS measuring through a conductive enclosure → high purity / sealed applications

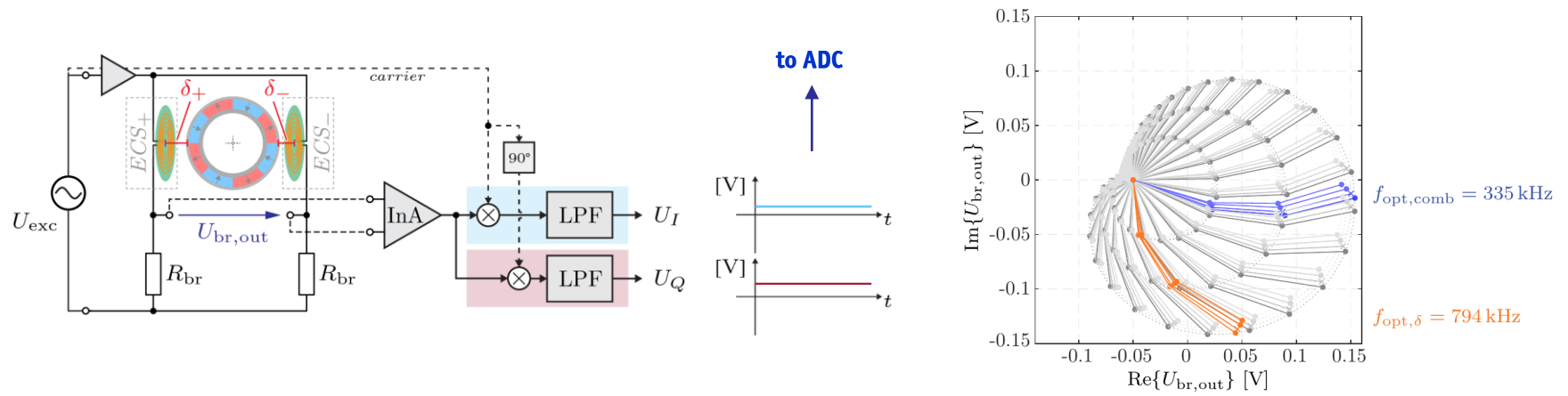


Source: Giuffrida et al, 2022

- Possible in a specific frequency range defined by shield and target properties
- Rule of thumb: make the enclosure thinner and/or of a less conductive material wrt the target

Eddy Current Sensor "Seeing Through Walls"

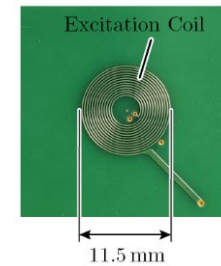
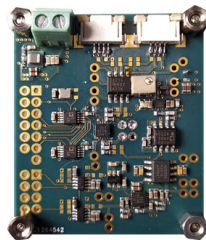
- Realized hardware prototype: PCB coil + evaluation board / analysis and verification of thermal drift
- Measurement circuit with quad. demod. → distinguish between distance δ and temperature T variations



Source: Giuffrida et al, 2022

Temperature-controlled setup

Realized Evaluation Board



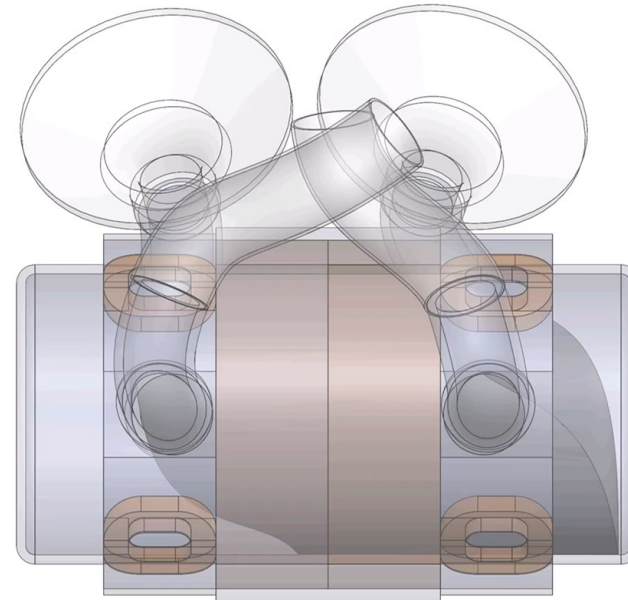
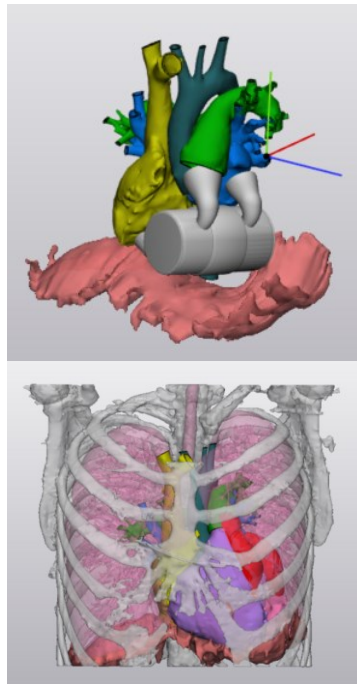


LiRA with HBs: ShuttlePump

*Machine Design
Sensor System
Built Prototype*

ShuttlePump

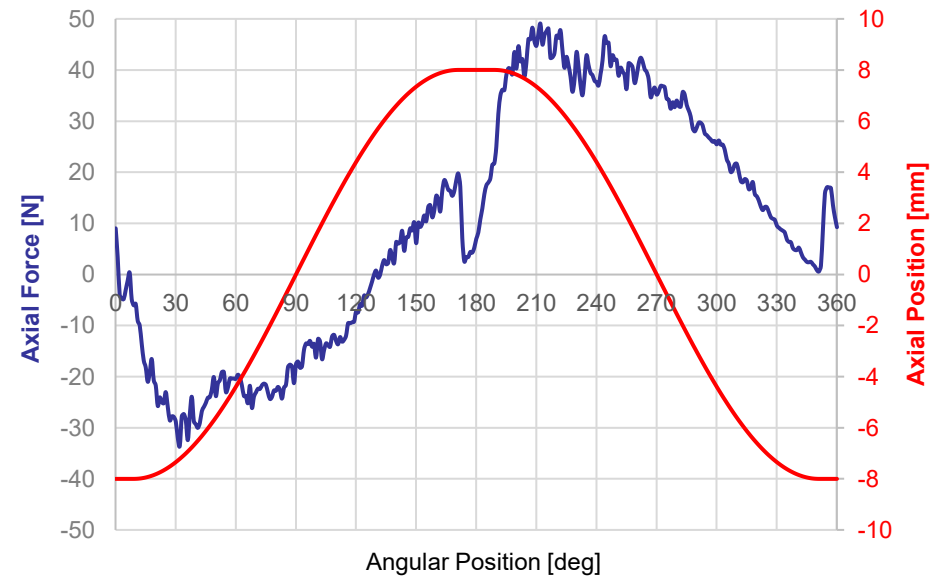
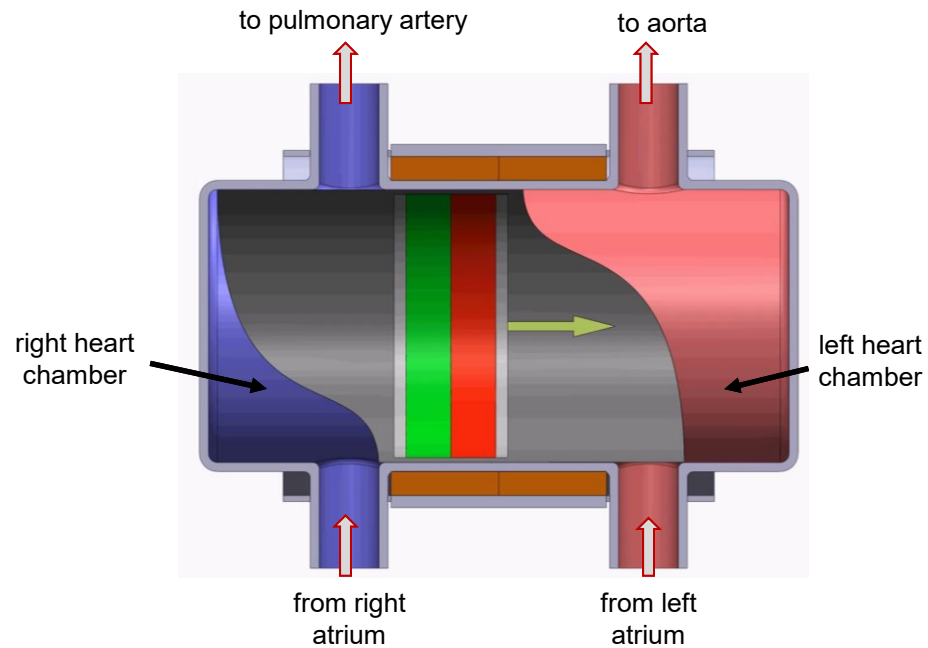
- **Implantable TAH based on a LiRA** → opening/closing of inlets/outlets @5 Hz → **valveless!**
- **Pulsatile flow** → physiological



- **Design of the LiRA Motor Drive System @ PES** – under realization

ShuttlePump

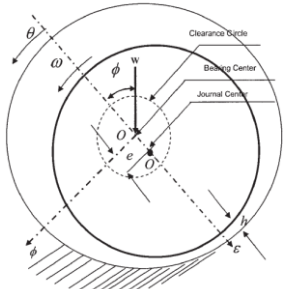
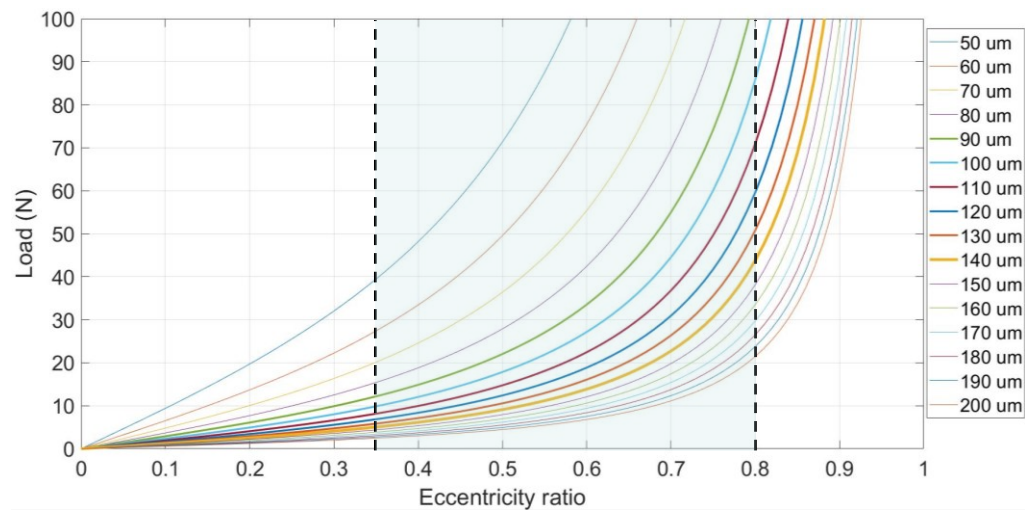
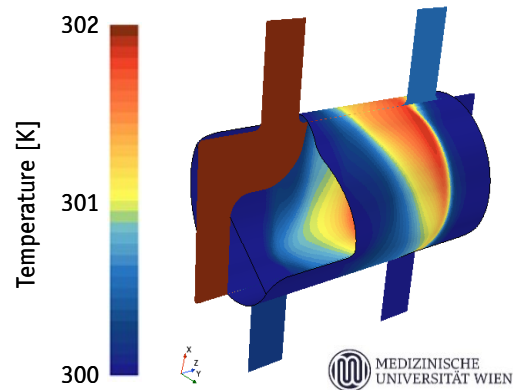
- **Linear Actuator: push blood in circulation → motion profile with force requirement**
- **High power density (up to 10 W peak in 200 cm³)**



- **Important constraints:**
 - 1) **blood temperature increase < 2°C → minimize losses**
 - 2) **overall device weight < 900 g, minimize piston weight**
 - 3) **outer diameter < 70 mm**

ShuttlePump – Hydrodynamic Bearing

- **Rotary Actuator: continuous 3 mNm axial torque** → establish journal HB
- **CFD simulations from Medical University of Vienna / HB design**



- W** – load
- e** – eccentricity
- c** – clearance
- Φ** – attitude angle
- ε** – eccentricity ratio e/c
- ω** – angular velocity
- h** – minimum film thickness

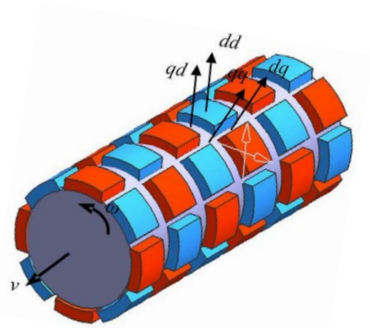
- **Acceptable eccentricity ratio: 0.35 – 0.8**
- **May be unstable if $\epsilon < 0.35$ or $\epsilon > 0.8$**

Source: Khonsari et al., 2017

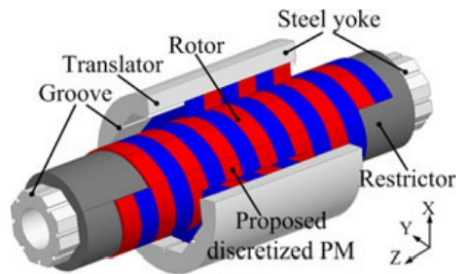
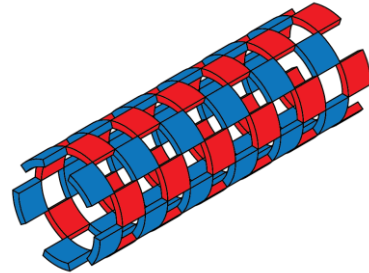
- **Blood gap thickness: trade off radial load / blood heat-up** → Suggested blood gap: 140 μm

ShuttlePump – Motor Concept

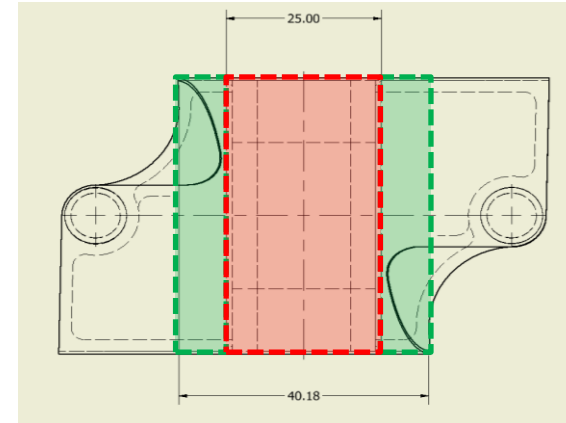
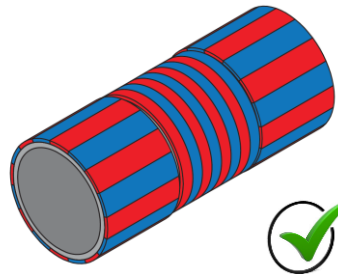
- Permanent Magnet Synchronous Machine (PMSM): high power density, PMs embedded in the piston
- Minimize drive unit's complexity, i.e. number of phases / half bridges



Source: Jin et al., 2012



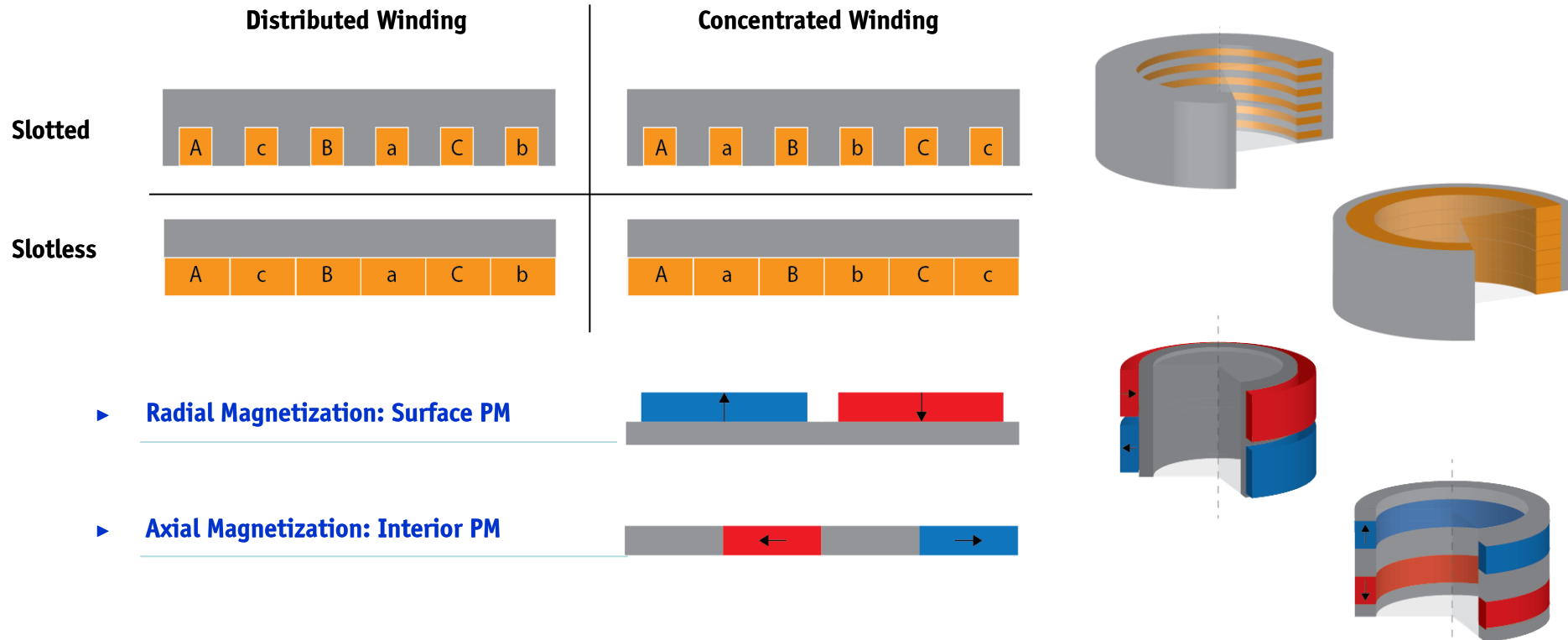
Source: Ling et al., 2018



- Requirements for LA and RA highly differ → “Independent” machine design of LA and RA, 3 + 3 ph.
→ maximum lateral surface for LA

ShuttlePump – LA Design

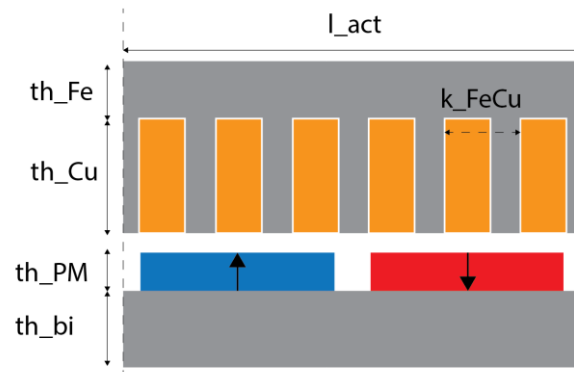
- **Tubular Linear Actuator (TLA), simplest possible stator / mover designs (1 pole pair)**



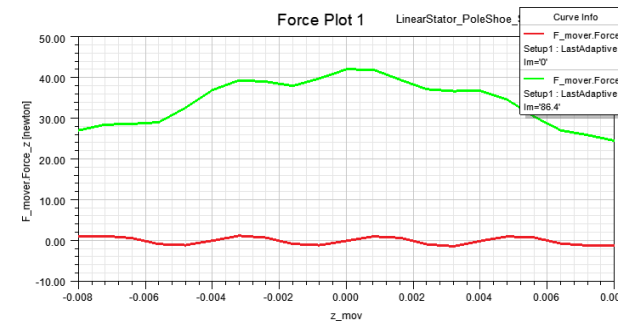
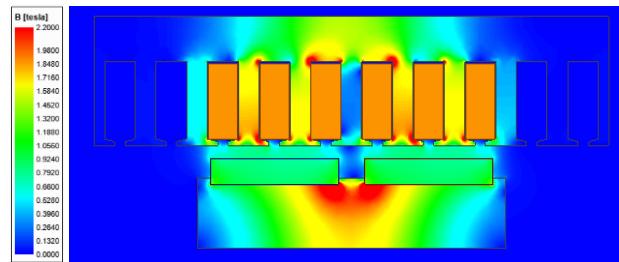
- **Stator: if slotted → minimum air gap, higher flux density, less current needed → less losses**
- **Mover: both radial and axial magnetization possible, manufacturability**

ShuttlePump – LA Design

- Parameterization + Optimization with Finite Element Methods (FEM) simulations
- For fixed output axial force (43 N), objectives: least losses | least weight



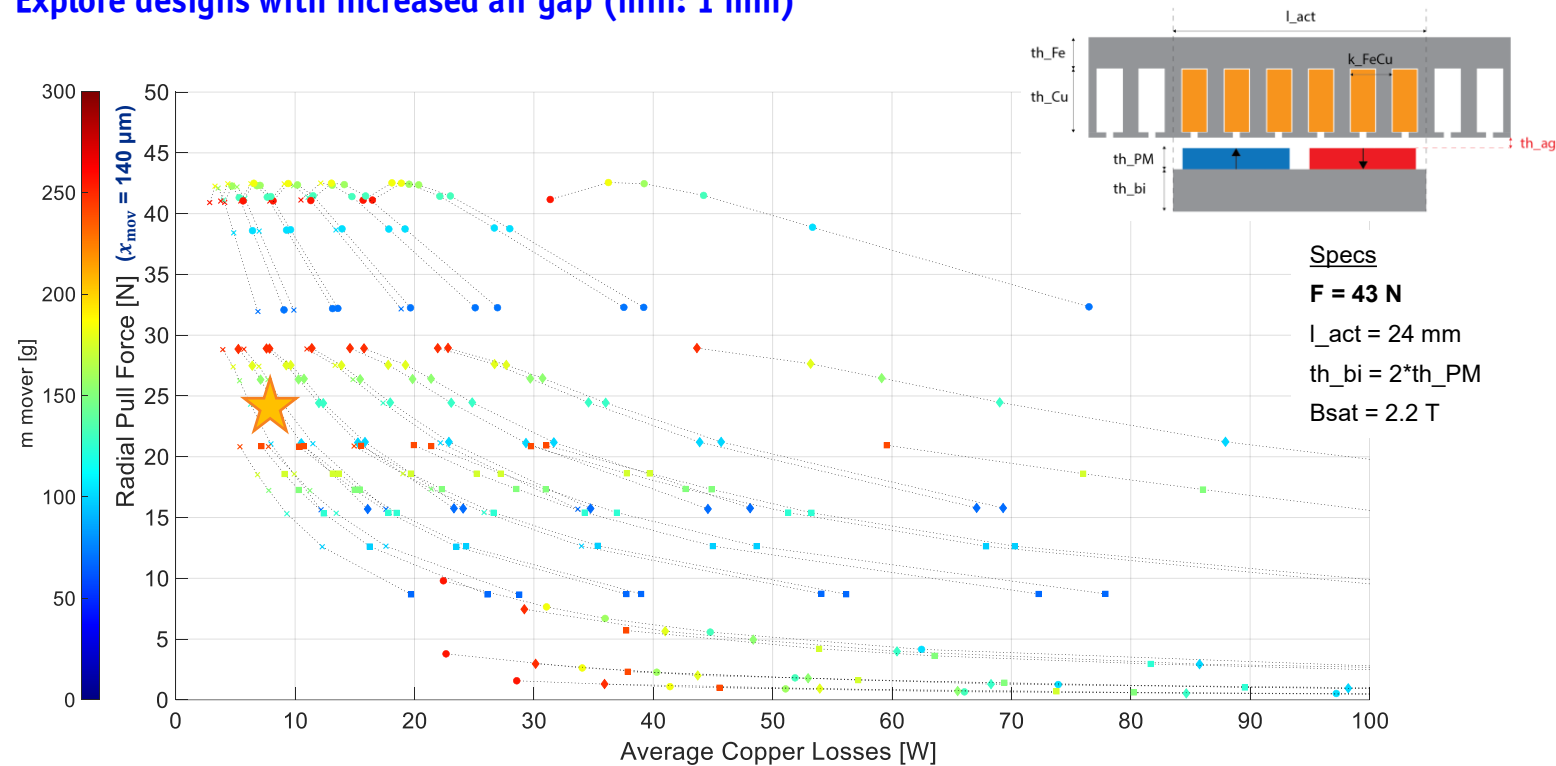
- l_{act} Actuator length
- th_{Fe} Stator back iron thickness
- th_{Cu} Copper layer thickness
- k_{FeCu} Ratio iron/copper per slot pitch (0 → slotless)
- th_{PM} Permanent Magnet thickness
- th_{bi} Mover back iron thickness



- Maximize copper cross-section, while guaranteeing that iron does not saturate
- Important: edge effects, reluctance shaping, pole shoes, iron extensions

ShuttlePump – LA Design and Radial Pull

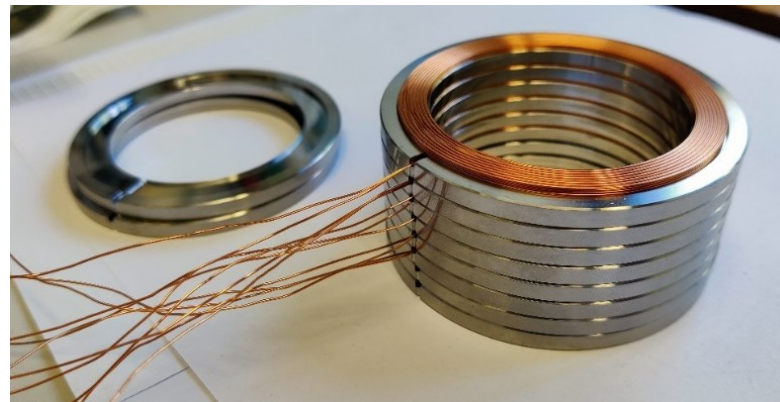
- Stator: if slotted → minimum air gap, higher flux density, higher reluctance forces (radial pull!)
- Explore designs with increased air gap (min: 1 mm)



- Trade-off: radial pull force vs axial force, i.e. copper losses
- ★ Selected design: least copper losses (≈ 8 W) for maximum allowed radial pull (≈ 20 N)

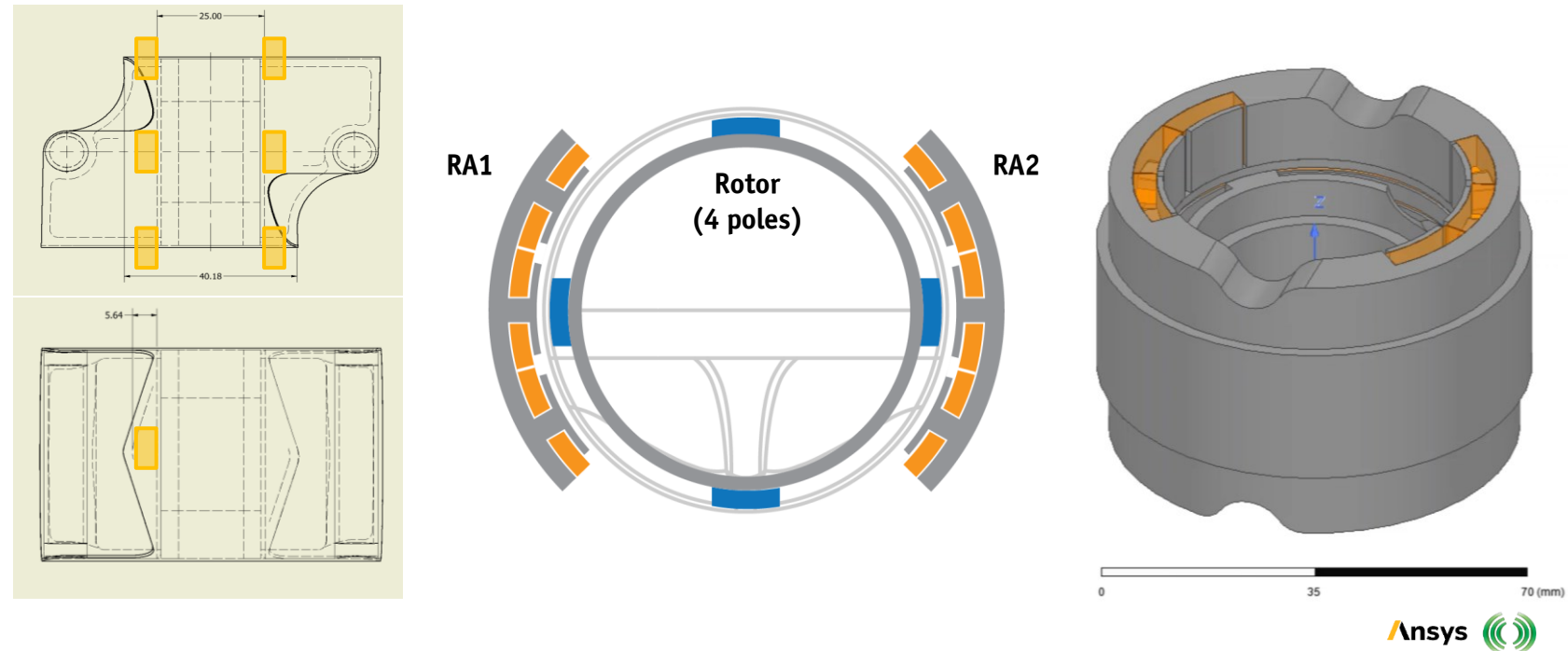
ShuttlePump – LA Hardware Prototype

- **Stator realization: stacked rings, VACOFLUX50 (high $B_{sat} = 2.3\text{ T}$) + ring coils**
- **Mover realization: discrete N50 neodymium PMs on VACOFLUX50 back-iron rings**



ShuttlePump – RA Design

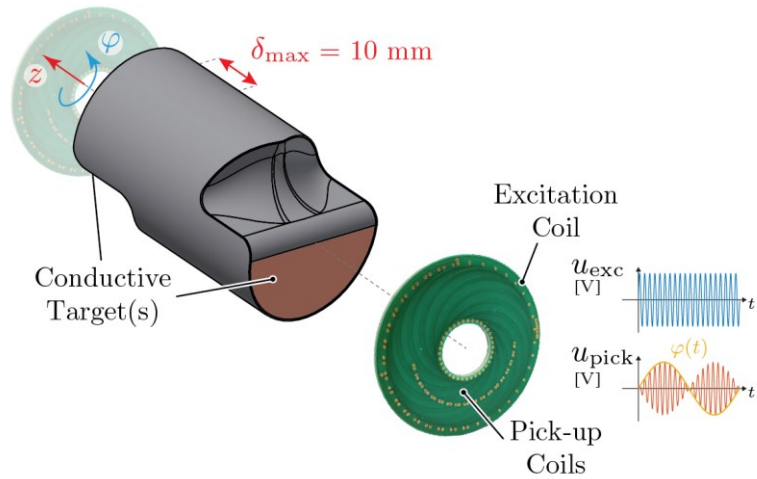
- **Spatial constraints:** mover geometry → 4 poles, only magnets of the same polarity
inlets/outlets location → split the stator into two independent ones



- **Slotted design** → air gap unchanged, axial reluctance profile kept, no edge effects for the LA
- **Two steps optimization** → 2D FEM for RA only, final 2D FEM together with LA (full LiRA)

ShuttlePump – Sensor Concept

- Contactless linear and rotary sensor needed. Enclosure: non-conductive
- Lateral surface occupied by LiRA stators. Far-away target: high sensitivity needed

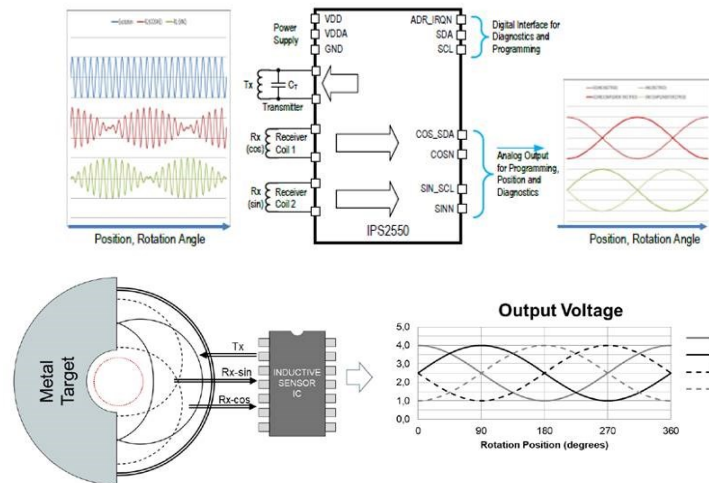


► Renesas IPS2550



Source: renesas.com

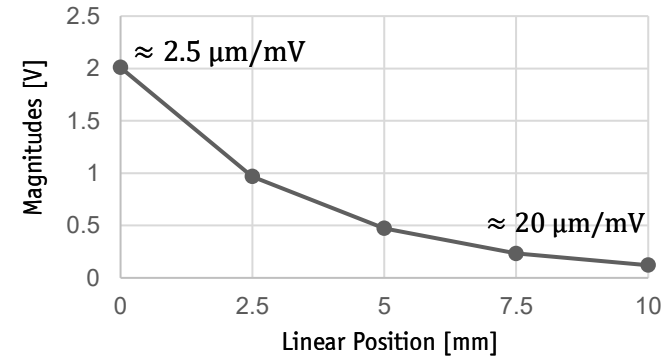
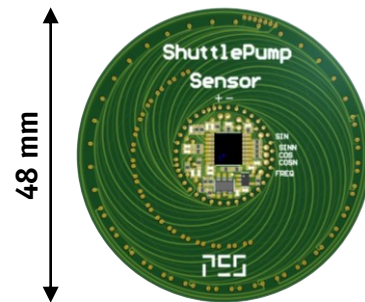
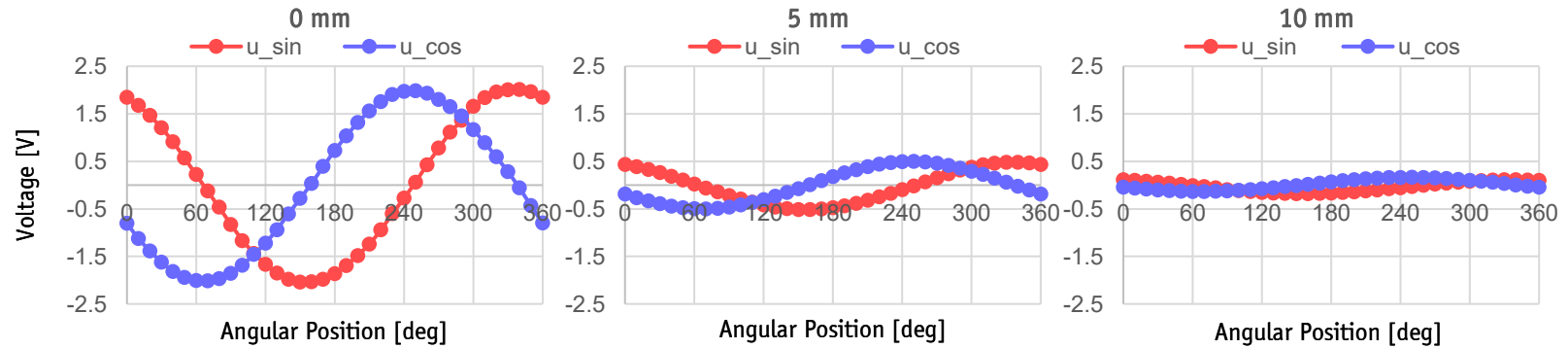
Figure 6. Response of the IPS2550



- Differential ECS system (from the cylinder bases) | Specially-shaped PCB-embedded pick-up coils
- Compact sensor interface: excitation + AM-demodulation in one chip, analog output

ShuttlePump – Sensor Concept

- Contactless linear and rotary sensor needed. Needed resolution ≈ 0.1 mm and ≈ 1 deg
- From rotary sensor can also extract linear position information ('mag' and 'arg')

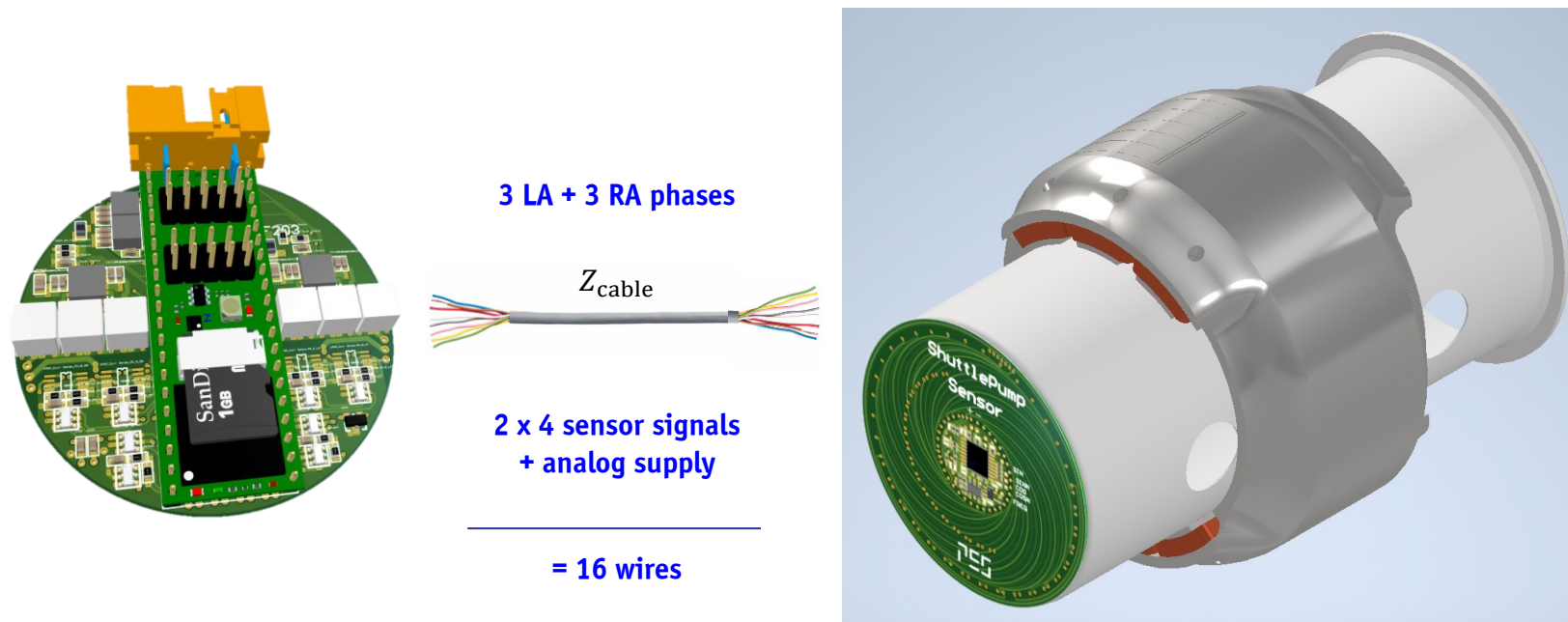


$f_{exc} = 3 \text{ MHz}$

- Differential ECS system further enhances sensitivity and linearity

ShuttlePump – System Overview

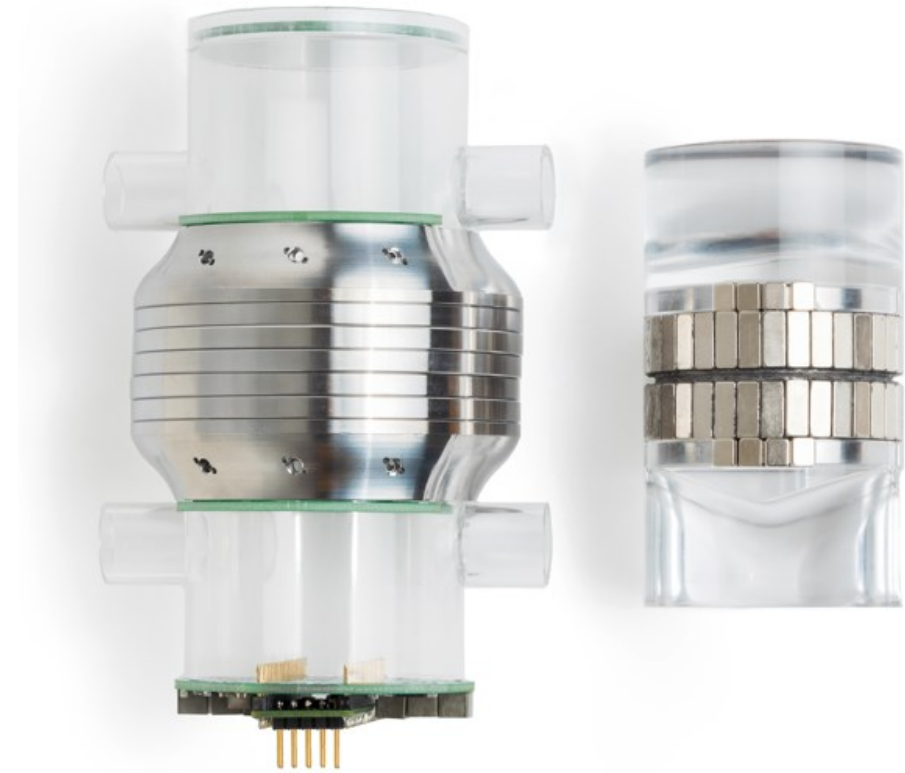
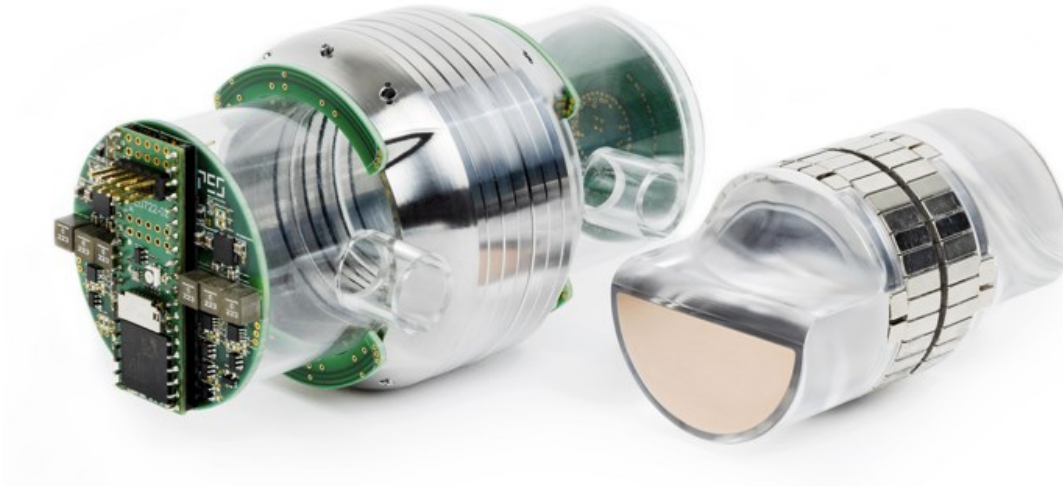
- Inverter + Control PCB: hosts Zynq 7010 SoC / 2 inverter modules switching @1MHz with output filters
- First prototype: external drive → percutaneous cable connection



- ShuttlePump Firmware: current control / position + speed control / reference generation / fault detection / serial monitoring

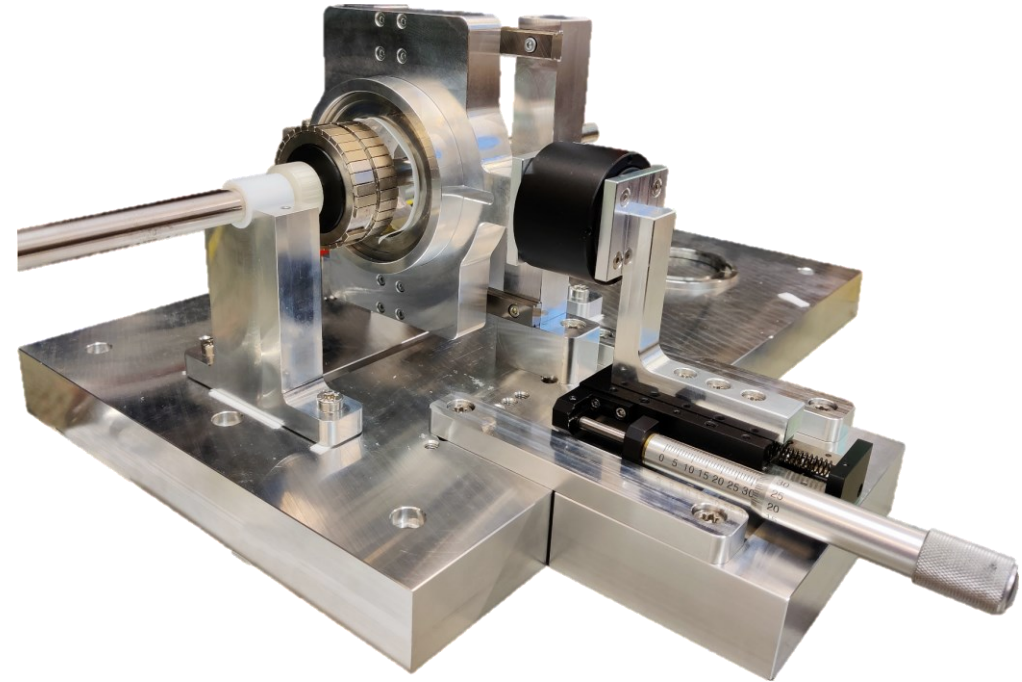
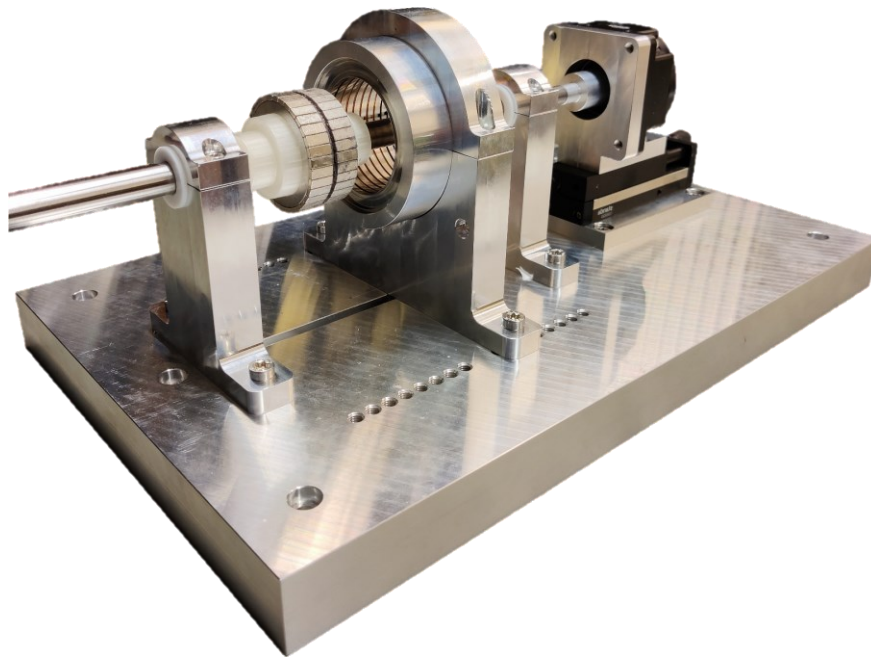
ShuttlePump – Hardware Realization

- **Inverter + Control PCB: hosts Zynq 7010 SoC / 2 inverter modules switching @1MHz with output filters**
- **First prototype: external drive → percutaneous cable connection**



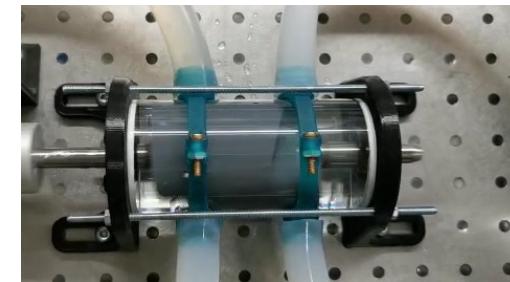
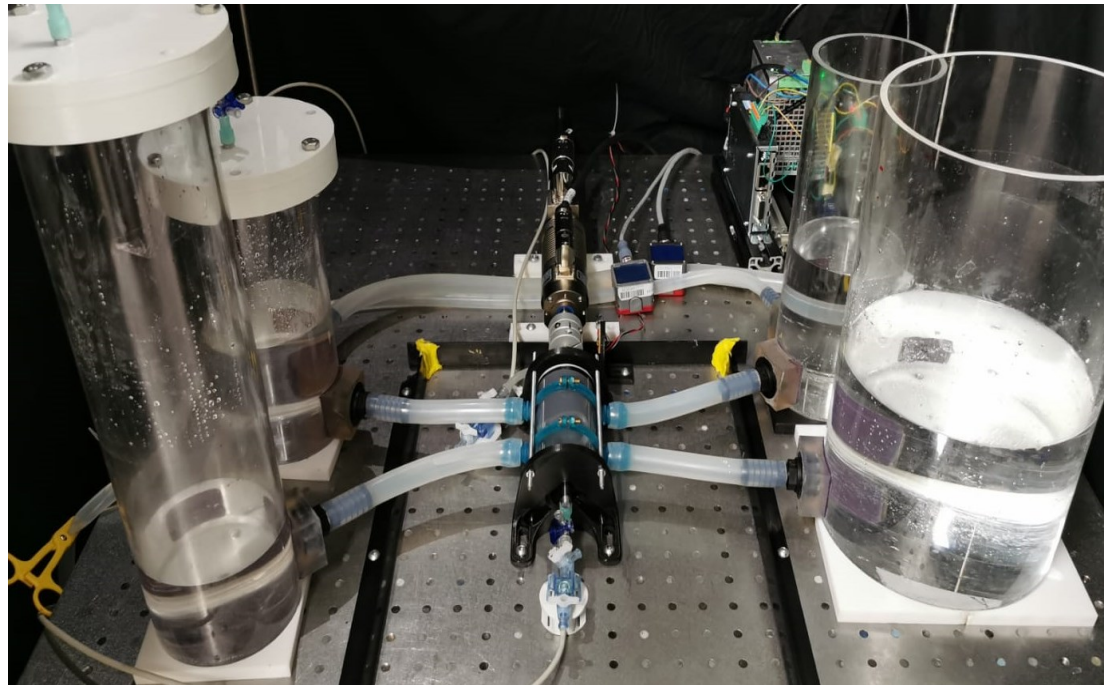
ShuttlePump – Experimental Verification

- Mechanical test bench: LiRA commissioning / machine constants and radial pull verification



ShuttlePump – Experimental Verification

- Hydrodynamic test bench (Mock Circulatory Loop) @ Charite' Berlin
- Sealed tanks \approx blood vessels' compliance | Pressure and flow-rate sensors



140 mmHg, up to 10 L/min

Source:  CHARITÉ
UNIVERSITÄTSMEDIZIN BERLIN

- Tested with external LiRA \rightarrow next: with realized LiRA prototype



—— *Outlook* ——

Part 2 Outlook

- Overview on **Blood Pumps**: types, use, existing systems
- Overview on **non-contact position sensors** for SB-LiRAs: types, use in machines
- Example SB-LiRA with HB: **ShuttlePump** - LiRA design, sensor system, realization

The collage illustrates various blood pumps and sensor technologies. It includes:

- A grid of different pump and sensor models.
- Diagrams for **Capacitive** (Probe Electrode, Guard Electrode, Target), **Magnetic** (MR Sensor, Hall Sensor), **Eddy Current** (Conducting Target, Magnetic Field, Coil, Probe Body, Eddy Current), and **Optical** (3D surface, continuous wave, phase shift, photodetector, linear scale, light source, emitter, detector) sensors.
- Anatomical diagrams of the heart and chest area.
- A detailed diagram of a sensor system showing an **Excitation Coil** (u_{exc} [V]) and **Pick-up Coils** (u_{pick} [V]), with a maximum distance $\delta_{max} = 10$ mm. It also shows a phase shift $\varphi(t)$.
- A photograph of a physical sensor assembly on a metal base.

Outline

Part 1

- ▶ *Introduction*
- ▶ *LiRA Examples / Applications*
- ▶ *Linear Actuator with Integrated MBs*
- ▶ *Position Sensors*
- ▶ *Dynamic Modeling, Controller Design*
- ▶ *Generalized Complex Space Vector*
- ▶ *Double Stator LiRA*

- ▶ *Outlook*

Part 2

- ▶ *Introduction*
- ▶ *Application: Blood Pumps*
- ▶ *Sensors for SB-LiRAs*
- ▶ *Design Example: the ShuttlePump*

- ▶ *Outlook*

Part 3

- ▶ *Introduction*
- ▶ *WPT to Linear Actuators*
- ▶ *Orthogonal and Parallel Field Concept*
- ▶ *Supplying Multiple Receivers*
Voltage & Current Impressed WPT

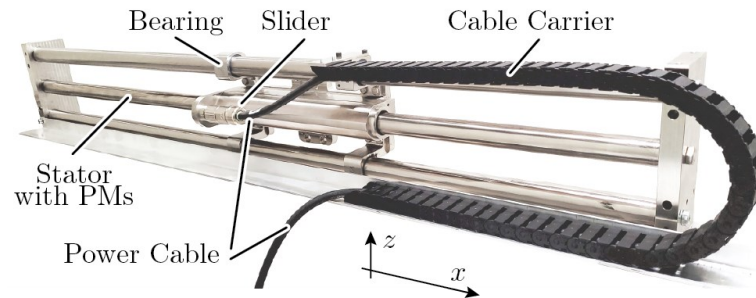
- ▶ *Outlook*



— *Introduction* —

Motivation

- Supply power to a linear actuator which is enclosed in stainless steel (SS) housings.
- **Highest hygiene** in pharmaceutical, and semiconductor processing industries.



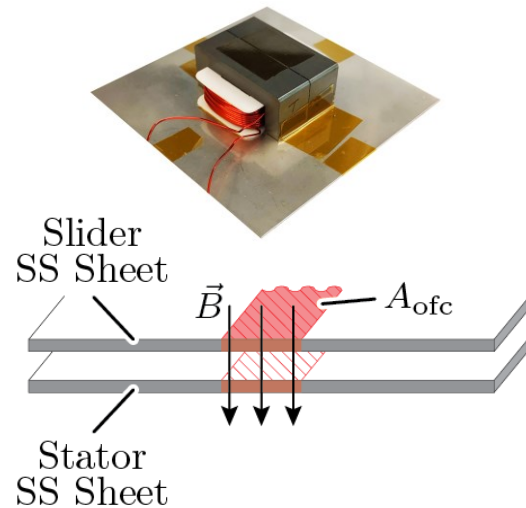
◀ **SS-enclosed linear actuator with cable carriers.**



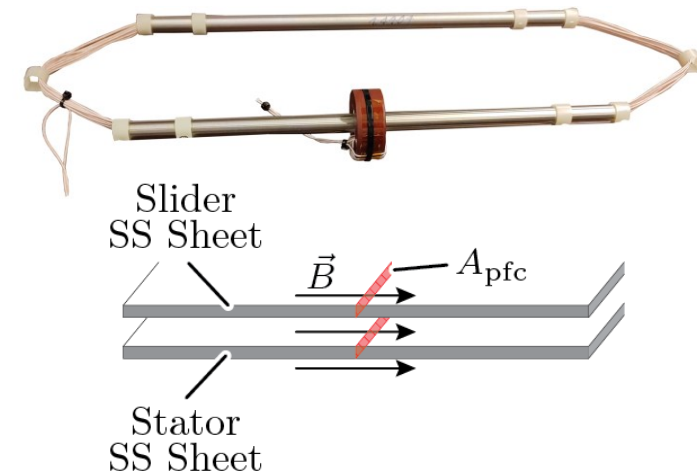
- Supply cables and cable carriers → **difficult to seal & thoroughly clean.**
- WPT through SS allows the **removal of cables and cable carriers.**

Introduction

- B through the SS sheets \rightarrow induced eddy current losses.
- Different types of WPT through SS \rightarrow cause different eddy currents leading to different losses.



▲ Orthogonal-field Concept (OFC).

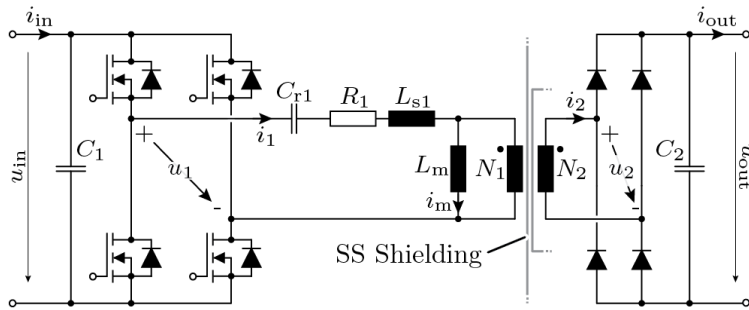


▲ Parallel-field Concept (PFC).

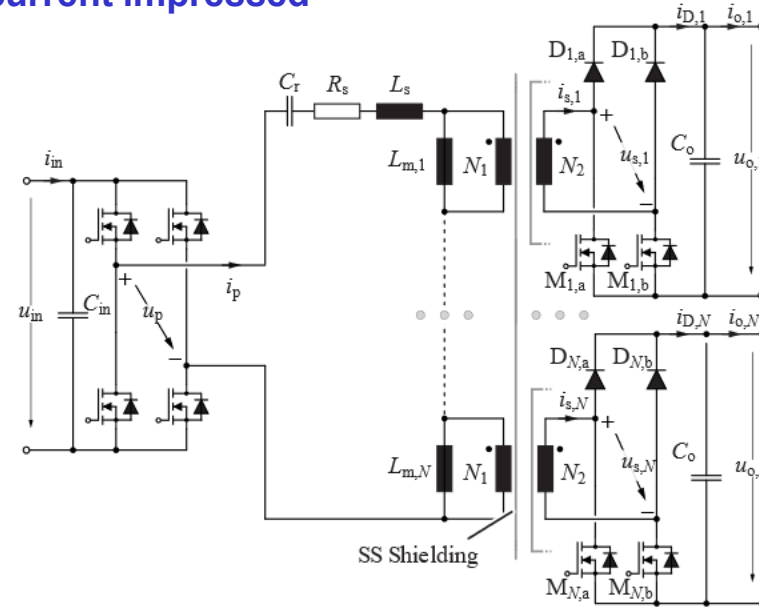
- In OFC, the magnetic material area A_{ofc} can be large $\rightarrow p \propto A_{ofc} \rightarrow$ High losses (e.g. 72% efficiency).
- A_{ofc} is much smaller \rightarrow eddy current induced is lower \rightarrow high efficiency \rightarrow PFC is studied.

Supply WPT

- Power supply for a single receiver → voltage impressed WPT
- Multiple receivers → voltage sharing or current impressed



▲ Single Receiver



▲ Multiple Receivers

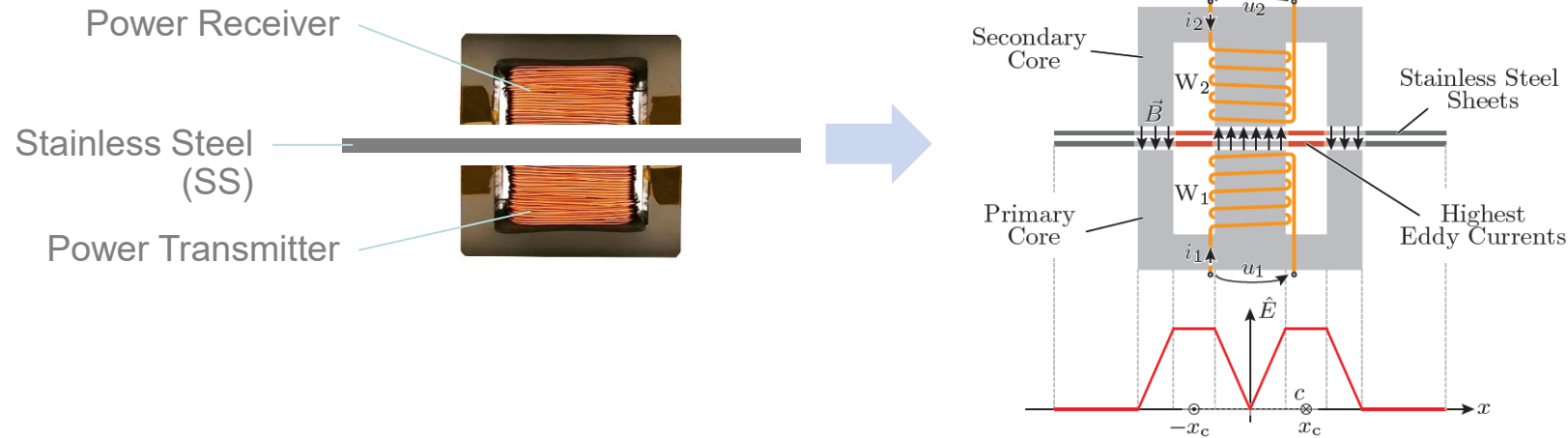
- In the case of PFC → high coupling due to closed toroidal core



—— *Orthogonal Field Concept (OFC)* ——

Field Orthogonal to the SS Enclosure

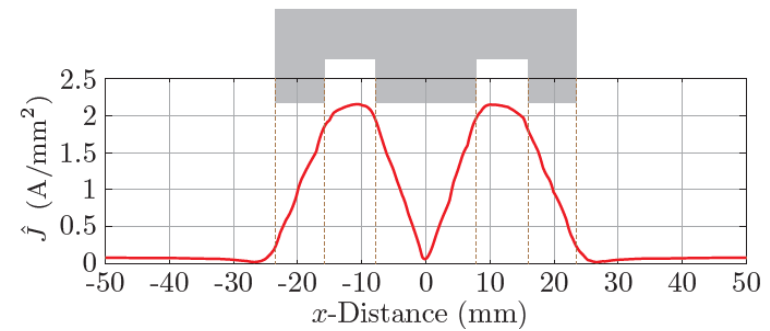
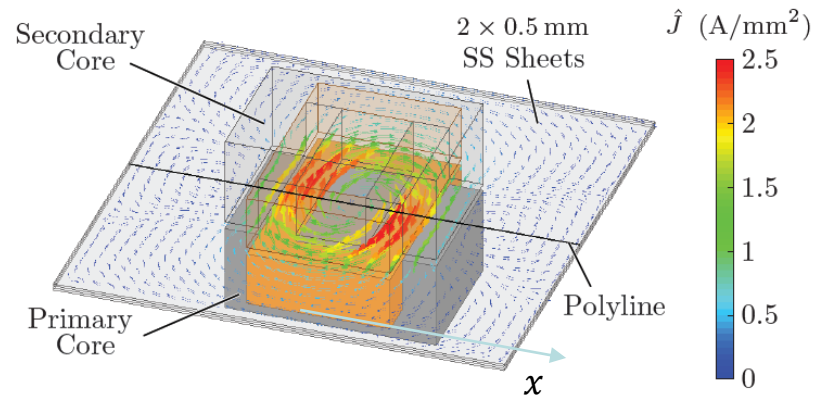
- Analyzed WPT through SS: E-core primary and secondary
- Transmitter & receiver: represented with W_1 and W_2



- Core flux density \vec{B} penetrates through the SS sheets in the air gap
- Flux density integration \rightarrow back emf $\hat{E} \rightarrow$ induced eddy currents in SS

SS Eddy Current Distribution

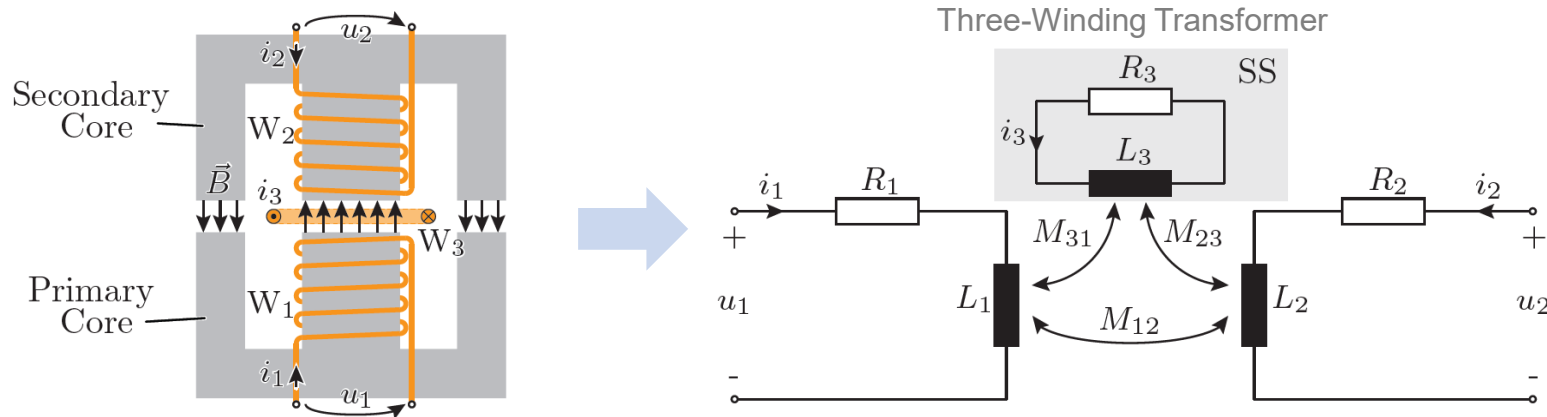
- Analysis of the eddy current distribution: 3D-FEM
- Simulation parameters: primary 100 A – turns, secondary 0 A – turns, 1 kHz exc. freq.



- Most of the current induced in the SS concentrated between the limbs

WPT Through SS Modeling

- Most of the induced current between the limbs → replace SS with a short circuit winding W_3
- Windings W_1 , W_2 and W_3 → three-winding transformer



$$u_1 = R_1 i_1 + L_1 \frac{di_1}{dt} + M_{12} \frac{di_2}{dt} + M_{31} \frac{di_3}{dt}$$

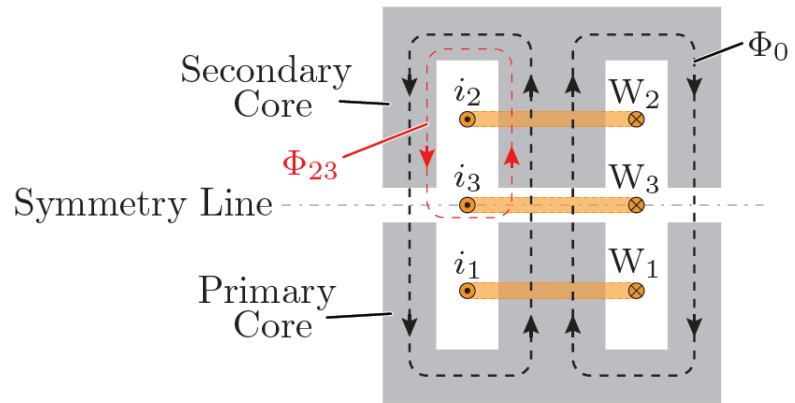
$$u_2 = R_2 i_2 + L_2 \frac{di_2}{dt} + M_{12} \frac{di_1}{dt} + M_{23} \frac{di_3}{dt}$$

$$0 = R_3 i_3 + L_3 \frac{di_3}{dt} + M_{23} \frac{di_2}{dt} + M_{31} \frac{di_1}{dt}$$

- Impact of the SS in the air gap → a third short-circuited winding coupled with the primary & secondary
- Equivalent circuit of the WPT through SS system →

WPT Through SS Equivalent Circuit (1)

- Mutual inductance per turn (M_0) is equal for W_1 , W_2 and W_3 , otherwise mag. sym. is violated
- Equal M_0 assumption \rightarrow scale mutual inductances with number of turns N_1 , N_2 and N_3



$$M_{12} = N_1 N_2 \cdot M_0$$

$$M_{23} = N_2 N_3 \cdot M_0$$

$$M_{31} = N_3 N_1 \cdot M_0$$

$$u_1 = R_1 i_1 + L_1 \frac{di_1}{dt} + nM_{12} \frac{di_2}{dt} + mM_{31} \frac{di_3}{dt}$$

$$nu_2 = n^2 R_2 i_2 + n^2 L_2 \frac{di_2}{dt} + nM_{12} \frac{di_1}{dt} + nmM_{23} \frac{di_3}{dt}$$

$$0 = m^2 R_3 \frac{di_3}{dt} + m^2 L_3 \frac{di_3}{dt} + nmM_{23} \frac{di_2}{dt} + mM_{31} \frac{di_1}{dt}$$

$$nM_{12} = mM_{31} = nmM_{23} = N_1^2 M_0 = M$$

Turns Ratios: $n = \frac{N_1}{N_2}$ $m = \frac{N_1}{N_3}$

- Magnetization inductance M can be defined \rightarrow equivalent circuit

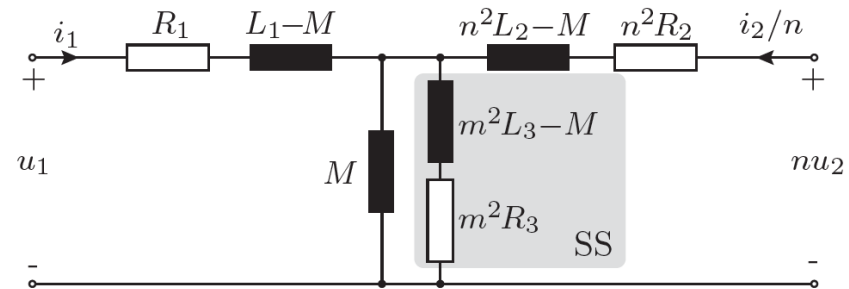
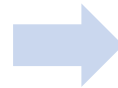
WPT Through SS Equivalent Circuit (2)

- Further rearranging of equations using magnetization inductance M
- The third equation has zero voltage \rightarrow in the SS branch connected to '-' potential

$$u_1 = R_1 i_1 + (L_1 - M) \frac{di_1}{dt} + M \frac{d}{dt} \left(i_1 + \frac{i_2}{n} + \frac{i_3}{m} \right)$$

$$nu_2 = n^2 R_2 \frac{i_2}{n} + (n^2 L_2 - M) \frac{di_2}{dt} + M \frac{d}{dt} \left(i_1 + \frac{i_2}{n} + \frac{i_3}{m} \right)$$

$$0 = m^2 R_3 \frac{i_3}{m} + (m^2 L_3 - M) \frac{di_3}{dt} + M \frac{d}{dt} \left(i_1 + \frac{i_2}{n} + \frac{i_3}{m} \right)$$

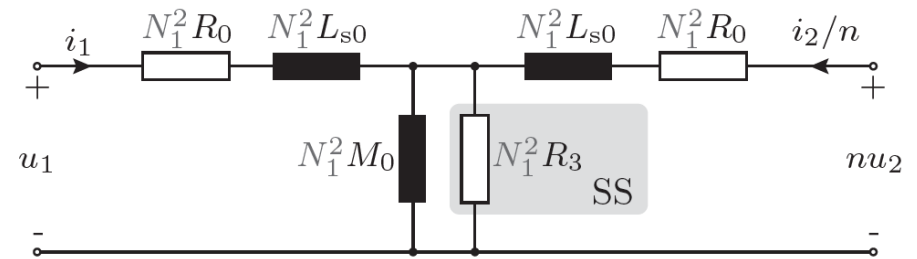
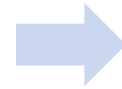
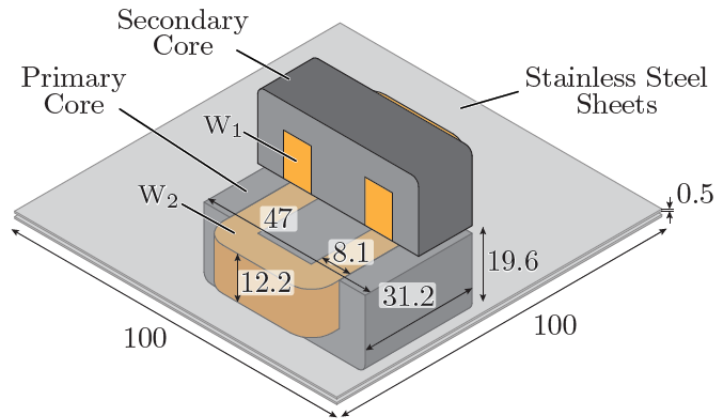


- Values of the parameters \rightarrow from 3D-FEM eddy-current simulation



WPT Through SS Equivalent Circuit Parameters

- WPT system geometry → determined such that 50W can be transferred
- Primary/secondary core → two stacked E 47/20/16 N87 ferrite cores



Per Turn Parameters
Valid for Exc. Freq. < 10 kHz

$$R_0 = 55.6 \mu\Omega$$

$$L_{s0} = 77.16 \text{ nH}$$

$$R_3 = 4.97 \text{ m}\Omega$$

$$M_0 = 172.84 \text{ nH}$$

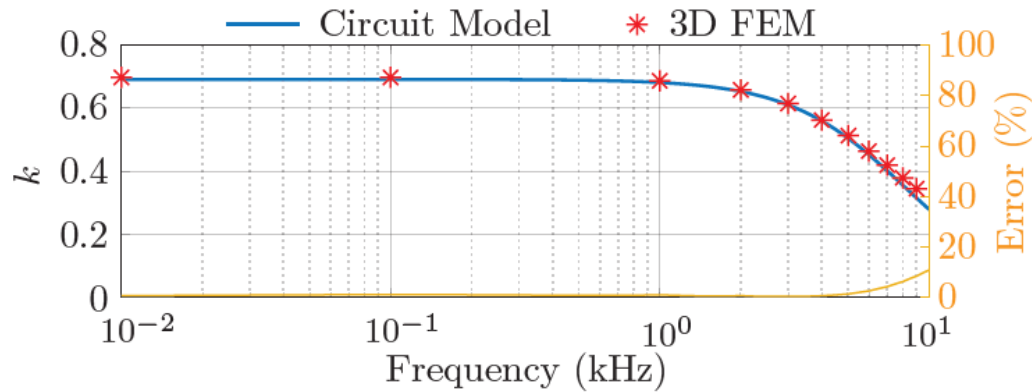
$$m^2 L_{s0} - M \approx 0$$

$$N_3 = 1$$

- Parameters obtained from 3D-FEM simulation using \underline{Z}_{11} , $\underline{Z}_{12} = \underline{Z}_{21}$ and \underline{Z}_{22} complex impedances

Model Verification with 3D-FEM: Coupling k Calculation

- Coupling coefficient k calculated from the equivalent circuit
- Series equivalent of the magnetization branch: $L_{12} = (M_0 R_3^2) / (R_3^2 + (2\pi f \cdot M_0)^2)$



$$k = \frac{L_{12}(f)}{L_{12}(f) + L_{s1}}$$

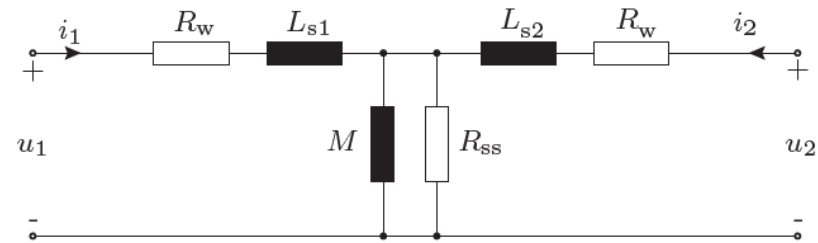
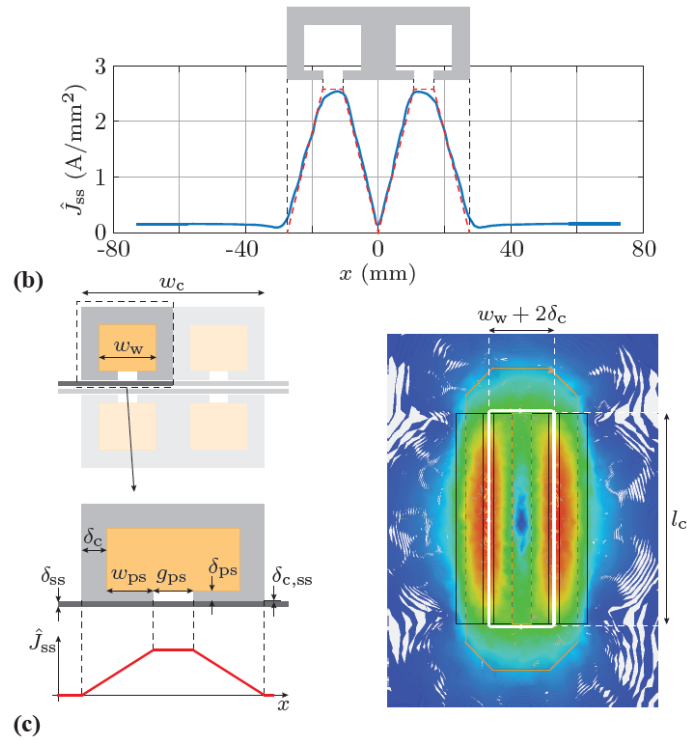
$$k = \frac{M_0}{\omega^2 \cdot L_{s1} \left(\frac{M_0}{R_3}\right)^2 + L_{s1} + M_0}$$

if $R_3 \rightarrow \infty$ then: $k = \frac{M_0}{L_{s1} + M_0}$

- Coupling k dependence on frequency \rightarrow second order low pass filter

Analytic Calculation of Circuit Parameters

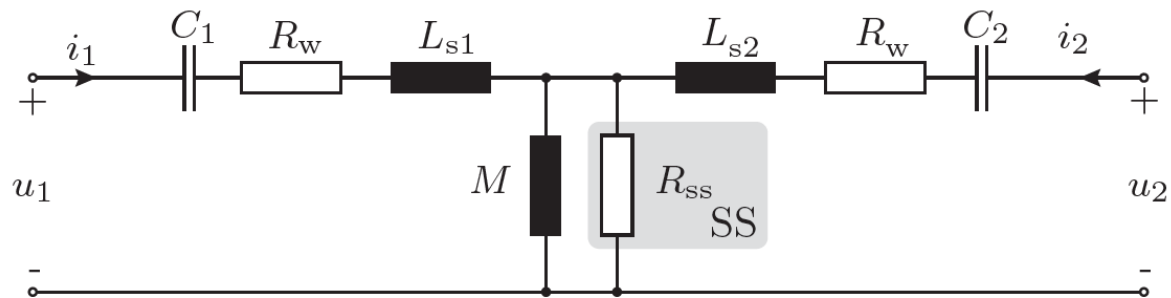
- Based on the current distribution in the SS → R_{SS} is calculated



- Inductances calculated based on the magnetic circuit model

WPT Through SS Resonant Compensation

- Series resonant compensation → self-inductance $L_{11} = L_{s1} + L_{12}$ or stray inductance L_{s1}
- Rather low SS resistance value → self-inductances L_{11}/L_{22} are frequency dependent



$$L_{12} = \Im(j\omega M || R_{ss}) \frac{1}{\omega}$$

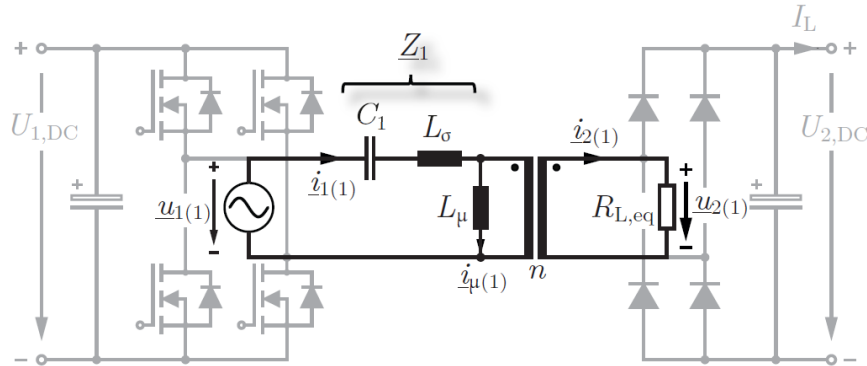
$$C_1 = \frac{1}{\omega^2 L_{s1}}$$

$$C_2 = \frac{1}{\omega^2 L_{s2}}$$

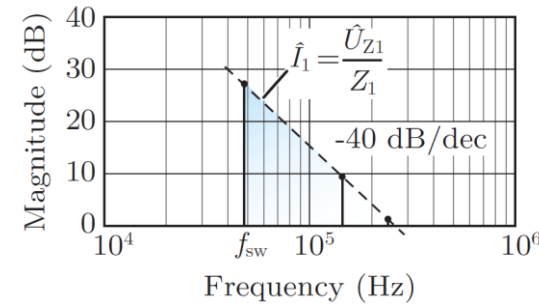
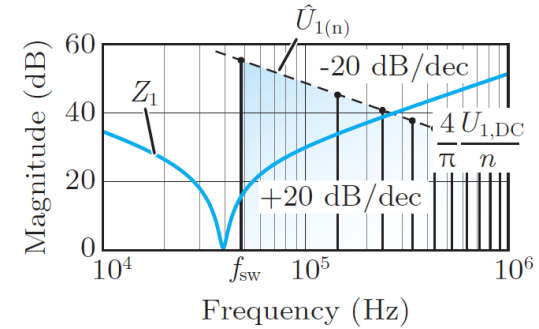
- Stray inductances L_{s1}/L_{s2} are not frequency dependent
- Compensation of stray inductances leads to higher efficiency

Fundamental Frequency Modeling, Equivalent Load Resistance

■ 'Notch'-pass characteristic of the input impedance

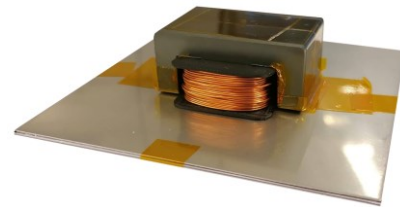


$$R_{L,eq} = \frac{8}{\pi^2} \frac{U_{2,DC}^2}{P_2}$$



- Pulsed input voltage → only fundamental component of the load current!
- Equivalent load resistance → models delivered output power P_2

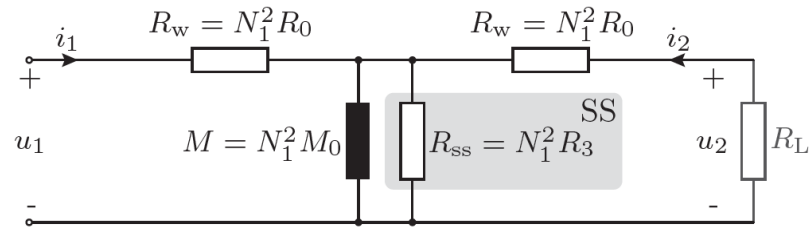
[Source]: Roman Bosshard, 'Multi-Objective Optimization of Inductive Power Transfer Systems for EV Charging', PhD Thesis, ETH Zurich, 2015.



Prototype Design

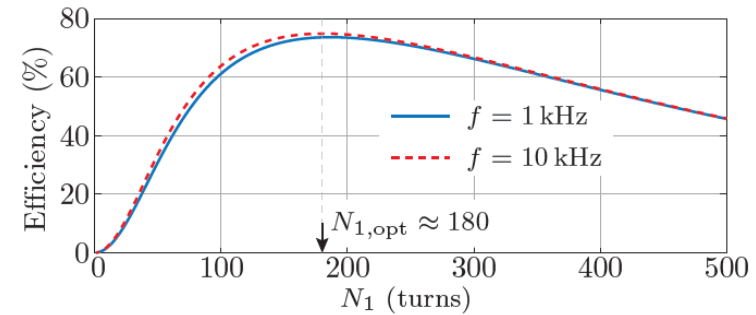
Optimum Number of Turns

- In this work primary & secondary number of turns assumed equal, $N_1 = N_2$
- $R_0, M_0, R_3 \rightarrow$ parameters per turn ($N_1 = N_2 = 1$) determined by the core geometry



Input Voltage	Output Voltage	Output Power
$\hat{U}_1 = 50 \text{ V}$	$\hat{U}_2 = 50 \text{ V}$	$P_2 = 50 \text{ W}$

$$R_{L,\text{nom}} = \frac{\hat{U}_2^2}{2P_2} = 25 \Omega$$

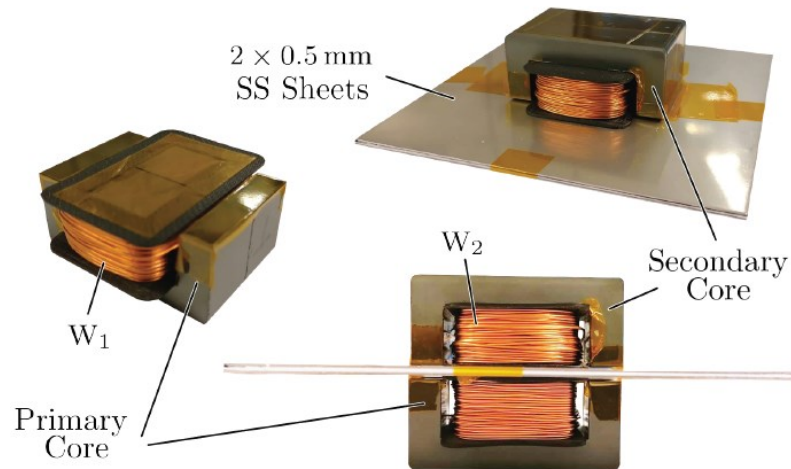


$$N_{1,\text{opt}} = \sqrt{\frac{R_{L,\text{nom}}}{\sqrt{R_0(R_0 + 2R_3)}}} \approx 180$$

- Optimum number of turns $\rightarrow R_{L,\text{nom}} > R_w$ and $R_{L,\text{nom}} < R_{ss}$

Hardware Prototype

- Primary & secondary cores → two stacked E 47/20/16 N87 ferrite cores
- Primary & secondary windings → $N_1 = N_2 = 180$, 0.5 mm wire diameter

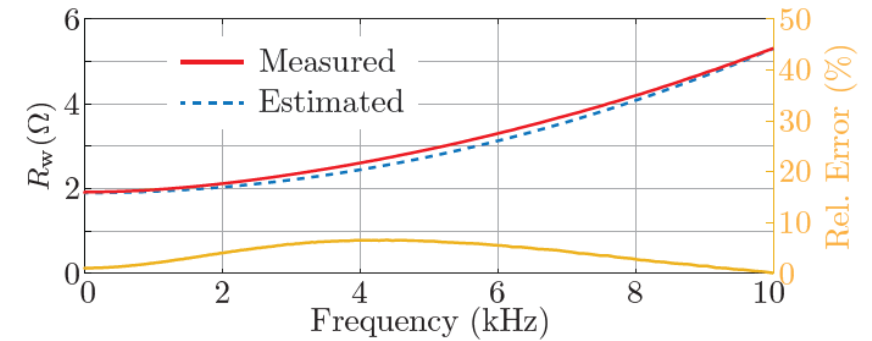
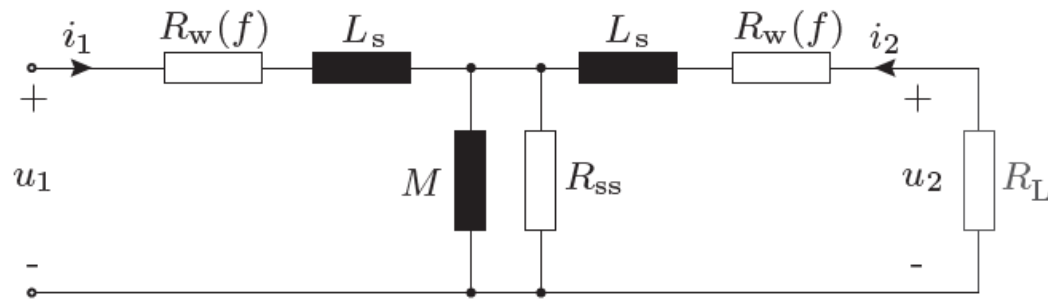


Parameter	3D FEM	Prototype	Rel. Error
$R_{w,dc}$	1.8 Ω	1.9 Ω	5.3 %
L_s	2.5 mH	2.62 mH	4.6 %
M	5.6 mH	5.4 mH	3.7 %
R_{ss}	160 Ω	155 Ω	3.2 %

- Model & prototype parameter values considered up to 10 kHz excitation frequency

AC Winding Resistance

- Impedance measurements on the prototype → proximity effects in the windings
- Frequency dependent winding resistance $R_w(f)$ → included in the model using $G_R(f)$



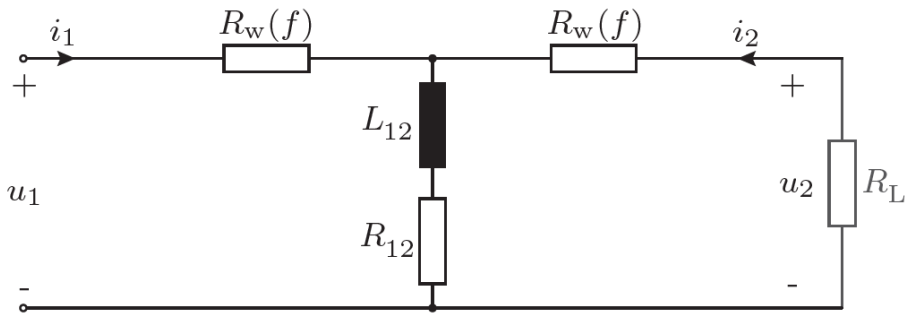
$$R_w(f) = R_{w,dc}(1 + 2G_R(f) \cdot H^2)$$

$$H^2 = \frac{\frac{R_w(10 \text{ kHz})}{R_{w,dc}} - 1}{2G_R(10 \text{ kHz})}$$

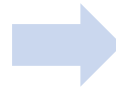
- Further details/references on $G_R(f)$ can be found in the paper manuscript

Optimal Excitation Frequency f_{opt}

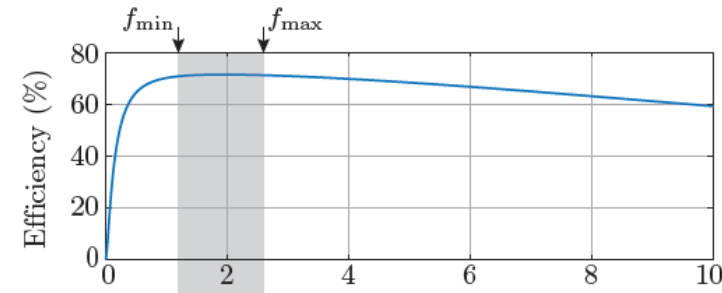
- Frequency dependent winding resistance $R_w(f)$ → there is f_{opt} s.t. efficiency is max.
- Frequency dependent winding resistance $R_w(f)$ → there is $R_L = R_{L,opt}(f)$ s.t. eff. is max.



$$R_{L,opt} = \frac{\sqrt{R_w} \sqrt{R_w^2 + 3R_w R_{12} + 2R_{12}^2 + 2(\omega L_{12})^2}}{\sqrt{R_w + R_{12}}}$$

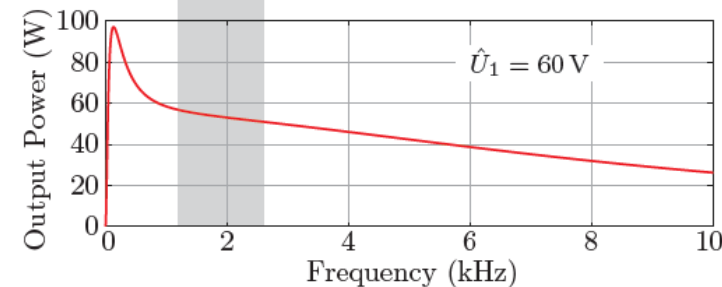
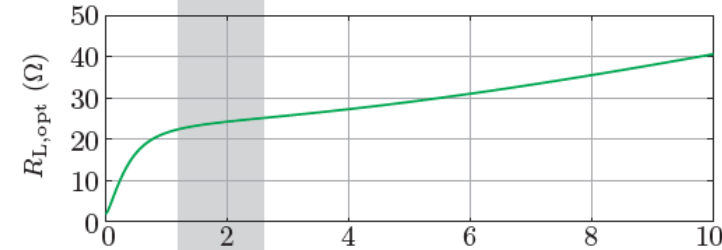


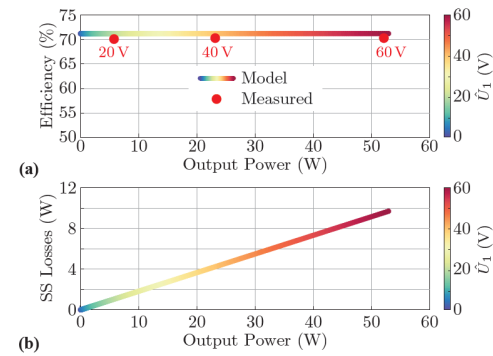
- 'Flat' eff. curve → range of freq.
- Res. comp. caps. → $C_1 = C_2 = 1.9 \mu\text{F}$
- Operation frequency → 2.25 kHz (71.2% efficiency)



$f_{min} = 1.6 \text{ kHz}$

$f_{max} = 2.3 \text{ kHz}$

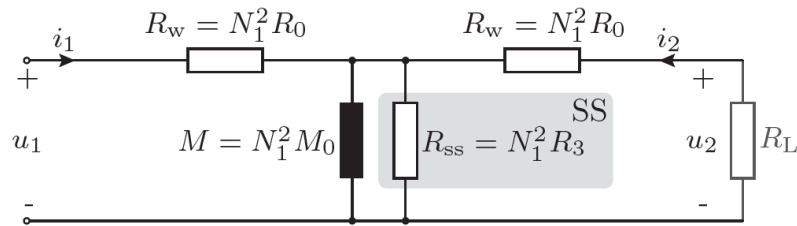




Power & Efficiency Measurements

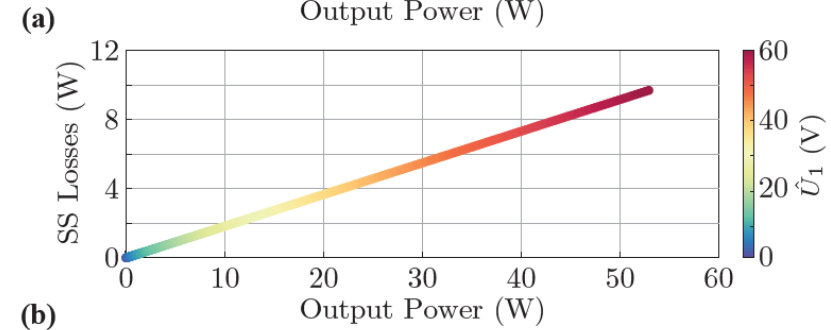
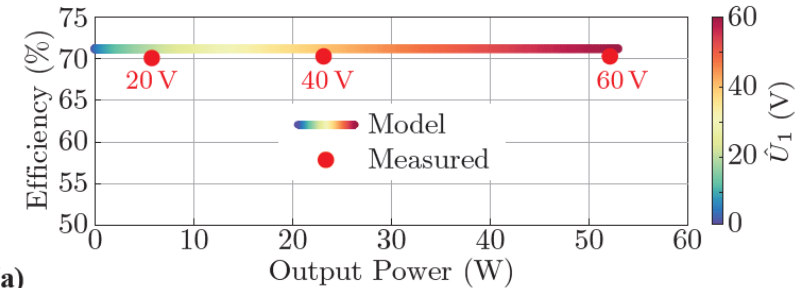
Regulation of Power via Input Voltage

- Verification of the circuit model with the power & efficiency measurements



$$R_L = 24 \Omega$$

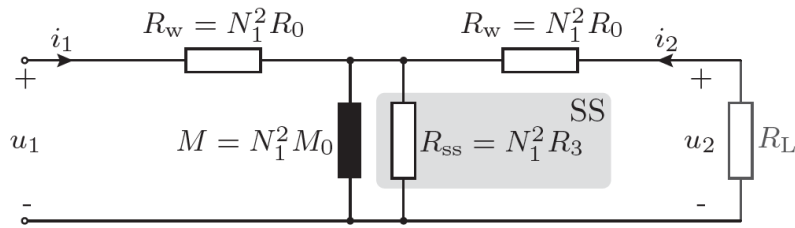
$$\frac{P_{SS}}{P_2} = \frac{R_{12}(R_L + R_w)^2}{R_L(R_{12}^2 + X_{12}^2)}$$



- Efficiency does not depend on the input voltage
- SS losses P_{SS} increase linearly with the output power P_2 (R_L is constant!)

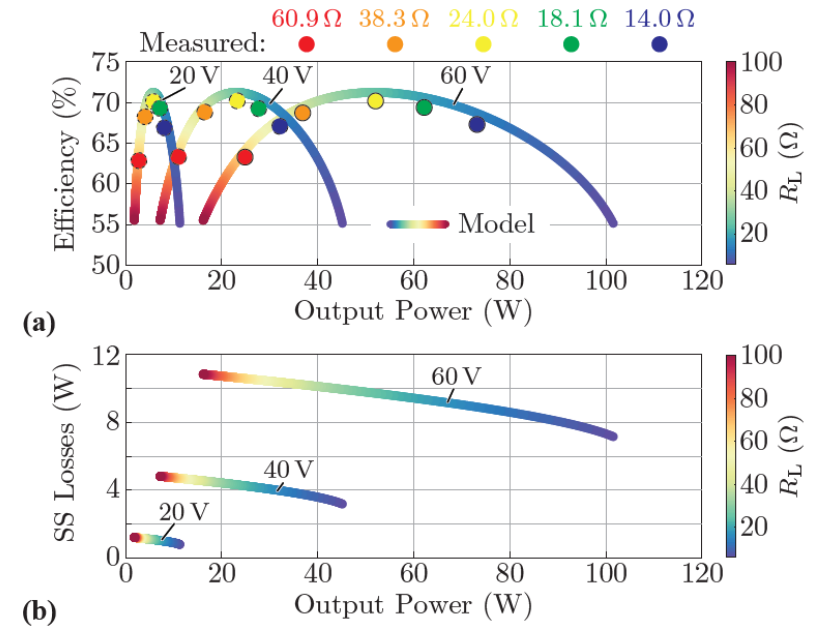
Regulation of Power via Load Resistance R_L

- Verification of the circuit model with the power & efficiency measurements



$$\hat{U}_1 = [20, 40, 60] \text{ V}$$

$$\frac{P_{SS}}{P_2} = \frac{R_{12}(R_L + R_w)^2}{R_L(R_{12}^2 + X_{12}^2)}$$



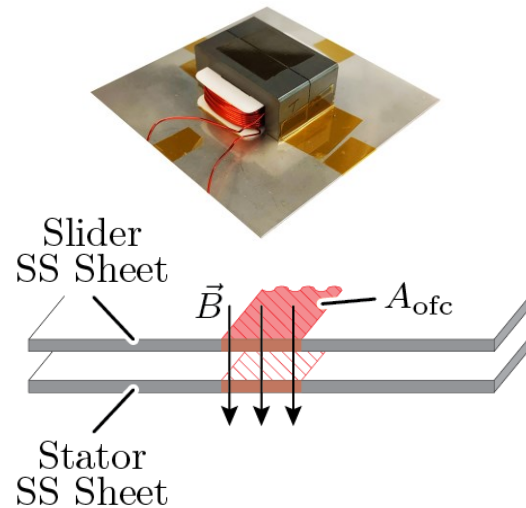
- Efficiency heavily depends on the load resistance R_L
- Larger output power P_2 , while keeping the SS losses P_{SS} limited



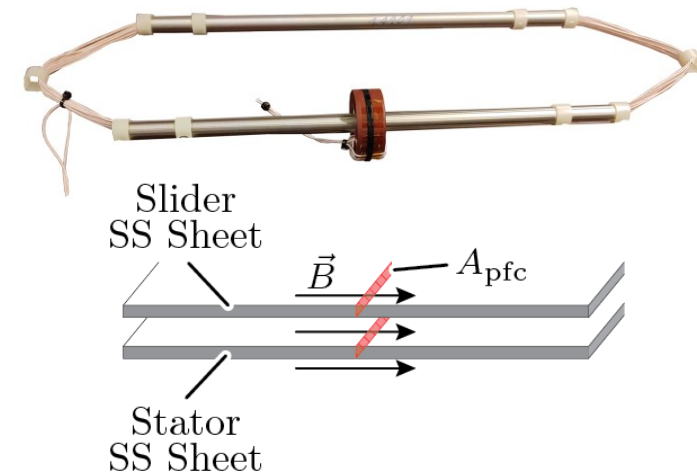
—— *Coaxial WPT (PFC)* ——

OFC and PFC

- B through the SS sheets \rightarrow induced eddy current losses.
- Different types of WPT through SS \rightarrow cause different eddy currents leading to different losses.



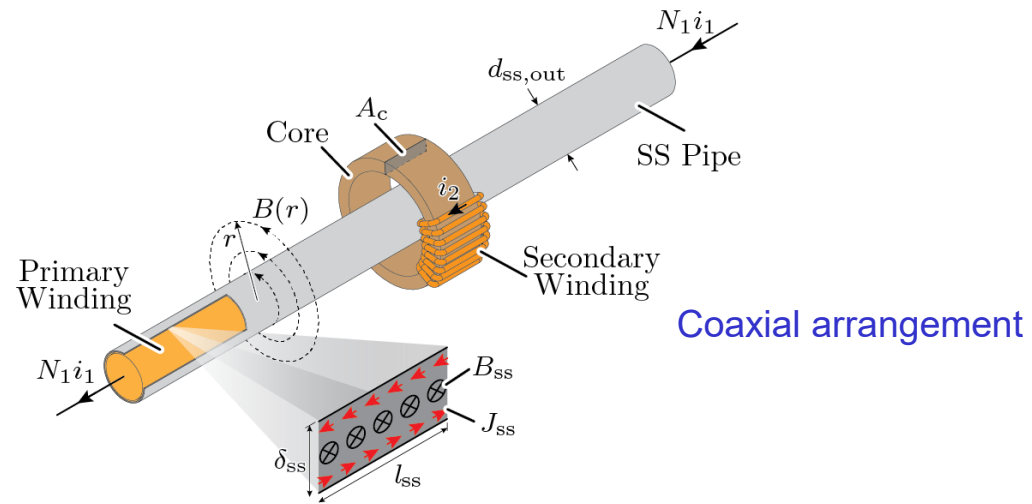
▲ Orthogonal-field Concept (OFC).



▲ Parallel-field Concept (PFC).

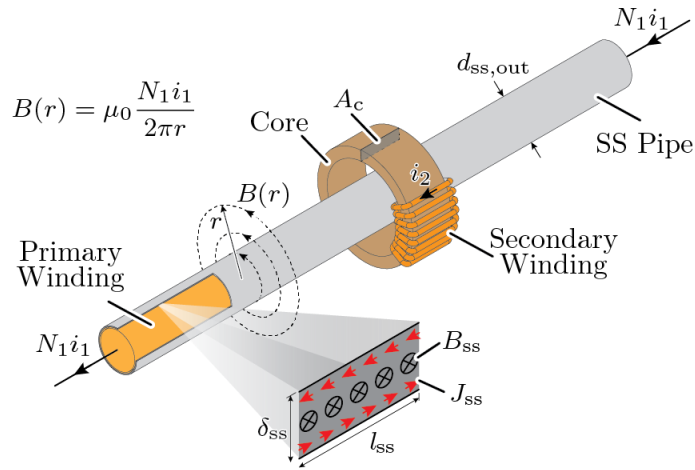
- In OFC, the magnetic material area A_{ofc} can be large $\rightarrow p \propto A_{ofc} \rightarrow$ High losses (e.g. 72% efficiency).
- A_{ofc} is much smaller \rightarrow eddy current induced is lower \rightarrow high efficiency \rightarrow PFC is studied.

Parallel-field Concept WPT

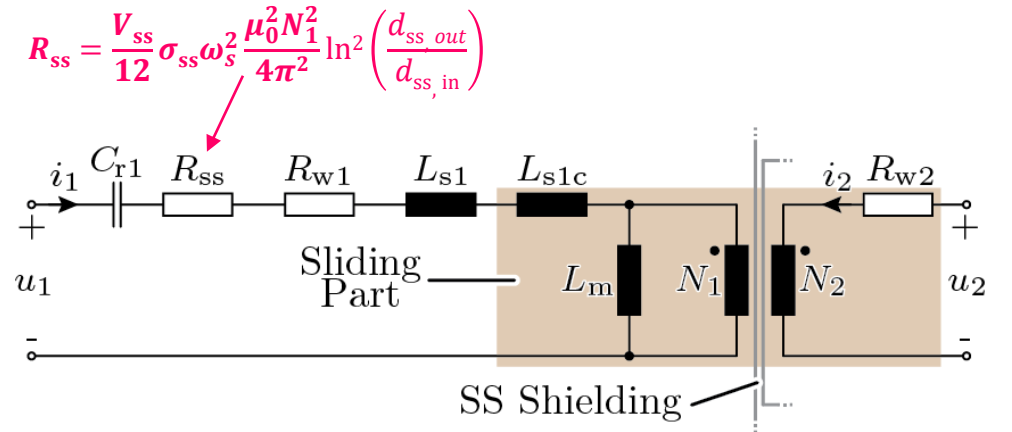


Parallel-field Concept WPT — SS Loss Model

- Calculation of eddy-current losses $\rightarrow P_{ss} \propto V_{ss}, F(\chi), \sigma_{ss}, \delta_{ss}, \omega_{ss}, F(\chi), \hat{B}_{ss}$
- SS losses depend only on the primary current.



▲ Arrangement of the PFC WPT.

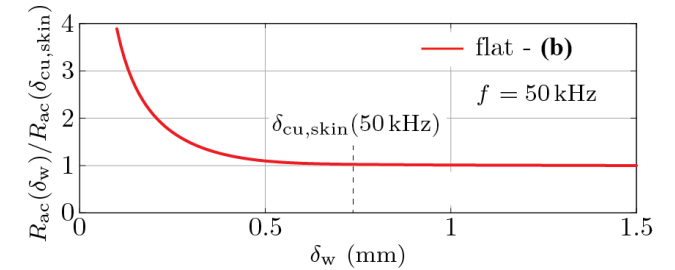
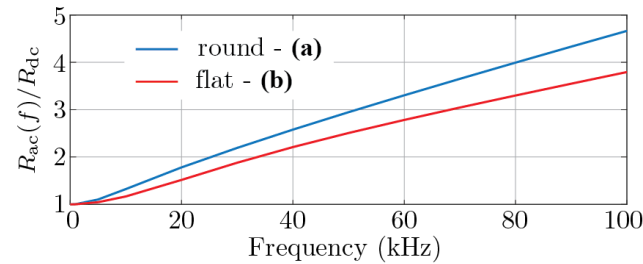
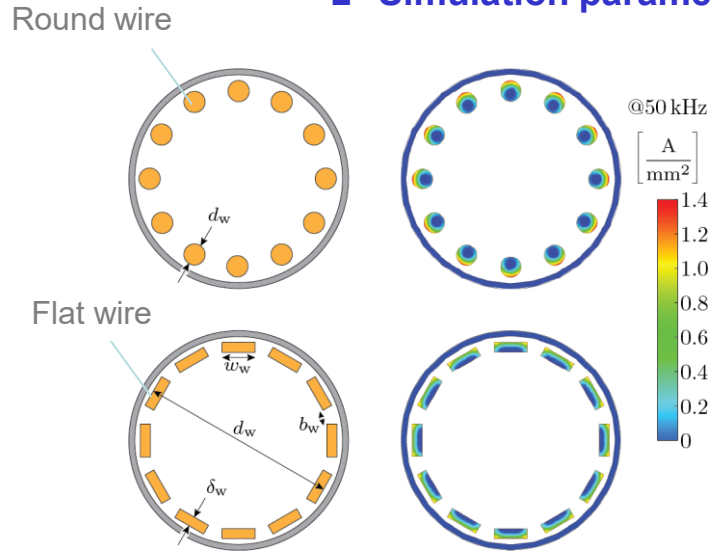


▲ Electrical equivalent circuit.

- The SS losses can be modeled in the same way as (primary-side) winding losses.

Parallel-field Concept WPT — Primary Winding Design

- To find the best arrangement of the wires: 2D-FEM at $N_1 = 12$, $f_{sw} = 50$ kHz.
- Simulation parameters: Round $\rightarrow d_w = 1.85$ mm ; Flat $\rightarrow \delta_w = 0.9$ mm , $b_w = 1.2$ mm, and $d_w = 17$ mm.



▲ 2D-FEM of analysis of different arrangement of wires.

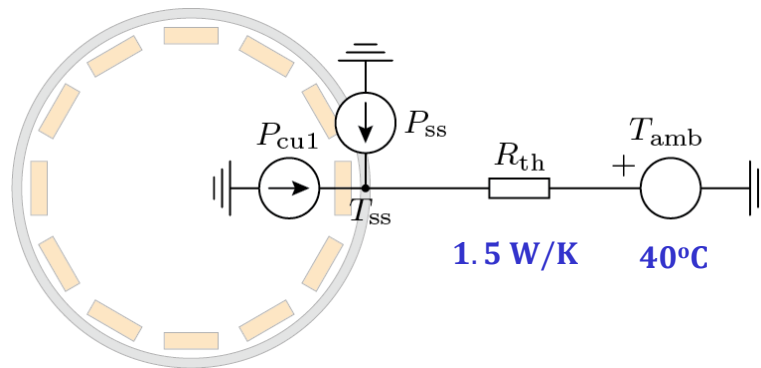
▲ R_{ac}/R_{dc} vs Frequency.

▲ Normalized Winding resistance vs Winding thickness δ_w .

- The lowest AC resistance \rightarrow the wires at the **circumference**, i.e., the flat wire should be used.
- Increasing δ_w above the skin depth **does not lead to a further reduction** of the winding resistance anymore.

Parallel-field Concept WPT — SS Tube Thermal Model

- The SS surface T_{ss} should be kept below 60°C.



▲ Primary-side thermal model.

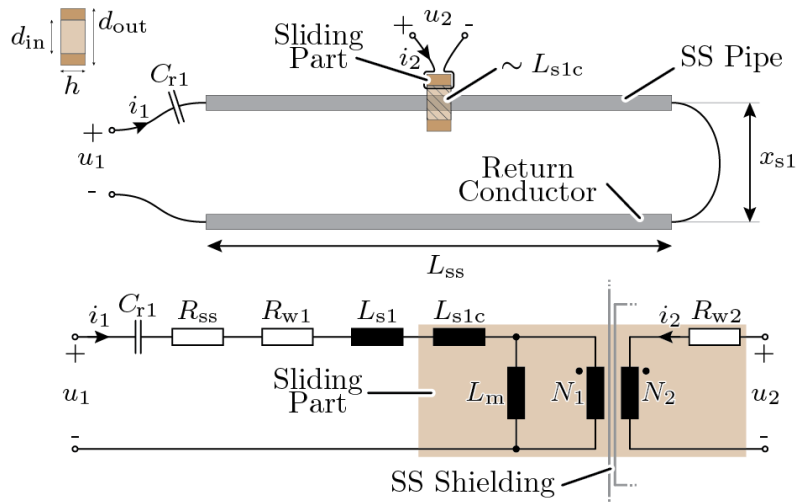


Circulate the current through the pipes, and measure the power and the temperature increase.

- To keep $T_{ss} < 60^\circ\text{C}$ at $T_{amb} = 40^\circ\text{C}$, the losses in the primary should be $P_{ss} + P_{cu1} < 13.3 \text{ W}$.

Parallel-field Concept WPT — Electric Equivalent Circuit

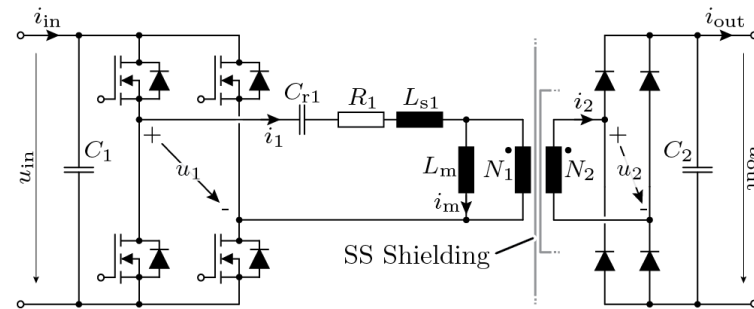
- $R_{w1,w2}$ depends on the operating frequency and the winding geometry $\rightarrow R_{w1,w2} = R_{ac}(f_{sw})$.
- L_{s1} is the external stray inductance $\rightarrow L_{s1} = \mu_0 \log[x_{s1}/(d_w/2)]L_{SS}N_1^2/\pi$.
- L_{s1c} is much smaller than L_{s1} $\rightarrow L_{s1c} = L_{s1}(h/L_{SS})$.
- L_m is calculated from the A_L value of the core $\rightarrow L_m = A_L N_1^2$.
- C_{r1} is resonant capacitor $\rightarrow C_{r1} = 1/[\omega^2 \cdot (L_{s1} + L_{sc1})]$.



◀ PFC WPT system with a single receiver: conceptual physical arrangement and electrical equivalent circuit.

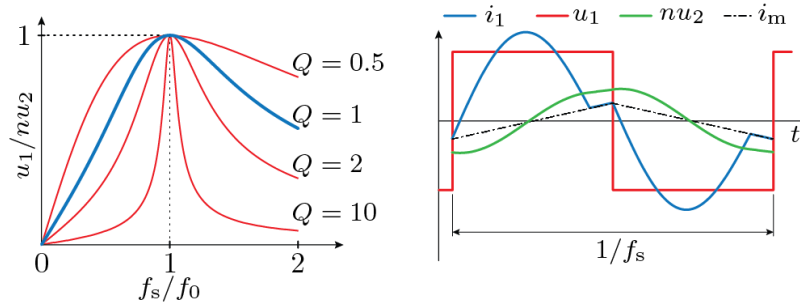
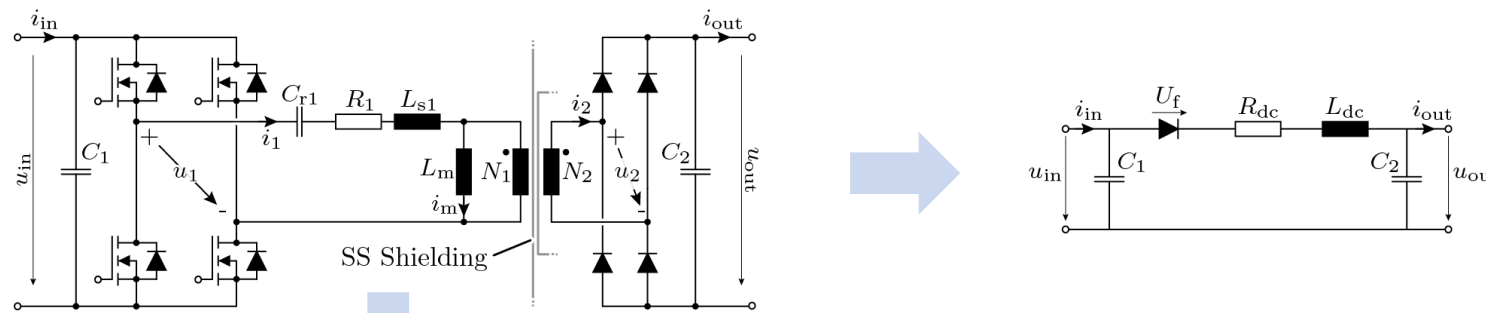
- Different from the OFC WPT, SS losses do not depend on the air gap field in PFC WPT.

Mode of Operation



Parallel-field Concept WPT — Voltage-Impressed DCX Operation

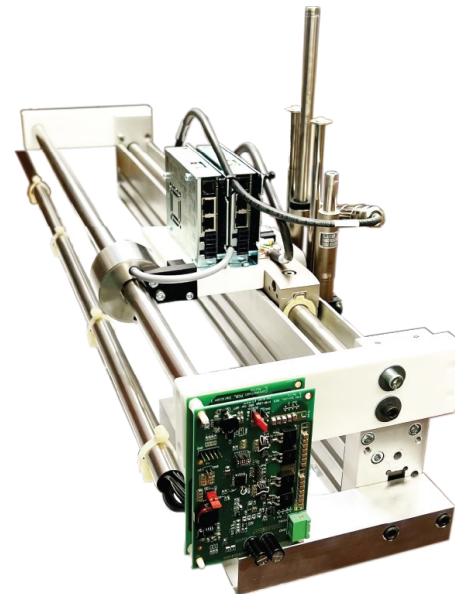
- High magnetic coupling → operation of the WPT system as a series resonant converter.
- Switching frequency \leq resonant frequency → soft switching achieved → **“DC transformer” (DCX)**.



◀ Operation of the PFC WPT system as a “DC transformer”.

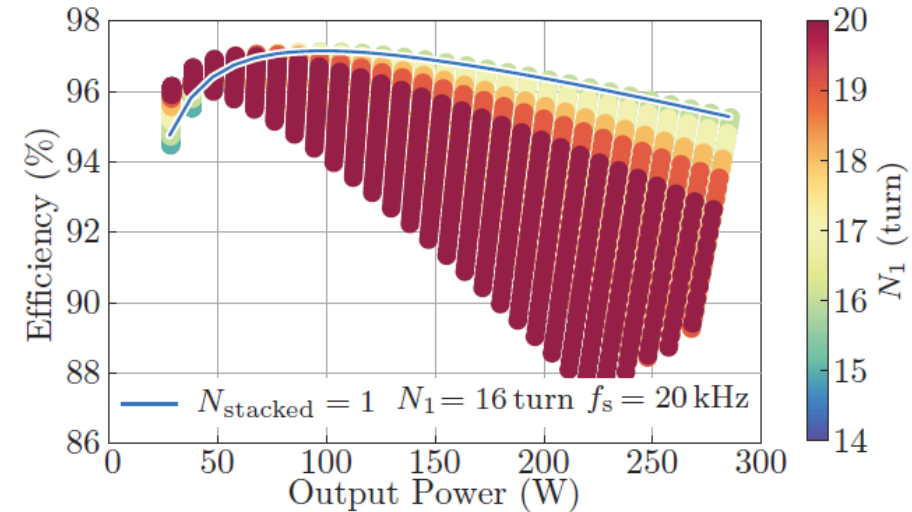
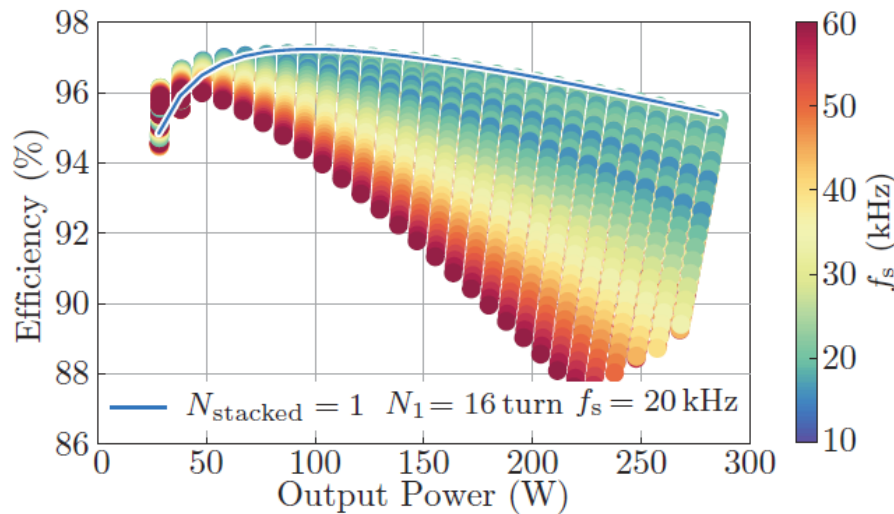
- The DCX couples the output voltage tightly to the input voltage **without the need for closed-loop control**.
- There is **no need for a communication link** between the primary and the secondary side.

— *Hardware Prototype* —



Hardware Prototype — Optimization result

- Swept parameters for different power levels: frequency $f_s = 5 \dots 60$ kHz, turns $N_1 = N_2 = 4 \dots 20$ turns.
- Number of secondary cores: $N_{\text{stacked}} = 1$.

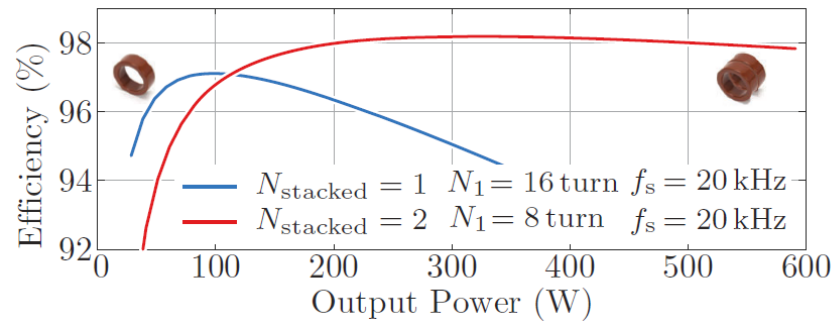


▲ Efficiency vs output power in dependence of the operating frequency f_s and the number of turns in the primary N_1 .

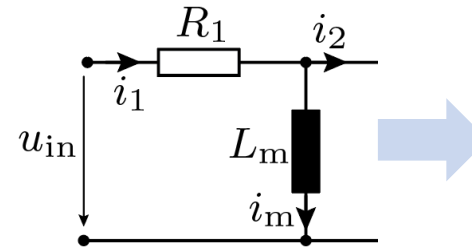
- Optimum operation frequency \rightarrow consequence of the core loss model: $P_{\text{core}} \propto B^a \cdot f^b$.
- The blue line indicates the best design with one stacked core ($N_{\text{stacked}} = 1$, $N_1 = 16$ turns, $f_s = 20$ kHz).

Hardware Prototype — Number of Cores on the Secondary

- The magnetic material area A_{fe} is increased by increasing the number of stacked cores $N_{stacked}$.
- 1 core \rightarrow 90 gram, 2 stacked cores \rightarrow 180 gram.



▲ Efficiency versus output power in dependence of the number of stacked cores.



▲ Equivalent circuit.

$$\Psi_m = \frac{U_{in}}{4 \cdot f_s} = \frac{72}{4 \cdot 20k} = 0.9 \text{mWb}$$

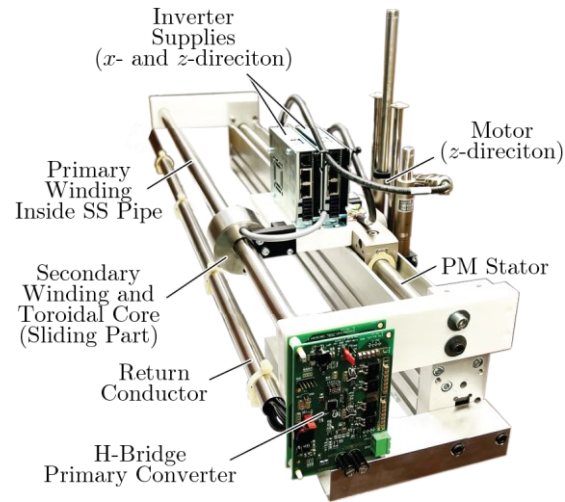
$$\Phi_m = \frac{\Psi_m}{N_1} = B_m \cdot A_{fe} = B_m \cdot N_{stacked} \cdot A_{core}$$

$$B_m = \frac{\Psi_m}{N_1 \cdot N_{stacked} \cdot A_{core}}$$

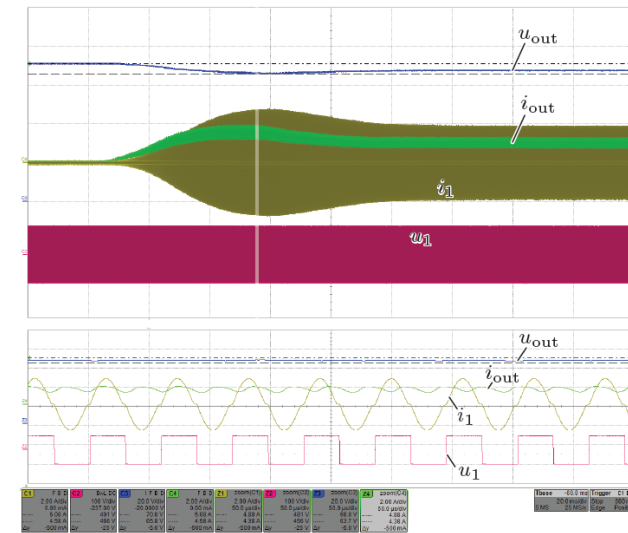
- Higher efficiency and/or power transfer can be achieved with two cores ($N_{stacked} = 2$).
- Stacking the cores \rightarrow lower $N_1 \rightarrow$ reduce the R_1 accordingly \rightarrow larger efficiency and output power.

Hardware Prototype — Measurement

- Prototype of a linear $x - z$ actuator with a PFC WPT system $\rightarrow V_{dc} = 72 \text{ V}$, $f_s = 20 \text{ kHz}$, and $P_{out} = 300 \text{ W}$.
- The inverters supplying the linear motors move together with the linear actuator's slider (in the x-direction).



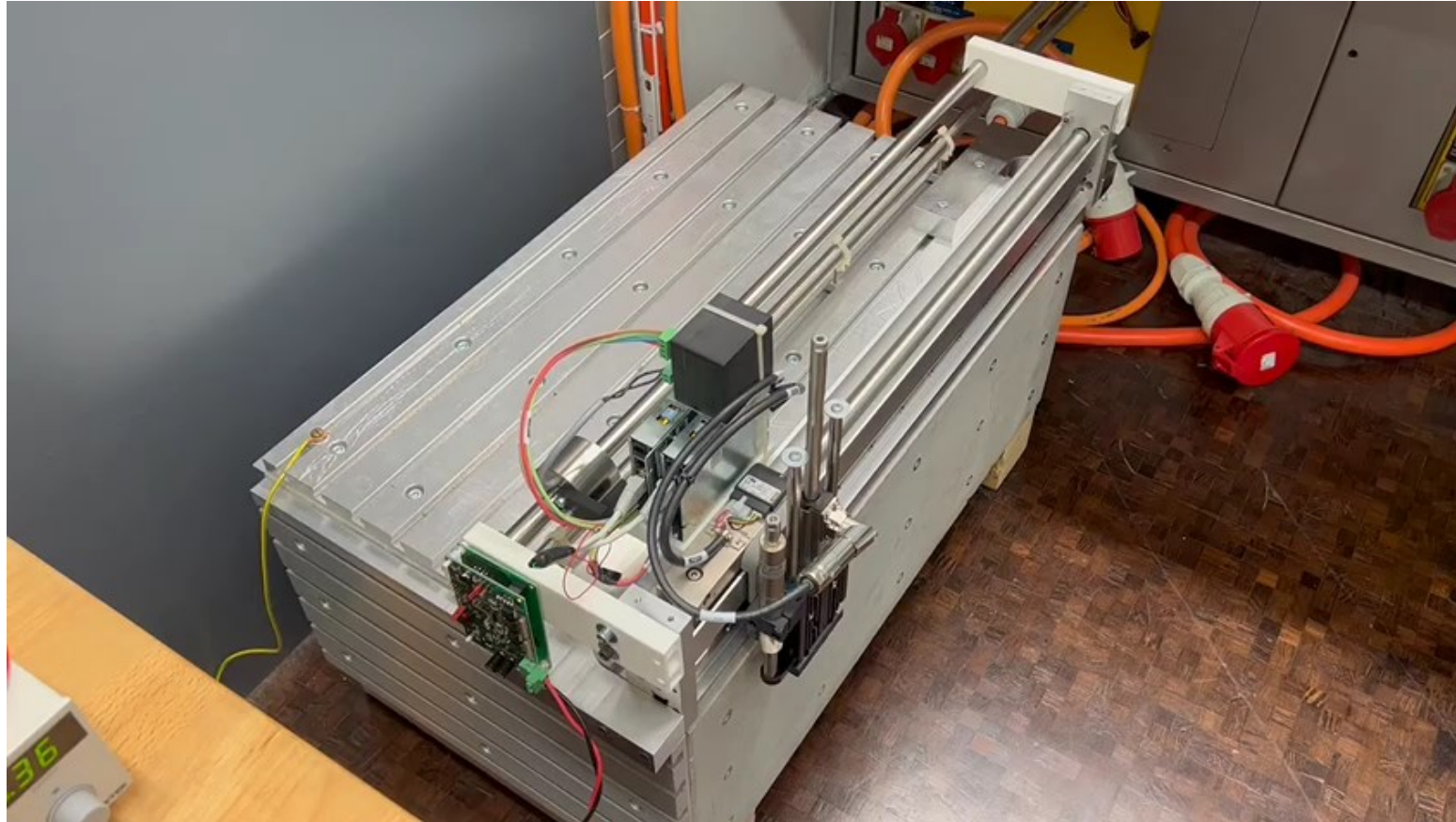
▲ Prototype



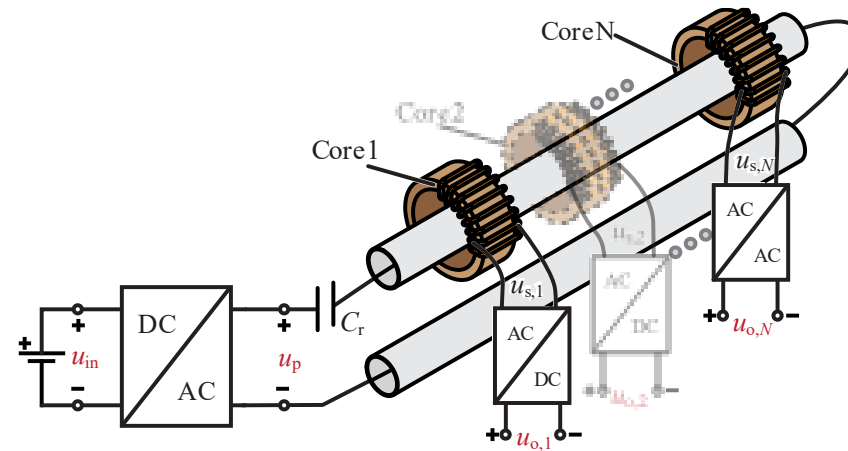
▲ Measured key waveforms during a mechanical load step

- The efficiency is up to **97%** through SS (Wireless power transfer efficiency).
- **Good load regulation** without the need for a closed-loop control system.

Hardware Prototype — Operation

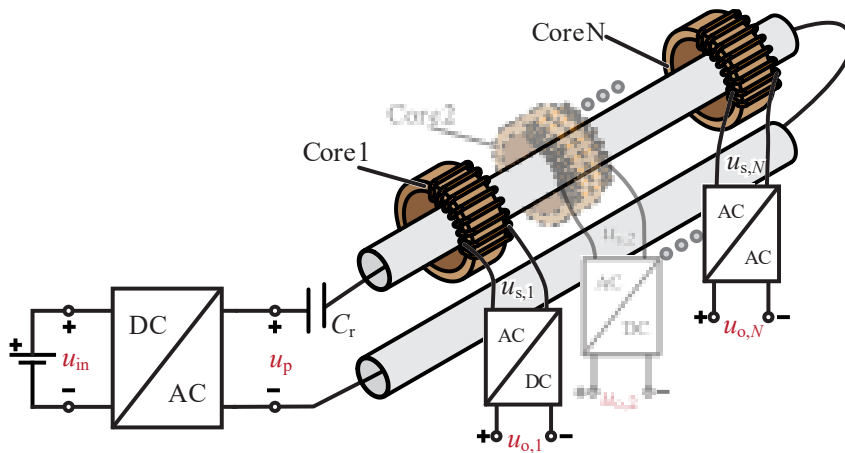


Multi-Receiver PFC WPT

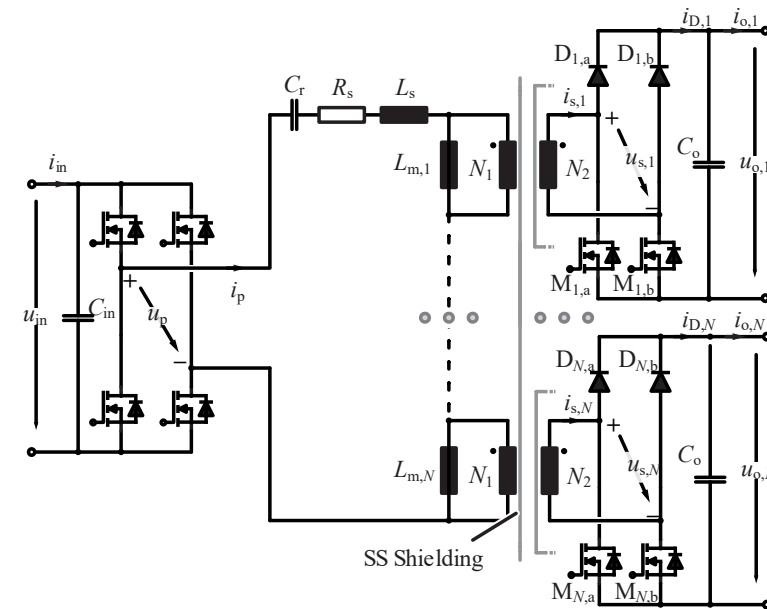


Multiple Receivers— Automatic Time-Sharing Operation

- More than one receiver → magnetic series connection of the secondary windings → the output voltage is uncontrollable (shared by the number of secondaries).
- Automatic time-sharing operation for the PFC WPT linked to multiple receivers without communication and close-loop control.



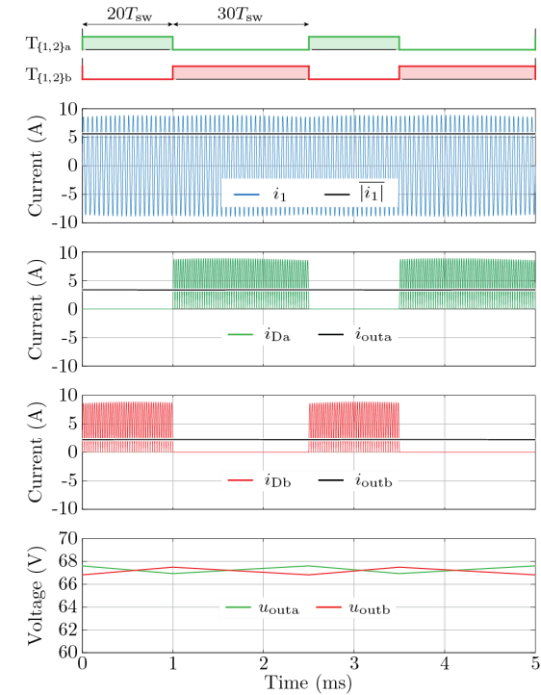
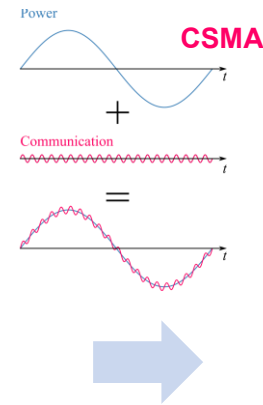
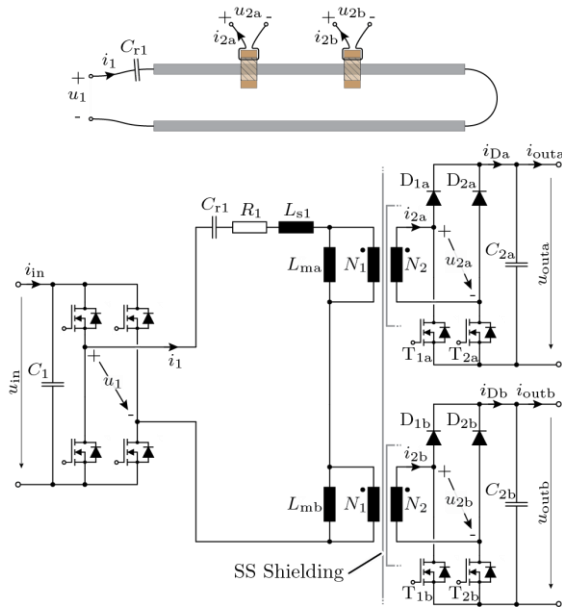
▲ Conceptual physical arrangement of multiple receivers



▲ Electrical equivalent circuit of multiple receivers

PFC WPT — Operation with Multiple Receivers

- Multiple independent drivers and power suppliers → coupling between the receivers.
- Time-sharing approach for multiple receivers.



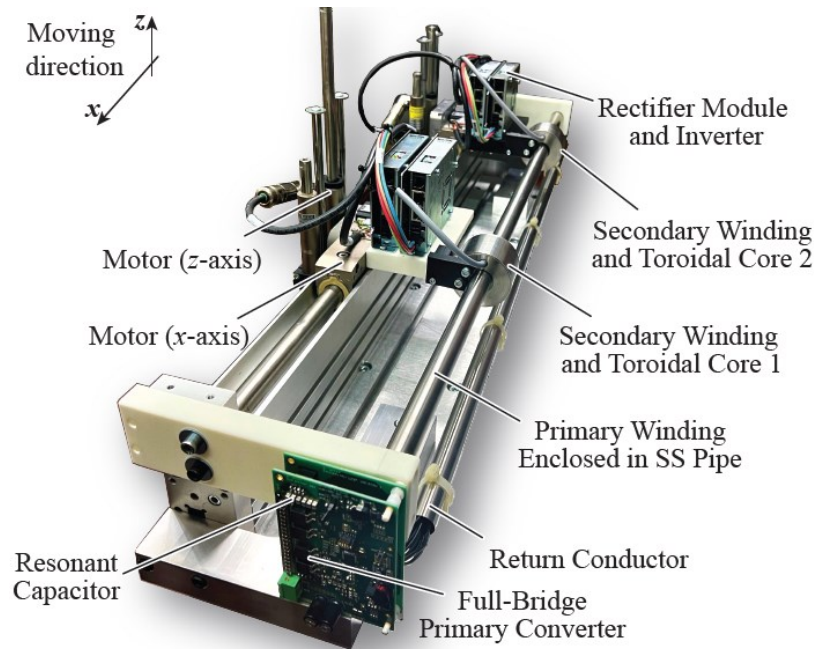
▲ Two receivers WPT circuit.

▲ Simulation results.

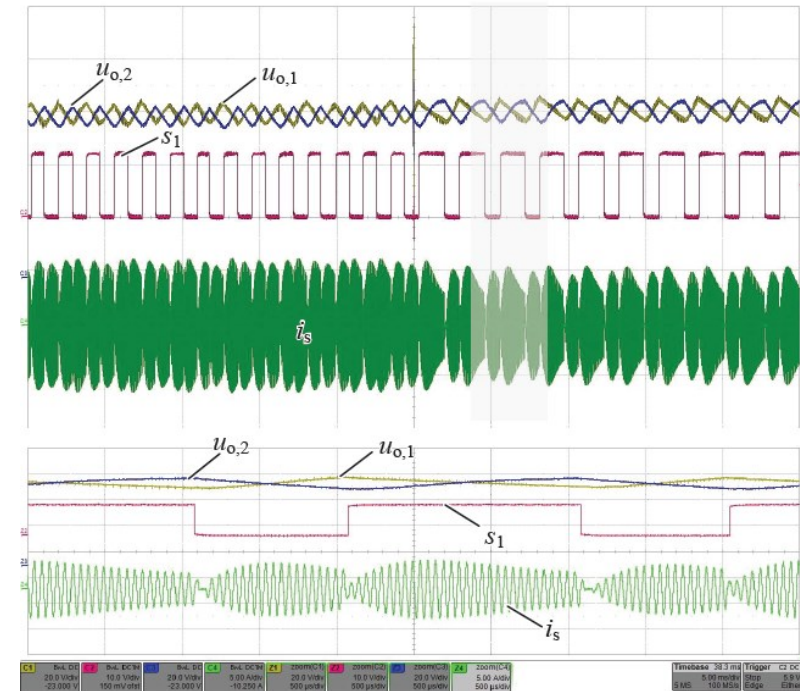
- The relative on-times depend on the respective output powers as: $D_{a \text{ or } b} = \frac{P_{a \text{ or } b}}{P_a + P_b}$.

Hardware Prototype — Two receivers

- Prototype of 2 linear $x - z$ actuators with a PFC WPT system → $V_{dc} = 72 \text{ V}$, $f_s = 20 \text{ kHz}$, and $P_{out} = 100 \text{ W} * 2$.
- Automatically adjusts switching duration of each module.



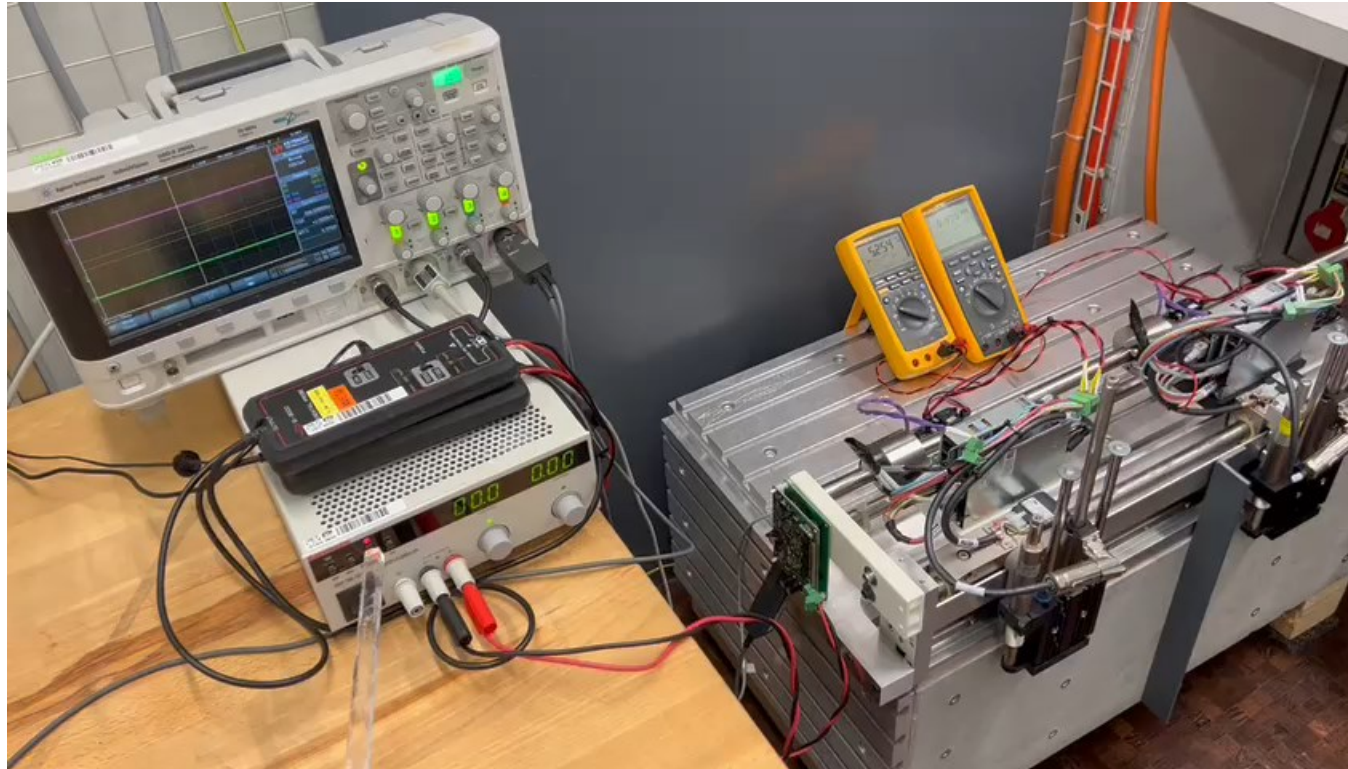
▲ Hardware prototype



▲ Experimental result at transition.
 (One module has a load step change from full load to half load, while the other is at full load.)

Hardware Prototype — Two receivers

- Video

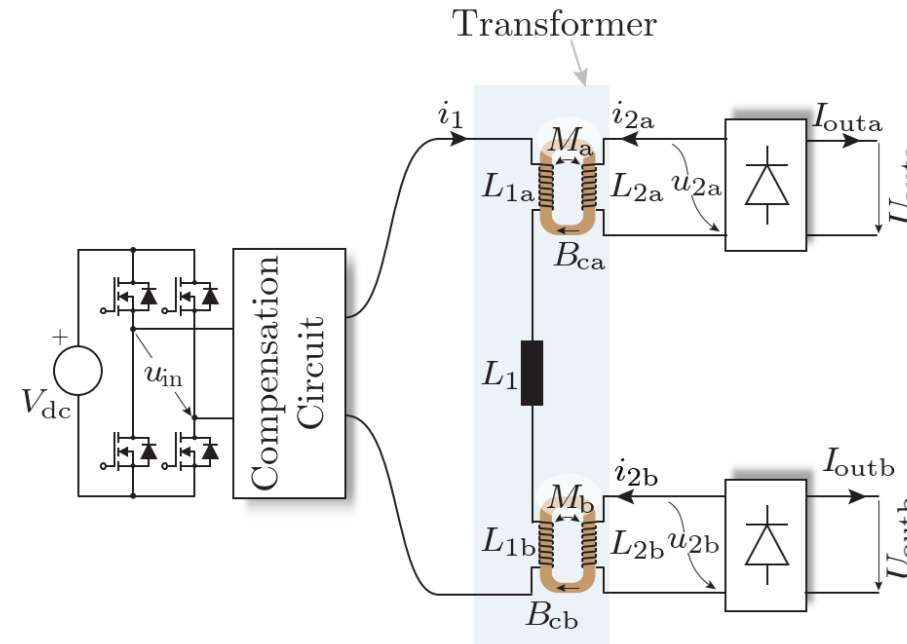
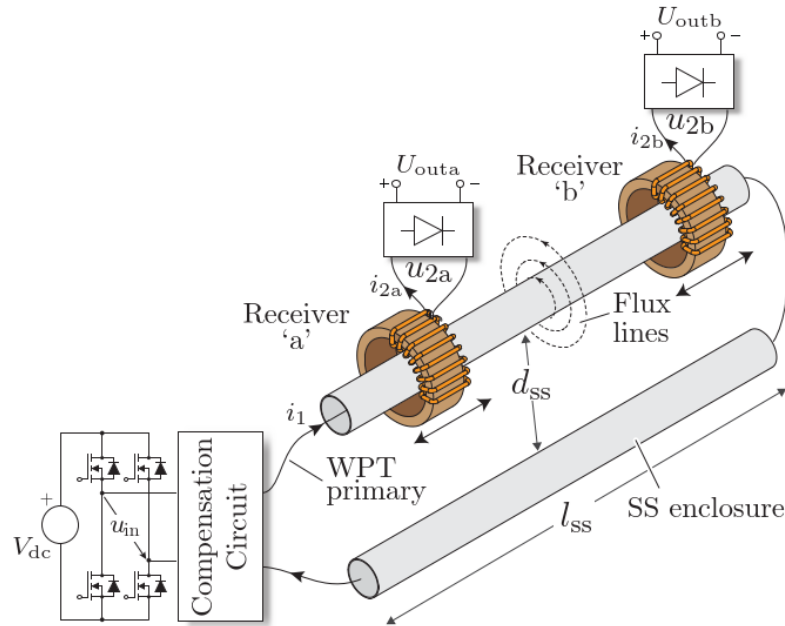




—— *Current Impressed PFC* ——

WPT to Multiple Sliders

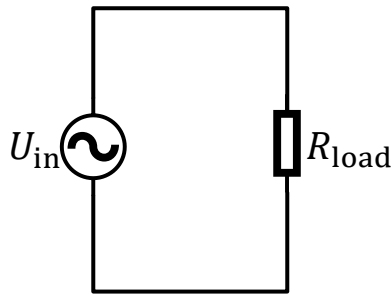
- Multiple independent sliders to be wirelessly powered
- Load-independent operation → Voltage control is not required
- Cross-interaction between multiple loads → Synchronization and/or time-sharing is required



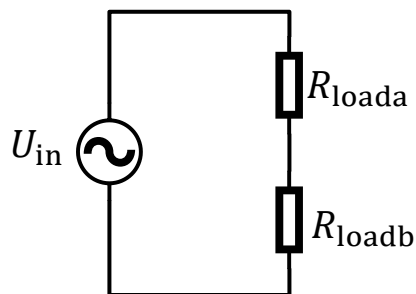
- Magnetic flux density in the core should be within the saturation limits

Voltage-Impressed WPT vs. Current-Impressed WPT

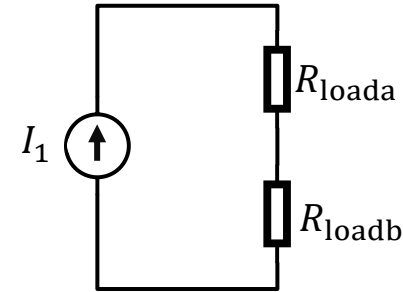
- Single receiver with voltage-impressed WPT (DC-X) → load-independent operation
- Multiple receivers → Equivalent to multiple loads connected in series
 - Voltage-impressed WPT → Voltage is shared between loads → time sharing control
 - Current-impressed WPT → load-independent operation



- ▲ Voltage-impressed WPT
- ▲ Single-receiver

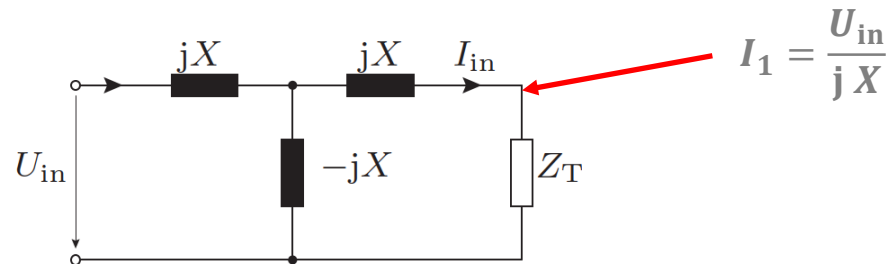


- ▲ Voltage-impressed WPT
- ▲ Multiple-receivers



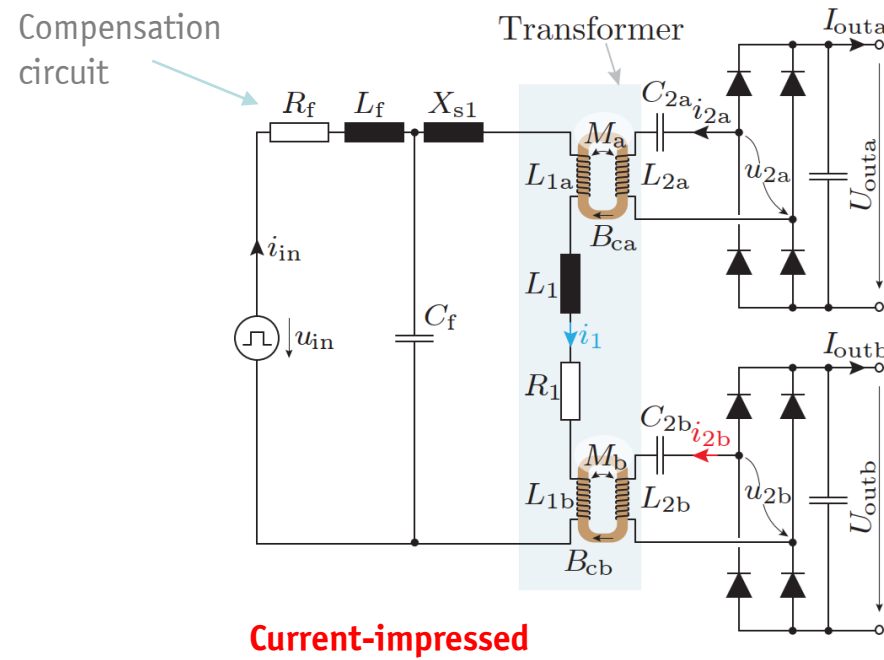
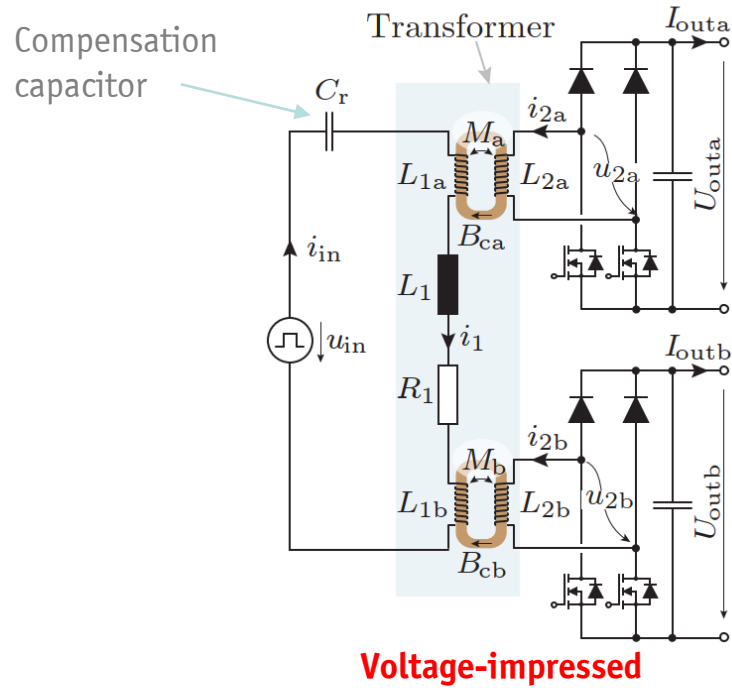
- ▲ Current-impressed WPT
- ▲ Multiple-receivers

- Voltage-impressed system can be converted to a current-impressed system
- Symmetric T-network:



Conventional Methods

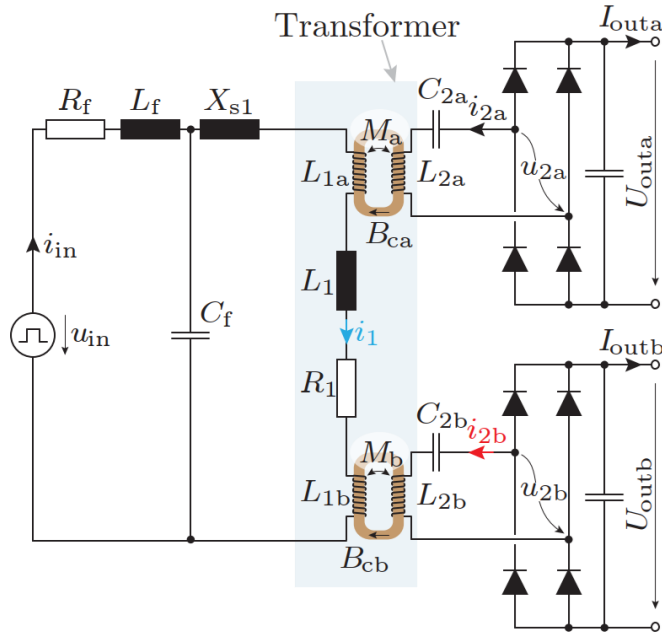
- Voltage-impressed and current-impressed methods
- Compensation circuits change the voltage/current impressed transformer



- Voltage-impressed → Cross-interaction between multiple loads → Requires time-sharing
- Current-impressed → Independent operation of multiple receivers → No control is needed

Conventional Current-Impressed Method

- Primary current is impressed
- Load independent output voltage
- Primary and secondary currents are 90 degrees out of phase



$$I_1 = \frac{U_{in}}{j \omega L_f}$$

$$I_{2\{a,b\}} = -j \left(\frac{\omega M_{\{a,b\}}}{R_{eq\{a,b\}}} \right) I_1 =$$

$$U_{2\{a,b\}} = \frac{M_{\{a,b\}}}{L_f} U_{in} \quad \leftarrow \text{Load-independent voltage}$$



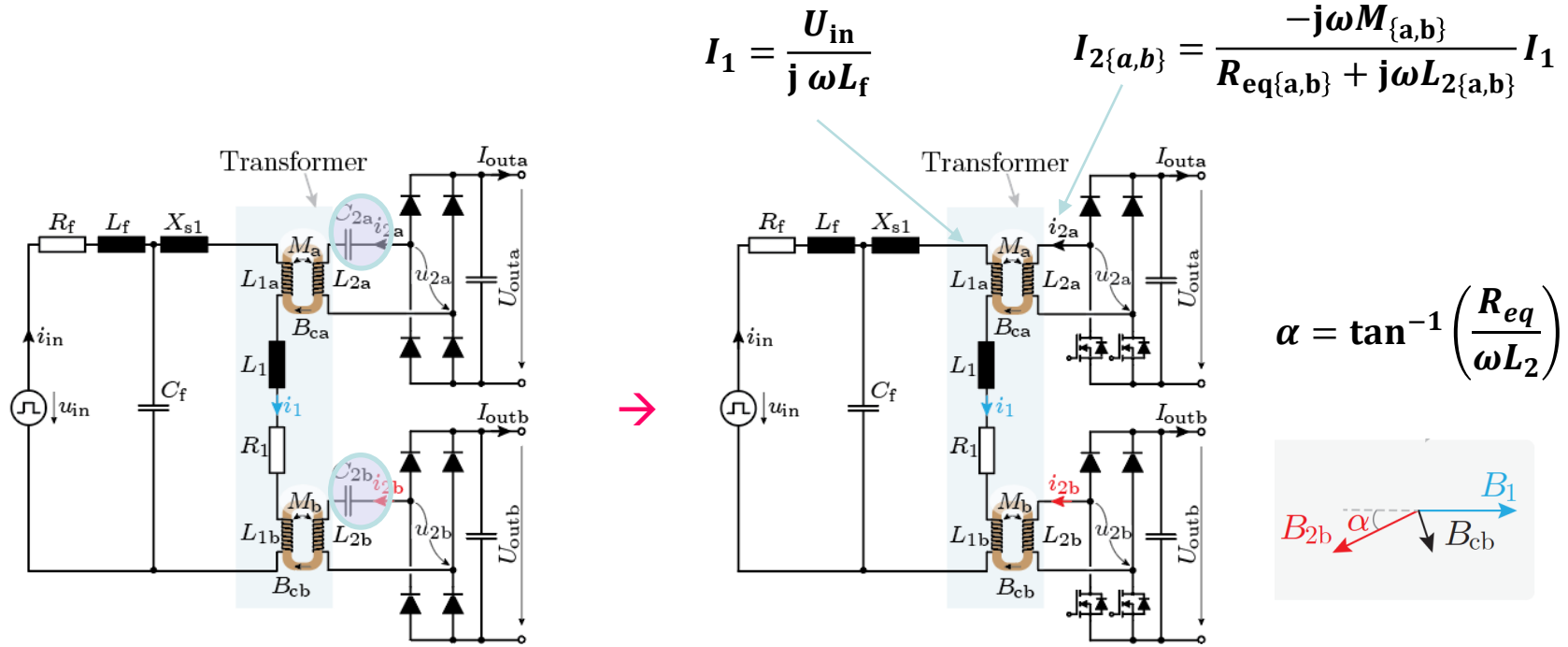
- Load-dependent flux density
- Core flux density increases with high-permeability

$$|B_{c\{a,b\}}| = G_v U_{in} \sqrt{\frac{N_2^2 \mu^2}{l_e^2 R_{eq\{a,b\}}^2} + \frac{1}{k_{\{a,b\}} A_e \omega^2 N_2^2}}$$

A_e and l_e - effective area and length of the core
 N_2 - secondary number of turns
 μ - effective permeability of core material
 $k_{\{a,b\}} = M_{\{a,b\}} / \sqrt{L_{1\{a,b\}} L_{2\{a,b\}}}$ - coupling coefficient

Proposed Current-Impressed Method

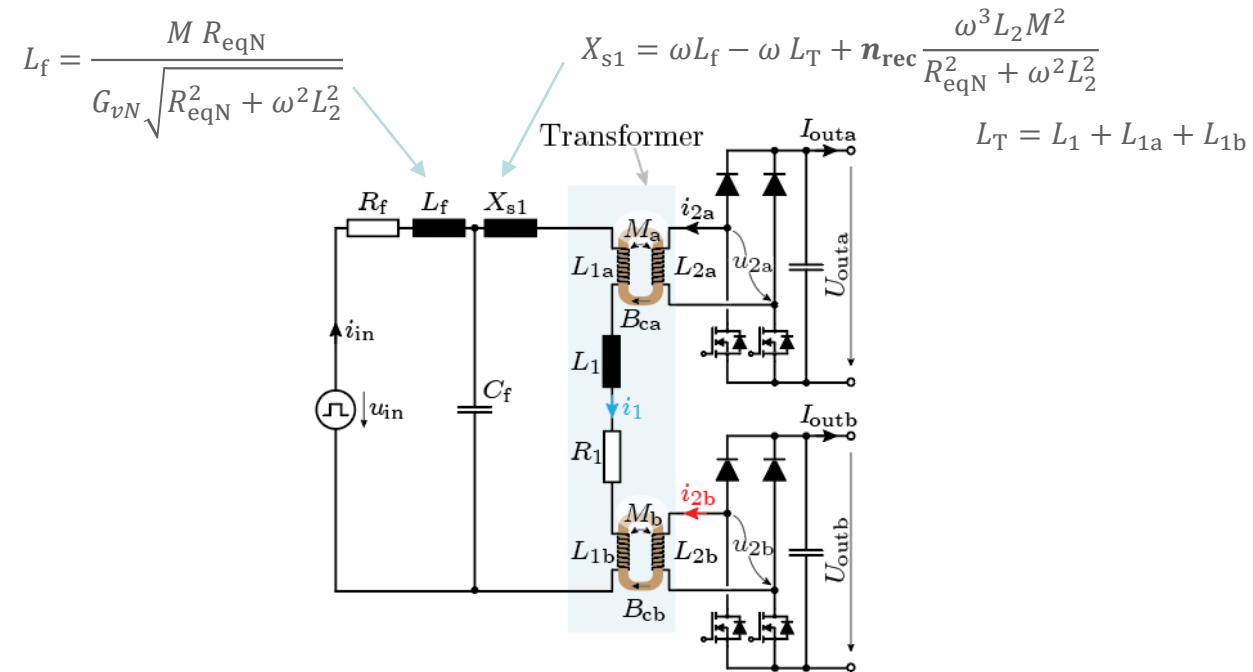
- Secondary compensation is removed
- Primary and secondary currents compensate core flux density



- Output voltage is load dependent
- The circuit is designed at a nominal load

Proposed Method - Circuit Design

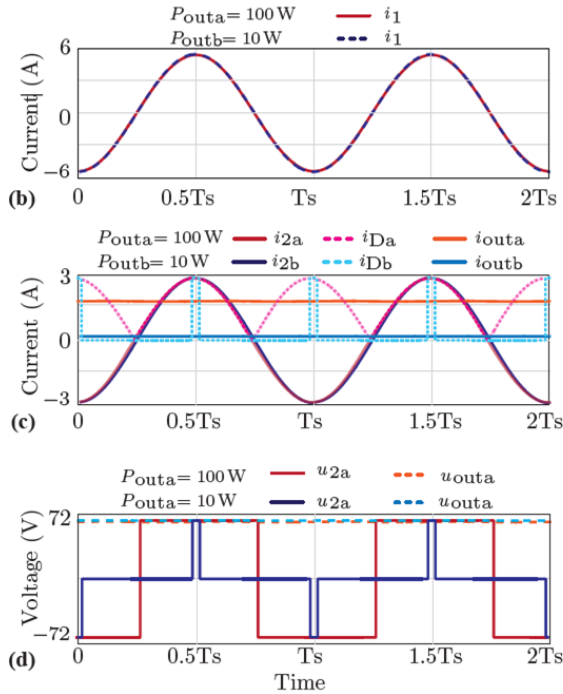
- Designed at nominal load
- The compensation inductor defines the voltage gain
- Series reactance X_{s1} is tuned to have zero-phase-angle at the input



- Load voltage needs to be controlled by changing the load
- Active rectifiers connected to multiple sliders work independently

Proposed Method – Control

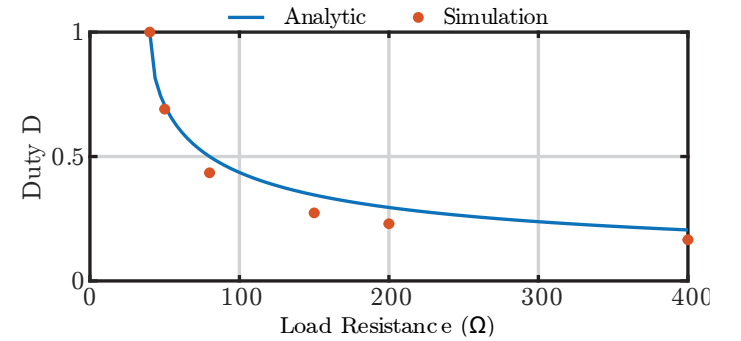
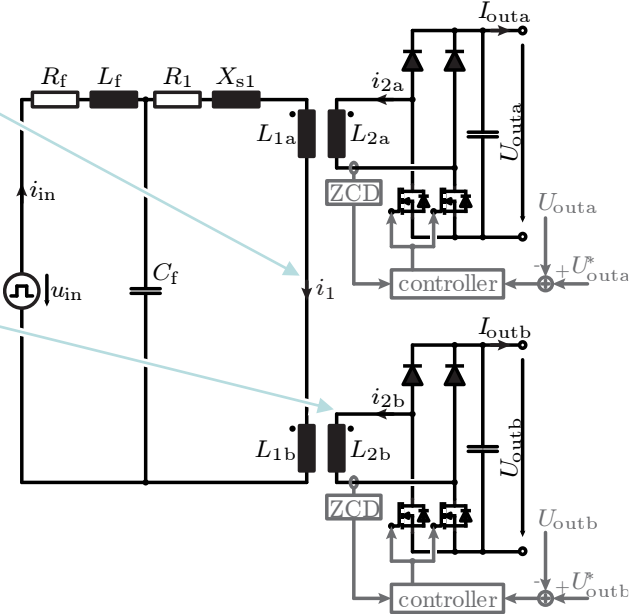
- Continuous control of active rectifier duty will allow voltage control at partial load
- Maximum load power at duty $D=1$



Primary current

Secondary current

Secondary voltage



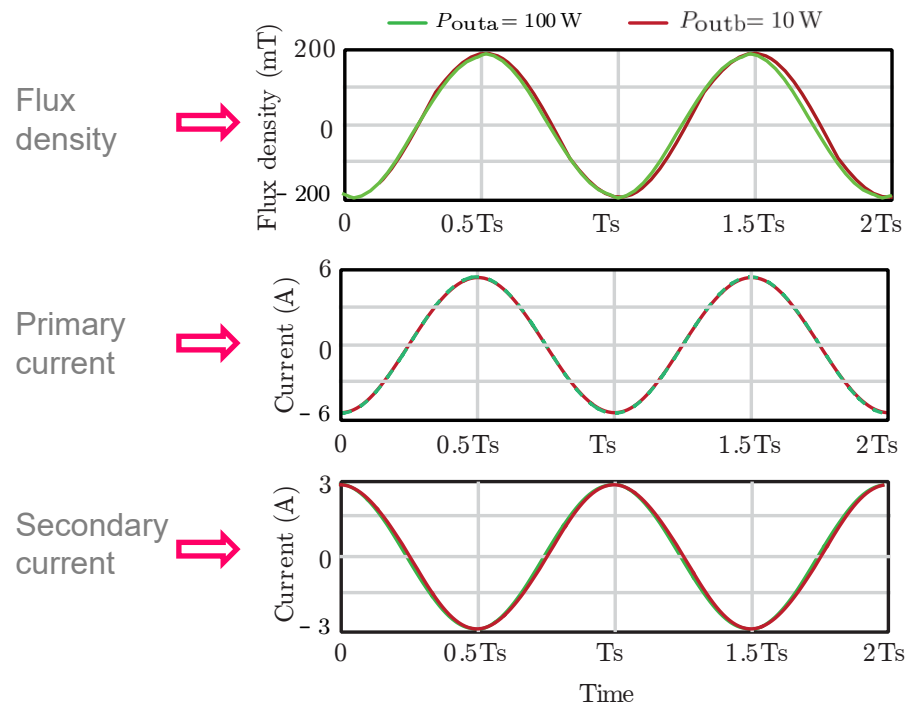
$$D_{\{a,b\}} = \frac{\pi}{2} \cos^{-1} \left(1 - \frac{R_{loadN}}{R_{load\{a,b\}}} \sin^2 \left(\frac{D_N \pi}{2} \right) \right)$$

R_{loadN} - Nominal load resistance
 D_N - Nominal duty at nominal load
 $R_{load\{a,b\}}$ - Load resistance

- Natural overload protection
- $D_N < 1 \rightarrow$ overload is allowed

Core Flux Density

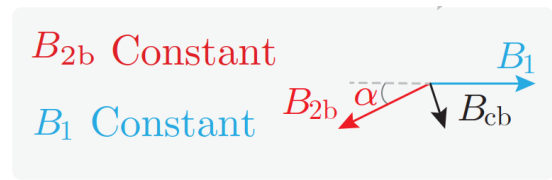
- Both primary and secondary currents are impressed
- Almost compensating core flux density



$$|B_{c\{a,b\}}| = \frac{G_v U_{in}}{8k} \sqrt{\frac{64}{\omega^2 A_e^2 N_2^2} + \frac{\pi^2 (1 - k_{\{a,b\}})^2 N_2^2 \mu^2}{l_e^2 R_{load\{a,b\}}^2 \sin^4\left(\frac{\pi D_N}{2}\right)}}$$

$$k_{\{a,b\}} \approx 1$$

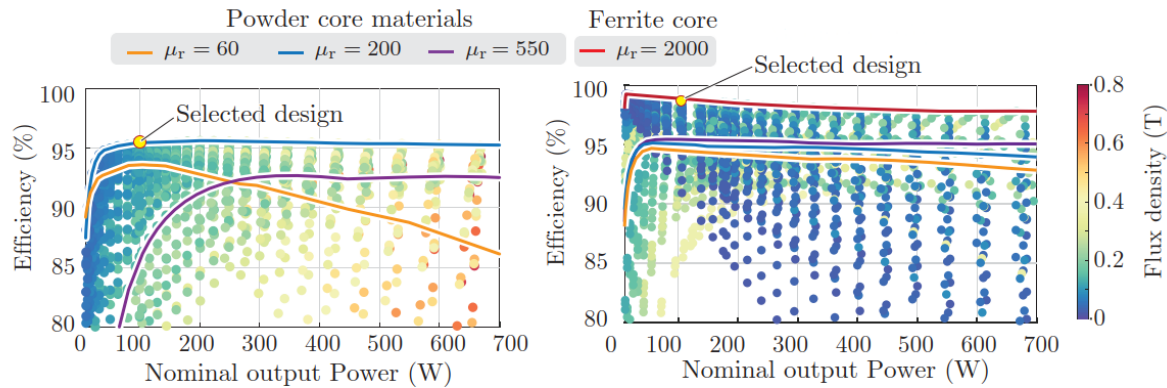
$$|B_{c\{a,b\}}| = \frac{G_v U_{in}}{\omega A_e N_2}$$



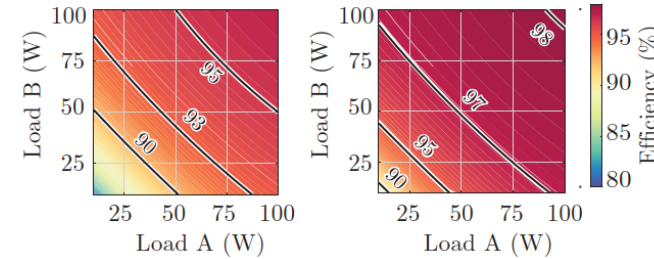
- Load independent core flux density
- Low magnetizing current due to compensating primary and secondary currents

Optimization

- **Conventional current-impressed approach**
 - 96% efficiency with MPP 200 powder core
 - Limited cores types μ [200 300] due to higher flux density
- **Proposed current-impressed approach**
 - 98 % efficiency with conventional ferrite core
- **Low partial load efficiency due to impressed currents**



Parameter	Symbol	Value	Unit
DC input voltage	U_{dc}	72	V
DC output voltage	$U_{out\{a,b\}}$	72	V
Output power (per receiver)	$P_{out\{a,b\}}$	100	W
Length of SS pipe	l_{ss}	118	cm
Distance between SS pipes	d_{ss}	10	cm



Parameter	N_1	N_2	f_s	R_{loadN}
Range	[5, 30]	[5, 50]	[5 kHz, 50 kHz]	[5 Ω , 400 Ω]

Comparative Evaluation – for Multiple Receivers

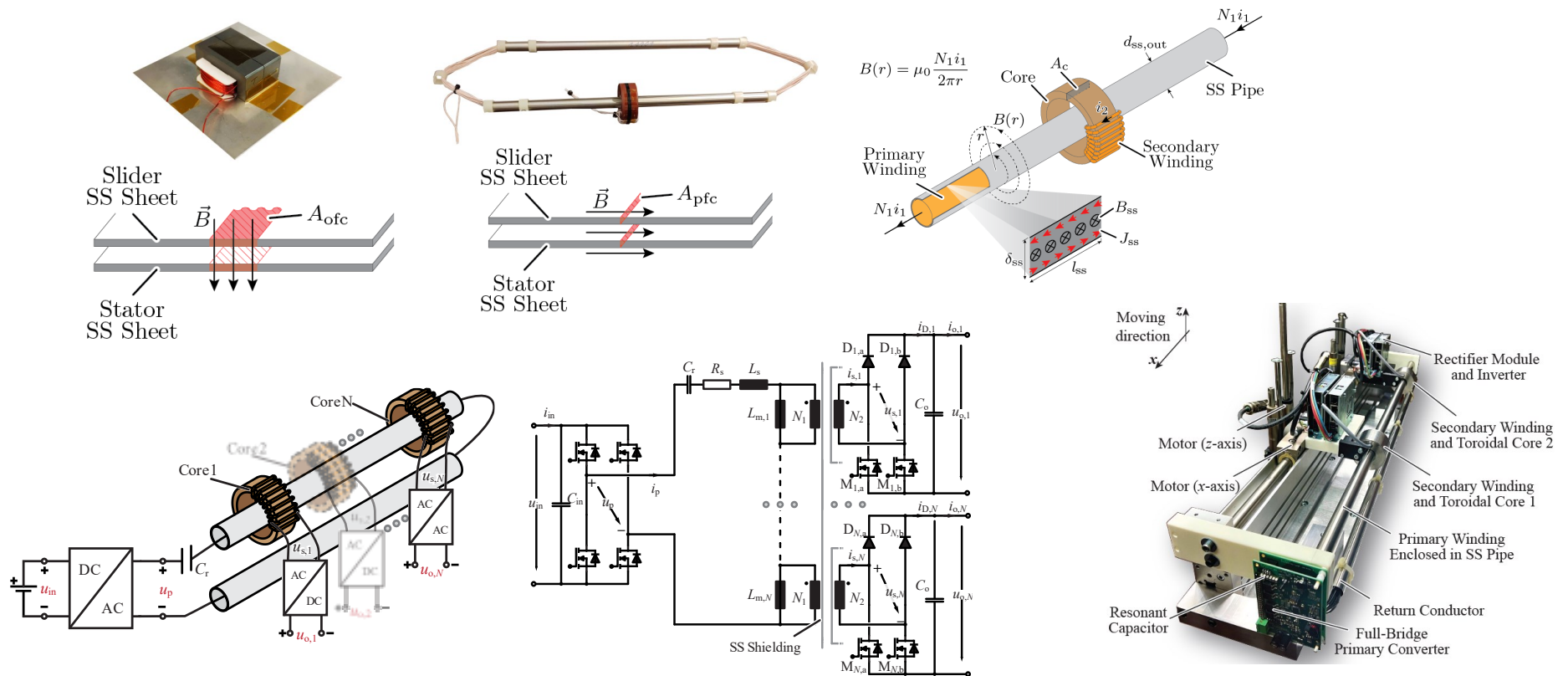
- Both systems have similar
 - components values (compensation circuit)
 - Voltage and current stresses
- Proposed approach results in significantly low core flux densities

	Conventional	Proposed
Voltage control	Not needed	Needed for individual loads – no synchronization needed
Overload	Possible core saturation	Inherent overload protection
Sensitivity	Robust against slight variations of resonance	Sensitive to resonance tuning
Material	Limited material choices due to core saturation	Conventional ferrite materials can be used

Parameter	Conventional	Proposed
Core material	MPP 200	Ferrite
Frequency	25 kHz	30 kHz
Primary turns N_1	10	10
Secondary turns N_2	35	25
Primary inductance $L_1 + L_{1a} + L_{1b}$	279.2 μ H	1.0 mH
Secondary inductance $L_{2\{a,b\}}$	306.2 μ H	2.8 mH
Mutual inductance M	87.5 μ H	1.1 mH
Primary resistance R_1	240 m Ω	266 m Ω
Compensation inductance L_f	87.5 μ H	88.5 μ H
Primary capacitance ¹ ($-1/\omega X_{s1}$)	211 nF	967 nF
Secondary capacitance $C_{2\{a,b\}}$	132 nF	–
Efficiency at nominal load	95.8 %	98 %
Core weight	190 g	120 g
Core losses	2.6 W	300 mW
Primary current (rms) at nominal load	4.7 A	3.9 A
Secondary current (rms) at nominal load	1.43 A	1.43 A
Phase between primary and secondary currents	90°	-175.5°

Part 3 Outlook

- OFC and PFC wireless power transfer
- Multiple receivers → Voltage impressed & Current impressed





— *Biography* —

Biography of the Speaker



Spasoje Mirić received his B.Sc., M.Sc., and Ph.D. degrees in electrical engineering from the University of Belgrade, School of Electrical Engineering in 2012, 2013, and 2018 respectively, focusing on power electronics systems and drives. In 2021 he defended his second Ph.D. thesis at ETH Zurich at the Power Electronic Systems Laboratory (PES) in advanced mechatronic systems. During his Ph.D. project, he focused on linear-rotary actuator systems with magnetic bearings, which resulted in two new machine topologies patented. Since 2021, he has been with PES as a post-doc researcher, focusing on WBG power converter optimization with hard and soft-switching, new modulation techniques of flying capacitor converters, wireless power transfer systems, and eddy-current-based position sensor systems.

From **1st of January 2023** → TT Ass. Prof. @ University of Innsbruck

New Laboratory:

Drive and Energy Systems Laboratory (**i-DES**)

miric@lem.ee.ethz.ch
spasoje.miric@uibk.ac.at





Thank you!

